Advanced Signal Processing Techniques for Real-Time Estimation and Control of Harmonics in Smart Electric Grid

Thesis
Submitted in partial fulfillment of the requirements
for the award of the degree of

Doctor of Philosophy
in
Electrical Engineering

by

O.V.S.R.Varaprasad
(Roll No. 701232)

Supervisor

Dr. D.V.S.S.Siva Sarma
Professor (HAG)

Department of Electrical Engineering
NATIONAL INSTITUTE OF TECHNOLOGY WARANGAL
(An Institute of National Importance)
Warangal – 506 004, Telangana State, India
December – 2019

APPROVAL SHEET

This Thesis entitled "**Advanced Signal Processing Techniques for Real-Time Estimation and Control of Harmonics in Smart Electric Grid**" by **Mr. O.V.S.R.Varaprasad** is approved for the degree of Doctor of Philosophy

Examiners

_____

_____

_____

Supervisor

Dr. D.V.S.S.Siva Sarma
Professor (HAG)
EED, NIT Warangal

Chairman

Dr. S.Srinivasa Rao
Professor & Head,
EED, NIT Warangal

Date: _____

DEPARTMENT OF ELECTRICAL ENGINEERING
NATIONAL INSTITUTE OF TECHNOLOGY WARANGAL
WARANGAL – 506 004

DEPARTMENT OF ELECTRICAL ENGINEERING

NATIONAL INSTITUTE OF TECHNOLOGY WARANGAL

CERTIFICATE

This is to certify that the thesis entitled **"Advanced Signal Processing Techniques for Real-Time Estimation and Control of Harmonics in Smart Electric Grid"**, which is being submitted by **Mr. O.V.S.R.Varaprasad** (Roll No. 701232), is a bonafide work submitted to National Institute of Technology Warangal in partial fulfilment of the requirements for the award of the degree of **Doctor of Philosophy** in Electrical Engineering. To the best of my knowledge, the work incorporated in this thesis has not been submitted elsewhere for the award of any degree.

Date:

Place: Warangal

Dr. D.V.S.S.Siva Sarma
(Thesis Supervisor)
Professor (HAG)
Department of Electrical Engineering
National Institute of Technology Warangal
Warangal – 506004

DECLARATION

This is to certify that the work presented in the thesis entitled "**Advanced Signal Processing Techniques for Real-Time Estimation and Control of Harmonics in Smart Electric Grid"** is a bonafide work done by me under the supervision of **Dr. D.V.S.S.Siva Sarma**, Department of Electrical Engineering, National Institute of Technology Warangal, India and was not submitted elsewhere for the award of any degree.

I declare that this written submission represents my ideas in my own words and where others ideas or words have been included; I have adequately cited and referenced the original sources. I also declare that I have adhered to all principles of academic honesty and integrity and have not misrepresented or fabricated or falsified any idea/date/fact/source in my submission. I understand that any violation of the above will be a cause for disciplinary action by the institute and can also evoke penal action from the sources which have thus not been properly cited or from whom proper permission has not been taken when needed.

Date:

Place: Warangal

O.V.S.R.Varaprasad
(Roll No: 701232)

Dedicated to

AMMA-NANNA

for

Nurturing Sincerity and Integrity in me

which made me ***who I am*** *that I am proud of*

My Sincere Gratitude

Apart from personal efforts and steadfastness to work, constant inspiration and encouragement given by a number of individuals acted as the driving force in attaining this day in my life. To quote them all may be an onerous task but direct and indirect assistance and guidance received is gratefully acknowledged. I would like to express my feelings of gratefulness and submit my gratitude for them further in the following lines.

I express my deep sense of gratitude my beloved parents **Smt. Sakuntala and Sri. Somanadham Oruganti** for the permission to carry research. I am fortunate to be showered with heir sincere prayers, blessings, constant encouragement, shouldering the responsibilities and moral support rendered to me throughout my life, without which my research work would not have been possible.

I take this opportunity to express my sincere gratitude to my august supervisor **Dr. D.V.S.S.Siva Sarma,** Professor (HAG), Department of Electrical Engineering, National Institute of Technology Warangal, for his valuable guidance, support, and suggestions. His knowledge, suggestions, and discussions helped me to become a capable researcher. He has shown me the interesting side of this wonderful and potential research area. His continued encouragement helped me to overcome the difficulties encountered in my research.

I am honoured to receive Power System Operation Corporation Limited (POSOCO) Power System Award (PPSA) – 2017 for this research from POSOCO Ltd., India in collaboration with Foundation for Innovation & Technology Transfer (FITT), IIT Delhi.

I am very much thankful to **Dr. S.Srinivasa Rao**, Professor & Head, Department of Electrical Engineering for his constant encouragement, support and cooperation.

I take this privilege to thank all my Doctoral Scrutiny Committee members, **Dr. M.Sydulu**, Professor (HAG), Department of Electrical Engineering, **Dr. A.V.Giridhar**, Assistant Professor, Department of Electrical Engineering and **Dr. R.B.V.Subramanyam**, Professor & Head, Department of Computer Science Engineering for their detailed review, constructive suggestions and excellent advice during the progress of this research work.

I wold also thank former Heads of the Department of Electrical Engineering **Dr. N.Subrahmanyam, Dr. N.Vishwanathan, Dr. V.T.Somasekhar** for their valuable suggestions and concern during my research work.

I also appreciate the encouragement from teaching, non-teaching staff, and fraternity of Department of Electrical Engineering of NIT Warangal. They have always been encouraging and supportive.

I wish to express my sincere thanks to **Prof. N.V.Ramana Rao**, Director, NIT Warangal for his official support and encouragement.

I acknowledge my earnest gratitude to the Ministry of Human Resources Development (MHRD), Government of India for granting me the Ph.D stipend for five years.

I gratefully acknowledge the Department of Science & Technology (DST), Govt. of INDIA and Indo – US Science & Technology Forum (IUSSTF) for sponsoring me under Bhaskara Advanced Solar Energy (BASE) Fellowship – 2015.

I convey my utmost respects to **Prof. Marcelo Godoy Simões** for accepting me as a visiting scholar under BASE fellowship – 2015 at the Advanced Control of Energy Power Systems (ACEPS) research group of Electrical Engineering Department at Colorado School of Mines, USA. I express my sincere appreciation for introducing me to Conservative Power Theory which has opened up new vistas for this research. I would like to thank the management of Colorado School of mines for their support.

I convey my special thanks to my roommates **Dr. Sumedh, Mr,Yeswath, Mr.Surya, Dr.Swaroop guggilam, Dr.Sukriti Manna, Mr. D.Vinay** for good company during my stay in USA. I would like to thank **Dr. Abdullah, Dr. Ali, Dr. Farnaz, Dr. Mohhammad, Dr. Bannaeh, Mr. Ricardo, Mr. Hakeem** for their support in ACEPS lab in USA. I also thank **Prof. Helmo, Dr. Tiago** for their support and help during this thesis work.

I would also convey my sincere thanks to **Mr. Raviteja Chivukula** for introducing to NI-cRIO hardware architecture and configuration. I express my gratitude and indebtedness to **Dr. Ravi Kumar Varma Bhupatiraju** for extending me the support and inspiration during my research. I also thank my senior colleagues **Dr. N.Rama Devi, Mr. G.Sunil Kumar** for their help during my research.

I appreciate my friends and research scholars for their instant help, cooperation, advice, suggestion, and moral support during my stay. The list may go long but some of them I would like to mention are **Dr. K.Ramsha, Dr. B.Durga Hari Kiran, Dr.Venu, Dr.Praveen, Mr. Hareesh, Mr. L.Suresh, Dr. T.Kiran, Dr. Phani, Mr. Kalyan, Mrs. Pujitha, Mr. Hema Kumar** for staying with me during my ups and downs.

I acknowledge my sincere gratitude and special thanks to my well-wisher **Mr. Hari Prasad Devarapalli** for his valuable time, countless discussions.

I acknowledge my gratitude to all my teachers and colleagues at various places for inculcating interest in studies that continued with me through out.

I am glad to have my life partner, **Teju** even though she missed me a lot during my work. She has been very patient bearing me throughout while I am busy day and night at my lab during this research. I deeply regret for my absence, which was unavoidable.

My brother **Agnihothra Sarma** has always been my strength who supported my parents in my absence at home town, Amalapuram.

Above all, I express my deepest regards and gratitude to "**ALMIGHTY**" whose divine light and warmth showered upon me with perseverance, inspiration, faith and enough strength to keep the momentum of work high even at toughest moments of research work.

O.V.S.R.Varaprasad
Warangal, December 2019

Synopsis

The paradigm shift from the conventional electric grid to a smart electric grid leads to many operational challenges. The modern power electronic based nonlinear loads are causing severe harmonic pollution in the distribution system. A crucial challenge for the smart electric grid is to effectively estimate and control the harmonics in the power system, which requires precise and real-time estimation of the amplitude, phase, and frequency of the power system. The proliferation of harmonics, mainly in a distribution system produced by extensive diffusion of nonlinear loads, power electronic converters, will deteriorate the accuracy of estimation of amplitude, phase, and frequency and at the same time making it hard to track the power system voltage, current and frequency variations. The prime objective of this doctoral thesis work is to develop advanced signal processing techniques that can provide an accurate and fast estimation of all the current harmonic components and also develop selective control techniques to control the harmonics in a smart electric grid.

Consciousness to reduce harmonics in the low voltage distribution grid is increasing because these harmonics significantly affect the operation of the smart electric grid in terms of safety and economy. The methodology must be simple and allow fast computation for harmonics with retrofit computation capabilities. This research work contributes towards real-time estimation of harmonics and their compensation in a modern distribution network. Moreover, for real-time estimation and control of harmonics is essential to have fast and accurate algorithms and associated controllers.

The objective of this thesis is to develop and design methods to estimate and control current harmonics, which are introduced in the distribution system by various nonlinear loads such as consumer electronic equipment i.e. Compact Fluorescent Lamp (CFL), Light Emitting Diode (LED) bulbs, personal computers, printers, scanners, charging units and so forth. The current harmonics produced by the non-linear loads affect the performance of neighbouring linear loads and injects the same to grid which in turn impact the appliances of other innocent residential consumers who does not install harmonic compensation devices in their premises.

Chapter 1 gives the overview of current harmonics problem on smart electric grid, detailed literature survey on estimation and control of harmonics and the author’s contribution for estimation and control of current harmonics in the smart electric grid. Chapters 2 and 3 are dedicated to the estimation of current harmonics, which are periodic and also time-varying in real-time using National Instruments (NI) Compact reconfigurable input-output system (cRIO)

9082. Chapter 4 focus on control of harmonics with Conservative power theory (CPT) based Hybrid Active power filter, Chapter 5 introduces a think-ahead decision making algorithm & CPT based three-phase multifunctional grid-connected PV inverter which minimizes the grid consumption and exploits the full benefit of solar generation simulates various cases of load conditions and validates in real-time using OPAL-RT. Chapter 6 describes the multi-band hysteresis current controlled single-phase multifunctional grid-connected PV inverter interfaced with rooftop solar PV.

The estimation methods developed in this thesis also empower utilities to introduce policies to penalize causes injecting harmonics into the grid and further encourage the introduction of control mechanisms at the same and realize “Swatch Power” (a “Pure Power” with smart features).

Table of Contents

List of Figures

List of Tables

List of Abbreviations

AC	Alternating Current
ADC	Analog to Digital Converter
ADALINE	Adaptive Linear Element
ANN	Artificial Neural Network
APFs	Active Power Filters
API	Active Power Injection
AR	Auto-Regression
ARMA	Autoregressive Moving Average
ASF	Average Switching Frequency
AWs	Advanced Windows
BSS	Battery Storage System
CB	Circuit Breaker
CFL	Compact Fluorescent Lamp
CPT	Conservative Power Theory
CPU	Central processing unit
CW	Cosine Windows
CZT	Chirp Z-Transform
DAQ	Data Acquisition
DB-HCC	Double-Band-Hysteresis Current Control
DC	Direct Current
DC-DC	Direct Current-Direct Current
DFT	Discrete Fourier Transform
DSLIFFT	Dual-Spectrum Line Interpolated Fast Fourier Transform
DVSI	Dual Voltage Source Inverter
EA-AWNN	ESPRIT Assisted – Adaptive Wavelet Neural Network
EKF	Extended Kalman filter
EPLL	Extended Phase Locked Loop
ESPRIT	Estimation of Signal Parameters via Rotational Invariance Technique
FBD	Fryze-Buchholz-Depenbrock
FFT	Fast Fourier Transform
FPGA	Field-Programmable Gate Array

GCI	Grid-Connected Inverter
GI	Generalized Integrator
HAPF	Hybrid Active Power Filter
HB	Hysteresis Band
HCC	Hysteresis Current Control
HHT	Hilbert Hung Transform
IC	Implementation Complexity
IEA	International Energy Agency
IEC	International Electro-technical Commission
IEEE	Institute of Electrical and Electronics Engineers
IELI	Inverter Efficiency under Low Irradiation
IGBT	Insulated-Gate Bipolar Transistor
INC	Incremental Conductance
IPE	Inverter Peak Efficiency
IRPT	Instantaneous Reactive Power Theory
KF	Kalman Filter
LabVIEW	Laboratory Virtual Instrument Engineering Workbench
LC-HAPF	Inductor (L)-Capacitor (C) coupled - Hybrid Active Power Filter
LED	Light Emitting Diode
LF	Loop Filter
LPF	Low Pass Filter
LVDG	Low Voltage Distribution Grid
MATLAB	Matrix Laboratory
MB-HCC	Multi-Band Hysteresis Current Control
MGCPI	Multifunctional Grid Connected Photovoltaic Inverter
MPPT	Maximum Power Point Tracking
MSCW	Minimal Sidelobe Coisne Window
MUSIC	Multiple Signal Classification
NI-cRIO	National Instruments - compact Reconfigurable Input Output
OLG	Open loop gain
OLTF	Open Loop Transfer Function
P&O	Perturb & Observe
PC	Personal Computer

PCC	Point of Common Coupling
PD	Phase Detector
PFs	Passive Filters
PHD	Pisarenko Harmonic Decomposition
PI	Proportional Integral
PID	Proportional Integral Derivative
PLIS	Peak Location Index Search
PLL	Phase Locked Loop
PM	Phase Margin
PR	Proportional-Resonant
PQ	Power Quality
PQI	Power Quality Improvement
PQA	Power Quality Analyzer
PTW	Polynomial Time Window
PV	Photovoltaic
PWG	Performance under Weak Grid
PWM	Pulse Width Modulation
RBFNN	Radial Basis Function Neural Network
RDFT	Recursive Discrete Fourier transform
RT	Real-Time
RT-LAB	Real-Time-Laboratory
RTSPV	Rooftop Solar Photovoltaic
SB	Single-Band
SIL	Software-in-Loop
SMPS	Switch Mode Power Supply
SOC	State of Charge
SOGI	Second Order Generalized Integrator
SPV	Solar Photovoltaic
SRF	Synchronous Reference Frame Theory
SS&TC	Steady State & Transient Characteristics
SSD	Signal Slope Detection
STFT	Short Term Fourier Transform
SUVT	Sine Unit Vector Template

SVD	Singular Value Decomposition
TAD	Think Ahead Decision
THD	Total Harmonic Distortion
TKEO	Teager–Kaiser Energy Operator
TPF	True Power Factor
TRIAC	Triode for Alternating Current
TW	Tera-Watt
UKF	Unscented Kalman Filter
UPS	Uninterruptible Power Source
VCO	Voltage-Controlled Oscillator
VDB-HCC	Variable-Double Band Hysteresis Current Control
VSI	Voltage Source Inverter
WIFFT	Windowed Interpolated Fast Fourier Transform
WT	Wavelet Transform

List of symbols

N	Window Length
H	Window order
n	Sample index
h	Harmonic orders
a_h	Window coefficients
A	Amplitude
f	Frequency
φ	Phase angle
T_s	Sampling Time
k	Division factor
l_h	Integer harmonic frequency value
ξ_h	Fractional harmonic frequency value
τ	Threshold factor
I	Harmonic index
α	Symmetrical Coefficient
$d(j)$	Slope of the signal at instant j
Δt	Sampling period
$S(j)$	Index value of slope sum method
$i(j)$	Present sample
T_p	Threshold parameter
K_m	window scaling factor at the order value of m
i_{an}	Active current at phase n
v_n	Voltage at phase n
i_n	Current at phase n
G_n	Equivalent conductance of phase n
P	Active power
W	Reactive energy
$\hat{v}_n$	Unbiased time integral of the voltage
B_n	Equivalent susceptance of phase n
$\underline{i}_{vn}$	Void current
$\underline{i}_{an}$	Active phase current

$\underline{i_{rn}}$	Reactive phase current
G^b	Equivalent balance conductance
$\underline{i_a^b}$	Balanced active current
$\underline{i_r^b}$	Balanced reactive current
B_n^b	Equivalent balance susceptance
$\underline{i_a^u}$	Unbalanced active current
$\underline{i_r^u}$	Unbalanced reactive current
$\hat{m}(t)$	Amplitude of the modulating signal
$\varepsilon(t)$	Phase of the modulating signal
C_{dc}	Capacitor of the DC-link
V_{dc}	DC link voltage
f_p	frequency of the pole
ω_{co}	crossover frequency
V_{pabc}	Grid supply peak voltage
R_s	Source line resistance
L_s	Source line inductance
L_b	Boost Inductor
C_{pv}	Interfacing capacitor between PV panel and boost converter
V_{mpp}	Voltage at maximum power point
D	Duty cycle of the boost converter
C_{pv}	PV side boost stage capacitor
D_b	Boost stage Diode
ΔI_{pv}	Change in PV current
f_{sw_b}	Boost converter switching frequency
I_{dc}	DC-link current
V_{ripple}	Ripple voltage
V_{bat}	Battery Voltage
E_{bat}	Battery no load voltage
I_{bat}	Battery current
R_{i_bat}	Internal resistance of the battery
E_0	Constant voltage (battery)
K	Polarization constant
Q	Maximum battery capacity

φ_{PM}	Desired Phase Margin
f_c	Desired cut-off frequency
A	Boltzmann's constant
v_s	Source voltage
v_{MGCPI}	MGCPI output voltage
V_{dcref}	Reference DC-link voltage
V_{dce}	DC-link voltage error
V_{rtpv}	Rooftop-PV output DC voltage
V_{oc}	Open circuit voltage
V_{rtpv}	Rooftop-PV output DC voltage
I_{sc}	Short circuit current
I_{rtpv}	Rooftop PV output current
I_d	Current through the Diode
I_{sat}	Saturation current
I_{mp}	Current at maximum power
I_p	Current through the parallel resistance
I_{ph}	Photovoltaic current
k	Ideality factor of the diode
C_{dc}	DC-link capacitor
f_{sw}	Switching Frequency of the MGCPI
h_{min}	Minimum Hysteresis Band
H	Maximum Hysteresis Band
k_m	Modulation Index
HB1	Main Hysteresis Band
HB2	Sub Hysteresis Band
h_1	Scaling Factor 1
h_2	Scaling Factor 2
i_s	Source current
i_{sref}	Reference current
i_{MGCPI}	MGCPI current
i_l	Load current
i_m	Peak value of the source current
k_p	Proportional Gain

k_i	Integral Gain
Ir	Irradiance
L_s	Source inductance
L_{MGCPI}	MGCPI interfacing inductance
L_b	Boost stage inductor
P_s	Source active power
P_l	Load active power
P_{MGCPI}	Active power from MGCPI
P_{pv}	Active power generated from SPV
PI	Proportional Integral Controller
Q_s	Source reactive power
Q_l	Load reactive power
Q_{MGCPI}	Reactive power from MGCPI
q	Electron charge
R_{se}	Single diode model series resistance
R_p	Single diode model Parallel resistance
S_1, S_2, S_3, S_4	IGBT Switches
S_b	Boost stage IGBT switch
T	Junction temperature in Kelvin
U_s	Unit vector template

Chapter 1

Introduction

1.1 Smart Electric Grid

Smart electric grid allows bidirectional power flow and have two-way communication of information and controls consumer loads for better utilization. Some of the important features of smart electric grid are better integration of consumer owned power generation systems including renewable energy systems such as roof-top solar – photovoltaic (PV) energy systems, effective integration of monitoring and control of the power system to facilitate interoperability, efficient distribution of harmonic free electrical power to consumers, reduction of peak demand, which helps lower electricity tariffs. Smart electric grid should also enhance the utilization of existing infrastructure with new functionality [1]. The basic smart electric grid architecture is illustrated in Fig. 1.1.

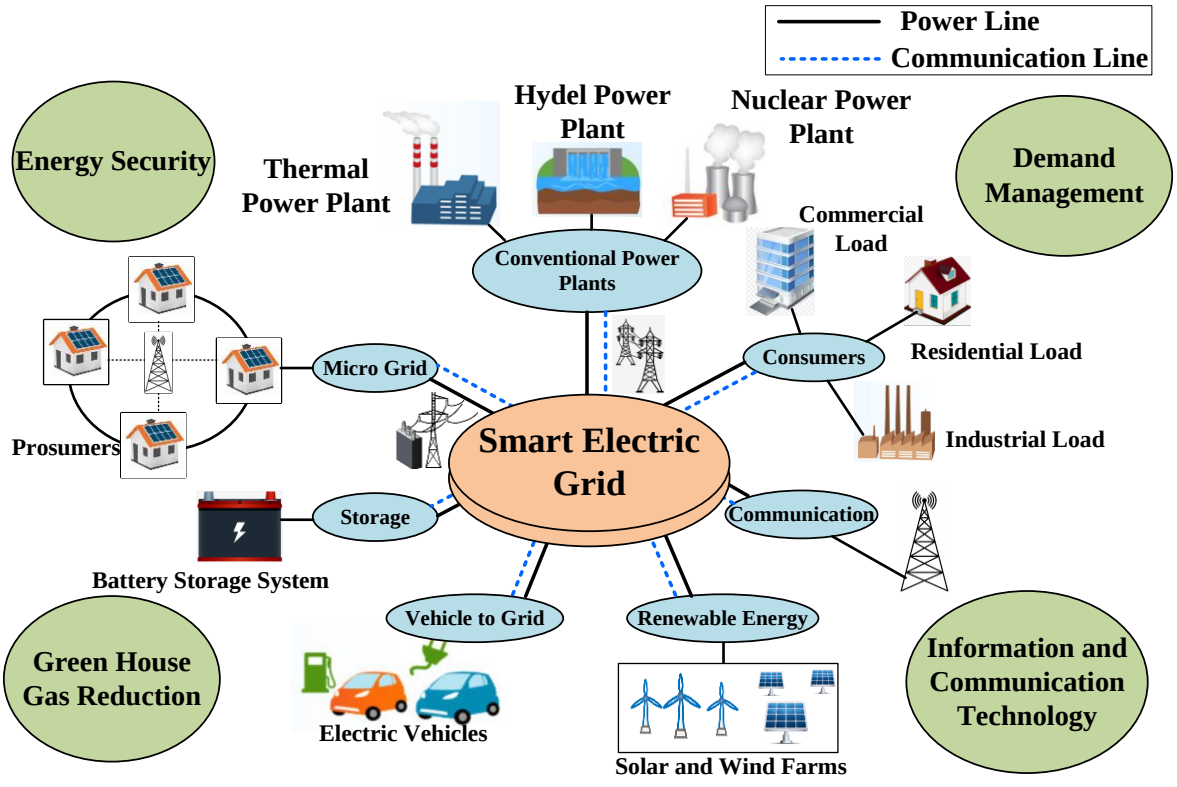

Fig. 1.1 Smart Electric Grid architecture

The limitations of the traditional electric grid are poor real-time monitoring and control is focused on generation and transmission and not much on the distribution. Further, the traditional system is not flexible to inject electric power from renewable sources into the grid and cannot offer new services desired by the consumers. The future smart electric grid should take care of all the needs and concerns of the consumers by employing emerging technologies and evolve into a smarter, better, and sustainable grid [1,2].

Some of the other important characteristics of a smart electric grid are the following:

- Self-healing: Reconfiguration of the system against faults while balancing multiple supplies of power to minimize grid utilization in order to maximize the consumption of local power.
- Flexible: The quick and safe interconnection of distributed generation and battery storage at any point of common coupling at all times. Better management of distributed generation and battery storage to minimize the need for system expansion and hence reduce the total cost of energy**.**
- Efficiency and Reliability: Evolution of smart electric grid throws up a tradeoff challenge between efficiency and reliability due to poor power quality. In general, reliability is preferred over efficiency and hence, attention to power quality (PQ) is warranted.

1.2 Challenges in Smart Electric Grid

Growing per capita income is harbouring proliferation of power electronics based nonlinear loads and the large-scale access of distributed energy generations based on power electronic based devices into life style of the common man which on the negative side introduces undesirable current harmonics into distribution grid [3-9]. The total harmonic distortion (THD) of current due to various real-world nonlinear loads are depicted in Fig. 1.2. It is quite evident that the percentage THD of current due to nonlinear loads is well above the recommended Institute of Electrical and Electronics Engineers (IEEE) standard of 519-2014 [10], which will negatively impact both consumers and utility. Overheating of distribution transformers and rotating machines, false tripping and malfunction of protection switchgear, nonlinear loading of sandwiched bus bars, burning of capacitor banks installed for compensation of reactive power, neutral conductor burnouts, communication interference, imprecise metering, skin effect, eddy current loss and corona loss are some of the issues on the

utility front. Linear loads will underperform impacted by the harmonics introduced by non-linear loads is an issue on consumer front [9].

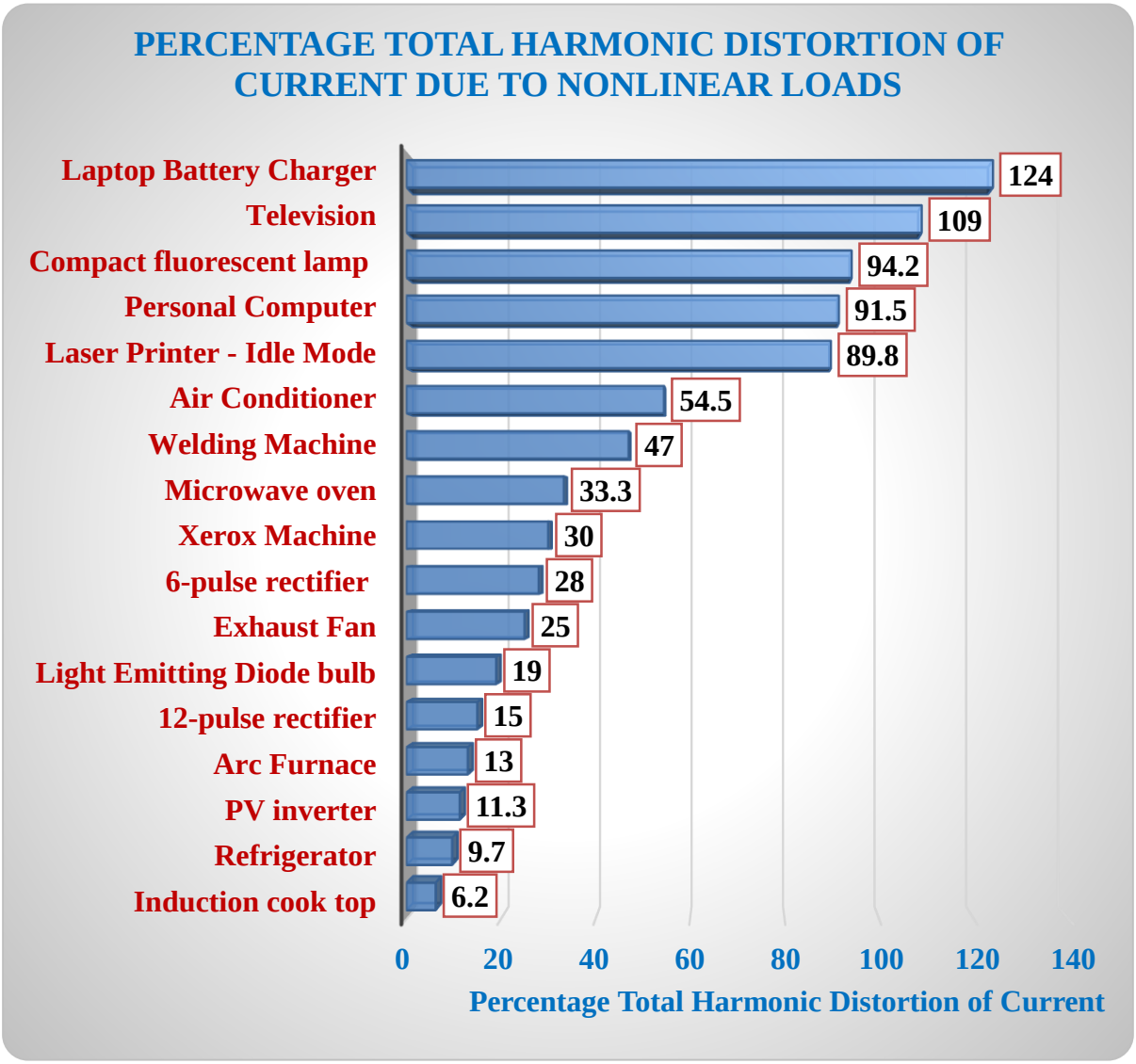

Fig. 1.2 The Total Harmonic Distortion of Current due to various real-world Nonlinear Loads

Wider penetration of renewable energy resources into the distribution systems, integration of power electronics applications into power systems and associated issues challenge today's smart electric grid. Typically power converters which are the interface between smart electric grid and local power sources produce undesirable harmonics and in turn to be mitigated by a compensator, which is also a power electronics based converter [11]. Therefore, estimation and control of current harmonics attract many researchers in this provocative field.

The major benefits of adopting smart electric grid are self-healing capability from PQ issues, exploiting energy portfolio effectively, remote smart metering for demand side management, integration of renewable energy systems and battery storage units [12].

The major contributions of this thesis are the improvement of PQ by accurate estimation, precise control of current harmonics in the distribution grid and integration of multifunctional grid-connected PV inverters with improved characteristics which are essential for delivering the benefits of the smart electric grid.

1.3 Signal Processing for estimation and control of harmonics in smart electric grid

The signal processing methodology used for the estimation and control of harmonics in a smart electric grid is depicted in Fig. 1.3. Initially, the harmonic signal is pre-processed through data acquisition (DAQ) system to identify the nature of the signal for estimation. Later on, it is processed through any one of the time domain or frequency domain or time-frequency domain techniques to estimate the harmonic parameters. During the process of estimation of harmonic parameters, the signal sampling and window length play a crucial role in the accuracy and precision of the estimated harmonic parameters and also to control the harmonics [13-16].

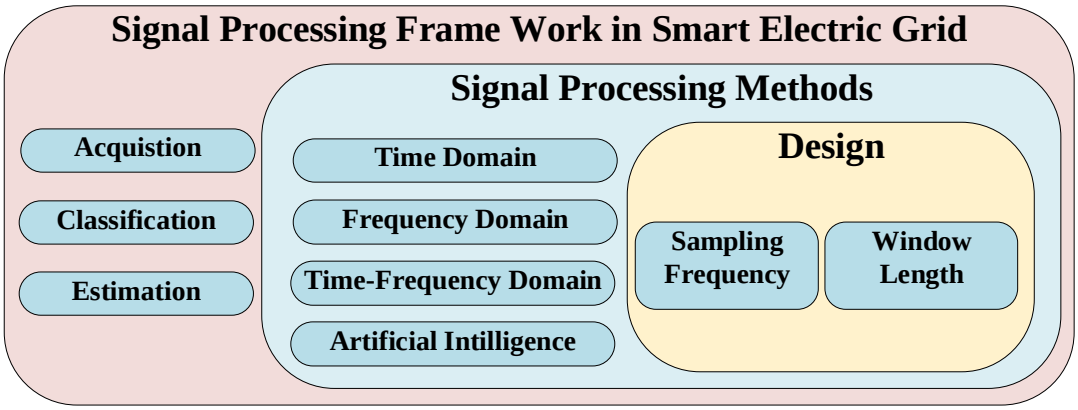

Fig. 1.3 Signal Processing Methodology

1.4 Estimation of Harmonics using Signal Processing methods

Accurate estimation of current and voltage harmonics is essential for power electronic based nonlinear loads and the integration of renewables in the modern distribution network. The methodology has to be a simple and fast estimation of harmonics, with retrofit computation capabilities. Accuracy of the estimation method should meet the requirements of international standards such as Institute of Electrical and Electronics Engineers (IEEE) 1159-2009,

International Electro-technical Commission (IEC) 61000-4-7-2009, IEC 61000-4-30-2015 [17-19], and helps to identify appropriate compensation devices. The total harmonic distortion limits must be maintained at less than 5% as per the IEEE standard 519-2014 [10].

Numerous signal processing methods have been adopted for the estimation of power system harmonics [20,21]. These methods are classified as non-parametric and parametric methods as reviewed by S.K.Jain *et al.* (2011) in [20]. In order to attain higher resolution and better accuracy of the harmonic estimation the traditional parametric methods such as Auto-Regression (AR), Autoregressive Moving Average (ARMA), Estimation of Signal Parameters via Rotational Invariance Technique (ESPRIT), Multiple Signal Classification (MUSIC), Pisarenko Harmonic Decomposition (PHD), Singular Value Decomposition (SVD) and Prony method are adopted in the recent times. Recursive techniques such as Kalman Filtering (KF), Adaptive Linear Element (ADALINE), Phase Locked Loop (PLL) and Extended Phase Locked Loop (EPLL) and Artificial intelligence based techniques such as Artificial Neural Network (ANN), Radial Basis Function Neural Network (RBFNN) are also gaining attention in estimation of the power system harmonics [20,21]. However, these methods require prior information of the estimation signal for modeling; otherwise, it leads to erroneous results. The computation time requirements of these methods are comparatively high based on the nature of the harmonics with noise.

C.Tao *et al.* (2010) have proposed an M-estimators based parametric method with ESPRIT for estimation of harmonics to overcome the limitations of noise effect in parametric methods [22]. However, the computation burden is high to estimate the higher order harmonics under variable frequency condition. L.Zhou *et al.* (2016) have presented a multi-innovation identification theory based multi-innovation stochastic gradient (MI-SG) algorithm to estimate the harmonic parameters [23]. However, the estimation of all the harmonics with variable frequency condition needs to be explored. P.Nayak *et al.* (2017) have presented an Unscented Kalman Filter (UKF) based harmonic estimation method in a micro-grid environment [24]. However, estimation of inter-harmonics under variable frequency condition needs to be exploited.

Non-parametric methods such as Fast Fourier Transform (FFT), Short Term Fourier Transform (STFT), Chirp Z-Transform (CZT), Wavelet Transform (WT), S-Transform, Hilbert Hung Transform (HHT) and improved chirplet transform are also evolved to improve the accuracy of the harmonic estimation [20,21,25]. Given computational efficiency and simplicity, FFT is considered to be a highly suitable estimation method among all other parametric methods

[21]. However, the FFT method has a limitation of spectral leakage and picket fence effect because of non-synchronous sampling due to variation in fundamental frequency [26]. To minimize the spectral leakage, window functions are adopted, and interpolation algorithms have been proposed to minimize the picket fence effect [26–42]. Thus, Windowed Interpolated FFT (WIFFT) algorithms have come into existence. However, due to fluctuating nature of harmonics caused by modern nonlinear loads and variations in fundamental frequency, there is no standard window and its associated interpolation algorithm for estimation of all types of power system current harmonics.

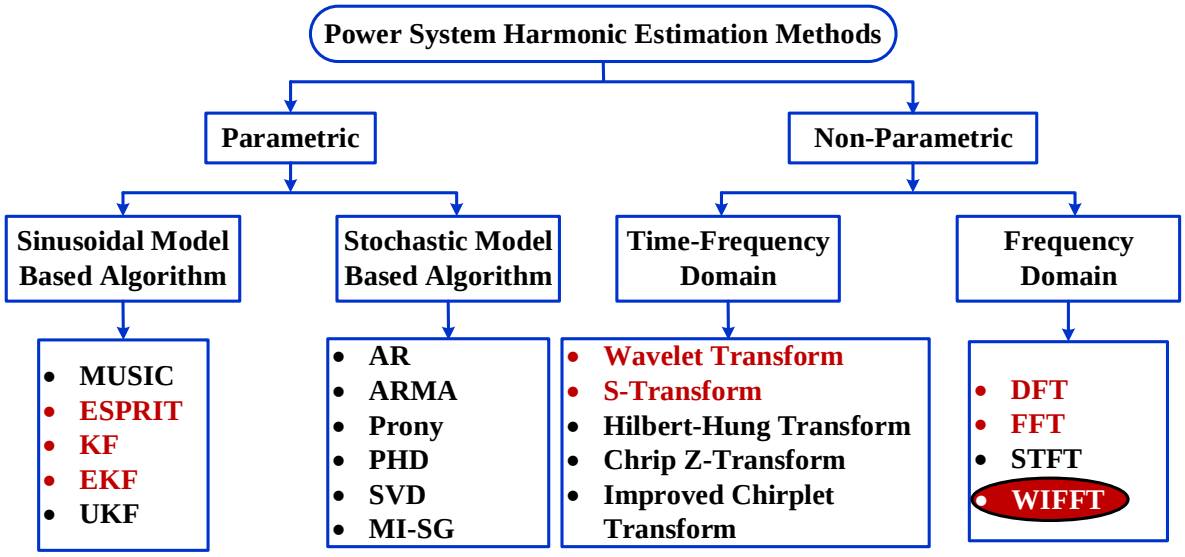

Fig. 1.4 Outline of power system harmonic estimation methods

The accuracy of the harmonic estimation depends on the type of window and its corresponding interpolation algorithm. The window is selected based upon the narrowed main lobe, smaller sidelobe width, and rapid sidelobe roll of rate. The precise estimation of amplitude, frequency, and phase of the fundamental, as well as harmonics, depends on the window properties. Moreover, the minimization of spectral leakage is dependent on window length, window coefficients, and sampling frequency [21]. In [27–29] detailed discussion of windows and its properties are reported, especially for harmonic estimation. From the past two decades, various WIFFT algorithms using Hanning Window, Hamming Window, Blackman Window, Advanced Cosine Windows, Hanning Self-Convolution Window, Cosine Self-Convolution Window, Triangular Self-Convolution Window, Adaptive Kaiser Self-Convolution Window, Mutual Multiplication Window Nuttal-Kaiser Window and Nuttall

Window with triple-spectrum line interpolation for estimation of harmonic parameters are reported in the literature [26,30–42]. The detailed literature survey on periodic harmonic estimation is described in the next sub section.

1.4.1 Literature Survey & State of the Art on Periodic Harmonic Estimation

Various WIFFT based estimation of periodic harmonics in recent times are described in this section. H.Wen *et al.* (2009) have proposed a Hanning self-convolution window and its application to harmonic analysis [32]. However, the convolution of the window function leads to complex calculations. P.Singla *et al.* (2010) have proposed desired order continuous polynomial-time window functions for harmonic analysis [29]. However, high magnitude and high order harmonics estimation have poor accuracy under variable grid frequency conditions. B.Zeng *et al.* (2011) have proposed parameter estimation of power system signals based on cosine self-convolution window with desirable side-lobe behaviors [33]. However, the convolution of the window leads to excessive computation.

H.Wen *et al.* (2011) have proposed a simple interpolated FFT algorithm based on minimized sidelobe windows for power-harmonic analysis [34]. However, it is difficult to determine a suitable frequency resolution with desirable suppressions of spectral leakage. B.Zeng *et al.* (2013) have proposed a novel approach for harmonic parameters estimation under non-stationary situations [35]. However, the harmonics estimation with low amplitude fundamental signal leads to estimation errors. H.Wen *et al.* (2014) have highlighted the performance of WIFFT for frequency estimation in [37]. However, the application of WIFFT for lower magnitude harmonics and inter-harmonics estimation needs to be explored. S.R. Chintakindi *et al.* (2015) have proposed an improved hanning WIFFT for power system harmonic analysis [38]. However, estimation of inter-harmonics under variable frequency condition needs to be examined.

P.Rai et al. (2016) have given an overview of triangular self-convolution window application in harmonic analysis. However, inter-harmonic analysis under variable frequency condition needs to be explored [39]. T.A.Tianyuan *et al.* (2016) have proposed harmonic analysis based on time-domain mutual-multiplication window [40]. However, the mutual multiplication of the window increases the computation burden. T.Jin *et al.* (2017) have proposed a novel power harmonic analysis method based on Nuttall-Kaiser combination window double spectrum interpolated FFT algorithm [41]. However, Nuttall is a cosine

window, hence combining the cosine window with non-cosine window leads to the complex calculation for the highly distorted harmonic cases.

Y.Zhu *et al.* (2017) have reported a Nuttall Window with triple-spectrum line interpolated FFT for analysis of harmonics in [42]. However, a Dual-Spectrum Line Interpolated FFT (DSLIFFT) algorithm has been widely used for most of the above stated windows. Moreover, the DSLIFFT with the above windows is focused on voltage harmonics estimation. However, the estimation of current harmonics is also important to explore [18]. Regarding current harmonics, the fundamental amplitude is lower. In this case, the DSLIFFT algorithm accuracy is low because of the identical harmonic spectral lines on different frequency bins. Moreover, the computation complexity is also another factor, which demands the enhancement of existing DSLIFFT for current harmonic estimation. Therefore, during the estimation of current harmonics, the following issues need to be addressed. WIFFT is a simple and easy-to-implement method for voltage harmonics estimation; however, selection of the suitable window function and improvement of existing DSLIFFT for accurate estimation of the current harmonics are essential.

1.4.2 Literature Survey & State of the Art on Time-varying Harmonic Estimation

C.Gherasim *et al.* (2006) have compared the time-varying harmonic estimation FFT, WT and KF methods. The conclusions of the comparison study are each method has its own merit and demerits and the accuracy and computation burden are dependent on the selection of the right computation parameters for estimation of harmonics under different operating conditions [43]. J.R.Carvalho *et al.* (2007) have proposed a PLL based filter bank and multi-rate processing to estimate the time-varying harmonic distortion. However, the estimation accuracy under variable frequency condition needs to be explored [44]. Y.B.Lim *et al.* (2010) and C.A.Duque *et al.* (2010) have described the time-varying harmonic estimation using filter banks and adaptive filter banks. However, the estimation accuracy is dependent on the filter bank design for the appropriate harmonic frequencies and also the noise considerations [45,46].

S.K.Jain *et al.* (2011) have presented the estimation of harmonics in a single-phase system using Adaptive Wavelet Neural Network. However, estimation of inter-harmonic under variable frequency condition needs to be explored [47]. M.Biswal *et al.* (2012) have proposed a fast adaptive discrete generalized S-Transform algorithm with an adaptive window function to overcome the computational complexity issue of traditional S-Transform for estimation of

time-varying power quality indices in [48]. However, the estimation of harmonics and inter-harmonics under variable frequency condition needs to be explored. S.K.Jain *et al.* (2012) have proposed an ESPRIT assisted artificial neural network for harmonics detection of time-varying signals [49], however low magnitude multi-harmonic estimation needs to be explored.

C.A.G. Marques *et al.* (2013) have reported the FFT application for estimation of time-varying harmonics in a smart electric grid [50]. S.K.Jain *et al.* (2013) have proposed a fast harmonic estimation of stationary and time-varying signals using ESPRIT Assisted – Adaptive Wavelet Neural Network (EA-AWNN) [51]. However, inadequate data leads to erroneous results. C.I.Chen *et al.* (2014) have compared various parametric, non-parametric and artificial intelligence based time-varying harmonic and inter-harmonic methods in [52]. Based on the comparison, it is not so straightforward to judge the superiority of the performance. Hence the estimation method is selected based upon the signal nature and the power system conditions.

P.Nayak et al. (2015) have proposed an adaptive robust Extended Kalman filter (EKF) based on H-infinity filter concepts in [53] to improve the accuracy of the time-varying harmonic estimation. However, the computation process involved to improve the accuracy of the time-varying harmonic estimation is more. S.K.Jain et al. (2015) have proposed an algorithm for dealing with the time-varying signal within sliding-window for harmonics estimation. However, the sampling process is fixed with the sliding window length [54]. W.Yao *et al.* (2016) proposed the measurement of power system harmonic based on adaptive Kaiser Self-convolution window. However, the usage of linear filter banks and Teager–Kaiser Energy Operator (TKEO) will increase the computation time [55].

In view of the above cited literature, the development of simple, accurate and computationally efficient estimation methods, as well as discussion of new standards for time-varying harmonics, is necessary as per the needs and demands of the smart electric grid. Thus, there is a scope to explore and improvise the WIFFT algorithm for estimation of periodic and time-varying harmonic estimation. Hence, WIFFT algorithm is enhanced to estimate current harmonics produced by modern power electronic based nonlinear loads and also extended for the estimation of time-varying harmonics and inter-harmonics in this thesis and is highlighted in Fig 1.4.

1.5 Harmonic Control

As discussed in section 1.2, current harmonics are one of the major PQ issues in the smart electric grid. Harmonic compensation is performed by both utility end and consumer end.

The selection of the harmonic filtering device is based on the level of percentage THD harming the power system. The power system harmonic filtering devices are classified in Fig 1.5.

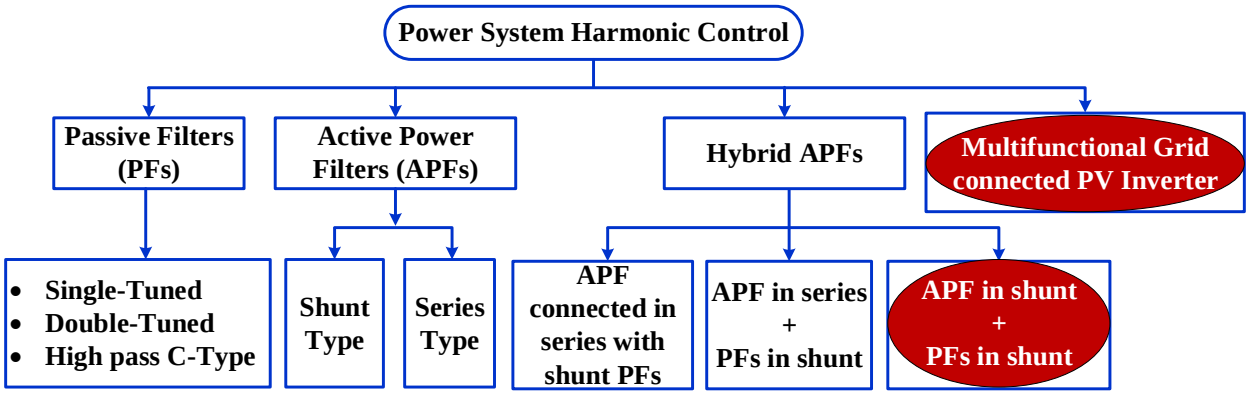

Fig. 1.5 Outline of power system harmonic control configurations

State of the art dealing with a power factor correcting capacitors, power filters, and grid-connected inverters with power conditioning capabilities are addressed separately. The smart grid requires holistic solutions for well-defined issues that reflect a ground reality where all such power conditioning devices should coexist to realize smart electric grid objectives of improved efficiency with harmonic free power by reducing losses significantly.

Passive Filters (PFs) are a well-known low-cost solution to compensate the industrial power system harmonics discussed by J.C.Das (2004) but, it has a limitation of resonance effect due to dynamic load variation [56]. Active Power Filters (APFs) are introduced to overcome the disadvantages of PFs. APFs have evolved over the past 10-15 years due to rapid advancements in power electronic devices, faster signal processing, a variety of converter topologies and control strategies. However, the costs of APFs are comparatively high. The major limitation of shunt APF is high power rating requirement for compensating high peak harmonic current and its allied costs. Hybrid APF (HAPF) is the best alternative approach to minimize the rating and its associated cost as described by M.Maciążek *et al.* (2015) in [57]. In this thesis, a shunt APF and shunt PF based HAPF and Multifunctional grid-connected PV inverter is explored for harmonic control in smart electric grid as highlighted in Fig. 1.5. The detailed literature survey & state of the art on harmonic control using HAPFs and multifunctional grid-connected PV inverter are described in following sub sections 1.5.1, 1.5.2 and 1.5.3.

1.5.1 Literature Survey & State of the Art on Harmonic control using Hybrid Active Power Filter

Nowadays, HAPFs constitute a cost-effective solution for harmonic and reactive power compensation in industrial power systems, as discussed by M.Maciążek *et al.* (2015) in [57]. For example, the high pass filter has a tendency to consume too much reactive power, so by compensating it, this extra reactive power will not be routed through the grid and losses on transmission lines or other harmful effects can be avoided. The reference current generation system, current controller, and DC voltage controller are the major blocks in HAPF design. H.Akagi (2005) has reported the HAPFs with different circuit configurations such as shunt and/or series passive and shunt and/or series active to enhance the behaviour of the filtering characteristics [58,59].

H.Fujita *et al.* (2000) have designed a series APF, and a parallel PF based HAPF for harmonic resonance damping in industrial power system [60]. However, the harmonic resonance damping is affected with the proposed HAPF under distorted grid condition. S.P.Litrán *et al.* (2012) have developed a state model–based control strategy for series APF and a parallel PF based HAPF for harmonic compensation [61]. However, under distorted grid condition, the harmonic and reactive power compensation is poor.

Nowadays, research is focusing on transformer less LC coupling HAPF (LC-HAPF) for both three-phase three-wire and four-wire distribution system configurations. The LC-HAPF has a benefit of improved switching performance with minimum DC-link voltage. Recently Lam *et al.* (2012) have proposed the three-phase four-wire center-split LC-HAPF with a tuned neutral inductor and its control with linear hysteresis control [62,63]. The LC-HAPF offer feasible and cost-effective solutions to harmonic, reactive power and unbalance compensation. However, they have difficulty in applying for old installations where the transformers are essential. The complexity of the system will increase with LC-HAPF, where the transformer requirement is mandatory. Hence in this thesis, a shunt tuned PF with APF is considered.

P.Dey *et al.* (2013) have presented a comparative study of Adaptive reference current detection method, Instantaneous reactive power theory, Synchronous reference frame theory, time-domain current decomposition algorithm and *IcosΦ* algorithm for reference current estimation of HAPF. The comparative study concludes that *IcosΦ* algorithm has superior performance. However, this method requires a Phase-locked loop (PLL) to generate the reference to the HAPF. The design and tuning of the PLL parameters is computational intensive [64]. T.Demirdelen *et al.* (2013) have described various HAPF topologies, reference current

generation methods and controllers [65] in his exhaustive review. However, he felt that further research needs to be done for them to adapt to sensitive and complex dynamic nonlinear loads for the improvement of PQ in the modern smart electric grid.

S.A.Rahmani *et al.* (2014) have developed a thyristor-controlled reactor in series with shunt APF for harmonic and reactive power compensation [66]. However, under distorted grid condition, the harmonic and reactive power compensation needs to be investigated. T.N.Nguyen *et al.* (2014) have presented an injection circuit based HAPF [67] to address the issues of PF parameter variation. However, this HAPF requires a coupling transformer to integrate with the PCC of the supply system. L.Herman *et al.* (2014) have designed a proportional-resonant current controller for selective harmonic compensation with HAPF composed of a two-level voltage source inverter connected in parallel with the inductor of a shunt single-tuned PF [68]. The performance of the HAPF for compensation harmonics and reactive power is demonstrated. However, performance unbalanced linear and nonlinear loads condition needs to be investigated. Moreover, a variation of the PF system parameters may seriously impact the HAPF performance.

A.K.Unnikrishnan *et al.* (2015) demonstrated the performance of a transformer less LC coupled HAPF for harmonic compensation in [69]. However, performance of the HAPF under weak grid is not discussed. T.L.Lee *et al.* (2015) demonstrated a transformer less LC coupled HAPF with variable conductance for suppression of harmonic resonance in the industrial power system in [70]. However, the unbalance compensation needs to be exploited. P.Dey *et al.* (2015) have presented a modified D–Q theory for current harmonic compensation using three-phase four-wire shunt HAPF [71]. However, this theory uses a modified PLL and D-Q transformation to generate the reference current signal to the current controller. Moreover, hysteresis current controller in the HAPF has a limitation of the variable switching frequency.

Various control strategies are reported for HAPF, but still, the reference current generation and the current controller design is suffering from certain limitations, such as computational burden sensitive under the distorted grid and poor dynamic behaviour due to resonance effect caused by the PFs. There is different reference current generation schemes reported in the literature. These schemes are classified as time domain and frequency domain as tabulated in Table 1.1.

Table 1.1 Classification of reference current generation schemes

Domain	**Reference current generation schemes**
Time-domain	Instantaneous reactive power theory (IRPT Theory) and its variants by H.Akagi *et al.* (2007) [72], Synchronous Reference Frame theory (SRF) and its variants described by M.Maciążek *et al.*(2012) [74], FBD (Fryze, Bucholtz, Depenbrock) Theory discussed by M.E.Balci *et al.* (2008) [75], Conservative power theory P.Tenti *et al.* (2011) [78].
Frequency domain	FFT, DFT and RDFT based harmonic detection methods described by L.Asiminoaei *et al.* (2007) [73]

The reference frame approaches such as PQ and SRF theory are widely adopted reference current generation schemes for APF applications. However, SRF Theory is the most frequently used methodology for harmonic, reactive power and unbalance compensation when compared to PQ theory because of the less computational burden. However, selective estimation of different PQ issues is not possible with SRF theory. The selective estimation of disturbing effect is needed in the case of HAPF design to perform effective compensation without resonance effect.

Balci *et al.* (2008, 2011) presented the detailed quantitative comparison of different power decomposition theories in [75-77]. The power decompositions defined by Budeanu, Kimbark, and Depenbrock, is not feasible for the unity power factor operation of active filtering. The power decompositions proposed by Fryze, Shepherd, Zakikhani, Czarnecki, Sharon, Kusters, and Moore can provide unity power factor operation, but the limitations are resonance effects and it is suitable only for constant supply voltage condition. Fryze-Buchholz-Depenbrock (FBD Theory) based reference generation scheme is not suitable during unbalance conditions. The frequency-domain approaches lead to complex calculations, which in turn increase the computation burden.

Given different limitations involved in reference current generation by the existing power decomposition methods, recently P.Tenti *et al.* (2011) have proposed a Conservative Power Theory (CPT) as one of the accurate, current decomposition methods for control harmonics in the smart electric grid by [78]. CPT has better features, such as accurate estimation under ideal and non-ideal grid voltages with a selective estimation of a disturbing effect. CPT

based current decompositions enable selective estimation of different PQ issues such as harmonics, unbalances, and reactive power. The CPT based orthogonal current decomposition instead of digital filters used in the SRF improves the reference current generation accuracy to extract the desired component of the current. CPT based orthogonal current decomposition offers flexibility to the selection of harmonic, reactive power and unbalance component in this research.

The distortion associated with the energy storage element is considered in the reactive energy definition of CPT, which is not considered in the existing power decomposition theories. The void currents definition based on the CPT is influenced by harmonic distortion and unbalance effect. CPT is capable of calculating the optimum compensation capacitance's value under ideal and distorted conditions. Thus, CPT is the most suitable reference current estimation scheme for HAPF design.

1.5.2 Literature Survey & State of the Art on Harmonic control using Three Phase Multifunctional Grid Connected PV Inverter

Solar energy is one of the most prominent renewable energy resources of the modern electric power grid. According to the International Energy Agency (IEA) report [79], a total of 402.5 GW solar-Photo-Voltaic (SPV) systems were installed worldwide until 2017. Further, it is estimated that installed solar energy generation will reach approximately 1TW by the year 2022. Most governments have schemes to subsidize the SPV installations in their countries [79-81]. The promotion of SPV systems is of foremost environmental concern because nuclear and thermal power generation increases the carbon footprint. The sustainability of our planet requires further efficient renewable energy conversion and integration to the utility grid. However, the penetration of SPV systems causes concerns of PQ in smart electric grids. The common PQ issues are the circulation of reactive power, harmonics, unbalanced currents, and neutral currents.

An APF is an attractive solution to control harmonics in a smart electric grid. However, it requires an exclusively Voltage Source Inverter (VSI) [58,59]. Another solution is to employ a Grid-Connected Inverter (GCI) interfacing renewable energy sources to work as APF simultaneously [82-84], turning into a multifunctional device without any changes in the structure. This solution should comply with the specification of international standards such as IEEE 929-2000, IEEE 1547a-2018, and IEC 61727 [105], the technical requirements of GCI for grid integration and power conditioning as reported by Y.K.Wu *et al.* (2017) in [85].

Multifunctional GCIs are gaining significant importance because of its capabilities to compensate harmonics, reactive power, unbalance and neutral currents along with active power injection to the distribution system. Z.Zeng *et al.* (2013) and L.Hassaine *et al.* (2014) have discussed various Multifunctional GCI topologies and control strategies in [86,87]. O.V.S.R.Varaprasad *et al.* (2014) have proposed a three-level hysteresis current controlled GCI for multifunctional operation in [88]. In this case, the active power injection is limited due to the intermittent nature of solar energy. M.V.M.Kumar *et al.* (2015) have presented a dual voltage source inverter (DVSI) using instantaneous symmetrical component theory in [89]. The DVSI topology reduces the filter size and utilizes the full capacity of the inverter. However, it uses two inverters to achieve reliable operation. Z.Zeng *et al.* (2016) have presented a multi-objective control of GCI in [90], where a comprehensive PQ evaluation index is introduced which is derived based on the catastrophe decision theory for optimal utilization of the available renewable energy capacity. However, during the absence of renewable generation, it will perform only power conditioning.

F.Harirchi *et al.* (2016) in [91] proposed a multifunctional GCI with a DC-DC floating interleaved boost converter and a battery back-up with bi-directional DC-DC floating interleaved buck-boost converter in which the inverter is controlled by instantaneous power theory based proportional-integral-resonant controller. However, the coordination of multifunctional operations is not reported. M.Parvez *et al.* (2016) have presented a detailed review of the current control techniques using d-q based rotational frame theory, α-β based stationary reference frame theory for three-phase GCI in [92]. This summary illustrates the need for smart GCI inverter controllers for improved performance. D.C.Gaona *et al.* (2017) have presented the multifunctional inverter control using internal mode controllers with synchronous reference frame theory in [93]. A.Safa *et al.* (2017) proposed an improved sliding mode controller for a multifunctional photovoltaic grid-tied inverter in [94].

Several MPPT techniques have been reported in the literature [95,96]. Among them perturb and observe (P&O) technique is one of the commonly adopted for maximum power extraction [96]. Incremental conductance (INC)-based MPPT is another technique for maximum power extraction effectively under intermittent solar irradiation conditions. The advantages of INC-based MPPT over P&O-based MPPT are: (i) No need to compute power, (ii) better dynamic response, and (iii) low ripple power. Given the simplicity, efficiency, accuracy, and tracking capabilities, the INC-based MPPT technique is adopted for the DC-DC boost stage in this research work.

Selecting a suitable inverter topology and designing a smart, flexible and reliable control strategy with a simple reference current estimation method for multifunctional operation is a crucial concern that needs to be addressed all the previous mentioned researches their efficacy and legitimacy. However, Multifunctional Grid Connected PV Inverter (MGCPI) is not explored sufficiently for flexible, selective, and precise multifunctional operations. Such attributes are essential to advance MGCPI functionality. The coordination of the different function is very important in MGCPI operation to have an efficient, economical and quality power to the consumers.

1.5.3 Literature Survey & State of the Art on Harmonic control using Single-phase MGCPI

The number of installations of rooftop solar-PV (RTSPV) systems in single-phase Low-Voltage Distribution Grid (LVDG) is growing. Such a high penetration is due to the rise of consumer demand associated with high electricity tariffs furthering deterioration of environmental concerns [97,98]. The availability of low-cost SPV panels and advanced power electronic converters made RTSPV feasible and viable, reducing the dependency on conventional energy resources [99,100]. Moreover, government policies are encouraging consumers to install the RTSPV systems and become prosumers to receive payback for the energy supplied to the grid through net metering, which reduces consumption of grid power [100,101]. While the growth of grid-connected RTSPV systems is welcome, the poor PQ introduced by consumer electronic loads is not worthy. The other reason for the deterioration of PQ in LVDG is power electronic-based nonlinear loads [102-104]. This will influence the stability and the reliability of LVDG, impacting the national economy negatively.

A two-stage RTSPV integration is an efficient system for single-phase rooftop installations which perform both active power feeding and power conditioning at the point of common coupling (PCC) to the LVDG in tune with the global standards [105]. This approach helps us to avoid the use of power conditioning equipment [86,105–110]. A two-stage RTSPV integration system consists of a DC-DC boost stage and MGCPI stage. Literature survey suggests that the selection of an efficient maximum power point tracking (MPPT) technique for the DC-DC boost stage, designing of a simple control methodology for the inverter to coordinate the multi-functional operations such as grid synchronization with active power feeding, reactive power, and harmonic compensation are still major topics to be explored under both ideal and distorted grid conditions. However, designing simple control for single-phase,

the multi-functional system is not addressed sufficiently in the literature [109]. The INC based MPPT is adopted for the DC-DC boost stage for efficient tracking, as explained above in section 1.5.2.

The control technique is very crucial to improve the robustness and efficiency of an MGCPI. Z.Zeng *et al.* (2013) have presented the comparison of various single-phased grid-connected inverter current control techniques, with their own merits and demerits, depending on the system operating conditions in [86]. A.F.Cupertino *et al.* (2014) proposed a proportional-integral (PI) current control method in [111] to perform the multi-functional operations using a grid-connected SPV inverter. However, tuning the gain values of the PI controller as per the variations in solar irradiation and consumer loads is quite complicated. L.S.Xavier *et al.* (2018) have proposed the proportional–resonant (PR) controller for better dynamics over the PI controller [112], but the PR controller is a complex controller and selection of the individual harmonic frequency for compensation under distorted grid conditions is one of the limitations. A.Chatterjee *et al.* (2017) reported that the model predictive controller-based PV inverter integrated with the grid [113]. Nevertheless, the requirement of the high sampling frequency, i.e., 200 kHz, and the optimization process agnostic to the controller cost function and heavy computation during the operation of single-phase systems affected nonlinear loads. I.S.Kim (2006) proposed sliding mode control for grid-connected SPV systems. However, the time-varying surface selection is a complex task to perform multifunctional operations [114].

In contrast to the above methods, the hysteresis current control (HCC) is a simple method for multi-functional operation as it offers advantages such as rapid current controllability, easy implementation, load insensitivity concerning parameter variations, maximum current limit, and better stability [109,110,115–120]. However, the major limitation of the HCC is its high variable switching frequency to match variation in solar irradiation and associated compensation requirements that results in higher switching losses. To overcome the drawback of high variable switching frequency, advanced HCC methods are described in the literature [121–123].

E.R.Priandana *et al.* (2014) have presented a variable double-band (VDB)-HCC concept in [122] for single-phase full-bridge bi-directional converters. Moreover, P.A.Dahono (2009) & H.Komurcugil (2015) have presented the double-band (DB)-HCC concept for single-phase active filtering in [121,123]. The bandwidth of the DB-HCC method proposed in References [121,123] is constant, and the compensation objective depends on the bandwidth values. Moreover, there is an offset issue under distorted grid condition, which has a limitation in

compensation with highly distorted nonlinear load conditions. The VDB-HCC method is an alternative method to overcome the limitations mentioned above of the DB-HCC method. However, the selection of the optimum variable band to attain maximum efficiency needs to be examined.

Moreover, VDB-HCC is also not considered for MGCPI operation. It is to be noted that the performance of the inverter under weak grid condition is not sufficiently explored in the literature while active power injection is reported in most of the research studies, it has been found that inverter peak efficiency under low irradiation is quite low. Hence, it is necessary to overcome the limitations of VDB-HCC method concerning the fast, reliable, and efficient operation of the MGCPI to perform multifunctional tasks effectively.

1.6 Observations from the Literature survey

The observations from the literature survey of harmonic estimation and control are summarised in the below sub-sections.

1.6.1 Observations of the Literature survey on Periodic Harmonic Estimation

- Literature Survey reveals that the harmonic estimation in smart electric grid applications needs to be improved as per the transforming nature of the grid scenarios.
- Computation process needs to be simplified based on the harmonic signal nature.
- Sampling process and selection of the suitable window are important as per the main lobe, side-lobe and side-lobe roll of rates.
- Errors in harmonic estimation are high when the fundamental frequency deviates from the rated 50 Hz value based on the operating conditions for the current harmonics case.
- Accurate, current harmonic estimation is necessary in addition to the voltage harmonic estimation as per IEC 61000-4-30 standard.
- It is necessary to improve the conventional dual-spectrum line interpolated FFT algorithm for present trends.
- The above points are exploited in this thesis and presented in chapters 2.

1.6.2 Observations of the Literature survey on Time-Varying Harmonic Estimation

- The parametric methods require the prior information of the estimation signal for modelling.

- The computation time requirements of these methods are comparatively high based on the nature of the harmonics with noise.
- There is a necessity for simple and fast estimation of time-varying harmonics without using band-pass filters.
- The windowed interpolated FFT algorithms are not explored sufficiently for time-varying harmonic case in a smart electric grid environment.
- The above points are exploited in this thesis and presented in chapters 3.

1.6.3 Observations of the Literature survey on Harmonic Control using Hybrid Active Power Filter

- Harmonic current reference generation, controller designing is still an emerging area of research for different grid conditions.
- Customizing the low rated shunt APFs for the existing shunt PFs to form as a hybrid solution for dynamically varying power system harmonics with simplified control is still under research stage.
- Selective harmonic compensation without using conventional linear transformation methods is researching concerning the current literature for simplifying the compensation process.
- The selective estimation of disturbing effect is needed in the case of HAPF design to perform effective compensation without resonance effect.
- Design of suitable current controller and validation of its performance under dynamic conditions with selective compensation is not explored sufficiently.
- The above points are exploited in this thesis and presented in chapter 4.

1.6.4 Observations of the Literature survey on Harmonic Control using Three-Phase Multi-functional Grid Connected PV Inverter

- MGCPIs are gaining vital importance because of its capabilities to compensate harmonics, reactive power, unbalance, and neutral currents along with active power injection to the distribution system. However, coordinating the multifunctional tasks using a distributed generation with selective compensation capabilities using Conservative power theory (CPT) are not explored sufficiently to enhance power injection and power conditioning capabilities efficiently.

- To perform the seamless multi-functional tasks such as grid feeding and power conditioning by energizing the DC link of the MGCPI using solar PV and battery storage systems with proper energy management is need to be explored.
- The above points are exploited in this thesis and presented in chapter 5.

1.6.5 Observations of the Literature survey on Harmonic Control using Single-Phase MGCPI

- Highly variable switching frequency with the conventional Variable Double Band – Hysteresis Current Control (VDB-HCC) leads to switching losses, which in turn reduces the efficiency of the MGCPI.
- Selection of the optimum variable hysteresis band is not explored under ideal and weak grid conditions.
- The bandwidth of the VDB-HCC method is constant, which results in imbalance switching among the inverter switches. Moreover, the performance of the VDB-HCC under weak grid condition is not reported.
- The above points are exploited in this thesis and presented in chapter 6.

1.7 Research Approach

A comprehensive literature survey is carried out in the area of harmonics in a smart electric grid and did not find sufficient work on accurate estimation and effective control of current harmonics. The scope of the thesis is periodic harmonic estimation for continuous loads, time-varying harmonic estimation for intermittent loads. The synthesized input harmonic signal is used for verification of the developed algorithm under Laboratory Virtual Instrument Engineering Workbench (LabVIEW) simulation and verified with real-world non-linear loads such as compact fluorescent lamp, TRIode for Alternating Current (TRIAC) controlled exhaust fan, Light Emitting Diode (LED) lamp, Switch Mode Power Supply (SMPS) of the Personal computer, Frontend Bridge Rectifier using estimation test bed developed by National Instruments – compact Reconfigurable Input-Output system based Field-Programmable Gate Array (NI-cRIO based FPGA) platform [124].

Further, the work is extended to improvising the existing passive filters by hybridizing with CPT based active power filter for controlling harmonics during normal three-phase linear and non-linear load conditions. In this case, excessive loads are serviced by the utility, which is a burden. So the next work is enhanced to supply excessive commercial loads locally through a three-phase MGCPI with BSS at the consumer end, which reduced the burden on utility with

improved PQ. For single-phase residential loads with RTSPV installations, harmonics are controlled through MB-HCC based single phase MGCPI.

All of the above cases are simulated in MATLAB/Simulink 2013 environment and verified on OPAL-RT based RT grid simulator OP 4500 [125]. The results demonstrate the usefulness of this thesis work both for utility and consumers by reducing the harmonic effects such as Overheating of distribution transformers, false tripping of protection switchgear, burning of capacitor banks installed for compensation of reactive power, neutral conductor burnouts and Electromagnetic interference with neighbouring loads.

1.8 Research Contributions

This pictorial representation of the thesis contributions are depicted in Fig 1.6, and the detailed discussion on the contributions are described in the following sections.

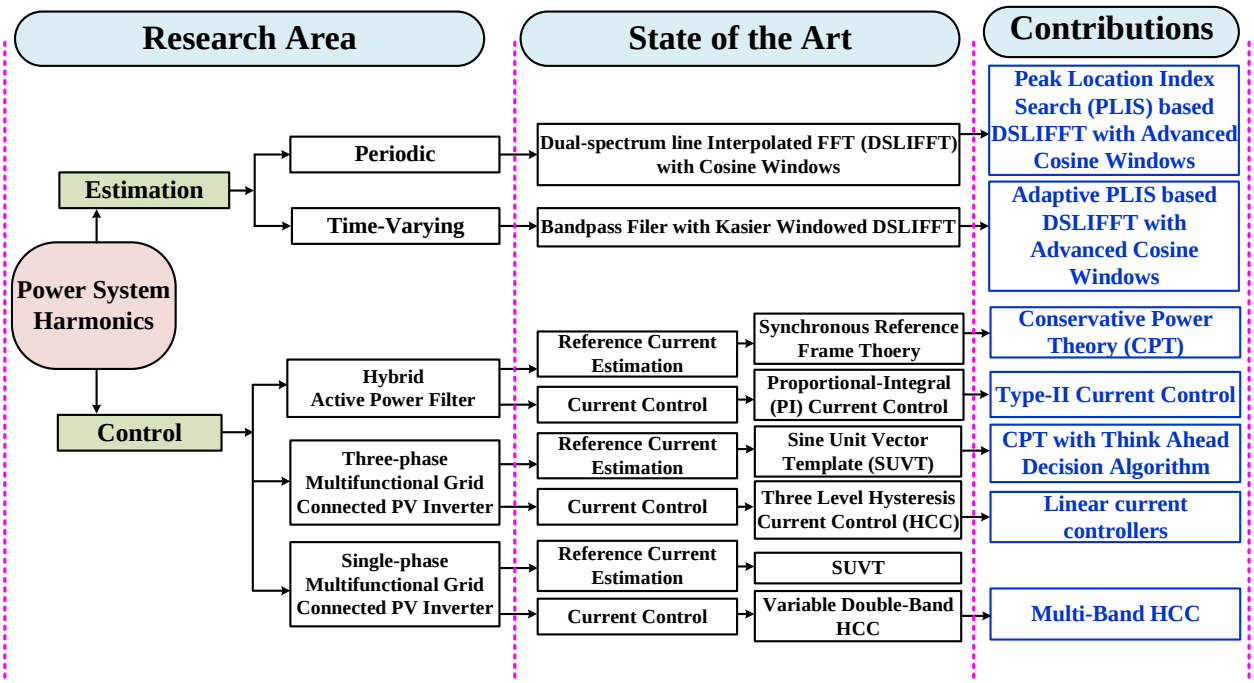

Fig. 1.6 Research Contributions

1.8.1 Estimation of Periodic Current Harmonics

The current harmonics polluted by the nonlinear loads are of different frequencies. Estimation of current harmonics and inter-harmonics in the smart electric grid has been identified as an issue of greater importance to address by L.An *et al.* (2016) in their review paper [126].

In order to estimate the current harmonics accurately and effectively, a Peak Location Index Search (PLIS)-based DSLIFFT algorithm using 4-Term Minimal Sidelobe Cosine Window (4-term MSCW) is presented as a generic approach to current harmonics estimation under variable frequency operation. Because of the reasonable main lobe, lower side lobe level and fast side lobe roll of the rate the 4-term MSCW has been adopted for PLIS-based DSLIFFT estimation process.

The Real-Time (RT) implementation of the PLIS-based DSLIFFT algorithm using a 4-term MSCW algorithm and its current harmonic estimation accuracy with real-world nonlinear loads has been presented

The contributions are as follows:

- A PLIS-based DSLIFFT algorithm is presented for simplifying the estimation process and improving the estimation accuracy of low-amplitude current harmonic signal parameters with a 4-term MSCW.
- The application of 4-term MSCW for current harmonic estimation has been explored.
- The PLIS-based DSLIFFT algorithm using 4-term MSCW is implemented and tested in real-time with real-world nonlinear loads.

1.8.2 Estimation of Time-Varying Current Harmonics

To estimate the time-varying current harmonics accurately and effectively, an adaptive PLIS based DSLIFFT algorithm using 4-term MSCW is presented as a generic approach to time-varying current harmonics estimation under variable frequency operation.

The Real-Time (RT) implementation of the Adaptive PLIS-based DSLIFFT using 4-term MSCW and its current harmonic estimation accuracy with real-world nonlinear loads has been presented

The contributions are as follows

- A Signal Slope Detection (SSD) technique [127] is adopted to find the change in the Time-varying harmonic signal.
- The window length is determined by the duration of the change; thereby the harmonic signal is sampled adaptively as per the sampling theorem and Nyquist criterion.
- The harmonic parameters are estimated using PLIS based DSLIFFT algorithm stated in the above section.

1.8.3 Control of Harmonics using CPT based HAPF

L.An *et al.* (2016) in [126] have also identified PQ control methods in large scale distributed industrial power plant as a prime candidate for immediate research and this thesis addresses sufficiently. With reference to the recent literature of CPT based active filtering, the design of suitable current controller and validation of its performance under dynamic conditions is still an important area of research. Usually, the proportional and integral (PI) controller is the most widely used linear controller for current control operation, but it has a poor dynamic response for the load variations. Hence in this thesis, a Type-II controller is designed to perform the current control task. In view of recent literature, there is a renewed interest in the design of Type-II controllers, compared with the most widely used PI-based current controllers.

PFs are the existing compensation devices in the industrial power system. However, they are not performing the compensation task effectively for dynamically varying load conditions. Hence Type-II controlled APF using CPT is merged with the existing PFs to form as HAPF. The major contribution in this thesis is the design of Type-II current controller for CPT based APF for supporting the existing PFs as HAPF. The proposed configuration performs the compensation tasks effectively without sacrificing the existing PFs functionality. The proposed HAPF is capable of compensating dynamically varying harmonics, reactive power and current unbalance simultaneously. The main objective of the proposed Type-II current-controlled HAPF is to provide the better harmonic isolation between the supply and load, consequently no harmonic resonance effect and no harmonic current effect in the supply mains.

1.8.4 Control of Harmonics using CPT based Three Phase MGCPI with BSS

L.An *et al.* (2016) have also emphasized that the pollution level and superposition nature of the PQ with grid integration are worth researching for better adoption of smart electric grid [126]. In order to coordinate the multifunctional operations such a PQ improvement and power injection seamlessly, this thesis presents a Think-Ahead Decision Algorithm for the effective operation of CPT based Three-phase MGCPI with auxiliary Battery Storage System (BSS).

The contributions are as follows:

- A Think-Ahead Decision Algorithm is developed to coordinate the multifunctional operation and to decide the best mode of operation for the MGCPI taking into account the SOC and the available power at the PV source.
- The CPT based current decomposition s adopted for computing the MGCPI current reference signals.

- Developed the linear controllers for the MGCPI as well as for the BSS, allowing bi-directional power exchange between the BSS and MGCPI using classical frequency analysis.

1.8.5 Control of Harmonics using Single Phase MGCPI

In this thesis, the authors propose a scaling factor-based multi-band (MB)-HCC with a simple switching logic by employing the two hysteresis bands with reduced switching frequency to reduce switching losses in the inverter and thereby increasing the inverter efficiency. Proposed MB-HCC bandwidths are adjusted as per the current reference value using scaling factors under ideal and distorted grid conditions. In the proposed MB-HCC-based two-stage RTSPV system, the DC-DC boost converter stage is controlled with the INC-based MPPT to extract the maximum power from RTSPV, and the MGCPI stage is tuned with the proposed MB-HCC, with scaling factors to execute the multifunctional operations to reduce the grid consumption and improve the PQ of the LVDG. The proposed system configuration is modelled and simulated in a MATLAB/Simulink environment using sim power system toolbox. The simulated results are validated in real-time (RT) using an RT grid simulator.

The contributions are as follows:

- Developed a scaling factor-based MB-HCC was proposed to MGCPI for power injection and power conditioning operations.
- Verified the proposed MB-HCC MGCPI operation under both ideal and distorted grid conditions using simulation and real-time experimental studies.
- Compared to the proposed MB-HCC method effectiveness with the conventional VDB-HCC method.

1.9 Organization of the Thesis

- **Chapter 1** introduces the smart electric grid, identifies challenges in a smart electric grid, explores signal processing methodologies of power system harmonics estimation and explains control for the smart electric grid. An exhaustive literature survey is presented, followed by the observations of the literature survey. Elaborates research approach and presented contributions in brief along with thesis organization.
- **Chapter 2** presents the PLIS based DSLIFFT using 4-term minimal sidelobe cosine window for periodic harmonics estimation and validates its performance by both simulation and virtual instrumentation based experimental results.

- **Chapter 3** demonstrates the adaptive PLIS based DSLIFFT using First-order polynomial-time window and 4-term minimal sidelobe cosine window for time-varying harmonics estimation and validates its performance by both simulation and virtual instrumentation based experimental results.
- **Chapter 4** describes the harmonic control using conservative power theory (CPT) based Type-II linear current controlled HAPF in industrial power systems and validates its performance by both simulation and OPAL-RT based real-time experimental results
- **Chapter 5** presents the Think Ahead Decision making algorithm and CPT based dual-stage MGCPI with bi-directional battery energy conversion system and validates its performance by both simulation and OPAL-RT based real-time experimental results
- **Chapter 6** illustrates the Multi-Band Hysteresis Current Controller (MB-HCC) based single-phase MGCPI for the integration of RTSPV to the low-voltage ideal and weak utility grid and validates its performance by both simulation and OPAL-RT based real-time experimental results
- **Chapter 7** concludes the thesis along with future scope to benefit utility and consumers in a smart electric grid.

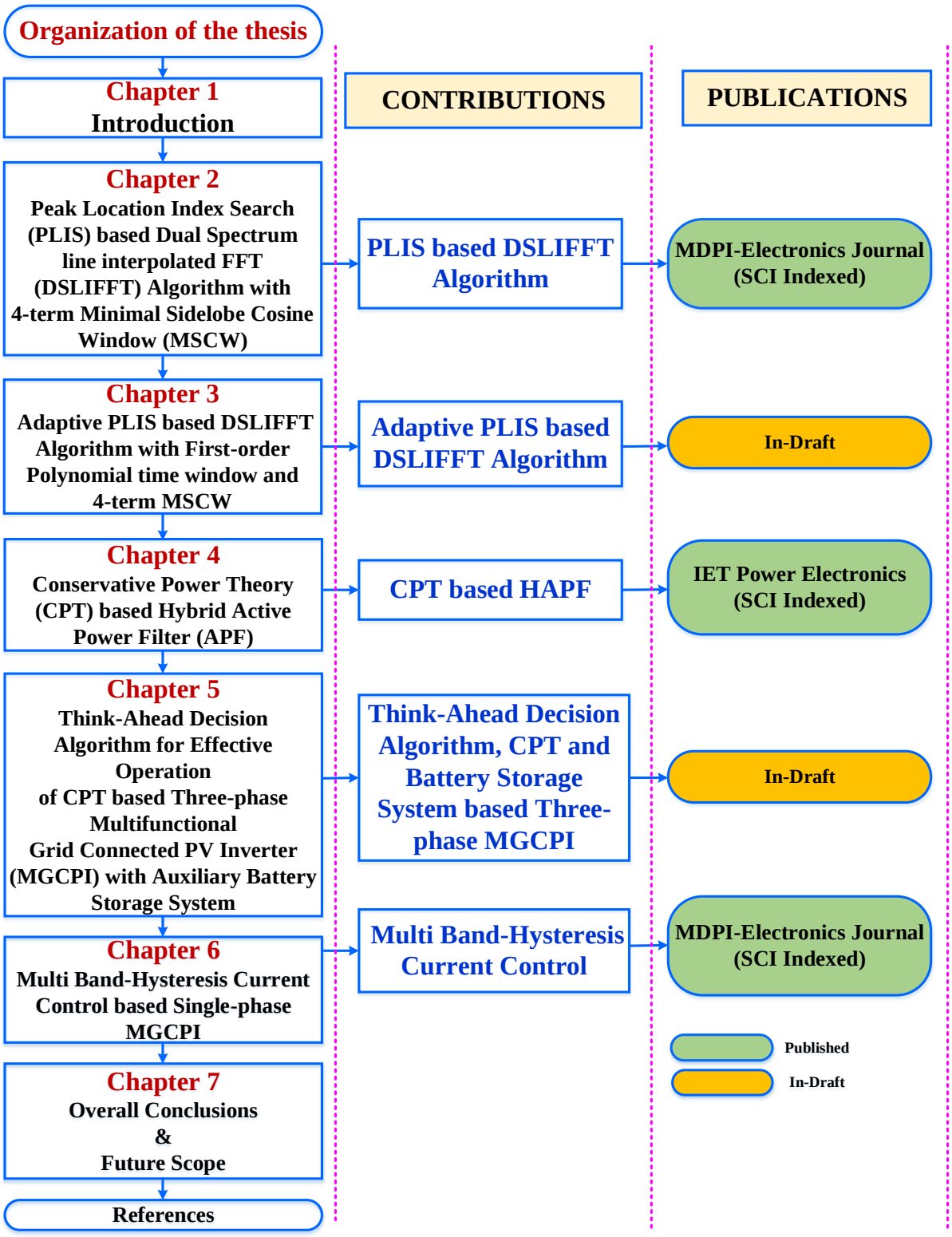

Fig. 1.7 Organization of the thesis

1.10 Conclusions

This work is very relevant to the utility, commercial and residential consumers through highly accurate and simple estimation of harmonics of all types and controlling these harmonics by designing suitable control methodologies for improving the effectiveness of compensation devices in the modern electric grid. This work attempts to take care of every possible type of non-linear loads now and those that may add in the future.

Chapter 2

Peak Location Index Search (PLIS) based Dual Spectrum Line Interpolated FFT (DSLIFFT) with 4-Term Minimal Sidelobe Cosine Window (MSCW)

2.1 Introduction

The proliferation of nonlinear loads and integration of renewable energy sources require attention for accurate harmonic estimation along with estimation of fundamental amplitude, frequency and phase angle for protection, improving power quality, and managing power effectively in a smart electric grid. There are currently several Windowed Interpolated Fast Fourier Transform (WIFFT) algorithms for voltage harmonic estimation, but estimation of current harmonics using WIFFT is not explored sufficiently. The existing WIFFT algorithms, when used for current harmonic estimation result in low accuracy due to spectral leakage and picket fence effect. A peak location index search (PLIS)-based Dual-Spectrum Line Interpolated Fast Fourier Transform (DSLIFFT) algorithm with 4-Term Minimal Sidelobe Cosine Window (MSCW) for estimating current harmonics under variable frequency conditions for high-penetration renewable energy utility grids has been developed and described in this chapter. The effectiveness of the PLIS based DSLIFFT algorithm wit 4-term MSCW is validated by simulation studies and real-time experimentation using the National Instruments (NI) compact Reconfigurable Input Output based embedded system NI cRIO 9082 under real-world nonlinear loading conditions. The detailed literature survey of various WIFFT algorithms have been discussed in chapter 1.4.1.

2.2 PLIS based DSLIFFT algorithm with 4-Term Minimized Sidelobe Cosine Window

The 4-Term MSCW functions and its corresponding PLIS-based DSLIFFT algorithm developed for current harmonic estimation is explained in detail in the following sections.

2.2.1 4-Term MSCW Function

Numerous window functions are reported in the literature for harmonic spectral estimation, but there is a compromise in accuracy because of the window properties, such as main lobe, sidelobe widths, and sidelobe roll-off rates [27,28]. However, Cosine Windows (CWs) such as Hanning, Hamming, and Blackman are the most common window functions adopted in harmonic spectral analysis. Moreover, various CWs are reported in the literature for harmonic estimation [26 – 28, 30–36,38–42]. Apart from another family of windows, CWs are well considered for harmonic estimation.

The basic discrete $Cos^{\alpha}x$ window function is expressed as follows [30-36]:

$$w(n) = cos^{\alpha}\left(\frac{\pi n}{N}\right), 0 \leq |n| \leq \frac{N}{2} \tag{2.1}$$

By changing the "α" value, different forms of CWs are developed. Here α takes integer values, and N is fixed to 2^k, where k is a natural number. Based upon the window function given in Eq. (2.1) Various advanced CWs are derived for harmonic estimation. Given the main lobe, sidelobe, and sidelobe roll of rate requirements a 4-Term MSCW is adopted for harmonic estimation, a PLIS-based DSLIFFT algorithm has been developed to improve its accuracy matching with the RT signal analysis. The objective of this algorithm is to estimate the spectral amplitude and phase angle of the harmonic current signals accurately. The discrete-time 4-Term MSCW with length *N* and order *H* is expressed as [30-36]:

$$\boldsymbol{w_{4MSCW}(n)} = \sum_{\boldsymbol{h=0}}^{\boldsymbol{H-1}} \boldsymbol{(-1)^h a_h cos\left(\frac{2\pi hn}{N}\right)} \qquad \textit{for n = 0, 1, ..., N-1} \tag{2.2}$$

where *n* represents the sample index, *N* represents the total number of samples, *h* denotes the fundamental and harmonic numbers and a_h represents the window coefficients. The CWs are developed based upon the *H* and a_h values to meet the computation requirements of the interpolation technique. The coefficients of a_h must comply with the following conditions.

$$\sum_{\boldsymbol{h=0}}^{\boldsymbol{H-1}} \boldsymbol{(-1)^h a_h = 0}, \sum_{\boldsymbol{h=0}}^{\boldsymbol{H-1}} \boldsymbol{a_h = 1} \tag{2.3}$$

The spectral window corresponding to the 4-Term MSCW derived from Eq. (2.1) by using the Discrete-Time Fourier transform (DTFT) is written as follows

$$W_{4MSCW}(n) = \sum_{h=0}^{H-1} \frac{a_h}{2} \left[e^{\frac{-j\pi(n-h)(N-1)}{N}} \frac{\sin((n-h)\pi}{\sin\left(\frac{(n-h)\pi}{N}\right)} + e^{\frac{-j\pi(n+h)(N-1)}{N}} \frac{\sin((n+h)\pi}{\sin\left(\frac{(n+h)\pi}{N}\right)} \right] \quad (2.4)$$

for n = 0,1,...,N-1

Concerning the 4-Term MSCW properties regarding the main lobe width between zero crossing, it must fulfill the following condition to get the $|W_{4MSCW}(n)|$ values as zeros.

$$\begin{cases} n \pm h = d \\ n \pm h \neq dN \end{cases} \quad \text{for d} = 0, \pm1, \pm2, \ldots, +\infty \quad (2.5)$$

The adopted 4-Term MSCW functions of type-1 and type-2 coefficients and properties adopted from [34] are tabulated in Table 2.1.

Table 2.1 4-Term MSCW Coefficients and Properties

4-Term MSCW Type	Window Coefficients				Main Lobe Width	Peak Sidelobe Level (dB)	Sidelobe Roll-off Rate (dB/oct)
	a_0	a_1	a_2	a_3			
type–1	0.355768	0.487396	0.144232	0.012604	4Hπ/N	- 93	18
type–2	0.312500	0.46875	0.1875	0.03125	4Hπ/N	- 61	42

2.2.2 Mathematical formulation of harmonic signal sampling and windowing

The mathematical formulation of the harmonic signal is represented as:

$$x(nT_s) = x(t) = \sum_{h=1}^{H} A_h \sin(2\pi f_h n T_s + \varphi_h) \text{ where n} = 0,1,\ldots N-1 \quad (2.6)$$

where the amplitude, frequency, and phase angle are denoted as A_h, f_h and φ_h, respectively. The sampling time of the signal is represented as T_s. Due to the unstable nature of the fundamental frequency, the sampling is non-synchronous, which leads to spectral leakage. To suppress the spectral leakage effect, the sampled signal is weighted by the window function. The FFT of the windowed sample signal under non-synchronous sampling is represented as:

$$X(k) = \sum_{h=1}^{H} \frac{A_h}{2j} \left[e^{j\varphi_h} W_{4MSCW}(k - k_h) - e^{j\varphi_h} W_{4MSCW}(k + k_h) \right] \tag{2.7}$$

where $k = 0, 1 \ldots (N - 1)$, W_{MSCW} indicates the FFT of the 4-Term MSCW function, k_h denotes the division factor of signal frequency and the frequency resolution, which is expressed as:

$$k_h = \frac{f_h N}{f_s} = l_h + \xi_h \tag{2.8}$$

where l_h is an integer value and ξ_h $(0 \leq \xi_h \leq 1)$ is the fractional part. The negative frequency part is ignored in Equation (2.7). The sampling frequency used for computation is represented as f_s. The l_h and ξ_h are computed by PLIS-based DSLIFFT algorithm as described in the next section.

2.2.3 Peak Location Index Search (PLIS) Method

The detailed flowchart of the developed PLIS-based DSLIFFT algorithm is depicted in Fig.2.1. The input current harmonic signal is sampled and weighted by the adopted 4-Term MSCW after that the spectrum is computed. To compute the fundamental and harmonic peaks, PLIS method is developed. In this method, a threshold factor (τ) is defined to ignore the estimation of peak locations of all the frequency bins. By defining the threshold factor, the peak location indexes are identified for the dominant harmonic frequency bins. Initially, the harmonic index is defined as *I,* and the threshold factor is considered to be 0.1% of the fundamental amplitude. The threshold factor is calculated from the relation between the fundamental and the considerable lowest harmonic amplitude which will contribute to the total harmonic distortion (THD). The importance of the threshold factor is to identify the significant harmonic peak value corresponding to the lower order harmonics.

The threshold factor of 0.1% in PLIS method is based on the considerable dominant harmonic peak value concerning its fundamental amplitude. Usually, the least harmonic amplitudes which will impact the signal quality in the current signal will be 0.1% of the fundamental amplitude based on the knowledge of different nonlinear load current harmonic data. Therefore, threshold factor is considered to be 0.1%, to obtain the harmonic peak amplitudes. Afterward, DSLIFFT correction is applied to estimate the amplitude, frequency and phase angle of the fundamental as well as all other harmonic orders. This procedure effectively decreases the computation process. However, the peak search process in the conventional DSLIFFT algorithm reported in the literature [31–42] will check for the entire frequency bin peak locations, which in turn increases the computation burden. The objective of the PLIS method is to identify the fundamental as well as adjacent harmonic spectral lines accurately.

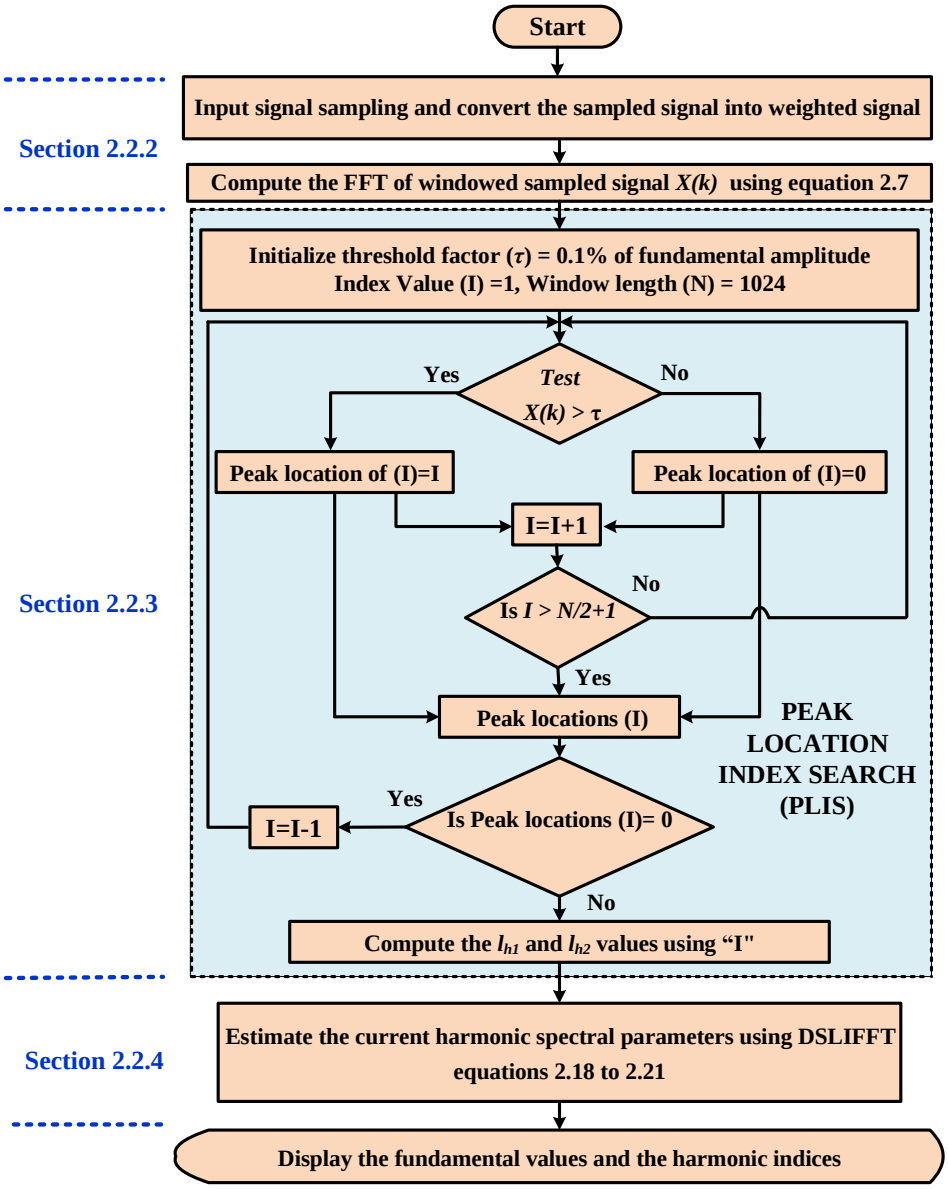

Fig. 2.1 PLIS based DSLIFFT algorithm

2.2.4 DSLIFFT Algorithm

After obtaining the locations of the spectral lines, an interpolation method is applied to estimate the amplitude, frequency and phase angle of the harmonic signal. The conventional DSLIFFT algorithm presented in the literature [31–42] is improved by using the PLIS method. The spectral line location of the h^{th} harmonic component can be obtained from the PLIS method. The ξ_h can be estimated from the interpolation method from which amplitude, frequency and phase angle of h^{th} harmonic can be accurately computed. The pictorial representation of the PLIS-based DSLIFFT using 4-Term MSCW is illustrated in Figure 2.2.

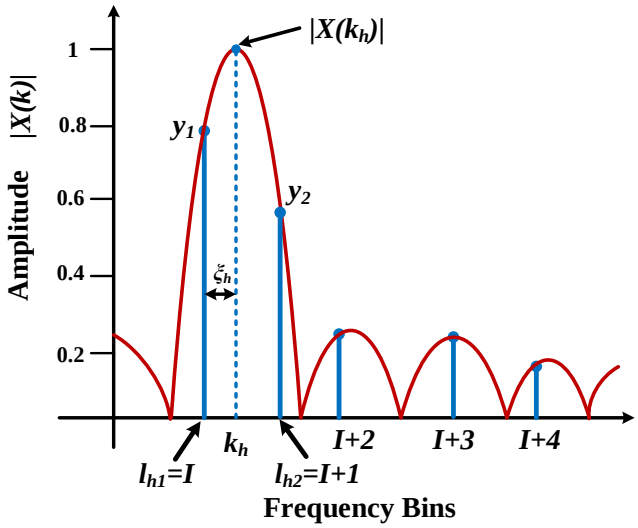

Fig. 2.2 PLIS-based DSLIFFT algorithm with 4-Term MSCW

The frequency spectrum expression is written as [31–42]:

$$X(\xi_h) = \frac{A_h}{2j}\left[e^{j\varphi_h} W_{4MSCW}(\xi_h - k_h)\right] \qquad \text{for } \xi_h = 0,1,.....N\text{-}1 \tag{2.9}$$

The two amplitude spectral lines represents the h^{th} harmonic is considered to be l_{h1} and l_{h2} (where $l_{h1} = I$, $l_{h2} = I + 1$, $l_{h1} < k_h < l_{h2}$). The peak locations of the harmonic amplitudes are obtained from PLIS method.

Let $y_1 = |X(I)|$and $y_2 = |X\ (I+1)|$, then y_1 and y_2 are written as follows:

$$y_1 = |X(I)| = |A_h|.|W_{4MSCW}(2\pi(I - k_h)/N| \tag{2.10}$$

$$y_2 = |X(I+1)| = |A_h|.|W_{4MSCW}(2\pi((I+1) - k_h)/N| \tag{2.11}$$

The least-square curve fitting is used to find the spectral amplitudes. The resultant expression of an independent variable α is expressed as

$$\alpha = k_h - l_{h1} - 0.5\ for - 0.5 \le \alpha \le 0.5 \tag{2.12}$$

The y_1 and y_2 are expressed as

$$y_1 = |X(I)| = |A_h|.|W_{4MSCW}(2\pi(-\alpha - 0.5)/N| \tag{2.13}$$

$$y_2 = |X(I+1)| = |A_h|.|W_{4MSCW}(2\pi(-\alpha + 0.5)/N| \tag{2.14}$$

To compute the harmonic parameters, a symmetrical coefficient β which is a function of α is considered, where *t*he β expression regarding α can be written as

$$\beta = g(\alpha) = \frac{(y_2 - y_1)}{(y_2 + y_1)} \tag{2.15}$$

From Equations (2.13) and (2.14), β can be expressed as

$$\beta = g(\alpha) = \frac{|W_{4MSCW}(2\pi(-\alpha + 0.5)/N)| - |W_{4MSCW}(2\pi(-\alpha - 0.5)/N)|}{|W_{4MSCW}(2\pi(-\alpha + 0.5)/N)| + |W_{4MSCW}(2\pi(-\alpha - 0.5)/N)|} \quad (2.16)$$

Based on the window polynomial order, the α expression concerning β is derived from the least-square curve fitting technique. The relation between α and β is derived as follows using the polynomial approximations.

$$\alpha = \alpha_0\beta + \alpha_1\beta^2 + \alpha_2\beta^3 + \alpha_3\beta^4 + \alpha_4\beta^5 \quad (2.17)$$

The polynomial coefficients of 4-Term MSCW type-1 and type-2 coefficients are tabulated in Table 2.2. Where the 4-Term MSCW with polynomial order 5 is named as type-1 and polynomial order 1 is named as type-2.

Table 2.2 4-Term MSCW Polynomial Coefficients

Window Type	a_0	a_1	a_2	a_3	a_4
4-Term MSCW type-1	2.6645	-	0.2806	-	0.1313
4-Term MSCW type-2	3.5	-	-	-	-

After calculating the α value, the amplitude, frequency and phase angle values are calculated based upon the following interpolated formulas

$$k_h = \alpha + I + 0.5 \quad (2.18)$$

$$A_h = \frac{2y_1}{|W_{MSCW}(2\pi(I - k_h))/N|} \quad (2.19)$$

$$f_h = \frac{k_h f_s}{N} \quad (2.20)$$

$$\varphi_h = \arg\big(X(I)\big) - \arg\left[W_{MSCW}\left(\frac{2\pi(I - k_h)}{N}\right)\right] + \frac{\pi}{2} \quad (2.21)$$

The major enhancement in this interpolation algorithm is a PLIS method, which is used to determine the amplitude of dominant harmonic frequency peak locations, instead of searching the amplitudes of all the frequency bins peak locations. Then interpolation is applied to estimate the amplitude, frequency and phase angle of the fundamental as well as harmonic components, where the fundamental component estimation is useful for synchrophasor processing. The PLIS based DSLIFFT algorithm with 4-term MSCW is developed in RT using Laboratory Virtual Instrument Engineering Workbench (LabVIEW) programmed National

Instruments (NI) compact Reconfigurable Input/output system (cRIO) system described in [124].

2.3 Simulation Results

This section demonstrates the simulation results of the developed PLIS-based DSLIFFT using 4-Term MSCW. Initially, the algorithm was simulated in a LabVIEW environment with a programmed harmonic test signal. The amplitudes and the corresponding phase angles of the programmed harmonic signal for fundamental frequency values of 49.5 Hz and 50.5 Hz are depicted in Table 2.3.

Table 2.3 Simulated harmonic test signal information

Parameters	**Harmonic Orders (Fundamental frequency = 49.5 Hz and 50.5 Hz)**								
	1	**3**	**5**	**7**	**9**	**11**	**13**	**15**	**17**
Amplitude (Amp)	2.5	0.4	0.35	0.3	0.25	0.2	0.2	0.15	0.2
Phase angle (deg)	40	115	−30	110	−20	100	−10	−90	0
Frequency (Hz)	49.5	148.5	247.5	346.5	445.5	544.5	643.5	742.5	841.5
	50.5	151.5	252.5	353.5	454.5	555.5	656.5	757.5	858.5

To justify the estimation accuracy under non-synchronous sampling frequency, the input signal is analyzed by using PLIS-based DSLIFFT with 4-Term MSCW under different fundamental frequency values of 49.5Hz and 50.5Hz respectively. The PLIS-based DSLIFFT using 4-Term MSCW results are compared with the conventional DSLIFFT algorithm reported in [31–42] using 4-Term MSCW. The simulated benchmark signal waveform representation is depicted in Fig.2.3.

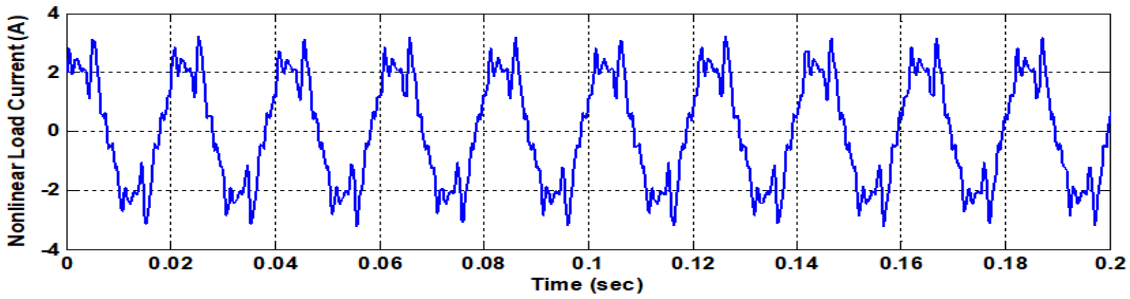

Fig. 2.3 Benchmark harmonic test signal

2.3.1 Amplitude Estimation

The amplitude estimation of the benchmark harmonic test signal and its error comparison for 4-Term MSCW type-1 and type-2 with fundamental frequency values of 49.5 Hz and 50.5 Hz are tabulated in Tables 2.4–2.7.

Table 2.4 (a) Amplitude estimation comparison using 4-Term MSCW type-1 with DSLIFFT and PLIS-based DSLIFFT, when the fundamental frequency = 49.5 Hz

Harmonic Order (h)	Amplitude (Amp) Estimation using 4-Term MSCW type-1		The Relative Error of Amplitude Estimation (%) using 4-Term MSCW type-1	
	with DSLIFFT [32–39]	with PLIS-based DSLIFFT	with DSLIFFT	with PLIS-based DSLIFFT
1	2.4824	2.4899	0.7028	0.4020
3	0.3753	0.3857	6.1643	3.5653
5	0.3375	0.3211	3.5652	8.2501
7	0.2998	0.2918	0.0502	2.7204
9	0.2448	0.2496	2.0958	0.1525
11	0.1831	0.1985	8.4625	0.7695
13	0.1967	0.1910	1.6485	4.5175
15	0.1498	0.1395	0.1524	6.9757
17	0.1916	0.1960	4.2013	1.9859

Table 2.5 Amplitude estimation comparison using 4-Term MSCW type-2 with DSLIFFT and PLIS-based DSLIFFT, when the fundamental frequency = 49.5 Hz

Harmonic Order (h)	Amplitude (Amp) Estimation using 4-Term MSCW type-2		The Relative Error of Amplitude Estimation (%) using 4-Term MSCW type-2	
	with DSLIFFT [32–39]	with PLIS-based DSLIFFT	with DSLIFFT	with PLIS-based DSLIFFT
1	2.4866	2.4998	0.5361	0.0071
3	0.3811	0.3999	4.7318	0.0035
5	0.3405	0.3498	2.7285	0.0371
7	0.2999	0.2988	0.0384	0.4133
9	0.2460	0.2497	1.6013	0.1162
11	0.1870	0.1988	6.5141	0.5870
13	0.1975	0.1999	1.2588	0.0111
15	0.1498	0.1496	0.1162	0.2658
17	0.1936	0.1970	3.2176	1.5171

Table 2.5 (b) The Relative Error and Mean square error of amplitude estimation comparison

Harmonic Order (h)	4-Term MSCW type-2		
	The Relative Error of Amplitude Estimation (%)		The Mean Square Error of Amplitude Estimation (%)
	with DSLIFFT [32–39]	with PLIS-based DSLIFFT	with PLIS-based DSLIFFT
1	0.5361	0.0071	1.640×10^{-06}
3	4.7318	0.0035	3.130×10^{-06}
5	2.7285	0.0371	5.800×10^{-06}
7	0.0384	0.4133	4.680×10^{-05}
9	1.6013	0.1162	8.900×10^{-07}
11	6.5141	0.5870	3.600×10^{-05}
13	1.2588	0.0111	8.500×10^{-08}
15	0.1162	0.2658	3.208×10^{-05}
17	3.2176	1.5171	4.505×10^{-06}

Table 2.6 Amplitude estimation comparison using 4-Term MSCW type-1 with DSLIFFT and PLIS-based DSLIFFT, when the fundamental frequency = 50.5 Hz

Harmonic Order (h)	Amplitude (Amp) Estimation using 4-Term MSCW type-1		The Relative Error of Amplitude Estimation (%) using 4-Term MSCW type-1	
	with DSLIFFT [32–39]	with PLIS-based DSLIFFT	with DSLIFFT	with PLIS-based DSLIFFT
1	2.3930	2.4977	4.2795	0.0931
3	0.3999	0.3967	0.0266	0.8342
5	0.3393	0.3455	3.0453	1.2898
7	0.2829	0.2874	5.7078	4.1883
9	0.2494	0.2483	0.2479	0.6866
11	0.1960	0.1890	2.0134	5.5007
13	0.1854	0.1995	7.3230	0.2709
15	0.1490	0.1395	0.6867	6.9756
17	0.1976	0.1999	1.1892	0.0447

Table 2.7 Amplitude estimation comparison using 4-Term MSCW type-2 with DSLIFFT and PLIS-based DSLIFFT, when the fundamental frequency = 50.5 Hz

Harmonic Order (h)	Amplitude (Amp) Estimation using 4-Term MSCW type-2		The Relative Error of Amplitude Estimation (%) using 4-Term MSCW type-2	
	with DSLIFFT [32–39]	with PLIS-based DSLIFFT	with DSLIFFT	with PLIS-based DSLIFFT
1	2.4181	2.4982	3.2777	0.0709
3	0.3999	0.3975	0.0210	0.6367
5	0.3418	0.3466	2.3292	0.9845
7	0.2869	0.2904	4.3793	3.2077
9	0.2495	0.2487	0.1888	0.5237
11	0.1969	0.1916	1.5380	4.2192
13	0.1887	0.1996	5.6291	0.2065
15	0.1492	0.1420	0.5237	5.3599
17	0.1982	0.1999	0.9077	0.0341

From the above tabulated results in Table 2.5 to Table 2.7 it is evident that the percentage relative error of the fundamental amplitude is impressively less in the case of PLIS based DSLIFFT with 4-Term MSCW type-2 compared to PLIS based DSLIFFT with 4-Term MCSW type-1 and DSLIFFT based 4-Term MCSW type-1 and type-2 as observed in the first row of all the tables. Moreover, the percentage relative errors of the remaining harmonic amplitudes are reasonably less, when PLIS based DSLIFFT with type 2 is compared with DSLIFFT using 4-Term MCSW type-1 and type-2.

It is evident that the amplitude estimation accuracy of the PLIS-based DSLIFFT with 4-Term MSCW of type-2 algorithm is in the order of 10^{-3} for fundamental frequency of 49.5 Hz and is of the order 10^{-2} for fundamental frequecny 50.5Hz. The PLIS based DSLIFFT with 4-Term MSCW type-2 exhibits better results than the 4-Term MSCW with conventional DSLIFFT algorithm.

The estimation accuracy of PLIS based DSLIFFT with 4-Term MSCW has been graphically demonstrated in Fig. 2.4 and Fig. 2.5. by comparing the percentage relative error variations of fundamental and harmonic amplitudes with conventional DSLIFFT using 4-Term MSCW type-1 and type-2 at frequency values of 49.5 Hz and 50.5 Hz.

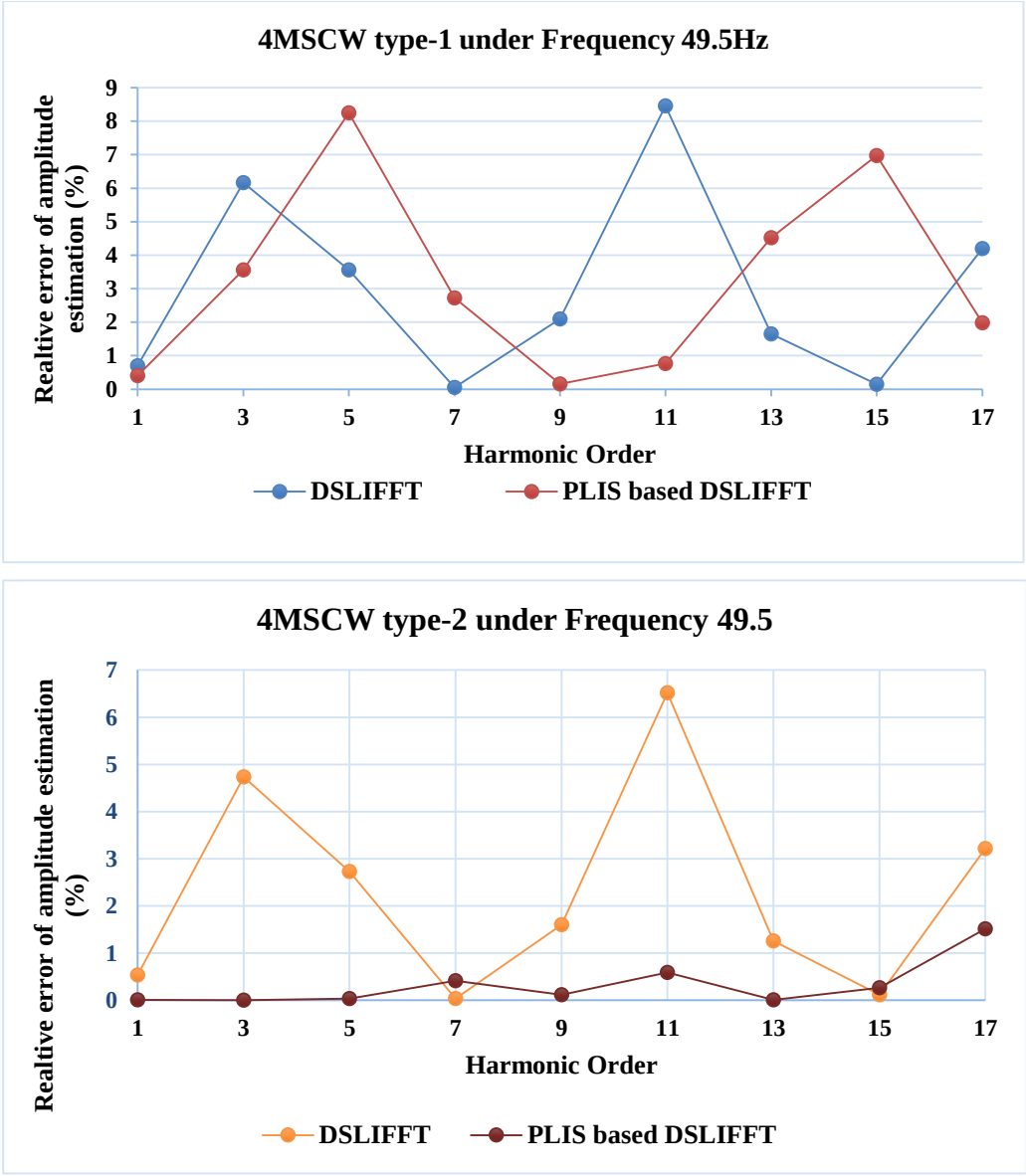

(a)

Fig. 2.4 Percentage relative errors variation of amplitude estimation to the harmonic order with PLIS-based DSLIFFT and conventional DSLIFFT using 4-Term MSCW type-1 and type-2 at the frequency is 49.5 Hz.

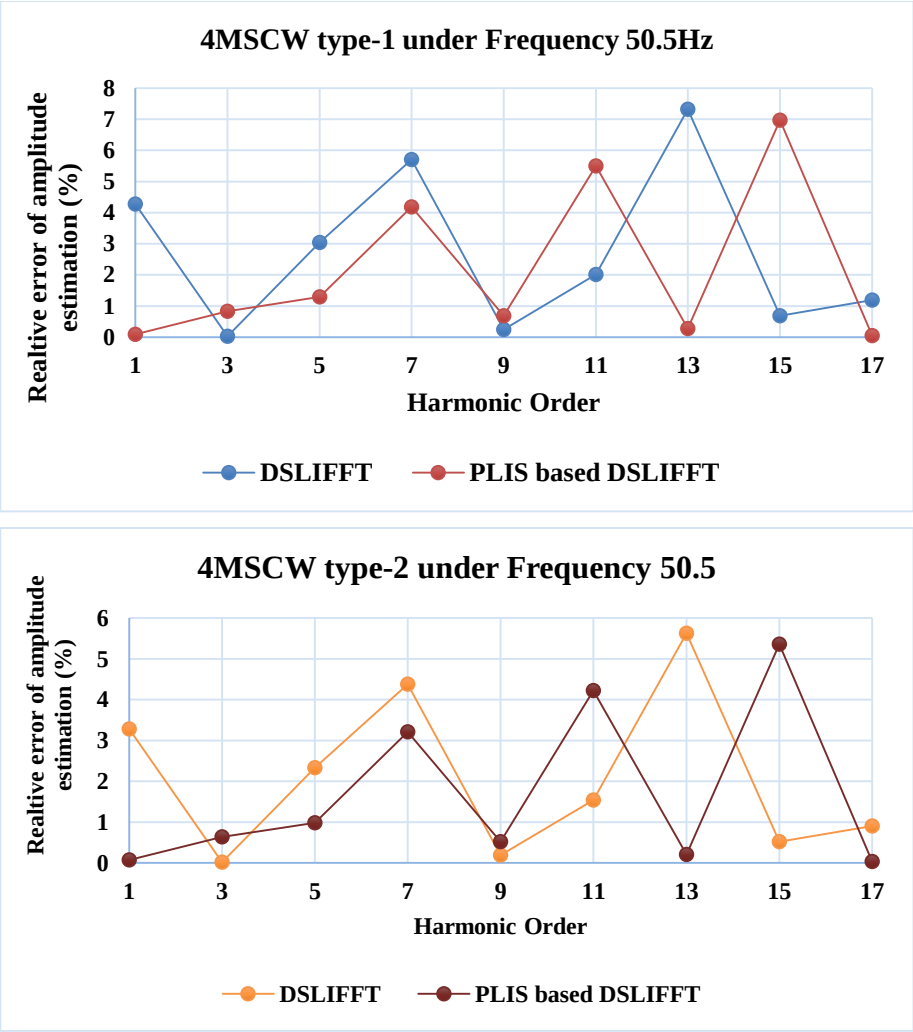

Fig. 2.5 Percentage relative errors variation of amplitude estimation to the harmonic order with PLIS-based DSLIFFT and conventional DSLIFFT using 4-Term MSCW type-1 and type-2 at the frequency 50.5 Hz

From the Fig. 2.4 and Fig 2.5 the percentage relative error variation of the fundamental amplitude estimation using PLIS-based DSLIFFT with 4-Term MSCW of type-2 appears low compared to PLIS based DSLIFFT with 4-Term MCSW type-1 and DSLIFFT based 4-Term MCSW type-1 and type-2 under different frequency cases of 49.5 Hz and 50.5 Hz. These line graphs clearly demonstrate that the amplitude estimation is more accurate using PLIS-based DSLIFFT with 4-Term MSCW of type-2.

2.3.2 Frequency Estimation

The frequency estimation of the benchmark harmonic test signal and its error comparison for 4-Term MSCW type-1 and type-2 with fundamental frequency values of 49.5 Hz and 50.5 Hz are tabulated in Tables 2.8–2.11.

Table 2.8 Frequency estimation comparison using 4-Term MSCW type-1 with DSLIFFT and PLIS-based DSLIFFT, when the fundamental frequency = 49.5 Hz

Harmonic Order (h)	Frequency (Hz) Estimation using 4-Term MSCW type-1		The Relative Error of Frequency Estimation (%) using 4-Term MSCW type-1	
	with DSLIFFT [32–39]	with PLIS-based DSLIFFT	with DSLIFFT	With PLIS-based DSLIFFT
1	49.5000346	49.5000368	-7.4406×10^{-05}	-6.9938×10^{-05}
3	148.5000878	148.5000365	-2.4595×10^{-05}	-5.9110×10^{-05}
5	247.5000069	247.5001234	-4.9840×10^{-05}	-2.7740×10^{-06}
7	346.5000111	346.5000139	-4.0007×10^{-06}	-3.2111×10^{-06}
9	445.5000269	445.4999988	2.7295×10^{-07}	-6.0283×10^{-06}
11	544.5000422	544.5002823	-5.1850×10^{-05}	-7.7484×10^{-06}
13	643.5000888	643.5000947	-1.4715×10^{-05}	-1.3799×10^{-05}
15	742.5000096	742.5000303	-4.0779×10^{-06}	-1.2987×10^{-06}
17	841.5000116	841.5000183	-2.1798×10^{-06}	-1.3728×10^{-06}

Table 2.9 Frequency estimation comparison using 4-Term MSCW type-2 with DSLIFFT and PLIS-based DSLIFFT, when the fundamental frequency = 49.5 Hz

Harmonic Order (h)	Frequency (Hz) Estimation using 4-Term MSCW type-2		The Relative Error of Frequency Estimation (%) using 4-Term MSCW type-2	
	with DSLIFFT [32–39]	with PLIS-based DSLIFFT	with DSLIFFT	with PLIS-based DSLIFFT
1	49.5000000	49.5000000	-3.1142×10^{-08}	-5.7960×10^{-10}
3	148.5000001	148.5000000	-6.7450×10^{-08}	-5.1360×10^{-09}
5	247.5000000	247.5000000	8.5180×10^{-09}	-9.5515×10^{-10}
7	346.4999999	346.5000000	4.0677×10^{-08}	1.1977×10^{-10}
9	445.4999999	445.5000000	2.9231×10^{-08}	-4.1347×10^{-10}
11	544.4999998	544.5000000	2.8381×10^{-08}	-4.7089×10^{-10}
13	643.5000001	643.5000000	-9.5225×10^{-09}	-1.1344×10^{-10}
15	742.4999999	742.5000000	7.0338×10^{-09}	-4.9105×10^{-10}
17	841.5000000	841.5000000	-1.5468×10^{-09}	1.6209×10^{-10}

Table 2.10 Frequency estimation comparison using 4-Term MSCW type-1 with DSLIFFT and PLIS-based DSLIFFT, when the fundamental frequency = 50.5 Hz

Harmonic Order (h)	Frequency (Hz) Estimation using 4-Term MSCW type-1		The Relative Error of Frequency Estimation (%) using 4-Term MSCW type-1	
	with DSLIFFT [32–39]	with PLIS-based DSLIFFT	with DSLIFFT	with PLIS-based DSLIFFT
1	50.5000422	50.5000159	-8.3555×10^{-05}	-3.14059×10^{-05}
3	151.4999135	151.5000478	5.7095×10^{-05}	-3.15744×10^{-05}
5	252.5001140	252.5000150	-4.5132×10^{-05}	-5.95614×10^{-06}
7	353.4999881	353.5000803	3.3715×10^{-06}	-2.27095×10^{-05}
9	454.5000656	454.5000181	-1.4439×10^{-05}	-3.98165×10^{-06}
11	555.5001266	555.5001078	-2.2782×10^{-05}	-1.93978×10^{-05}
13	656.5000193	656.5000285	-2.9417×10^{-06}	-4.34459×10^{-06}
15	757.5000407	757.5001457	-5.3686×10^{-06}	-1.92300×10^{-05}
17	858.5000624	858.5000213	-7.2647×10^{-06}	-2.48504×10^{-06}

Table 2.11 Frequency estimation comparison using 4-Term MSCW type-2 with DSLIFFT and PLIS-based DSLIFFT, when the fundamental frequency = 50.5 Hz

Harmonic Order (h)	Frequency (Hz) Estimation using 4-Term MSCW type-2		The Relative Error of Frequency Estimation (%) using 4-Term MSCW type-2	
	with DSLIFFT [32–39]	with PLIS-based DSLIFFT	with DSLIFFT	with PLIS-based DSLIFFT
1	50.5000001	50.5000000	$-2.2646\ x10^{-07}$	$-2.03743\ x10^{-09}$
3	151.4999994	151.5000000	$3.6736\ x10^{-07}$	$4.81584\ x10^{-09}$
5	252.5000000	252.5000000	$1.9738\ x10^{-08}$	$3.62380\ x10^{-10}$
7	353.4999999	353.5000000	$2.0310\ x10^{-08}$	$1.59258\ x10^{-10}$
9	454.5000001	454.5000000	$-1.5487\ x10^{-08}$	$1.36637\ x10^{-10}$
11	555.5000002	555.5000000	$-3.2930\ x10^{-08}$	$6.71479\ x10^{-11}$
13	656.5000001	656.5000000	$-7.9165\ x10^{-09}$	$-5.25211\ x10^{-10}$
15	757.5000000	757.5000000	$-4.0858\ x10^{-09}$	$-3.76255\ x10^{-11}$
17	858.5000000	858.5000000	$3.9645\ x10^{-09}$	$1.73331\ x10^{-10}$

From the above tabulated results in Table 2.8 to Table 2.11 it is evident that the percentage relative error of the fundamental amplitude is impressively less in the case of PLIS based DSLIFFT with 4-Term MSCW type-2 compared to PLIS based DSLIFFT with 4-Term MCSW type-1 and DSLIFFT based 4-Term MCSW type-1 and type-2 as observed in the first row of all the tables above. Moreover, the percentage relative errors of the remaining harmonic amplitudes are reasonably less, when PLIS based DSLIFFT with type 2 is compared with DSLIFFT using 4-Term MCSW type-1 and type-2.

It is evident that the frequency estimation accuracy of the PLIS-based DSLIFFT with 4-Term MSCW of type-2 algorithm is in the order of 10^{-9} for fundamental frequency of 49.5 Hz and is of the order 10^{-8} for fundamental frequecny 50.5Hz. The PLIS based DSLIFFT with 4-Term MSCW type-2 exhibits better results than the 4-Term MSCW with conventional DSLIFFT algorithm.

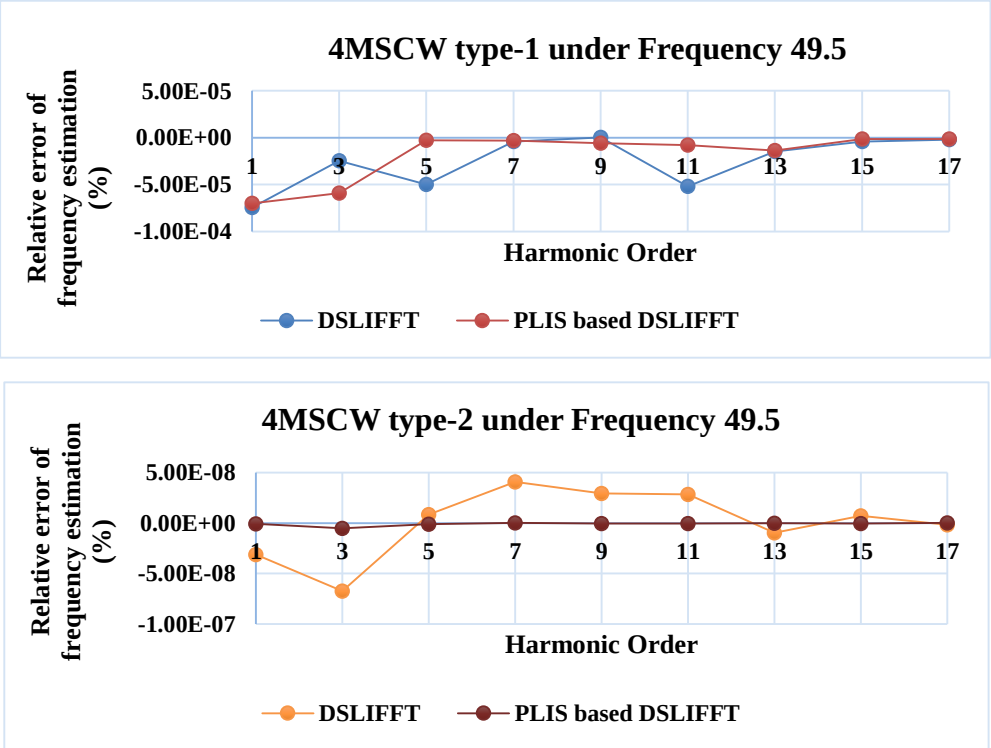

Fig. 2.6 Percentage relative errors variation of frequency estimation to the harmonic order with PLIS-based DSLIFFT and conventional DSLIFFT using 4-Term MSCW type-1 and type-2 at the frequency 49.5 Hz

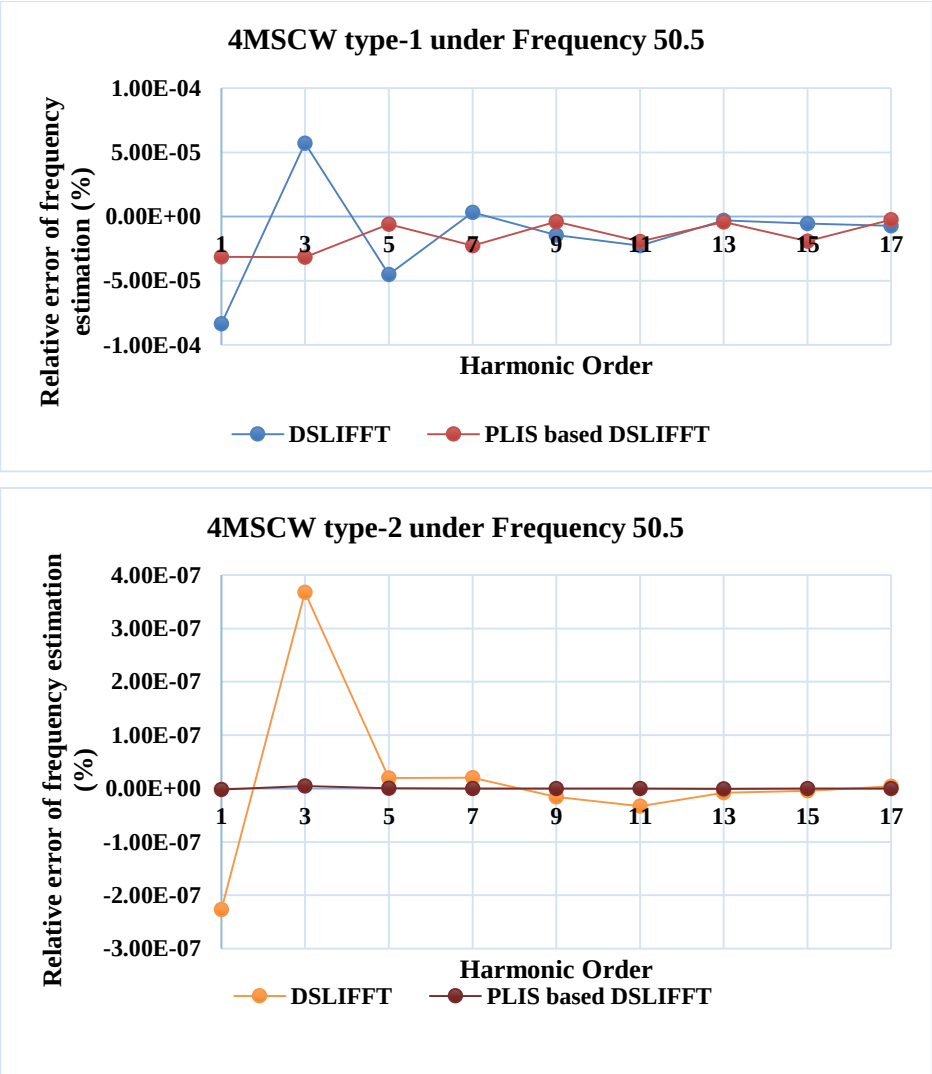

Fig. 2.7 Percentage relative errors variation of frequency estimation to the harmonic order with PLIS-based DSLIFFT and conventional DSLIFFT using 4-Term MSCW type-1 and type-2 at the frequency 50.5 Hz

The estimation accuracy of PLIS based DSLIFFT with 4-Term MSCW has been graphically demonstrated in Fig. 2.6 and Fig. 2.7., by comparing the percentage relative error variations of fundamental frequency and harmonic frequencies with conventional DSLIFFT using 4-Term MSCW type-1 and type-2 at frequency values of 49.5 Hz and 50.5 Hz.

2.3.3 Phase angle Estimation

The phase angle estimation of the benchmark harmonic test signal and its error comparison for 4-Term MSCW type-1 and type-2 with fundamental frequency values of 49.5 Hz and 50.5 Hz are tabulated in Tables 2.12–2.15.

Table 2.12 Phase angle estimation comparison using 4-Term MSCW type-1 with DSLIFFT and PLIS-based DSLIFFT, when the fundamental frequency = 49.5 Hz

Harmonic Order (h)	Phase angle (deg) Estimation using 4-Term MSCW type-1		The Relative Error of Phase angle Estimation (%) using 4-Term MSCW type-1	
	with DSLIFFT [32–39]	with PLIS-based DSLIFFT	with DSLIFFT	with PLIS-based DSLIFFT
1	39.9018	40.0345	0.2454	− 0.0861
3	114.7082	115.1044	0.2537	− 0.0908
5	− 29.7853	− 30.1692	0.7156	− 0.5640
7	110.0253	109.9035	− 0.0230	0.0877
9	− 20.1676	− 20.0241	− 0.8382	− 0.1207
11	100.3316	100.0481	− 0.3316	− 0.0481
13	− 9.8551	− 9.8817	1.4489	1.1826
15	− 90.0466	− 90.1555	− 0.0517	− 0.1728
17	− 0.0024	− 0.0008	0	0

Table 2.13 Phase angle estimation comparison using 4-Term MSCW type-2 with DSLIFFT and PLIS-based DSLIFFT, when the fundamental frequency = 49.5 Hz

Harmonic Order (h)	Phase angle (deg) Estimation using 4-Term MSCW type-2		The Relative Error of Phase angle Estimation (%) using 4-Term MSCW type-2	
	with DSLIFFT [32–39]	with PLIS-based DSLIFFT	with DSLIFFT	with PLIS-based DSLIFFT
1	39.9033	40.0366	0.2418	− 0.0914
3	114.7098	115.1098	0.2523	− 0.0954
5	− 29.7806	− 30.1688	0.7312	− 0.5625
7	110.0258	109.9043	− 0.0234	0.0870
9	− 20.1676	− 20.0225	− 0.8381	− 0.1125
11	100.3420	100.0507	− 0.3420	− 0.0507
13	− 9.8515	− 9.8763	1.4849	1.2375
15	− 90.0452	− 90.1549	− 0.0502	− 0.1721
17	− 0.0024	− 0.0008	0	0

Table 2.14 Phase angle estimation comparison using 4-Term MSCW type-1 with DSLIFFT and PLIS-based DSLIFFT, when the fundamental frequency = 50.5 Hz

Harmonic Order (h)	Phase angle (deg) Estimation using 4-Term MSCW type-1		The Relative Error of Phase angle Estimation (%) using 4-Term MSCW type-1	
	with DSLIFFT [32–39]	with PLIS-based DSLIFFT	with DSLIFFT	with PLIS-based DSLIFFT
1	39.7577	39.9156	0.6057	0.2110
3	114.9842	115.0985	0.0138	− 0.0856
5	− 29.8017	− 30.0666	0.6611	− 0.2219
7	109.7212	110.1140	0.2535	− 0.1036
9	− 20.0598	− 20.0490	− 0.2990	− 0.2448
11	100.1596	100.1303	− 0.1596	− 0.1303
13	− 10.3180	− 10.0318	− 3.1795	− 0.3177
15	− 90.0972	− 90.0900	− 0.1080	− 0.1000
17	0.0012	− 0.0001	0	0

Table 2.15 Phase angle estimation comparison using 4-Term MSCW type-2 with DSLIFFT and PLIS-based DSLIFFT, when the fundamental frequency = 50.5 Hz

Harmonic Order (h)	Phase angle (deg) Estimation using 4-Term MSCW type-2		The Relative Error of Phase angle Estimation (%) using 4-Term MSCW type-2	
	with DSLIFFT [32–39]	with PLIS-based DSLIFFT	with DSLIFFT	with PLIS-based DSLIFFT
1	39.7593	39.9166	0.6018	0.2086
3	114.9810	115.1013	0.0165	− 0.0881
5	− 29.7975	− 30.0656	0.6750	− 0.2188
7	109.7209	110.1189	0.2537	− 0.1081
9	− 20.0574	− 20.0478	− 0.2869	− 0.2391
11	100.1643	100.1369	− 0.1643	− 0.1369
13	− 10.3173	− 10.0300	− 3.1726	− 0.3000
15	− 90.0958	− 90.0980	− 0.1065	− 0.1089
17	0.0126	− 0.0012	0	0

From the above tabulated results in Table 2.12 to Table 2.15 it is evident that the percentage relative error of the fundamental phase is impressively less in the case of PLIS based DSLIFFT with 4-Term MSCW type-2 compared to PLIS based DSLIFFT with 4-Term MCSW type-1 and DSLIFFT based 4-Term MCSW type-1 and type-2 as observed in the first row of

all the tables above. Moreover, the percentage relative errors of the remaining harmonic phases are reasonably less, when PLIS based DSLIFFT with type 2 is compared with DSLIFFT using 4-Term MCSW type-1 and type-2.

From the above tabulated results in Table 2.8 to Table 2.11 it is evident that the percentage relative error of the fundamental amplitude is impressively less in the case of PLIS based DSLIFFT with 4-Term MSCW type-2 compared to PLIS based DSLIFFT with 4-Term MCSW type-1 and DSLIFFT based 4-Term MCSW type-1 and type-2 as observed in the first row of all the tables above. Moreover, the percentage relative errors of the remaining harmonic amplitudes are reasonably less, when PLIS based DSLIFFT with type 2 is compared with DSLIFFT using 4-Term MCSW type-1 and type-2.

It is evident that the phase estimation accuracy of the PLIS-based DSLIFFT with 4-Term MSCW of type-2 algorithm is in the order of 10^{-2} for fundamental frequency of 49.5 Hz and is of the order 10^{-1} for fundamental frequency 50.5Hz. The PLIS based DSLIFFT with 4-Term MSCW type-2 exhibits better results than the 4-Term MSCW with conventional DSLIFFT algorithm.

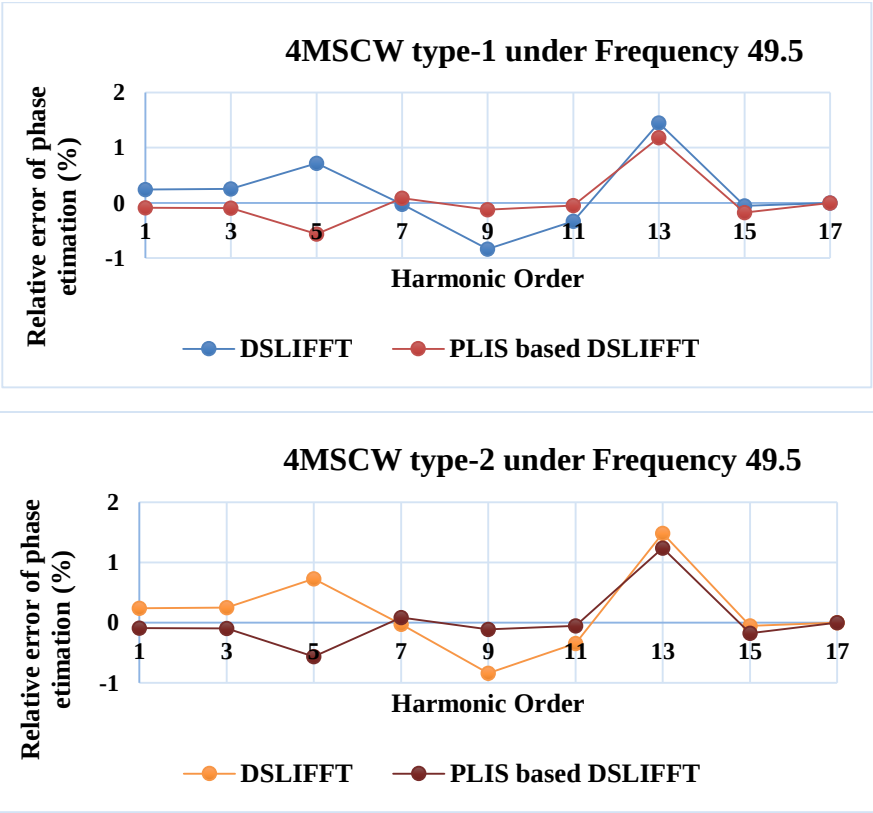

Fig. 2.8 Percentage relative errors variation of phase angle estimation to the harmonic order with PLIS-based DSLIFFT and conventional DSLIFFT using 4-Term MSCW type-1 and type-2 at the frequency 49.5 Hz

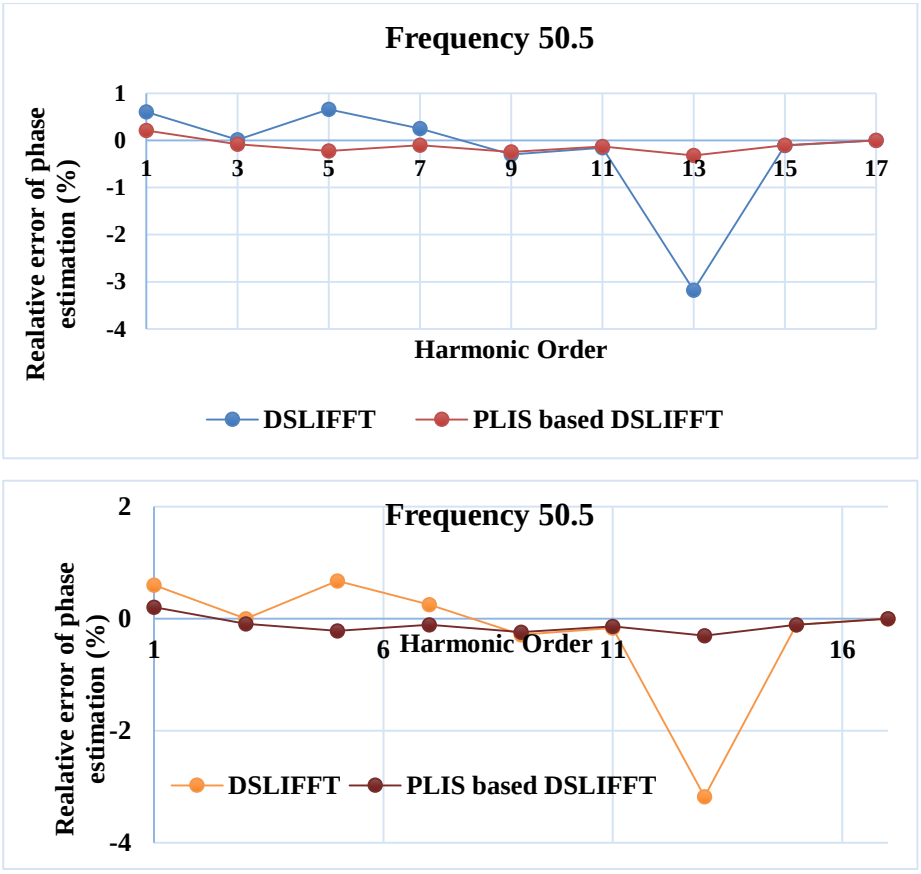

Fig. 2.9 Percentage relative errors variation of phase angle estimation to the harmonic order with PLIS-based DSLIFFT and conventional DSLIFFT using 4-Term MSCW type-1 and type-2 at the frequency is 50.5 Hz

The estimation accuracy of PLIS based DSLIFFT with 4-Term MSCW has been graphically demonstrated in Fig. 2.8 and Fig. 2.9 by comparing the percentage relative error variations of fundamental and harmonic phases with conventional DSLIFFT using 4-Term MSCW type-1 and type-2 at frequency values of 49.5 Hz and 50.5 Hz.

As per the responses of Figs. 2.4–2.9, it is evident that the 4-Term MSCW type-2 with PLIS-based DSLIFFT algorithm exhibits more accurate estimation over the 4-Term MSCW type-1 with PLIS-based DSLIFFT algorithm as well as 4-Term MSCW type-1 and type-2 with conventional DSLIFFT algorithm. Moreover, the fundamental amplitude, frequency, and phase angle estimation are more accurate in view of its lowest percentage relative error values under different fundamental frequency conditions The RT validation of the PLIS-based DSLIFFT algorithm on estimating the real-world harmonic signals are presented in the next section.

2.4 Real-Time Experimental Validation

The RT implementation of the PLIS-based DSLIFFT using 4-Term MSCW is discussed in this section. The detailed experimental setup and its drawing are depicted in Fig. 2.10. Precise

selection of sampling frequency and window length gives accurate results in RT. For better accuracy and minimized errors, the sampling frequency is considered to be 3 kHz and the window length is 1024 as per the sampling theorem concepts. Moreover, the sampling frequency satisfies the Nyquist frequency requirement. Based on the sampling frequency and the window length, the frequency resolution satisfies the measurement requirements as discussed in [21].

The common real-world loads such as Compact Fluorescent Lamp (CFL), Triode for Alternating Current (TRIAC) controlled exhaust fan and Switched Mode Power Supply (SMPS) of the Personal Computer (PC) to serve different nonlinear loads are considered for estimation. NI-cRIO-based virtual instrumentation experimental setup is developed for harmonic estimation. It is one of the potential RT estimation tools for the harmonic signal as per the international standards [17–19]. The cRIO uses a Field-Programmable Gate Array (FPGA) architecture for digital signal processing. The PLIS-based DSLIFFT using 4-Term MSCW has been deployed in the LabVIEW configured host computer and interfaced to the NI LabVIEW powered cRIO 9082 which is equipped with Intel Core-i7 dual-core with a Central Processing Unit (CPU) frequency of 1.33GHz [124]. It consists of a reconfigurable embedded chassis with integrated intelligent real-time controller and data acquisition modules for signal acquisition.

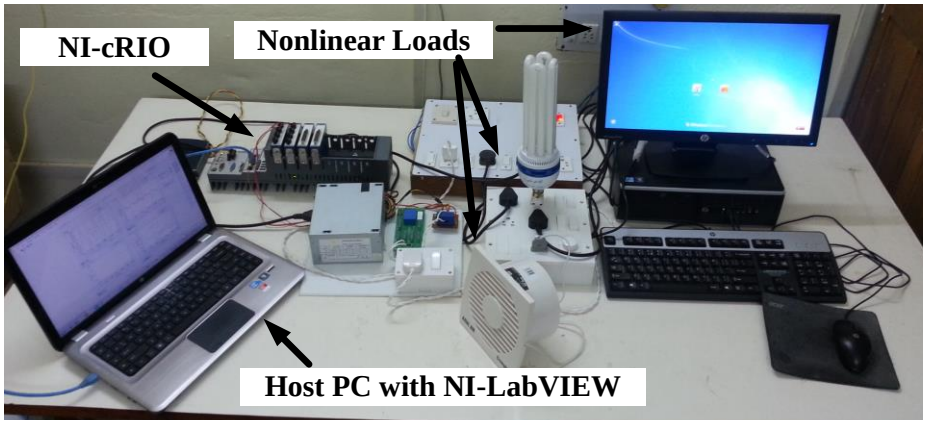

(a)

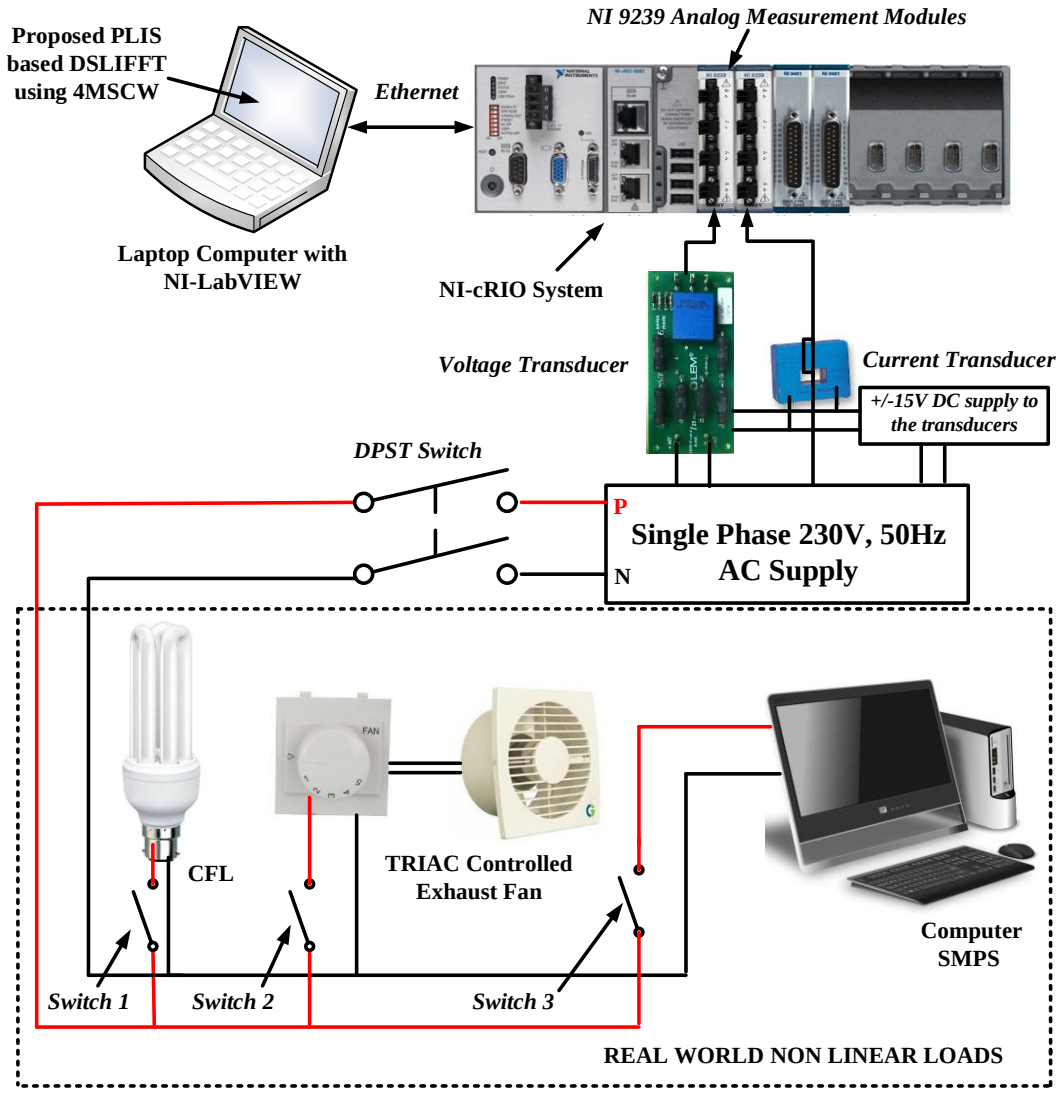

(b)

Fig. 2.10 NI-cRIO-based experimental setup. (a) Hardware setup; (b) Setup circuit diagram

The real-time estimation process flowchart in NI cRIO 9082 is shown in Fig.2.11.

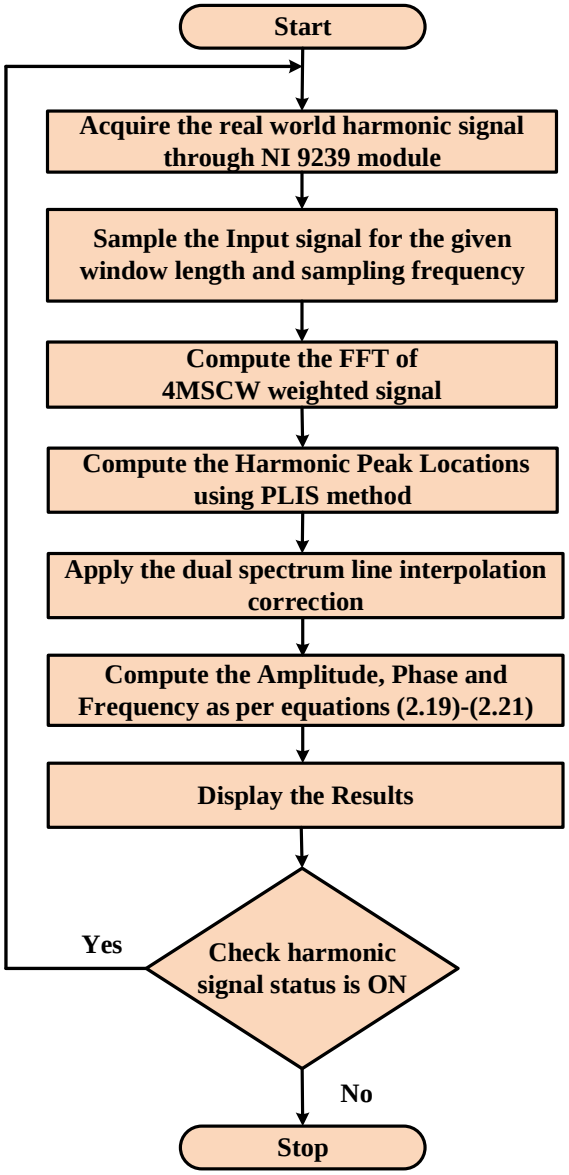

Fig. 2.11 Flowchart of the PLIS based DSLIFFT Algorithm with 4-Term MSCW in RT estimation

The real-world harmonic loads considered for RT harmonics analysis is shown in Table 2.16.

Table 2.16 Real-world nonlinear load specifications

Type of load	**Ratings**
Compact Fluorescent Lamp (CFL)	220–240 V, 50 Hz, 85 W
TRIAC controlled Exhaust Fan	220–240 V, 50 Hz, 20 W, 1750 rpm
SMPS of the PC	Input: 230 V AC, 50 Hz, Output: 12V DC, 0.3 A

The procedural steps to implement the PLIS-based DSLIFFT algorithm with 4-Term MSCW in RT	
Step 1:	Sampling the real-world harmonic signal, here the harmonic signal is acquired from real-world nonlinear load using NI 9239 analog module [128].
Step 2:	The acquired signal is processed through the FPGA I/Os of NI-cRIO 9082 system [124], then convert the sampled signal into a weighted signal using 4-Term MSCW and compute the weighted signal FFT.
Step 3:	The NI-cRIO 9082 system is interfaced to the host computer, where the PLIS-based DSLIFFT algorithm using 4-Term MSCW method is implemented in LabVIEW virtual instrumentation environment.
Step 4:	Use the PLIS-based DSLIFFT algorithm using 4-Term MSCW of type-2 to find out the fundamental as well as harmonic spectral amplitudes accurately.
Step 5:	Display the results.

2.4.1 Case 1: RT Harmonic Estimation of CFL and SMPS of the PC

The nonlinear loads (CFL+SMPS of the PC) current waveform acquired by using NI-cRIO is depicted in Fig.2.12, where the switch 1 and switch 3 of the nonlinear loads are in ON position and switch 2 of the exhaust fan is in OFF position. The NI-cRIO is a heterogeneous computing platform, where the signal acquisition is done by using FPGA configured input channels and computation is performed on the RT processor.

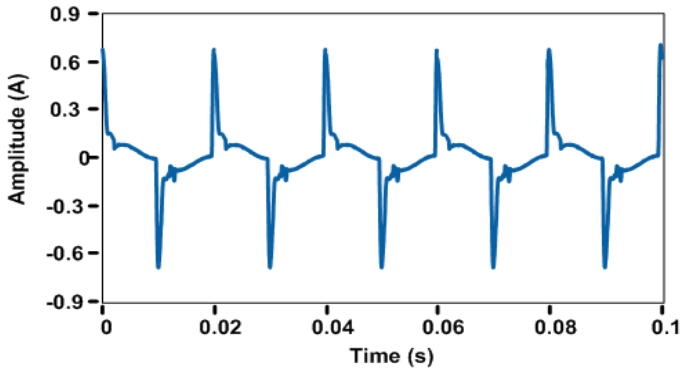

Fig. 2.12 CFL and Computer with UPS load current waveform

The amplitude, frequency and phase angle of the fundamental and harmonics estimated by the laboratory RT experimental test bench (NI-cRIO) and the Tektronix Power Quality Analyzer (PQA) model PA4000 [129] are tabulated in Tables 2.17–2.19. The Tektronix PA4000 is one of the standard instrument used for the voltage or current harmonic estimation.

The PQA results and the 4-Term MSCW type-2-based PLIS-based DSLIFFT configured RT estimation system results are relatively identical and the system exhibits better accuracy under the nonlinear loaded condition as per the requirement of international standards [17–19].

Table 2.17 Case 1: Comparison of PLIS based DSLIFFT with type-2 of 4-Term MSCW and Tektronix PQA

Harmonic Order (h)	Amplitude (Amp) Measured using PQA (Tek-PA4000)	Amplitude (Amp) Measured using PLIS based DSLIFFT with NI-cRIO	The Relative Error (%)
1	0.4977	0.4974	0.0698
3	0.2839	0.2821	0.6266
5	0.2154	0.2117	1.7319
7	0.1625	0.1570	3.3688
9	0.1333	0.1330	0.2404
11	0.1091	0.1091	0.0242
13	0.1076	0.1038	3.5233
15	0.1037	0.1018	1.8444
17	0.0880	0.0874	0.6956

Table 2.18 Case 1: Comparison of PLIS-based DSLIFFT with type-2 of 4-Term MSCW and Tektronix PQA

Harmonic Order (h)	Frequency (Hz) Measured using PQA (Tek-PA4000)	Frequency (Hz) Measured using PLIS based DSLIFFT with NI-cRIO	The Relative Error (%)
1	49.95	49.95000000	1.5123×10^{-09}
3	149.85	149.85000000	2.3758×10^{-10}
5	249.75	249.75000000	8.1686×10^{-11}
7	349.65	349.65000000	-8.0636×10^{-11}
9	449.55	449.55000000	-6.2287×10^{-11}
11	549.45	549.45000000	5.7149×10^{-11}
13	649.35	649.35000000	-8.0238×10^{-11}
15	749.25	749.25000000	6.0587×10^{-11}
17	849.15	849.15000000	1.0753×10^{-10}

Table 2.19 Case 1: Comparison of PLIS-based DSLIFFT with type-2 of 4-Term MSCW and Tektronix PQA

Harmonic Order (h)	Phase angle (deg) Measured using PQA (Tek-PA4000)	Phase angle (deg) Measured using PLIS based DSLIFFT with NI-cRIO	The Relative Error (%)
1	17.98	17.9564	0.14780
3	− 120.99	− 119.9192	0.88502
5	110.49	110.3468	0.12959
7	− 18.28	− 18.4017	− 0.61626
9	− 140.37	− 140.4560	− 0.06124
11	98.33	98.4469	− 0.11174
13	− 13.93	− 13.8060	0.94690
15	− 139.16	− 139.0005	0.11463
17	97.42	97.4327	− 0.00589

2.4.2 Case 2: RT Harmonic Estimation of TRIAC Controlled Exhaust Fan Load

The current drawn by the exhaust fan only when the CFL and SMPS of the PC loads are in OFF condition and is shown in Fig.2.13.

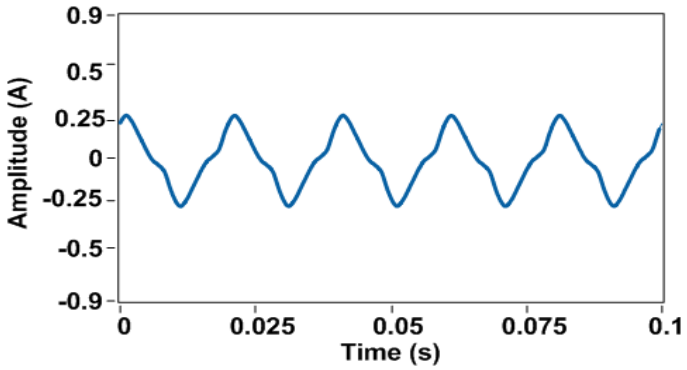

Fig. 2.13 TRIAC controlled Exhaust Fan load current waveform

The RT system and the PQA estimation results of amplitude, frequency, and phase angle for exhaust fan case also depicted in Tables 2.20–2.22. These results also exhibit the identical accuracy of the PLIS based DSLIFFT algorithm in RT estimation of fundamental and harmonic components.

Table 2.20 Case 2: Comparison of PLIS-based DSLIFFT with type-2 of 4-Term MSCW and Tektronix PQA

Harmonic Order (h)	Amplitude (Amp) Measured using PQA (Tek-PA4000)	Amplitude (Amp) Measured using PLIS based DSLIFFT with NI-cRIO	The Relative Error (%)
1	0.291	0.2907	0.0698
3	0.071	0.0709	0.0632
5	0.019	0.0186	1.7318

Table 2.21 Case 2: Comparison of PLIS-based DSLIFFT with type-2 of 4-Term MSCW and Tektronix PQA

Harmonic Order (h)	Frequency (Hz) Measured using PQA (Tek-PA4000)	Frequency (Hz) Measured using PLIS based DSLIFFT with NI-cRIO	The Relative Error (%)
1	49.95	49.9500000	1.2913×10^{-09}
3	149.85	149.8500000	$-\ 6.3863 \times 10^{-10}$
5	249.75	249.7500000	$-\ 1.3610 \times 10^{-09}$

Table 2.22 Case 2: Comparison of PLIS-based DSLIFFT with type-2 of 4-Term MSCW and Tektronix PQA

Harmonic Order (h)	Phase angle (deg) Measured using PQA (Tek-PA4000)	Phase angle (deg) Measured using PLIS based DSLIFFT with NI-cRIO	The Relative Error (%)
1	0	0.0001	0
3	158.90	158.88	0.0072
5	0	0.0008	0

It is clear that the PLIS-based DSLIFFT with 4-Term MSCW of type-2 has improved characteristics when compared to the conventional DSLWIFFT for nonlinear load current harmonic estimation. The developed PLIS-based DSLIFFT with 4-Term MSCW of type-2 has improved accuracy and better online response in compliance with PQA measured data as per IEC 61000-4-30 [18], which recommends the measurement of current harmonics. The above loads are the most common nonlinear loads using in the residential, commercial, and industrial

applications. There is a real need to compute these harmonics effectively for mitigation purpose. It is confirmed by both the simulation and RT results that PLIS-based DSLIFFT with type-2 of 4-Term MSCW has better accuracy.

2.5 Conclusions

The PLIS-based DSLIFFT with 4-Term MSCW has better accuracy and precision under non-synchronous sampling, low amplitude, and fractional harmonic frequency when compared to previous DSLIFFT solutions. Simulation and experimental results corroborate the effectiveness, using the techniques described in this chapter for current harmonic estimation under variable frequency conditions. Improved performance indices were examined with experimental results by considering real-world load harmonic signals. The percentage relative errors of the fundamental amplitude, frequency and phase angle estimation of PLIS based DSLIFFT are impressively less at an order of 10^{-2}, 10^{-9} and 10^{-1}, when compared to conventional DSLIFFT using 4-Term MSCW type–2 . The simulation and experimental results satisfy requirements of international standards such as IEC 61000-4-7 standard for Testing and measurement techniques - General guide on harmonics and inter-harmonics measurements and instrumentation, for power supply systems and equipment connected thereto, IEC 61000-4-30 standard for Testing and measurement techniques – Power quality measurement methods, and IEEE 1159-2009–Recommended Practice for Monitoring Electric Power Quality. Therefore, the developed PLIS-based DSLIFFT with 4-Term MSCW can estimate current harmonics, as well as voltage harmonics, even under distorted conditions and variable grid frequencies in real-time, ready to retrofit any power system or smart-grid installation.

Publication

This work is published and referenced below:

O.V.S.R.Varaprasad, D.V.S.S.Siva Sarma, H.K.M.Paredes, and M.G.Simões. "**Enhanced Dual-Spectrum Line Interpolated FFT with Four-Term Minimal Sidelobe Cosine Window for Real-Time Harmonic Estimation in Synchrophasor Smart-Grid Technology.**" *Electronics,* 8, no. 2 (2019): 191.

Chapter 3

Adaptive Peak Location Index Search (PLIS) based Dual Spectrum Line Interpolated Fast Fourier Transform (DSLIFFT) with Advanced Windows

3.1 Introduction

The estimation of time-varying current harmonics and inter-harmonics is one of the emerging topics of research. Parametric methods [20,21,43,49,51-53] have been widely used for estimating time-varying current harmonics and inter-harmonics, however the limitations of parametric methods are improper modelling, computational complexity based on the signal nature and selection of the right computation parameters for estimation of harmonics under different operating conditions. In order to overcome these limitations non-parametric Peak Location Index Search (PLIS) based Dual Spectrum Line Interpolated Fast Fourier Transform (DSLIFFT) has been improvised with a simple Signal Slope Detection (SSD) technique to estimate the time-varying current harmonics. The main objective of the SSD technique is segmentation of time-varying harmonic signals into periodic harmonic signal as per the changes in the amplitude for computing the window length adaptively. Based on the computed window length the harmonic signal is sampled using sampling theorem concept, thereby it is processed through the PLIS-based DSLIFFT with Advanced Windows (AWs) to estimate the current harmonics and inter-harmonics, under variable grid frequencies conditions in real-time as per the procedure detailed in chapter 2, section 2.2.

3.2 Signal Slope Detection Technique

The SSD technique has been developed by K.Nagaraju *et al.* (2011) in [127] for power system fault detection. It is a simple technique that is repurposed for segmentation of time-varying harmonic signal effectively without any need of filter-banks. In the SSD technique, an index is defined as the sum of the slopes of given signal over one cycle time. Under normal conditions, the index value will be zero and, with the change in the signal magnitude, its value becomes non-zero which helps to detect the change in the signal effectively in a short duration of time.

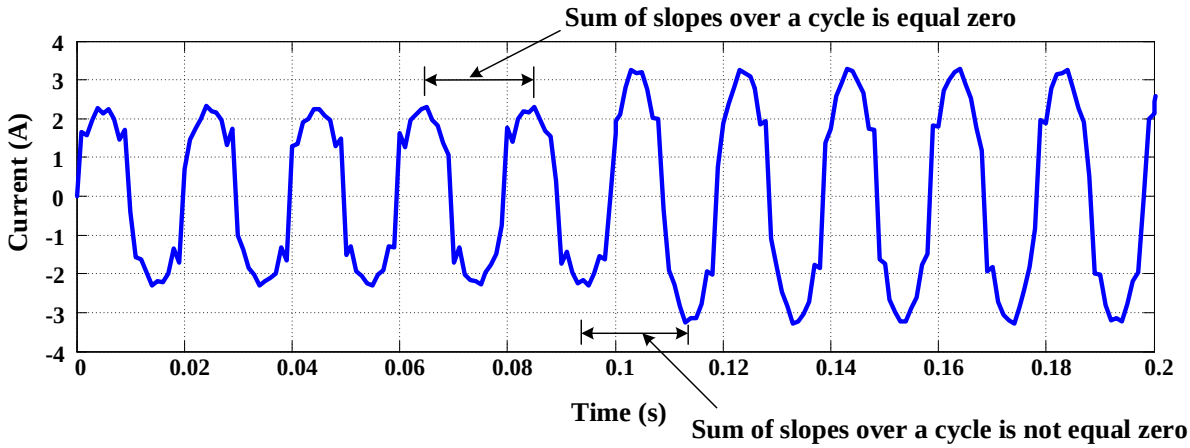

Fig. 3.1 Signal Slope Detection (SSD) technique illustration

The change detection is expressed mathematically as below.

$$d(j) = \frac{[i(j) - i(j-1)]}{\Delta t} \tag{3.1}$$

$$S(j) = \sum_{l=j-N+1}^{j} d(l) \tag{3.2}$$

Where *d(j)* is the slope of the signal at the instant *j*, Δt is the sampling period, *S(j)* is the index value of the proposed slope sum method, *N* is a number of samples per cycle and *i(j)* is the present sample value of the current signal. The change in the waveform is registered if,

$$|S(j)| > T_p \tag{3.3}$$

Where T_p is a threshold parameter. The T_p value is decided based on simulation studies on various load changes, in view of that the minimum value which can detect the change in the wave form is considered.

Equation (3.2) can be written in a recursive form as

$$S(j) = \frac{S(j-1) + [i(j) - i(j-1)]}{\Delta t} \tag{3.4}$$

3.3 Advanced Windows Overview

The following two advanced windows are considered in Adaptive PLIS based DSLIFFT algorithm for time-varying harmonic estimation in this chapter. They are Polynomial Time Windows (PTWs) introduced by P.Singla *et al.,* (2009) [29] and 4-term MSCWs [34,36].

3.3.1 Polynomial Window

The polynomial based time window function derived from [29] is given as

$$w_m(t) = 1 - K_m \sum_{n=0}^{m} A_{m,n} |t|^{2m-n+1}, -1 \le t \le 1 \tag{3.5}$$

Where K_m = window scaling factor, m represent the the order of the window and n represent the limit value, respectively. The Fourier transform of the polynomial window function is expressed as

$$W_m(\omega) = 2K_m \sum_{n=0}^{m} T_{2m-n-1} A_{m,n} \frac{(2m-n+1)(2m-n)}{\omega^2} \text{ , } m>0 \tag{3.6}$$

The time domain and frequency domain representation of the PTW for a different order of continuities i.e. m = 0 to 4 is shown in Fig. 3.2.

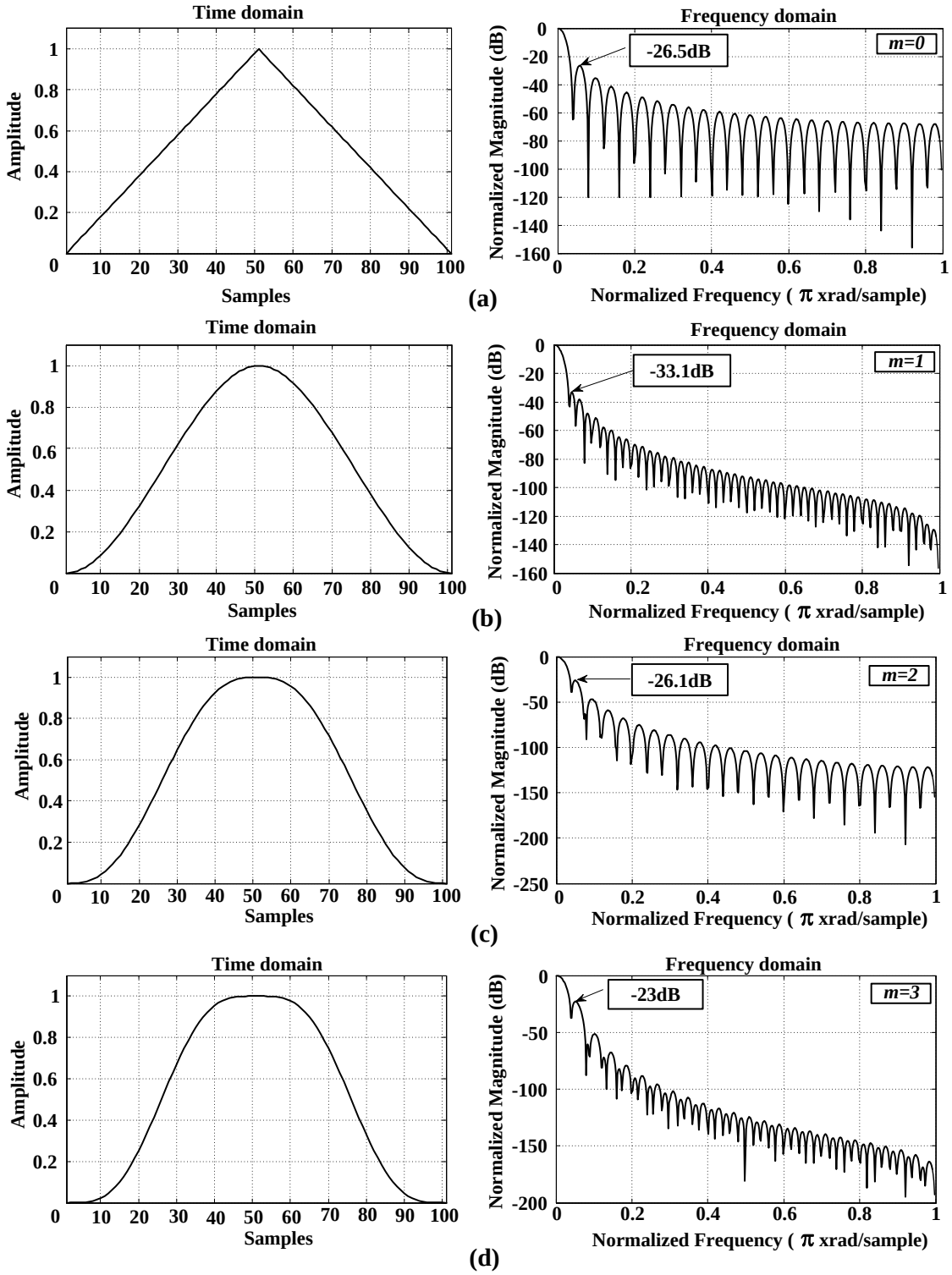

Fig. 3.2 Polynomial time window (PTW) characteristics of different orders (m)
(a) *m=0* (b) *m=1* (c) *m=2* (d) *m=3*

The leakage factor, main lobe width and relative sidelobe attenuation values of the PTW for different orders are computed for 100 samples and tabulated in Table 3.1.

Table 3.1 PTW Coefficients and Properties

Window Order *(m)*	PTW functions $w_m(t)$	Main Lobe Width	Peak Sidelobe Level (dB)	Sidelobe Roll-off Rate (dB/oct)
0	$1-\|t\|$	0.025391	-26.5	6
1	$1-t^2(3-2\|t\|)$	0.027344	-33.1	12
2	$1-\|t\|^3(10-15\|t\|+6t^2$	0.029297	-26.1	18
3	$1-t^4(35-84\|t\|+70t^2-20\|t\|^3)$	0.029297	-23	24

From the above tabulations, it is evident that the polynomial window of different orders has narrowed main lobe widths and reasonable side lobe levels. With an increase in order (*m*), the rapid side lobe roll of nature which is far from the main lobe is consistent with the predicted *6(m+1)* dB/oct roll-off with an $(m+1)^{th}$ order discontinuous derivative. The polynomial window performance for weak signal analysis is demonstrated in [29]. Further, the PTW performance with the Adaptive PLIS based DSLIFFT is investigated.

3.3.2 4-Term MSCW

The 4-term MSCW type-1 and type-2 coefficients and properties tabulated in Table 2.1 of chapter 2 are considered for Adaptive PLIS based DSLIFFT. The 4-term MSCW type-1 and type-2 window characteristics are depicted in Fig. 3.3.

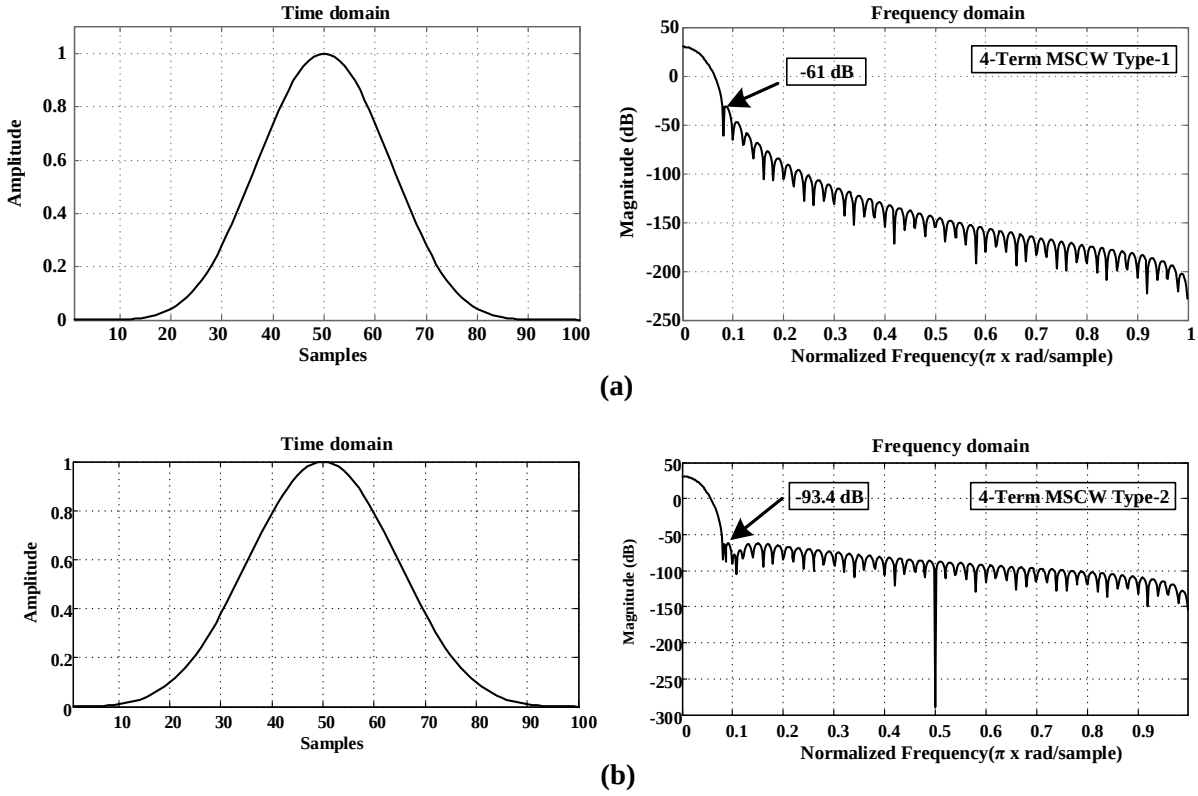

Fig. 3.3 4-Term MSCW windows characteristics (a) type-1 (b) type-2

Based on the window characteristics of PTWs and 4-Term MSCWs the First order (*m=1*) PTW and 4-term MSCW type-2 are considered for the windowing process of Adaptive PLIS-based DSLIFFT for estimation of various types of time-varying harmonics. The time-varying harmonic signal sampling procedure is described in the next section.

3.4 Mathematical formulation of Time-varying harmonic signal sampling and windowing

The mathematical formulation of the time-varying harmonic and inter-harmonic signal with noise is represented as:

$$\boldsymbol{x(nT_s) = x(t) = \sum_{h=1}^{H} A_h \sin(2\pi f_h n T_s + \varphi_h + \mu(t))} \text{ Where n is a non-integer} \qquad (3.7)$$

where the amplitude, frequency, and phase angle are written as A_h, f_h and φ_h, respectively. The sampling time of the signal is represented as T_s and $\mu(t)$ is the representation of white gaussian noise. To suppress the spectral leakage effect in the time-varying sampled signal, it is weighted by the advanced window (AW) functions described in section 3.3.

The FFT of the windowed sample signal under non-synchronous sampling is represented as:

$$X(k) = \sum_{h=1}^{H} \frac{A_h}{2j}\left[e^{j\varphi_h} W_{AW}(k - k_h) - e^{j\varphi_h} W_{AW}(k + k_h)\right] \tag{3.8}$$

where $k = 0, 1 \ldots (N - 1)$, W_{AW} indicates the FFT of the adopted AW function, k_h denotes the division factor of signal frequency and the frequency resolution, which is expressed as:

$$k_h = \frac{f_h N}{f_s} = l_h + \xi_h \tag{3.9}$$

where l_h is an integer value and ξ_h $(0 \leq \xi_h \leq 1)$ is the fractional part. The negative frequency part is ignored in Equation (3.8). The sampling frequency used for computation is represented as f_s. The l_h and ξ_h of the time-varying harmonics are computed by Adaptive PLIS-based DSLIFFT algorithm as described in the next section.

3.5 Adaptive Peak Location Index Search (PLIS) based DSLIFFT algorithm

The detailed flowchart of the developed Adaptive PLIS-based DSLIFFT algorithm is illustrated in Fig. 3.4.

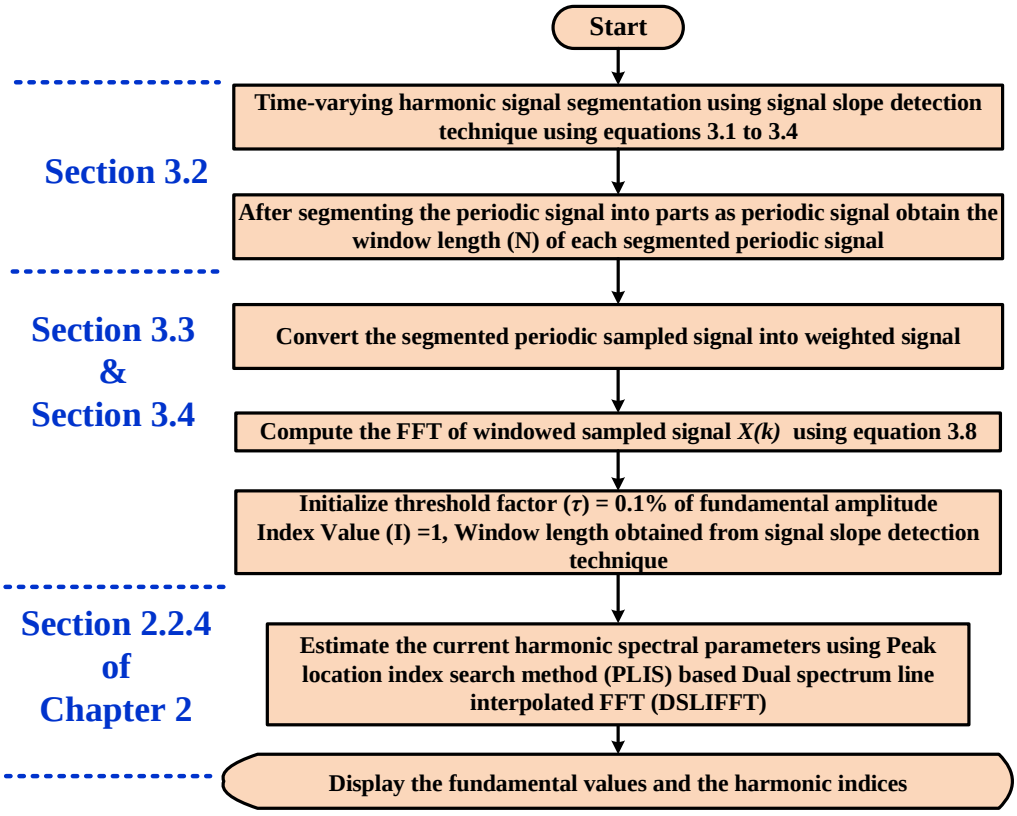

Fig. 3.4 Adaptive PLIS based DSLIFFT algorithm

The selection of window length and sampling frequency is important to enhance the estimation accuracy of the harmonics. SSD technique discussed in section 3.2 is used for deciding the window length of the time-varying harmonic signal. Nyquist sampling theorem concept described by C.I Chen *et al.,* (2014) in [21] is used to set appropriate sampling frequency.

The segmented periodic signals are sampled and weighted by the adopted window functions after that the spectrum is computed. To compute the fundamental and harmonic peaks, PLIS method is considered as described in chapter 2. Afterward, DSLIFFT correction is applied to estimate the amplitude, frequency and phase angle of the fundamental as well as all other harmonics and inter-harmonics.

The proposed algorithm is developed in Laboratory Virtual Instrument Engineering Workbench (LabVIEW) environment and validated in real-time using LabVIEW programmed National Instruments (NI) compact Reconfigurable Input/output system (cRIO) system described in [124].

3.6 Simulation Results

This section demonstrates the simulation results of the developed Adaptive PLIS-based DSLIFFT using first-order PTW and 4-term MSCW type-2 under time-varying multi-harmonic condition with the effect of noise. Initially, the algorithm simulated in a LabVIEW environment with a programmed harmonic test signal, which has three variations. The amplitudes and the corresponding phase angles of the programmed harmonic signal for fundamental frequency values of 49.5 and 50.5 Hz are depicted in Table 3.2 to 3.4, respectively.

Table 3.2 Simulated harmonic test signal information from *0* to *0.1s* time duration

Parameters	**Harmonic Orders (Fundamental frequency = 50.5 Hz)**								
	1	**3**	**5**	**7**	**9**	**11**	**13**	**15**	**17**
Amplitude (A)	4	0.4	0.35	0.3	0.25	0.2	0.2	0.15	0.2
Phase angle (deg)	40	115	−30	110	−20	100	−10	−90	0
Frequency (Hz)	50.5	151.5	252.5	353.5	454.5	555.5	656.5	757.5	858.5

Table 3.3 Simulated harmonic test signal information from *0.1s to 0.2s* time duration

Parameters	**Harmonic Orders (Fundamental frequency = 49.5 Hz) with Inter-harmonics**								
	1	**1.5**	**3**	**3.5**	**5**	**7**	**7.5**	**9**	**11**
Amplitude (A)	8	0.4	0.35	0.3	0.25	0.2	0.2	0.15	0.2
Phase angle (deg)	40	115	−30	110	−20	100	−10	−90	0
Frequency (Hz)	49.5	74.25	148.5	173.25	247.5	346.5	371.25	445.5	544.5

Table 3.4 Simulated harmonic test signal information from *0.2s to 0.3s* time duration

Parameters	**Harmonic Orders (Fundamental frequency = 50.5 Hz) with Inter-harmonics and white Gaussian noise effect (Signal-to-Noise Ratio (SNR)=30dB)**				
	1	**3**	**3.5**	**5**	**7.5**
Amplitude (A)	2	0.4	0.35	0.3	0.25
Phase angle (deg)	40	115	−30	110	−20
Frequency (Hz)	50.5	151.5	176.5	252.5	378.75

The Adaptive PLIS-based DSLIFFT using first-order PTW and 4-term MSCW type-2 are explored and the results are compared under fractional fundamental frequency values of 49.5 Hz and 50.5Hz. The simulated benchmark signal waveform representation is depicted in Fig. 3.5.

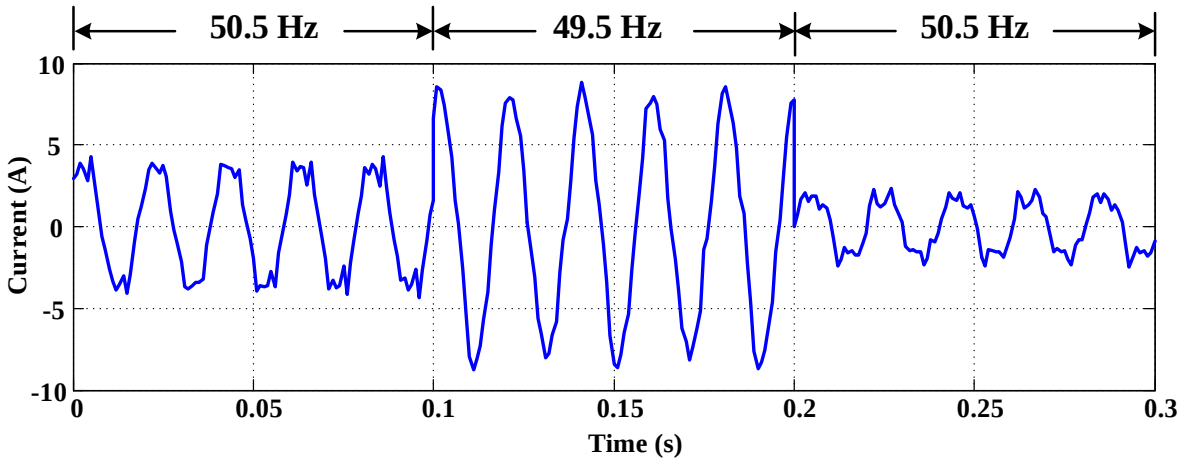

Fig. 3.5 Benchmark time-varying current harmonic test signal

3.6.1 Amplitude Estimation

The amplitude estimation of the benchmark time-varying multi-harmonic test signal and its error comparison for First-order PTW and 4-Term MSCW type-2 with fundamental frequency values of 49.5 Hz and 50.5 Hz under different time instants are tabulated in Tables 3.5–3.7.

Table 3.5 Amplitude estimation comparison using Adaptive PLIS-based DSLIFFT with First-order PTW and 4-Term MSCW type-2, when the fundamental frequency = 50.5 Hz during 0 to 0.1*s*

Harmonic Order (h)	Amplitude (Amp) Estimation using Adaptive PLIS-based DSLIFFT		The Relative Error of Amplitude Estimation (%) using Adaptive PLIS-based DSLIFFT	
	with First-order PTW	with 4-Term MSCW type-2	with First-order PTW	with 4-Term MSCW type-2
1	4.0029	3.9969	-0.0739	0.0774
3	0.3972	0.3988	0.6789	0.2949
5	0.3495	0.3495	0.1152	0.1469
7	0.2971	0.2984	0.9555	0.5216
9	0.2478	0.2483	0.8804	0.6865
11	0.1951	0.1989	2.4420	0.5007
13	0.1957	0.1995	2.1735	0.2709
15	0.1450	0.1495	3.3327	0.3089
17	0.1897	0.1999	5.1259	0.0447

Table 3.6 Amplitude estimation comparison using Adaptive PLIS-based DSLIFFT with First-order PTW and 4-Term MSCW type-2, when the fundamental frequency = 49.5 Hz during 0.1*s* to 0.2*s*

Harmonic Order (h)	Amplitude (Amp) Estimation using Adaptive PLIS-based DSLIFFT		The Relative Error of Amplitude Estimation (%) using Adaptive PLIS-based DSLIFFT	
	With First order PTW	With 4-Term MSCW type-2	With First order PTW	With 4-Term MSCW type-2
1	8.0047	7.9978	-0.0593	0.0269
1.5	0.3742	0.3828	6.4410	4.3068
3	0.3522	0.3475	-0.6293	0.7072
3.5	0.2967	0.2979	1.0833	0.6849
5	0.2512	0.2493	-0.4626	0.2501
7	0.1966	0.1966	1.6802	1.7216
7.5	0.2009	0.1992	-0.4573	0.3818
9	0.1490	0.1498	0.6609	0.1525
11	0.1958	0.1985	2.0963	0.7694

Table 3.7 Amplitude estimation comparison using Adaptive PLIS-based DSLIFFT with First-order PTW and 4-Term MSCW type-2, when the fundamental frequency = 50.5 Hz during 0.2*s* to 0.3*s*

Harmonic Order (h)	Amplitude (Amp) Estimation using Adaptive PLIS-based DSLIFFT		The Relative Error of Amplitude Estimation (%) using Adaptive PLIS-based DSLIFFT	
	With First order PTW	With 4-Term MSCW type-2	With First order PTW	With 4-Term MSCW type-2
1	2.0002	1.9985	-0.0119	0.0774
3	0.4001	0.4000	-0.0252	-0.0203
3.5	0.3550	0.3450	-1.4182	1.4267
5	0.2977	0.2961	0.7636	1.2897
7.5	0.2521	0.2498	-0.8352	0.0809

Table 3.5 to Table 3.7 illustrates the amplitude estimation results using Adaptive PLIS-based DSLIFFT algorithm with First-order PTW and 4-Term MSCW type-2. In view of the tabulated results of amplitude estimation, it is evident that the percentage relative errors of the First order-PTW and 4-Term MSCW of type-2 with Adaptive PLIS-based DSLIFFT algorithm are low. Moreover the percentage relative error of the fundamental amplitude is in the order of 10^{-3}. The estimation accuracy of Adaptive PLIS based DSLIFFT with First-order PTW and 4-Term MSCW has been graphically demonstrated in Fig. 3.6 to Fig 3.8 by comparing the percentage relative error variations of fundamental and harmonic amplitudes.

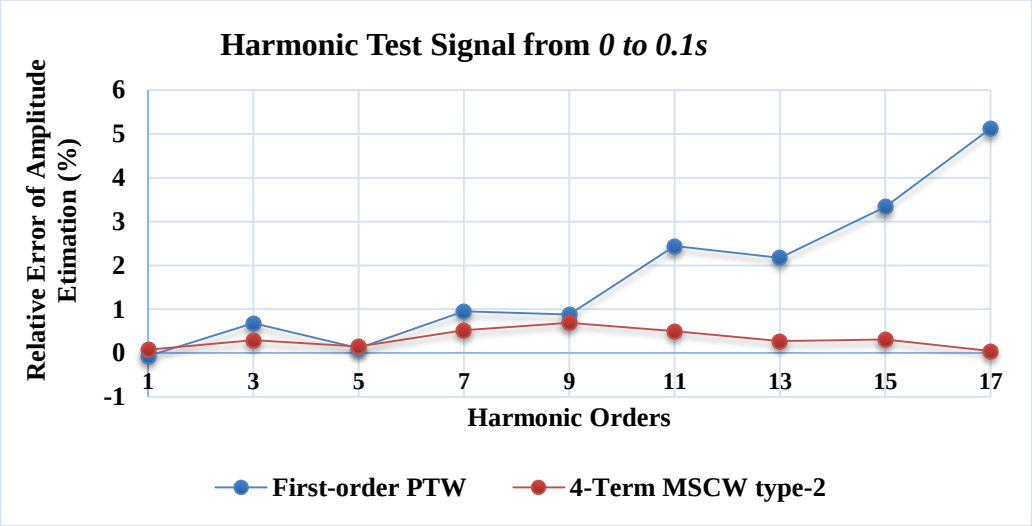

Fig. 3.6 Percentage relative errors variation of amplitude estimation to the harmonic order with Adaptive PLIS-based DSLIFFT using First-order PTW and 4-Term MSCW type-2 at the frequency is 50.5 Hz and the duration is *0 to 0.1s*

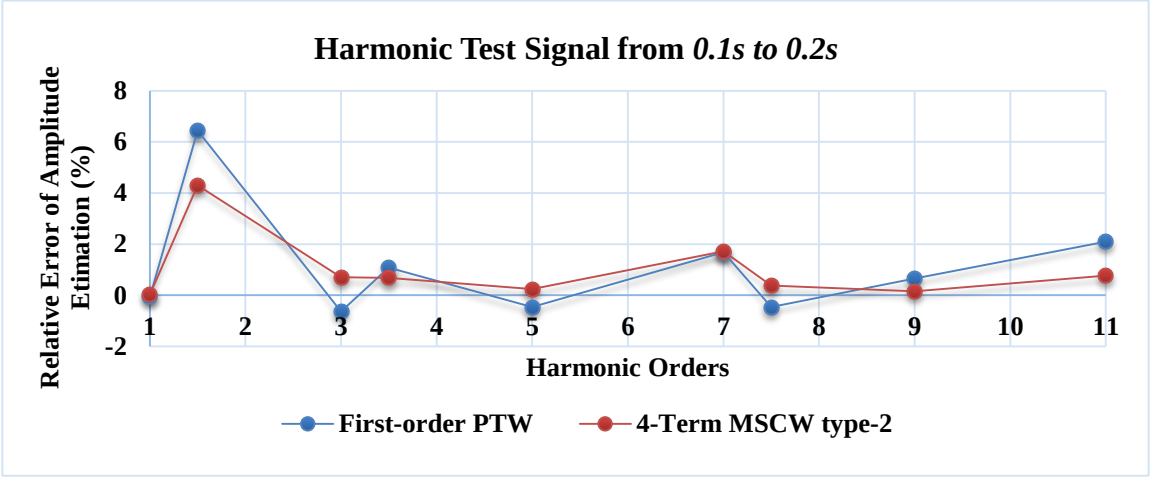

Fig. 3.7 Percentage relative errors variation of amplitude estimation to the harmonic order with Adaptive PLIS-based DSLIFFT using First-order PTW and 4-Term MSCW type-2 at the frequency is 49.5 Hz and the duration is *0.1s to 0.2s*

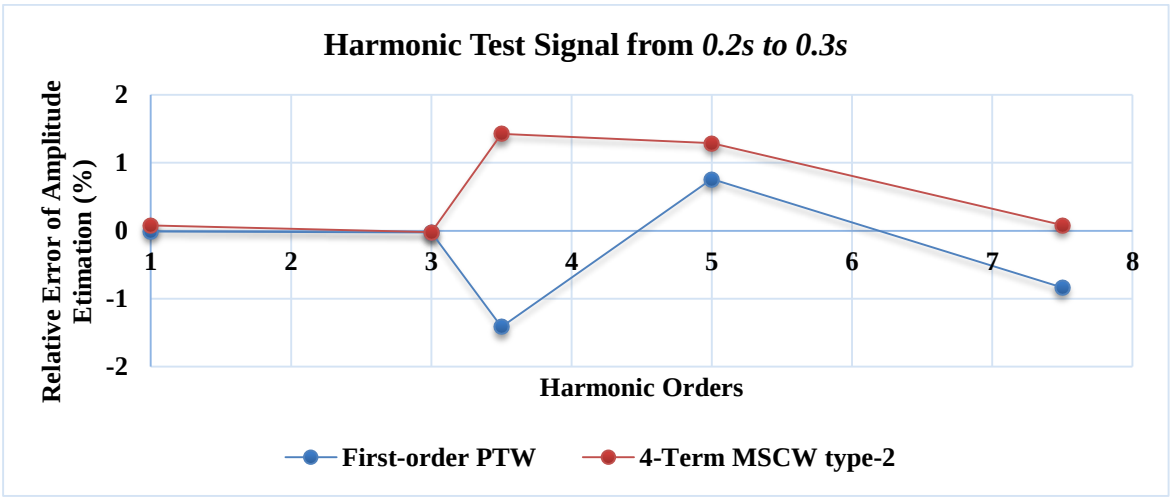

Fig. 3.8 Percentage relative errors variation of amplitude estimation to the harmonic order with Adaptive PLIS-based DSLIFFT using First-order PTW and 4-Term MSCW type-2 at the frequency is 50.5 Hz and the duration is *0.2s to 0.3s*

From the Fig. 3.6 to Fig 3.8 the percentage relative error variation of the fundamental amplitude estimation using Adaptive PLIS-based DSLIFFT with First-order PTW and 4-Term MSCW of type-2 appears low under time variations with the frequency values of 49.5 Hz and 50.5 Hz. These line graphs clearly demonstrate that the fundamental amplitude estimation is more accurate using Adaptive PLIS-based DSLIFFT.

3.6.2 Frequency Estimation

The frequency estimation of the benchmark harmonic test signal and its error comparison for First-order PTW and 4-Term MSCW type-2 with fundamental frequency values of 49.5 Hz and 50.5 Hz are tabulated in Tables 3.8–3.10.

Table 3.8 Frequency estimation comparison using Adaptive PLIS-based DSLIFFT with First-order PTW and 4-Term MSCW type-2, when the fundamental frequency = 50.5 Hz

Harmonic Order (h)	Frequency (Hz) Estimation using Adaptive PLIS-based DSLIFFT		The Relative Error of Frequency Estimation (%) using Adaptive PLIS-based DSLIFFT	
	With First order PTW	With 4-Term MSCW type-2	With First order PTW	With PLIS-based DSLIFFT
1	49.9845655	50.5000045	1.0207	-8.8531×10^{-06}
3	149.9567457	151.5000018	1.0186	-1.2165×10^{-06}
5	249.9488045	252.5000012	1.0104	-4.9344×10^{-07}
7	349.9399381	353.5000415	1.0071	-1.1735×10^{-05}
9	449.9421691	454.500002	1.0028	-4.4181×10^{-07}
11	549.9646824	555.5000667	0.9965	-1.1999×10^{-05}
13	649.9803799	656.5000101	0.9931	-1.5433×10^{-06}
15	750.0196998	757.5001019	0.9875	-1.3456×10^{-05}
17	850.0898643	858.5000006	0.9792	-7.3103×10^{-08}

Table 3.9 Frequency estimation comparison using Adaptive PLIS-based DSLIFFT with First-order PTW and 4-Term MSCW type-2, when the fundamental frequency = 49.5 Hz

Harmonic Order (h)	Frequency (Hz) Estimation using Adaptive PLIS-based DSLIFFT		The Relative Error of Frequency Estimation (%) using Adaptive PLIS-based DSLIFFT	
	With First order PTW	With 4-Term MSCW type-2	With First order PTW	With 4-Term MSCW type-2
1	49.9844297	49.5000003	-0.9786	-5.4132×10^{-07}
1.5	74.9407532	74.2490697	-0.9303	1.2529×10^{-05}
3	149.9668596	148.4999456	-0.9878	3.6612×10^{-05}
3.5	174.9507963	173.2498749	-0.9817	7.2231×10^{-05}
5	249.9516308	247.5000047	-0.9906	-1.8865×10^{-06}
7	349.9416718	346.5001109	-0.9933	-3.2012×10^{-05}
7.5	374.9402077	371.2501407	-0.9939	-3.7889×10^{-05}
9	449.9413944	445.5000134	-0.9969	-2.9983×10^{-06}
11	549.9601802	544.5000094	-1.0028	-1.7353×10^{-06}

Table 3.10 Frequency estimation comparison using Adaptive PLIS-based DSLIFFT with First-order PTW and 4-Term MSCW type-2, when the fundamental frequency = 50.5 Hz

Harmonic Order (h)	Frequency (Hz) Estimation using Adaptive PLIS-based DSLIFFT		The Relative Error of Frequency Estimation (%) using Adaptive PLIS-based DSLIFFT	
	With First order PTW	With 4-Term MSCW type-2	With First order PTW	With 4-Term MSCW type-2
1	49.9832659	50.5000035	1.0232	-6.90146×10^{-06}
3	149.9560048	151.5001546	1.0191	-1.02064×10^{-05}
3.5	174.9671589	176.7501198	1.0087	-6.77955×10^{-05}
5	249.9413059	252.5000118	1.0133	-4.65503×10^{-06}
7.5	374.9403266	378.7500076	1.0059	-2.01447×10^{-06}

Table 3.8 to Table 3.10 demonstrates frequency estimation results using Adaptive PLIS-based DSLIFFT algorithm with First-order PTW and 4-Term MSCW type-2 window. In view of the tabulated results of frequency estimation, it is evident that the accuracy of the 4-Term MSCW of type-2 with adaptive PLIS-based DSLIFFT algorithm is impressively less compared to First-order PTW. Moreover the percentage relative error of the 4-Term MSCW type-2 fundamental amplitude is in the order of 10^{-6}.

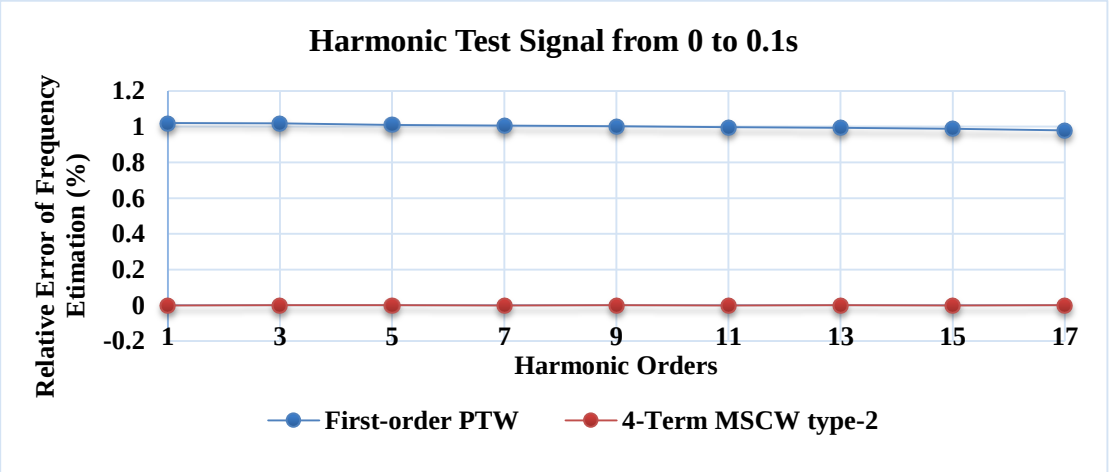

Fig. 3.9 Percentage relative errors variation of frequency estimation to the harmonic order with Adaptive PLIS-based DSLIFFT using First-order PTW and 4-Term MSCW type-2 at the frequency is 50.5 Hz and the duration is *0 to 0.1s*

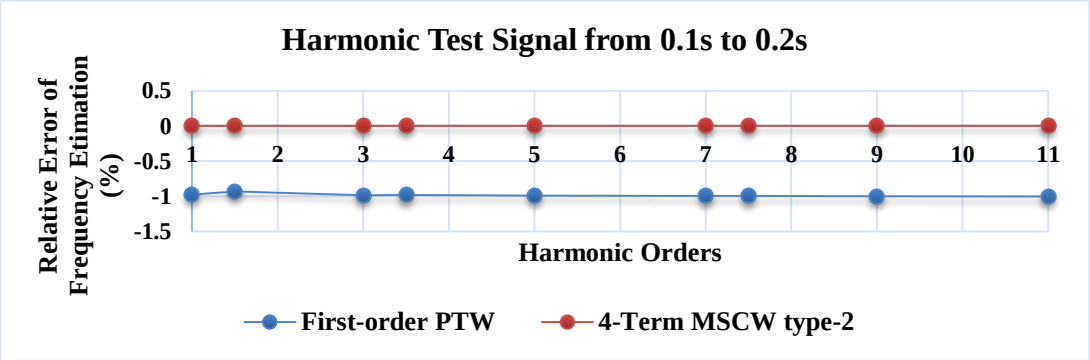

Fig. 3.10 Percentage relative errors variation of frequency estimation to the harmonic order with Adaptive PLIS-based DSLIFFT using First-order PTW and 4-Term MSCW type-2 at the frequency is 49.5 Hz and the duration is *0.1s to 0.2s*

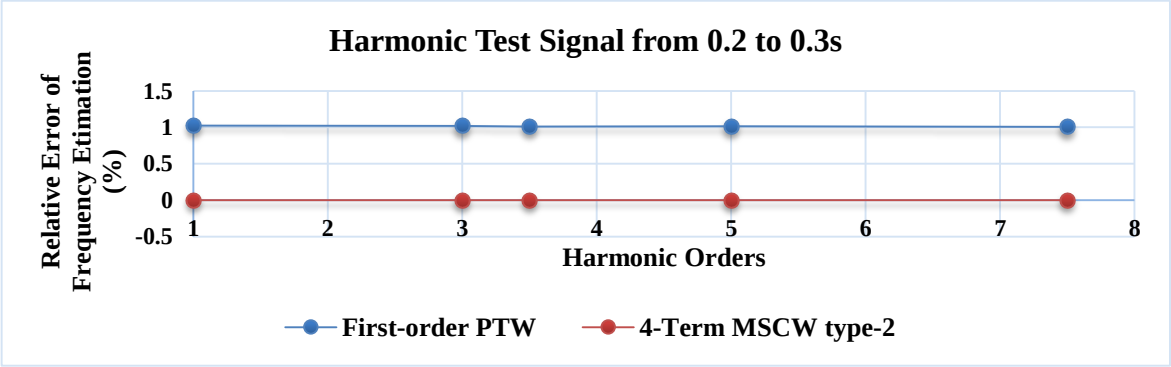

Fig. 3.11 Percentage relative errors variation of frequency estimation to the harmonic order with Adaptive PLIS-based DSLIFFT using First-order PTW and 4-Term MSCW type-2 at the frequency is 50.5 Hz and the duration is *0.2s to 0.3s*

The percentage relative error variations of fundamental and harmonic frequencies estimation to the harmonic orders with First-order PTW and 4-Term MSCW type-2 using Adaptive PLIS based DSLIFFT are depicted above in Fig. 3.9 to Fig.3.11.

From Fig. 3.9 to Fig 3.11 the percentage relative error variation of the fundamental and harmonic frequencies using Adaptive PLIS-based DSLIFFT with First-order PTW and 4-Term MSCW of type-2 appears low under different harmonic and noise effect cases of 49.5 Hz and 50.5 Hz. These line graphs clearly demonstrate that the frequency estimation is highly accurate using Adaptive PLIS-based DSLIFFT with 4-Term MSCW of type-2.

3.6.3 Phase Angle Estimation

The phase angle estimation of the benchmark harmonic test signal and its error comparison for First-order PTW and 4-Term MSCW type-2 with fundamental frequency values

of 49.5 Hz and 50.5 Hz under the time-varying harmonic condition with noise effects are tabulated in Tables 3.11–3.13.

Table 3.11 Phase angle estimation comparison using Adaptive PLIS-based DSLIFFT with First-order PTW and 4-Term MSCW type-2, when the fundamental frequency = 50.5 Hz

Harmonic Order (h)	Phase angle (deg) Estimation using Adaptive PLIS-based DSLIFFT		The Relative Error of Phase angle Estimation (%) using Adaptive PLIS-based DSLIFFT	
	With First order PTW	With 4-Term MSCW type-2	With First order PTW	With 4-Term MSCW type-2
1	40.0138	39.9163	- 0.0345	0.2093
3	114.5941	115.1013	0.3529	-0.0881
5	-29.8211	-30.0657	0.5964	-0.2190
7	109.7411	110.1164	0.2353	-0.1058
9	-19.8407	-20.0479	0.7967	-0.2398
11	99.7084	100.132	0.2916	-0.1328
13	-9.8679	-10.0306	1.3208	-0.3064
15	-89.7372	-89.85	0.2920	0.1667
17	0.0487	-0.0122	0	0

Table 3.12 Phase angle estimation comparison using Adaptive PLIS-based DSLIFFT with First-order PTW and 4-Term MSCW type-2, when the fundamental frequency = 49.5 Hz

Harmonic Order (h)	Phase angle (deg) Estimation using Adaptive PLIS-based DSLIFFT		The Relative Error of Phase angle Estimation (%) using Adaptive PLIS-based DSLIFFT	
	With First order PTW	With 4-Term MSCW type-2	With First order PTW	With 4-Term MSCW type-2
1	40.0144	40.0365	-0.0361	- 0.0914
3	113.2926	114.9399	1.4847	0.0522
3.5	-29.7742	-29.8870	0.7525	0.3765
5	109.1559	109.9593	0.7673	0.0369
7.5	-19.7222	-20.1689	1.3889	- 0.8449
7	99.1411	99.8980	0.8589	0.1019
7.5	-9.7661	-9.9106	2.3394	0.8935
9	-89.1576	-90.0236	0.9360	- 0.0262
11	0.0824	0.0500	0	0

Table 3.13 Phase angle estimation comparison using Adaptive PLIS-based DSLIFFT with First-order PTW and 4-Term MSCW type-2, when the fundamental frequency = 50.5 Hz

Harmonic Order (h)	Phase angle (deg) Estimation using Adaptive PLIS-based DSLIFFT		The Relative Error of Phase angle Estimation (%) using Adaptive PLIS-based DSLIFFT	
	With First order PTW	With 4-Term MSCW type-2	With First order PTW	With 4-Term MSCW type-2
1	40.0172	39.9664	-0.0430	0.0841
3	114.6935	115.0926	0.2665	-0.0805
3.5	-29.7693	-30.1242	0.7689	-0.4139
5	109.7967	109.9333	0.1849	0.0606
7.5	-19.9060	-20.0991	0.4698	-0.4953

Table 3.11 to Table 3.13 depicts phase angle estimation results using Adaptive PLIS based DSLIFFT with First-order PTW and 4-term MSCW type-2. Based on the observations the accuracy of the First-order PTW and 4-Term MSCW of type-2 using Adaptive PLIS-based DSLIFFT algorithm concerning the percentage relative errors of the fundamental phase angle is in the order of 10^{-1} under the variable fundamental frequency values of 49.5 Hz and 50.5 Hz.

The percentage relative error variations of fundamental and harmonic phase angles estimation to the harmonic orders with Adaptive PLIS-based DSLIFFT using First-order PTW and 4-Term MSCW type-2 are depicted in Fig. 3.12 to Fig.3.14, where the percentage relative error values of all the harmonic orders are within the ranges of -0.5 to 1.5

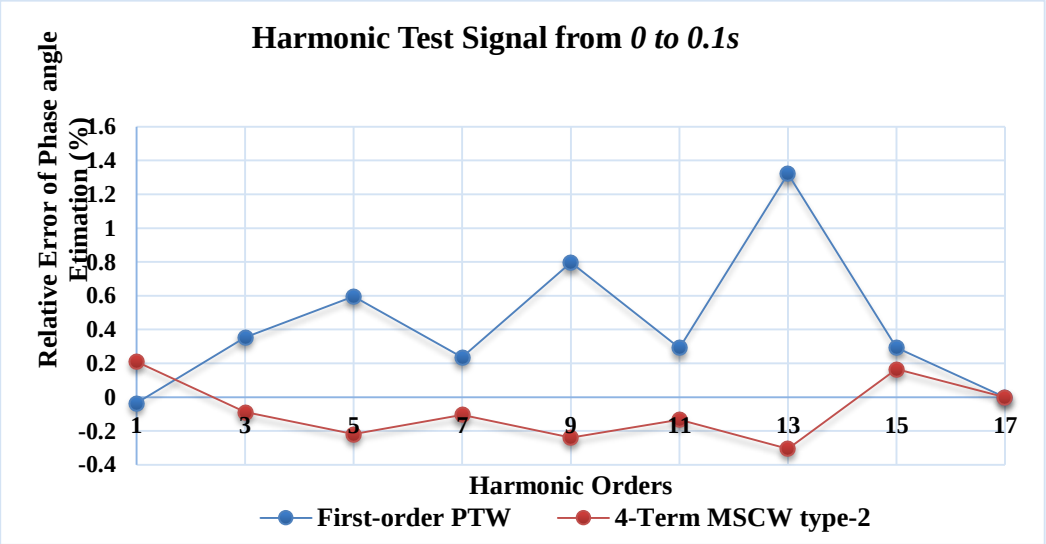

Fig. 3.12 Percentage relative errors variation of phase estimation to the harmonic order with Adaptive PLIS-based DSLIFFT using First-order PTW and 4-Term MSCW type-2 at the frequency is 50.5 Hz and the duration is *0* to *0.1s*

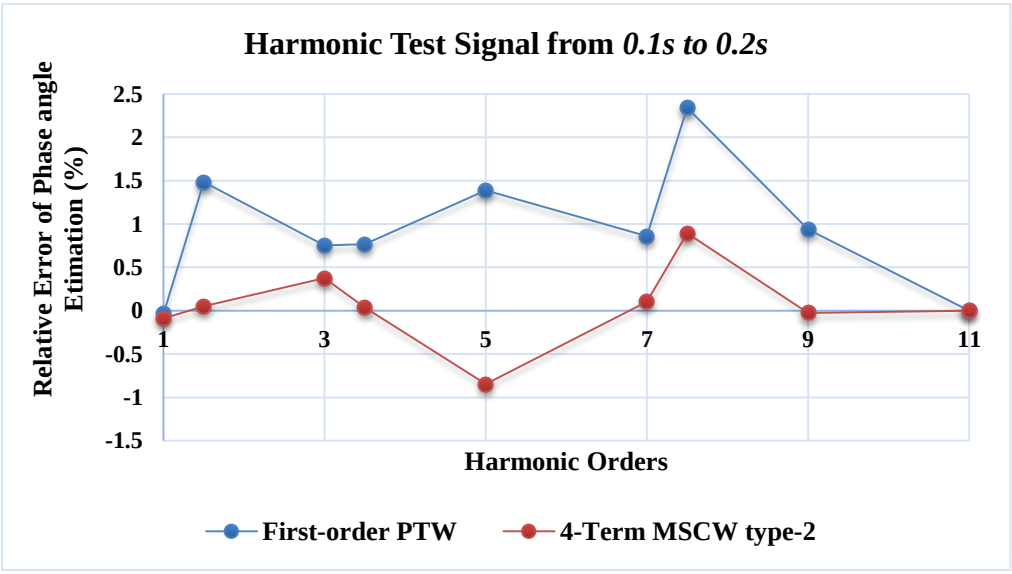

Fig. 3.13 Percentage relative errors variation of phase angle estimation to the harmonic order with Adaptive PLIS-based DSLIFFT using First-order PTW and 4-Term MSCW type-2 at the frequency is 49.5 Hz and the duration is *0.1* to *0.2s*

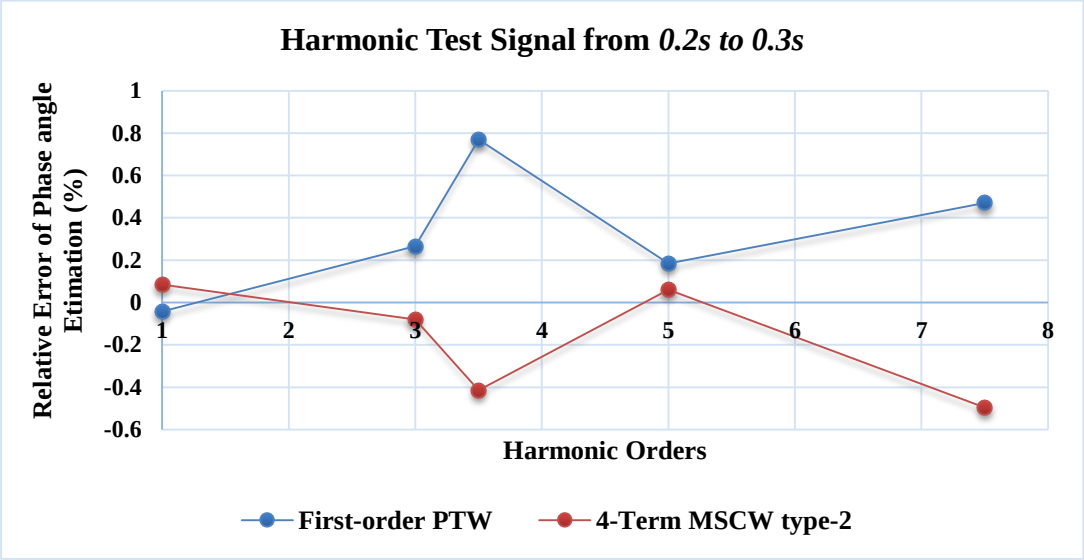

Fig. 3.14 Percentage relative errors variation of phase estimation to the harmonic order with Adaptive PLIS-based DSLIFFT using First-order PTW and 4-Term MSCW type-2 at the frequency is 50.5 Hz and the duration is *0.2* to *0.3s*

From the responses of Figs. 3.6–3.14, it is evident that the Adaptive PLIS-based DSLIFFT with 4-Term MSCW type-2 exhibits accurate estimation of amplitude, frequency and phase under different time instants with the influence of inter-harmonic and white Gaussian noise. However, the First-order PTW also exhibits better accurate estimation of amplitude and phase-angle, the frequency estimation accuracy is low compared to the 4-term MSCW type-2. Hence it is concluded that adaptive PLIS based DSLIFFT with 4 term MSCW type-2 exhibits better results for estimation of Time-varying multi-harmonics. The RT validation of the proposed Adaptive PLIS-based DSLIFFT algorithm on estimating the real-world harmonic signals are presented in the next section.

3.7 Real-Time Experimental Validation

The RT implementation of the Adaptive PLIS-based DSLIFFT using 4-Term MSCW type-2 is discussed in this section. The detailed experimental setup is depicted in Fig.3.15.

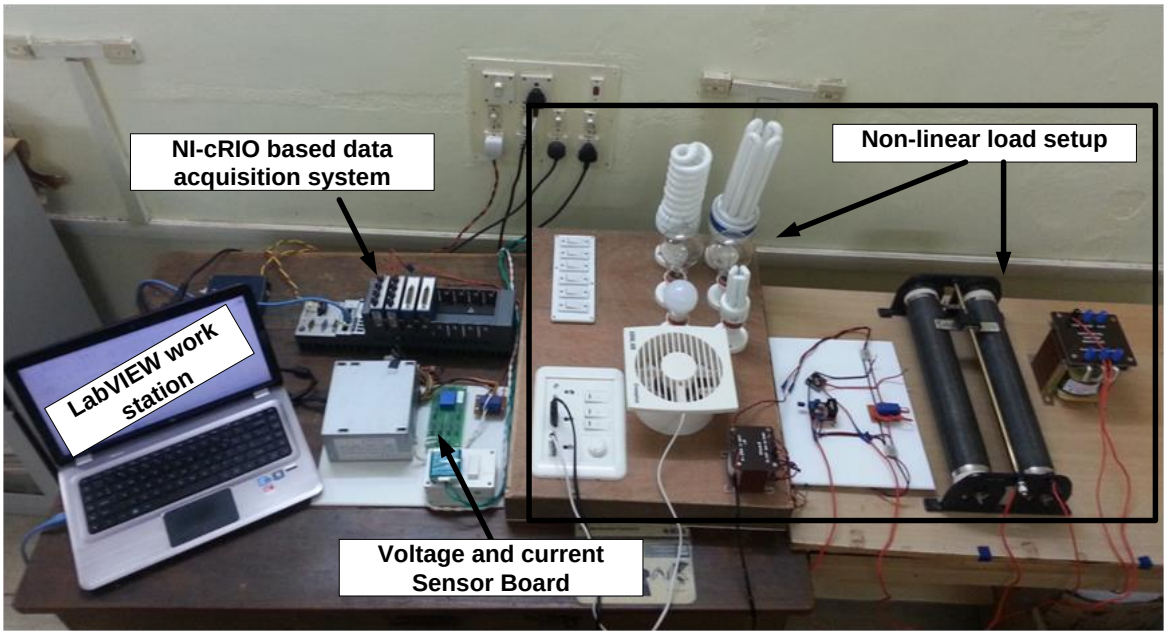

Fig. 3.15 NI-cRIO 9082 based harmonic estimation experimental setup

The common real-world loads such as Compact Fluorescent Lamp (CFL), Triode for Alternating Current (TRIAC) controlled exhaust fan and Switched Mode Power Supply (SMPS) of the Personal Computer (PC), Bridge rectifier with RL load, Incandescent Lamp, Light Emitting Diode (LED) Lamp to serve different nonlinear loads are considered for estimation. The real-world harmonic loads considered for real-time estimation is shown in Table 3.14.

Table 3.14 Real-world nonlinear load specifications

Load	Type of load	Ratings	Quantity
1	Compact Fluorescent Lamp (CFL)	220–240 V, 50 Hz, 85 W	2
2	TRIAC controlled Exhaust Fan	220–240 V, 50 Hz, 20 W, 1750 rpm	1
3	SMPS of the PC	Input: 230 V AC, 50 Hz, Output: 12V DC, 0.3 A	1
4	Bridge rectifier with RL load	230V/ 20V AC ,50Hz, R=10Ω/15A, L= 4mH	1
5	Incandescent lamp	230V, 50 Hz, 100W	2
6	Light Emitting Diode (LED) Lamp	230V, 50Hz, 9W	1

NI-cRIO-based virtual instrumentation experimental setup described in chapter 2 is used for harmonic estimation as illustrated in Fig. 3.15.

The Adaptive PLIS-based DSLIFFT using 4-Term MSCW has been deployed in the LabVIEW configured host computer and interfaced to the NI LabVIEW powered cRIO 9082. The process flowchart for real-time estimation of time-varying harmonics is shown in Fig.3.16.

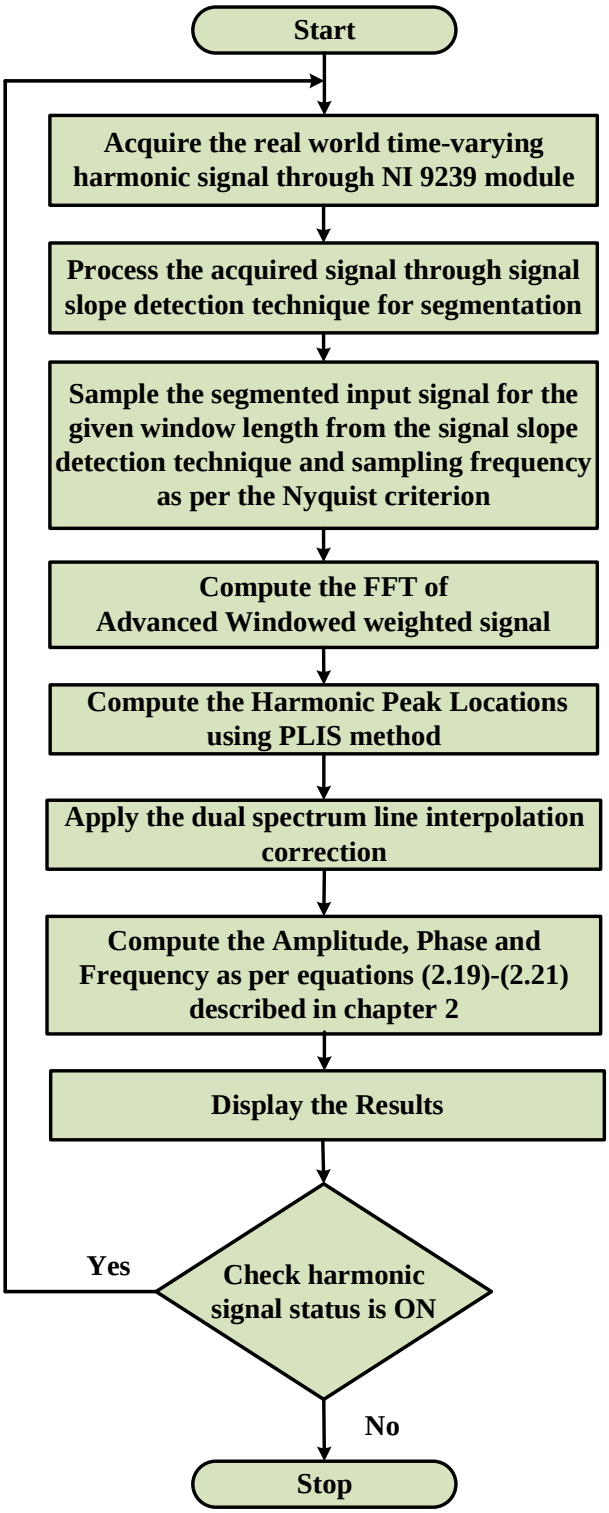

Fig. 3.16 Flowchart of the proposed PLIS based DSLIFFT Algorithm with 4-Term MSCW in RT estimation

The procedural steps to implement the Adaptive PLIS-based DSLIFFT algorithm with Advanced Window functions in RT	
Step 1:	Processing the acquired real-world time-varying harmonic signal through signal slope detection technique for segmentation into periodic signals.
Step 2:	Sampling the segmented real-world harmonic signal using sampling theorem concept.
Step 3:	The acquired signal is processed through the FPGA I/Os of NI-cRIO 9082 system [124], then convert the sampled signal into a weighted signal using advanced window functions: First order polynomial time window and 4-Term minimal sidelobe cosine window of type-2, subsequently compute the weighted signal FFT.
Step 4:	Use the PLIS-based DSLIFFT algorithm to find out the fundamental as well as harmonic spectral amplitudes accurately.
Step 5:	Display the results.

3.7.1 Case 1: RT Harmonic Estimation of Loads – 1,2&3 are in ON condition

The time-varying current waveform is acquired using NI-cRIO, during the load variation is depicted in Fig. 3.17. The estimation is performed for different loads as tabulated in Table 3.14. In this case, initially Loads 1,2 and 3 are in ON and the loads 4,5 and 6 are turned ON at t=16.27s. This change in load can be observed clearly from the harmonic waveform as illustrated in Fig. 3.17. The estimation results of amplitude, frequency and phase before change in the waveform and after change in the waveform are described below.

The amplitude, frequency and phase angle of the fundamental and harmonics are estimated by the Adaptive PLIS based DSLIFFT with 4-Term MSCW type-2 using laboratory RT experimental test bench (NI-cRIO) and the Tektronix Power Quality Analyzer (PQA) model PA4000 [129] and amplitude and percentage relative error are tabulated in Tables 3.15–3.17. The PQA results and the Adaptive PLIS-based DSLIFFT with 4-term MSCW of type-2 configured RT estimation system results are relatively identical and it exhibits better accuracy under the time-varying harmonic condition as per the requirement of international standards [17–19].

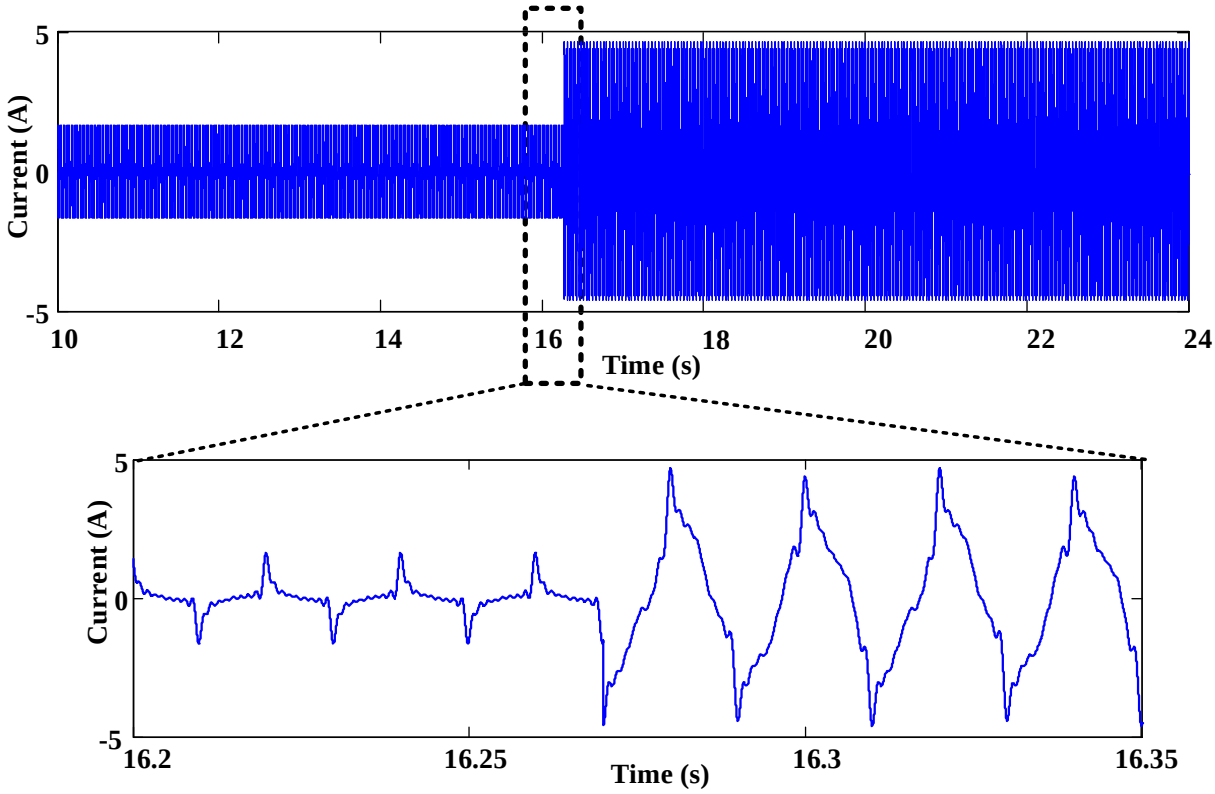

Fig. 3.17 Time-varying real-world nonlinear load current waveform

Table 3.15 Case 1: Amplitude estimation comparison of Adaptive PLIS based DSLIFFT with type-2 of 4-Term MSCW and Tektronix PQA, when load 1,2 and 3 are in ON condition

Harmonic Order (h)	Amplitude (A) Measured using PQA (Tek-PA4000)	Amplitude (A) Measured using Adaptive PLIS based DSLIFFT algorithm with NI-cRIO	The Relative Error (%)
1	0.4977	0.4972	0.0916
3	0.2839	0.2816	0.8214
5	0.2154	0.2105	2.2663
7	0.1625	0.1554	4.3976
9	0.1333	0.1238	7.1523
11	0.1091	0.1010	7.4235
13	0.1076	0.1027	4.5982
15	0.1037	0.1012	2.4132
17	0.0880	0.0872	0.9117

Table 3.16 Case 1: Frequency estimation comparison of Adaptive PLIS based DSLIFFT with type-2 of 4-Term MSCW and Tektronix PQA, when load 1,2 and 3 are in ON condition

Harmonic Order (h)	Frequency (Hz) Measured using PQA (Tek-PA4000)	Frequency (Hz) Measured using Adaptive PLIS based DSLIFFT algorithm with NI-cRIO	The Relative Error (%)
1	49.95	49.9500023	-4.6499×10^{-06}
3	149.85	149.8500023	-1.5491×10^{-06}
5	249.75	249.7500018	-7.1069×10^{-07}
7	349.65	349.6500018	-5.1258×10^{-07}
9	449.55	449.5500010	-2.1639×10^{-07}
11	549.45	549.4501125	-2.0481×10^{-05}
13	649.35	649.3500506	-7.7974×10^{-06}
15	749.25	749.2500197	-2.6246×10^{-06}
17	849.15	849.1500073	-8.5861×10^{-07}

Table 3.17 Case 1: Phase angle estimation comparison of Adaptive PLIS-based DSLIFFT with type-2 of 4-Term MSCW and Tektronix PQA, when load 1,2 and 3 are in ON condition

Harmonic Order (h)	Phase angle (deg) Measured using PQA (Tek-PA4000)	Phase angle (deg) Measured using Adaptive PLIS based DSLIFFT algorithm with NI-cRIO	The Relative Error (%)
1	17.98	17.9624	0.0978
3	−120.99	-120.9578	0.0264
5	110.49	110.4027	0.0789
7	−18.28	-18.4023	-0.6690
9	− 140.37	-140.5270	-0.1118
11	98.33	98.4828	-0.1554
13	−13.93	-13.8080	0.8758
15	−139.16	-138.9288	0.1659
17	97.42	97.4747	-0.0561

3.7.2 Case 2: RT Harmonic Estimation of All the loads are in ON condition

The estimation for all the loads are tabulated in Table 3.18 to Table 3.20.

Table 3.18 Case 2: Amplitude estimation comparison of Adaptive PLIS based DSLIFFT with type-2 4-Term MSCW and Tektronix PQA, when all the loads are in ON condition

Harmonic Order (h)	Amplitude (A) Measured using PQA (Tek-PA4000)	Amplitude (A) Measured using Adaptive PLIS based DSLIFFT algorithm with NI-cRIO	The Relative Error (%)
1	3.0582	3.0555	0.0916
2.5	0.2130	0.2129	0.0233
3	0.5062	0.5050	0.2293
4.5	0.1927	0.1928	-0.0402
5	0.3006	0.2938	2.2654
7	0.2244	0.2245	-0.0587
9	0.2547	0.2544	0.1060
11	0.1956	0.1911	2.3110
13	0.1859	0.1835	1.2807
15	0.1454	0.1419	2.4132

Table 3.19 Case 2: Frequency estimation comparison of proposed PLIS-based DSLIFFT with type-2 4-Term MSCW and Tektronix PQA when all the loads are in ON condition

Harmonic Order (h)	Frequency (Hz) Measured using PQA (Tek-PA4000)	Frequency (Hz) Measured using Adaptive PLIS based DSLIFFT algorithm with NI-cRIO	The Relative Error (%)
1	49.95	49.9500026	-5.2858×10^{-06}
2.5	124.875	124.8752300	-1.8415×10^{-04}
3	149.85	149.8500462	-3.0825×10^{-05}
4.5	224.775	224.7747791	9.8284×10^{-05}
5	249.75	249.7499244	3.0254×10^{-05}
7	349.65	349.6500028	-7.9774×10^{-07}
9	449.55	449.5500006	-1.2632×10^{-07}
11	549.45	549.4501139	-2.0732×10^{-05}
13	649.35	649.3500491	-7.5553×10^{-06}
15	749.25	749.2500180	-2.4032×10^{-06}

Table 3.20 Case 2: Phase angle estimation comparison of proposed PLIS-based DSLIFFT with type-2 4-Term MSCW and Tektronix PQA when all the loads are in ON condition

Harmonic Order (h)	Phase angle (deg) Measured using PQA (Tek-PA4000)	Phase angle (deg) Measured using Adaptive PLIS based DSLIFFT algorithm with NI-cRIO	The Relative Error (%)
1	0	-0.0176	0
2.5	12.09	12.1191	-0.2411
3	-123.95	-122.9449	0.8109
4.5	11.08	11.1110	-0.2799
5	107.89	107.9176	-0.0256
7	-30.1	-30.1222	-0.0739
9	-145.2	-145.1571	0.0296
11	99.1	99.1529	-0.0534
13	-23.99	-23.8782	0.4659
15	-149.98	-149.0891	0.5940

From the real-time estimation results tabulated above, it is clear that the Adaptive PLIS-based DSLIFFT with 4-Term MSCW of type-2 has better accuracy under time-varying harmonic condition. The developed Adaptive PLIS-based DSLIFFT with 4-Term MSCW of type-2 has improved accuracy and better online response for the estimation of time-varying harmonics and interharmonics under noise conditions. There is a real need to compute these harmonics effectively for mitigation purpose.

3.8 Conclusions

The Adaptive PLIS-based DSLIFFT with Polynomial Time Window and 4-Term MSCW has better accuracy and precision under non-synchronous sampling, low amplitude, and fractional harmonic frequency. Simulation and real-time test results demonstrate the effectiveness of Adaptive PLIS based DSLIFFT for time-varying current harmonic estimation under variable frequency conditions. Improved performance indices were examined with experimental results by considering real-world load harmonic signals. The simulation and experimental results satisfy requirements of international standards such as IEC 61000-4-7, 4-

30, and IEEE 1159-2009. Therefore, the developed Adaptive PLIS-based DSLIFFT with 4-Term MSCW type-2 can estimate time-varying current harmonics, as well as voltage harmonics, even under distorted conditions and variable grid frequencies in real-time.

Chapter 4

Conservative Power Theory based Hybrid Active Power Filter for Industrial Power System

4.1 Introduction

Passive Filters (PFs) are one of the conventional solutions for compensating harmonics and are well in use by industrial power systems because of its low cost even though they do not perform well in dynamic load variations. To make the shunt PFs effective in industrial power system, a shunt Active Power Filter (APF) is augmented with the existing PFs and is termed as Hybrid APF (HAPF).

Usually, the proportional and integral (PI) controller is the most widely used linear controller for current control operation, but it has a low dynamic response for the load variations due to the poor tuning of the current control parameters. The recent literature reveals that the design of a suitable current controller and validation of its performance under dynamic conditions is identified as an important area of research [65]. Hence a Type-II current controller is designed to perform the current control task. The objective of the Type-II current controlled HAPF is to provide better harmonic isolation between the supply and load. Consequently, there is no harmonic resonance effect and no harmonic current effect on the source.

Phase-Locked Loops (PLLs) and digital filters are used in the Synchronous Reference Frame (SRF) theory based reference current generation scheme in the PI controller. This scheme lacks selective harmonic compensation. Hence CPT based orthogonal current decomposition is adopted for Type-II current controller. CPT offers better features, such as accurate estimation under ideal and weak grid conditions and enables selective estimation of different power quality (PQ) issues such as harmonics, unbalances, and reactive power [78].

The industrial power system with CPT based Type-II current controlled HAPF is modelled in MATLAB/Simulink 2013 environment and implemented in real-time using OPAL-RT based OP 4500 real-time grid emulator [125].

4.2 Power System Configuration

A simplified diagram of a typical industrial power system is illustrated in Fig 4.1. It consists of the main supply from the grid, distribution transformers and two points of common couplings (PCCs). The PCC1 is composed of lighting and linear loads, whereas the PCC2 is feeding the linear and nonlinear loads. The non-linear loads are DC drive, Bridge Rectifier fed to other DC loads. There is 5^{th} & 7^{th} order tuned PF and a capacitor bank serving the system for harmonic compensation. However, due to dynamic variations in the nonlinear loads, the existing PFs are not performing the compensation tasks effectively. In view of already installed PFs which belongs to an old investment in the industrial power system, A Type-II controlled shunt APF using CPT is added without changing the existing PFs. The combination of shunt APF and shunt tuned PF are considered as HAPF in order to eliminate the adverse effects of tuned PFs. Here the current controlled voltage source inverter is operating as an APF.

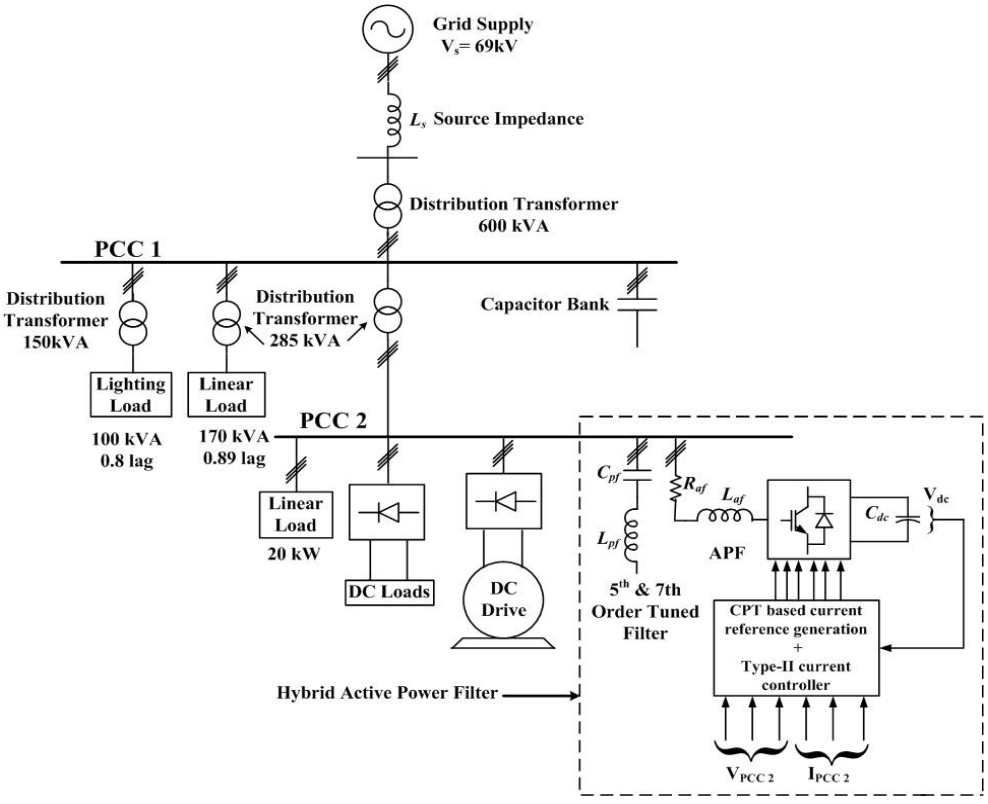

Fig. 4.1 Industrial power system configuration with CPT based HAPF

4.3 Conservative Power Theory Framework

In the HAPF configuration, current decomposition is conducted based on the CPT. CPT is one of the time domain theory introduced by Tenti *et al.* based on the orthogonal current

decomposition methodology [78], where the harmonic current has been decomposed into active, reactive and void components. CPT defines these quantities obtained by the scalar product of voltage, currents and its integrals. The benefit of using CPT is that there is no need to use the PLLs, linear transformation for reference generation and digital filters for harmonic extraction, which will reduce the computation burden [130]. Based on the CPT definitions the active, reactive, void and unbalance currents are computed as follows.

The active current expression based on CPT definition is

$$i_{an} = \frac{\langle v_n, i_n \rangle}{\|v_n\|^2} v_n = \frac{P_n}{V_n^2} v_n = G_n v_n \tag{4.1}$$

Where v_n and i_n are the voltage and the current measured at phase *n*. The term $G_n = \frac{P_n}{V_n^2}$ is the equivalent conductance of phase *n*. The active current has no impact on reactive energy.

The reactive current expression based on CPT definition is

$$i_{rn} = \frac{\langle \hat{v}_n, i_n \rangle}{\|\hat{v}_n\|^2} \hat{v}_n \ = \frac{W_n}{\hat{V}_n^2} \hat{v}_n = B_n \hat{v}_n \tag{4.2}$$

Where $\hat{v}_n$ is the unbiased time integral of the voltage of phase *n*. The term $B_n = \frac{W_n}{\hat{V}_n^2}$ is the equivalent susceptance of phase *n*. The reactive current has no impact on active power.

The void current is written as

$$\underline{i}_{vn} = \underline{i}_n - \underline{i}_{an} - \underline{i}_{rn} \tag{4.3}$$

The active and reactive phase currents can be further decomposed into balanced and unbalanced terms. The balanced active and reactive currents based on the CPT definitions are as follows

$$\underline{i}_a^b = \frac{\langle \underline{v}, \underline{i} \rangle}{\left\|\underline{v}\right\|^2} \underline{v} = \frac{P}{V^2} \underline{v} = G^b \underline{v} \tag{4.4}$$

Here the term G^b is the equivalent balance conductance.

$$\underline{i}_r^b = \frac{\langle \underline{\hat{v}}, \underline{i} \rangle}{\left\|\underline{\hat{v}}\right\|^2} \underline{\hat{v}} = \frac{W}{\hat{V}^2} \underline{\hat{v}} = B^b \underline{\hat{v}} \tag{4.5}$$

Here the term B_n^b is the equivalent balance susceptance.

The unbalanced active and reactive current definitions based on CPT are as given below

The unbalanced active current is expressed as

$$\underline{i_a^u} = \underline{i_a} - \underline{i_a^b} \rightarrow i_{an}^u = (G_n - G^b)v_n \tag{4.6}$$

The unbalanced reactive current is expressed as

$$\underline{i_r^u} = \underline{i_r} - \underline{i_r^b} \rightarrow i_{rn}^u = (B_n - B^b)\hat{v}_n \tag{4.7}$$

Based on (4.1) to (4.7) the reference current vector is expressed as

$$\underline{i} = \underline{i_a^b} + \underline{i_r^b} + \underline{i_a^u} + \underline{i_r^u} + i_v \tag{4.8}$$

Here all the currents are orthogonal to each other. The estimated reference currents on each phase are processed through a current controller. The current controller generates the compensation signal to the inverter, in order to inject the counter harmonic current to the PCC2. The current controller is designed based on Type–II controller. So this eliminates the usage of PLL in the control loop.

The instantaneous complex power expression based on CPT definitions are written as

$$s = p + jq = \underline{v} \circ \underline{i} + j\underline{\hat{v}} \circ \underline{i} \tag{4.9}$$

The resultant average values of active power and reactive energy are calculated as follows:

$$P = \overline{p} = \langle \underline{v}, \underline{i} \rangle = \frac{1}{T}\int_0^T \underline{v}\,(t).\,\underline{i}(t)dt \tag{4.10}$$

$$W = \overline{q} = \langle \underline{\hat{v}}, \underline{i} \rangle = \frac{1}{T}\int_0^T \underline{\hat{v}}\,(t).\,\underline{i}(t)dt \tag{4.11}$$

Equations (4.10) and (4.11) are used for the active and reactive power reference generation. The control methodology is discussed in the next section.

4.4 Methodology for Harmonic Control

The objective of the controller is to generate the compensating current to HAPF within acceptable limits. Furthermore, the DC-link voltage control of HAPF is also the responsibility of the controller. The HAPF injects the compensation current at PCC2 of the industrial power system. Therefore, the harmonics produced by the nonlinear loads as well as the unbalanced

current due to the unbalanced load at PCC2 are compensated.

4.4.1 Type-II Current Controller Design

The current controller is designed based on the Type-II controller where the reference currents are generated in the α-β reference frame. The controller does not require PLL since the Type-II can track the reference accurately. The block diagram of the current controller for α-axis is shown in Fig 4.2(a), the same loop is adopted for the β-axis also. The HAPF current is controlled by the inner current loop and it has a faster response. The block power calculation uses the active and reactive power references to produce a current reference which in turn will be multiplied by the DC-link controller output signal. The resulting signal is the α-axis current reference. The three-phase modulating signal ($m_{abc}(t)$) of HAPF can be expressed as

$$m_a(t) = \hat{m}(t)\cos[\varepsilon(t)] \tag{4.12}$$

$$m_b(t) = \hat{m}(t)\cos\left[\varepsilon(t) - \frac{2\pi}{3}\right] \tag{4.13}$$

$$m_b(t) = \hat{m}(t)\cos\left[\varepsilon(t) - \frac{4\pi}{3}\right] \tag{4.14}$$

Where $\hat{m}(t)$ represents the amplitude of the modulating signal. $\varepsilon(t)$ is the phase of the modulating signal. During the dynamic conditions, depending on the type of disturbance and the closed-loop bandwidth of the current controller $\hat{m}(t)$ can have large overshoots. In view of the fact that the instant at which $\hat{m}(t)$ reaches a peak is unknown, hence it is necessary to ensure that $\hat{m}(t) \leq 1$, so that the modulating signal lies between -1 and 1. In this modulation index is consider as 1 to compensate the maximum gain that can be seen in the open-loop transfer function.

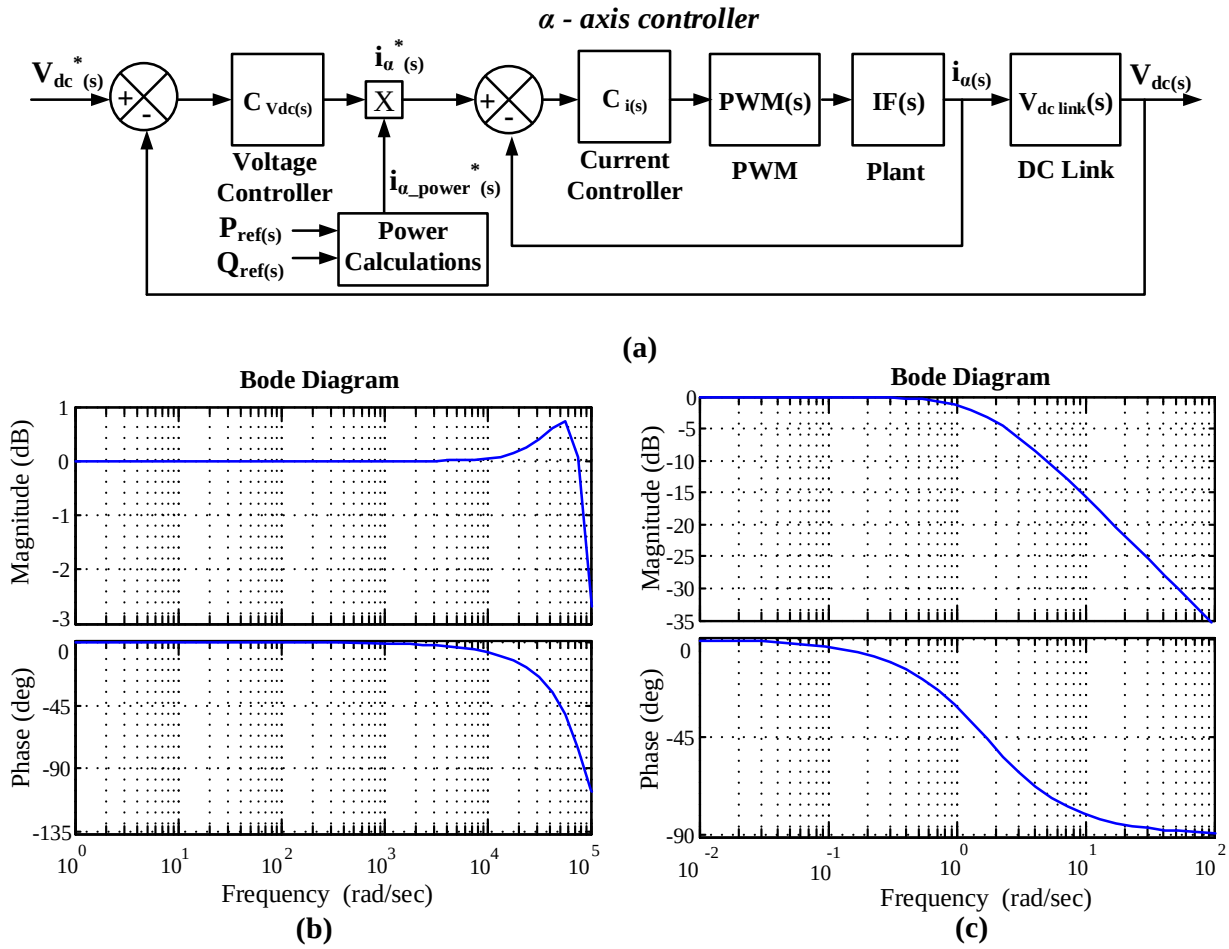

Fig. 4.2 HAPF Control loop block diagram and its frequency response (a) axis controller (b) Current control loop (c) Voltage control loop

The power calculations block shown in Fig 4.2(a) and are expressed as follows [131]:

$$i_{\alpha_{power}}(s) = \frac{2}{3}\frac{1}{v_{s\alpha}^2 + v_{s\beta}^2}\left[v_{s\alpha}P_{ref}(s) + v_{s\beta}Q_{ref}(s)\right] \tag{4.15}$$

The DC-link plant transfer function is expressed as:

$$V_{dc}(s) = \frac{2}{sC_{dc}V_s} \tag{4.16}$$

Where, C_{dc} is the capacitor of the DC-link and V_s is the phase voltage of the AC circuit. The Filter and PWM plant transfer function is represented as:

$$F(s) = \frac{V_{dc}}{2}\left(\frac{1}{sL + R}\right) \tag{4.17}$$

Where V_{dc} is the voltage of the DC-link and L, R is the inductance and resistance of the line

filter, respectively. The Type-II current controller is composed of the lead-lag controller. The DC-link voltage controller is designed by using a PI-controller. Both are designed based on the classical frequency-response technique. The Type-II current controller offers an origin pole, one zero and one high-frequency pole. It provides a phase boost up to 90 degrees [133]. The transfer function of the Type-II current controller is written as

$$G(s) = k\frac{(1+sT)}{sT}\frac{1}{(1+sT_p)} \tag{4.18}$$

Where k is the gain of the controller considered as 1, T is the time constant of the controller, f_p is the frequency of the pole. The Type-II current controller is the modified version of PI-controller consists of a PI-controller with a pole at the frequency f_p, where $f_p = \omega_p/(2\pi)$, and $T_p = 1/\omega_p$. The equation (4.18) is simplified as follows:

$$G(s) = \frac{k}{T_p}\frac{\left(s+\frac{1}{T}\right)}{\left(s+\frac{1}{T_p}\right)} \tag{4.19}$$

With reference to [131], ω_z and ω_p values are obtained by using the *K*-factor approach.

Where

$$K = tan\left(\frac{\theta_{comp}}{2}\right) \tag{4.20}$$

The phase angle of the Type-II current controller at crossover must be adequate to give a phase margin of at least 45 degrees. The compensation angle is the desired phase angle of the controller at the crossover frequency. In Type-II current controller maximum phase, boost is obtained at the geometric mean of pole-zero frequencies. Normally this geometric mean frequency is considered as a crossover frequency of the controller the detailed mathematical approach is presented in [132,133]. The geometric mean frequency of the Type-II current controller is 322 rad/sec. Hence, the crossover frequency (ω_{co}) is considered as 322 rad/s. For the selected crossover frequency, the phase (θ_{comp}) to be compensated is 179.61 degrees respectively. Generally, the compensating phase angle of the controller can range from 0 to 180 degrees for $0 < K < \infty$. The ω_z and ω_p values are obtained as follows:

$$K = tan\left(\frac{\theta_{comp}}{2}\right) = 293.8 \tag{4.21}$$

$$\omega_z = \frac{1}{T} = \frac{\omega_{co}}{K} = 1.1 \tag{4.22}$$

$$\omega_p = \frac{1}{T_p} = K\omega_{co} = 94604 \tag{4.23}$$

Substituting (4.22) and (4.23) in (4.19) will give the transfer function of the Type-II current controller as follows:

$$C_{i(s)} = 94604\left[\frac{(s+1.1)}{s(s+94604)}\right] \tag{4.24}$$

Equation (4.24) is simplified as follows

$$C_{i(s)} = \frac{0.9s+1}{9.55e^{-6}s^2+0.9s} \tag{4.25}$$

4.4.2 DC-link voltage Controller Design

The DC-link voltage PI control loop is designed based on the MATLAB/Simulink PID auto-tuning procedure by considering the response of the inner current loop as follows:

- Based on the inner loop response, make sure that what needs to be improved.
- Add PI-controller and tune the PI values to obtain the required overall response using PID tool in MATLAB/Simulink.

The designed transfer function for the stable response of the DC-link voltage loop controller is expressed as follows:

$$C_{vdc(s)} = \frac{325s+13540}{s} \tag{4.26}$$

Where K_p and K_i values of the DC-link voltage PI controller are 325 and 13540. The frequency response of the closed-loop current and voltage controllers are shown in Fig 4.2(b) and 4.2(c). As noted from the Bode plot the desired responses for voltage and current controller were achieved within the required frequency. From the magnitude and phase, it can be inferred that the designed controller is stable and the voltage and current reference will be tracked as desired.

4.5 Simulation Results

The industrial power system feeding different linear and nonlinear loads with CPT based Type-II current controlled HAPF has been modelled and simulated in MATLAB/Simulink 2013 environment. The steady-state and the dynamic behaviour of the CPT based HAPF system have been verified by both simulation and OPAL-RT based RT studies. The system parameters used for industrial system modelling are given in Table 4.1, and is carried out in Center for the Advanced Control of Energy and Power Systems (ACEPS) at Colorado School of Mines, USA, under BASE Fellowship sponsored by the Department of Science & Technology (DST), Govt. of INDIA and Indo-US Science & Technology Forum (IUSSTF).

Table 4.1 Industrial power system parameters (Geography: USA)

Parameter	**Value**
Source Voltage RMS	V_s=69kV
PCC1 voltage	13.8kV
PCC2 voltage	480V
Source Impedance	R_s=0.19Ω, L_s =2.57mH
Distribution Transformer 1	S= 600kVA, *f*=60 Hz, V_{pr}=69kV, V_{se}=13.8kV
Distribution Transformer 2 at PCC1	S= 150kVA, *f*=60 Hz, V_{pr}=13.8 kV, V_{se}=480V
Linear Load at PCC1	100kVA with 0.8 lagging p.f.
Distribution Transformer 3 at PCC1	S= 285kVA, *f*=60 Hz, V_{pr}=13.8 kV, V_{se}=480V
Lighting load at PCC1	170kVA with 0.89 lagging p.f.
Distribution Transformer 4 at PCC2	S= 285 kVA, *f*=60 Hz, V_{pr}=13.8 kV, V_{se}=480V
DC Drive	S= 3 HP, $V_{dc\ drive}$= 575V, I_{arm} = 5A
Controlled Bridge Rectifier 1	V_{BR}= 575V, α=25°, I_{load1} = 30A
Controlled Bridge Rectifier 2	V_{BR}= 575V, α=50°, I_{load2} = 15A
Linear load (Resistive)	20 kW Unbalanced load
Passive Filter	$Vpcc_2$= 480V, *f*=60Hz, Tuned harmonic orders = 5^{th} and 7^{th} , Quality factor = 20
Tuned Capacitor	V_c=13.8kV, *f*=60Hz, Q_c = 150 kVAR

The simulation results of HAPF in comparison with existing PFs have been presented under ideal and non-ideal voltage conditions. To test the efficacy of the CPT based HAPF system under non-ideal voltage condition, 20% of voltage distortion with unbalance has been

created using a programmable voltage source in Simulink SIM power system toolbox. The parameters of the HAPF are tabulated in Table 4.2.

Table 4.2 HAPF parameters

Parameter	**Value**
Power Rating	60 kVA
Interfacing inductor *(L_{af})*	3mH
Interfacing resistance (R_{af})	0.6 Ω
DC link capacitance *(C_{dc})*	9600uf
DC link voltage *(V_{dc})*	1400 V
PWM switching frequency	9kHz
Type-II current controller pole frequency *(ω_p)*	94604 rad/sec
Type-II current controller zero frequency *(ω_z)*	1.1 rad/sec
DC voltage controller *Kp* value	325
DC voltage controller *Ki* value	13540
Sampling Time (T_s)	33.33usec

The ideal and non-ideal voltage waveforms are presented in Fig. 4.3(a) and 4.3(c). The current behaviour at PCC1 with the PFs and CPT based HAPF under ideal voltage condition are shown in Fig. 4.3(b) simultaneously the current behaviour under non-ideal voltage condition is shown in Fig. 4.3(d). At time t = 0.75sec there is a rise in nonlinear load at PCC2, due to that change the PFs are unable to keep the PCC1 current stable and there is an effect of resonance. It is also observed in Fig. 4.3(b) that the reactive power compensation is not performed by the existing PFs effectively. After introducing the CPT based HAPF the current behaviour is improved by reducing the percentage THD from 2.17% to 1.39% under ideal voltage case and in distorted voltage case it is brought down from 5.68% to 3.82% within the limits of IEEE 519-2014 recommended practice and requirements for harmonic control in electric power systems and the reactive power is also compensated effectively.

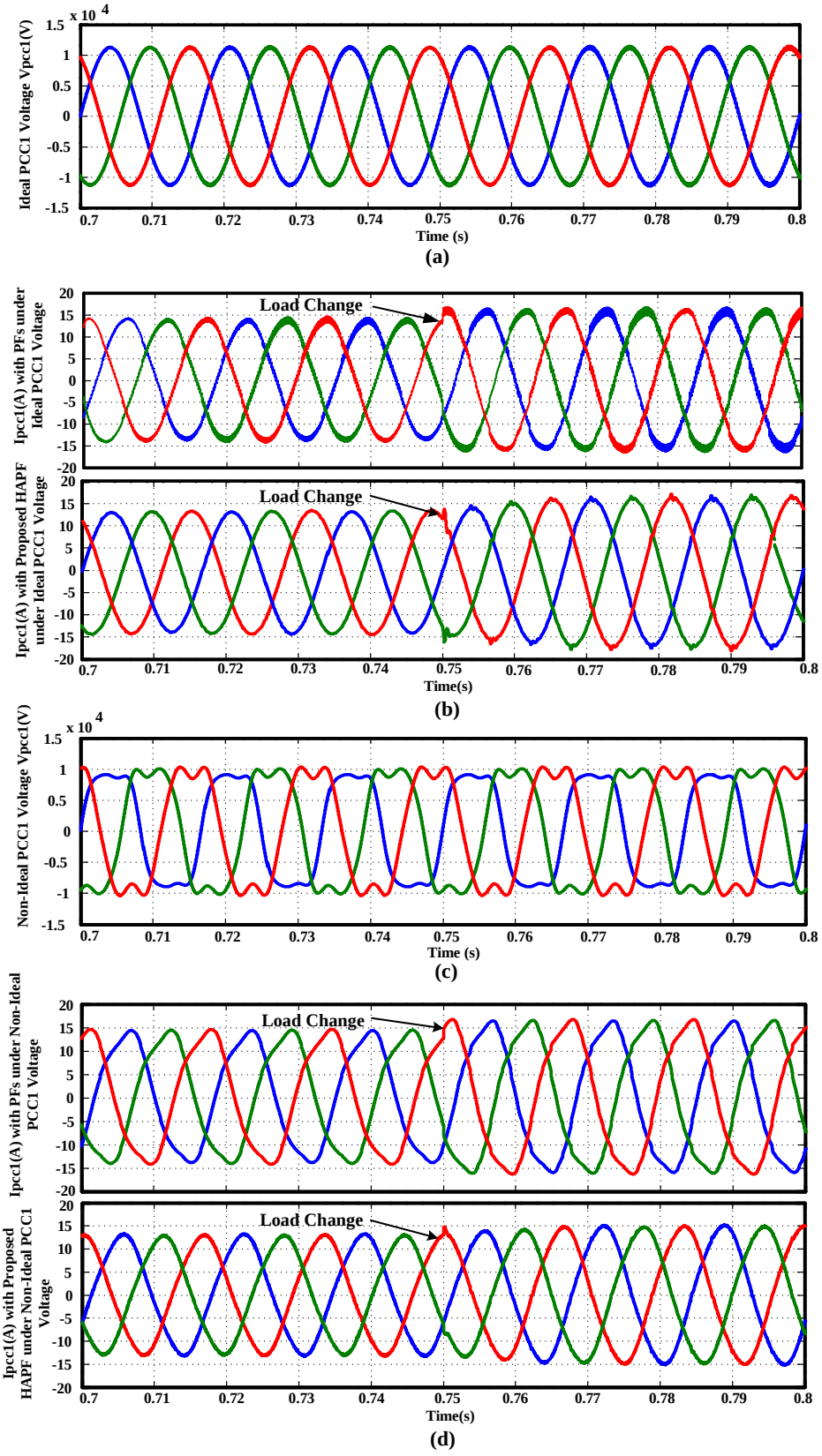

Fig. 4.3 Waveforms at PCC1 (a) Ideal voltage (b) Current response with PFs and with CPT based HAPF under ideal voltage (c) Non-Ideal voltage (d) Current response with PFs and with CPT based HAPF under non-ideal voltage

The CPT based HAPF performance at PCC2 and its comparison with PFs for ideal and non-ideal voltage conditions are presented in Fig. 4.4. The load current at PCC2 with PFs and with HAPF under both ideal and non-ideal voltage conditions are presented in Fig. 4.4(b) and 4.4(d), some notches are existing in the waveform due to inverter switching. Here the dynamic variations after t=0.75s are also handled smoothly by HAPF. The APF with PFs combination will take 2 to 3 cycles to reach the balance condition during the load change. During this processes, a small unbalance is observed due to the combined effect of APF and PF. The results demonstrate that the unbalance is minimized and it is within the acceptable limits as per IEEE 1159-2009 standards [19] and also the reactive power is compensated effectively where the voltage and current waveforms after compensation are in phase. The active (P) and reactive (Q) power values of both ideal and non-ideal supply conditions are 0.2MW and 0.1MVAr when all the loads are connected.

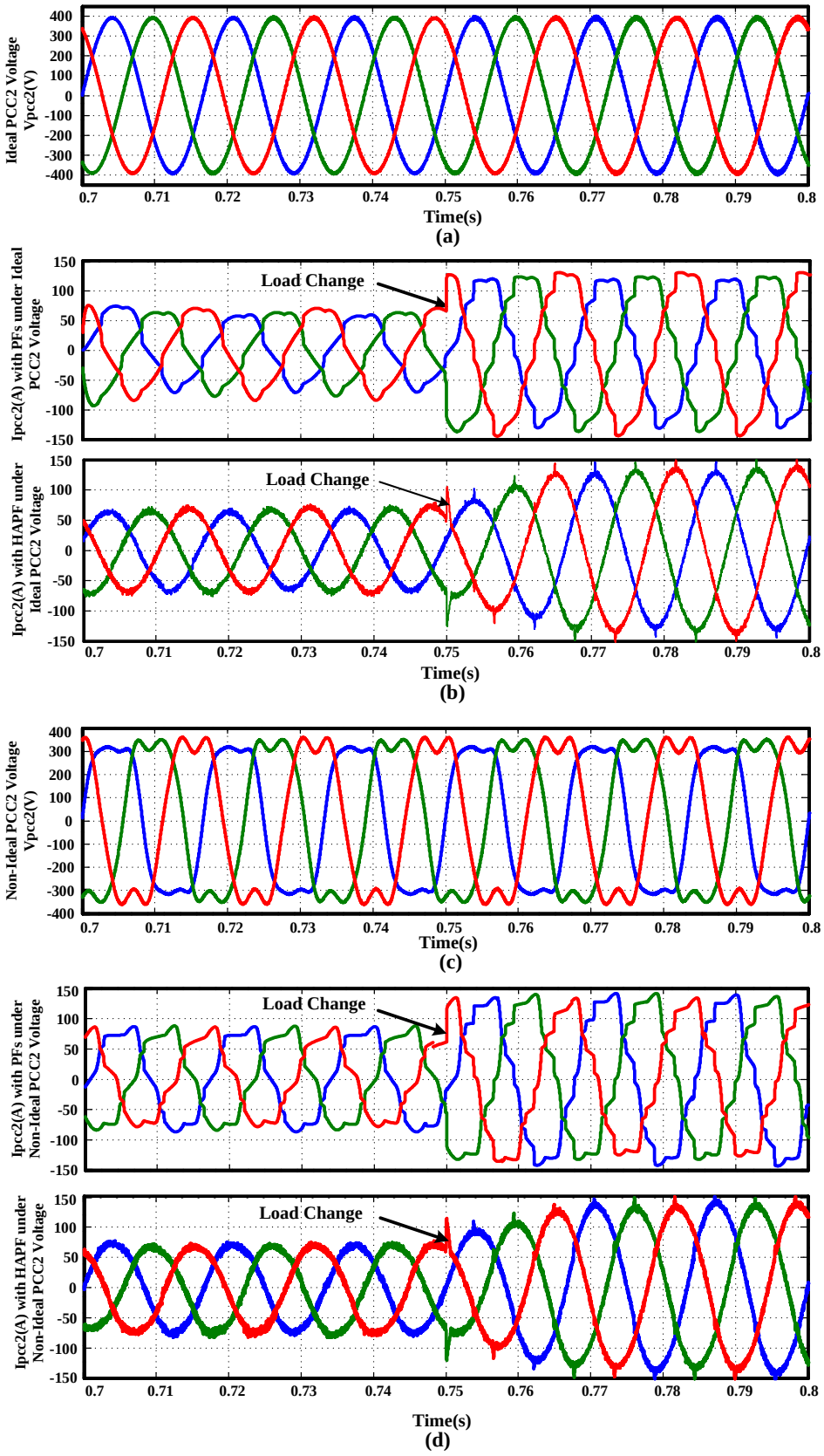

Fig. 4.4 Waveforms at PCC2 (a) Ideal voltage (b) Current response with PFs and with CPT based HAPF under ideal voltage (c) Non-ideal voltage (d) Current response with PFs and with CPT based HAPF under non-ideal voltage

The compensating reference currents generated in each phase by using CPT under ideal and non-ideal voltage conditions are shown in Fig. 4.5(a) and 4.5(b) respectively. The CPT currents are processed through the Type-II current controller to inject the compensating current at PCC2 by using HAPF. The DC-link voltage is also effectively handled by the PI-based voltage control loop under ideal and non-ideal voltage conditions.

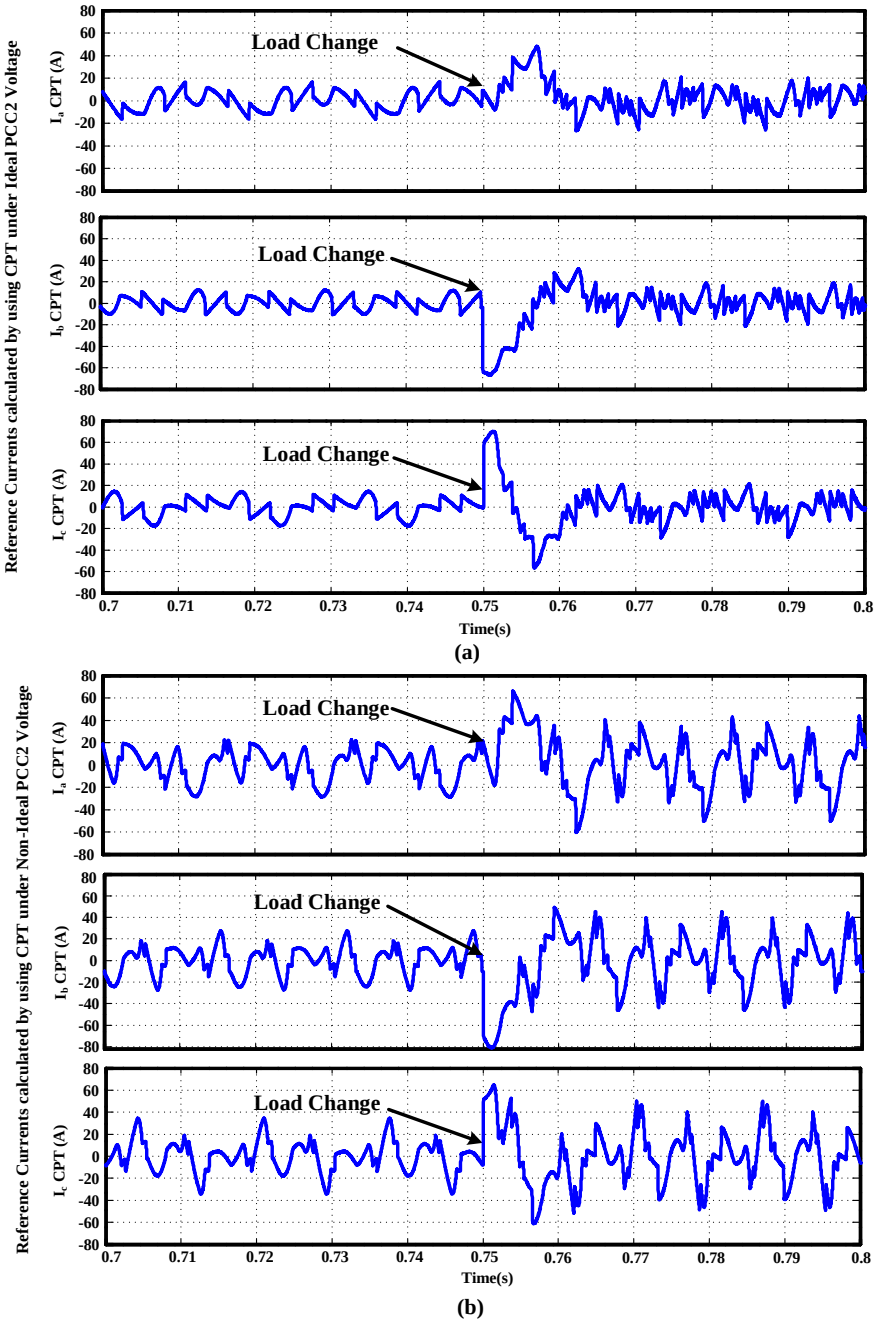

Fig. 4.5 Reference currents estimated by CPT (a) Phase a, Phase b, Phase c reference currents under ideal voltage (b) Phase a, Phase b, Phase c reference currents under non-ideal voltage

The DC-link voltage behaviour is shown in Fig. 4.6(a) and 4.6(b) respectively. It is observed that the DC-link voltage is stable under ideal and non-ideal voltage conditions.

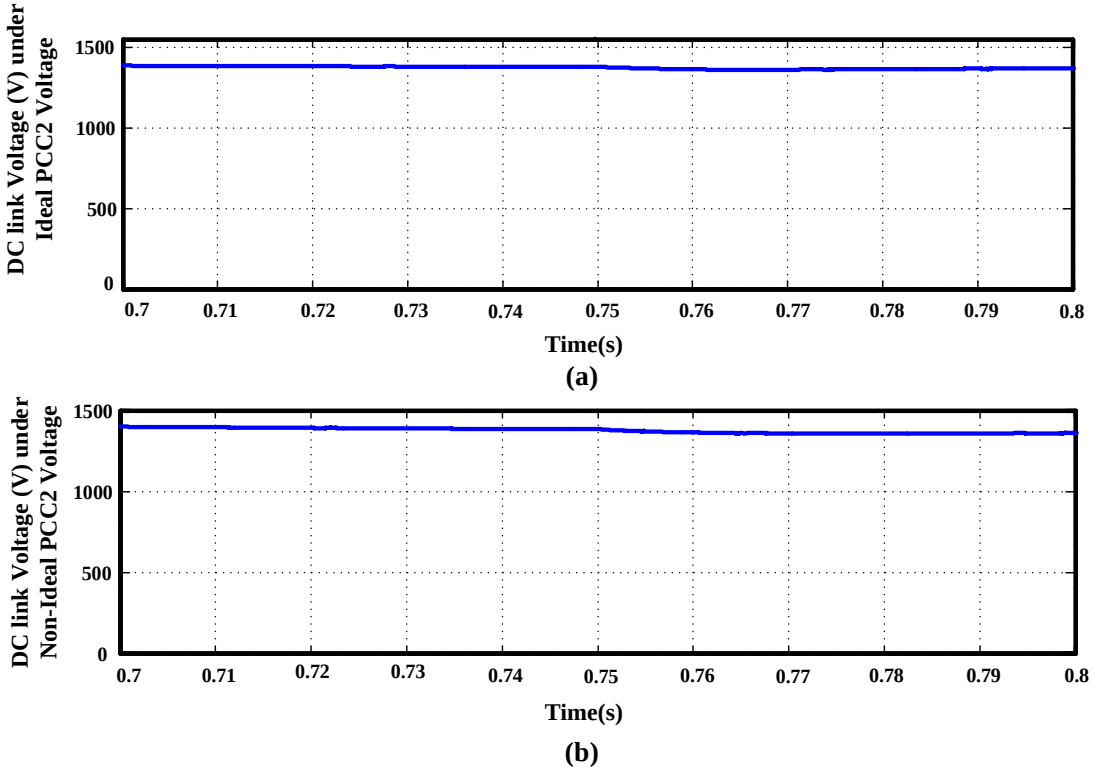

Fig. 4.6 DC link voltage (a) Ideal voltage case (b) Non-ideal voltage case

4.6 Real-Time Experimental Validation

The industrial power system modelled and tested by OPAL-RT based real-time grid emulator [134-136]. The Real-Time (RT) simulators are gaining importance to validate the performance of complex power system.

4.6.1 Real-Time Architecture

The CPT based HAPF is realised based on RT-LAB environment of OPAL-RT, using RT toolbox in MATLAB/Simulink. The detailed structure of the real-time system used to validate the HAPF system is illustrated in Fig. 4.7(a). The laboratory setup of the OPAL-RT system is shown in Fig. 4.7(b). It consists of a host computer and an RT system target. The CPT based HAPF system is modelled using the RT toolbox in Simulink, and then the HAPF system is deployed in the OPAL-RT target using the RT-LAB interface. The real-time implementation of CPT based HAPF system is depicted in Fig. 4.7(c).

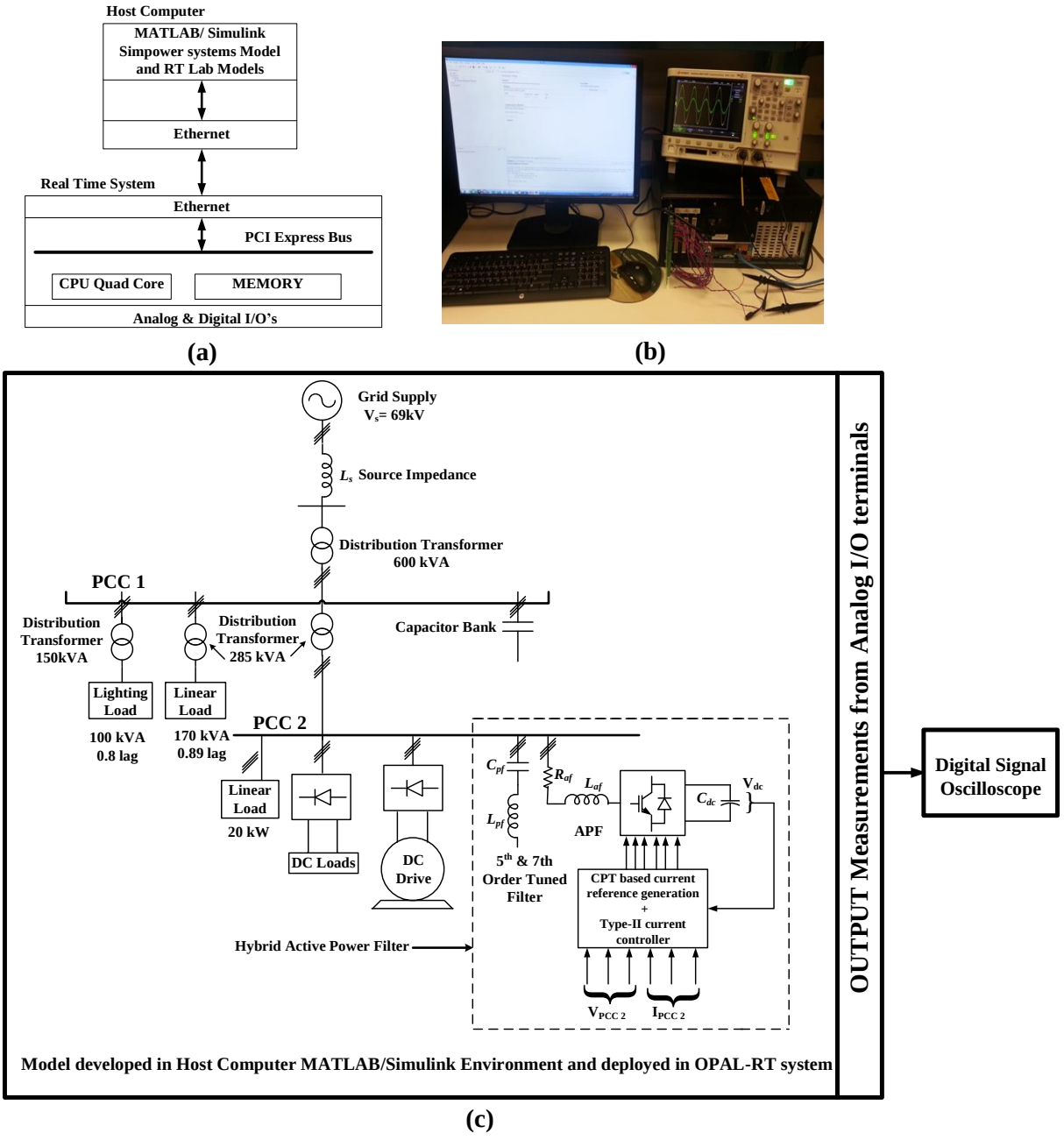

Fig. 4.7 Real-time system configuration (a) System architecture (b) Testing setup (c) CPT based HAPF system real-time implementation

4.6.2 Real-Time System Results

The real-time simulator results captured from analog output terminals of the OPAL-RT target system for phase *a* with PFs and with HAPF compensation under ideal and non-ideal voltage conditions at PCC1 are presented in Fig. 4.8. The reactive power effect at PCC1 using PFs and HAPF compensation under ideal voltage is shown in Fig. 4.8(a) and 4.8(b). Simultaneously under non-ideal voltage condition is illustrated in Fig. 4.8(c) and 4.8(d). The compensation results at PCC2 with PFs and with HAPF are depicted in Fig. 4.9. and Fig. 4.10.

At PCC1 the harmonic pollution is very low and it is within the limits due to linear load nature. But the harmonics are affecting the PCC2 due to the high penetration of different nonlinear loads. The harmonic content at PCC1 & PCC2 under ideal and non-ideal voltage conditions are tabulated in Table 4.3. With reference to the tabulated values in Table 4.3, the current harmonics are reduced and the THD percentage after compensation using CPT based HAPF is within the limits of IEEE 519-2014 standard [10]. The reactive power and unbalance are also compensated effectively.

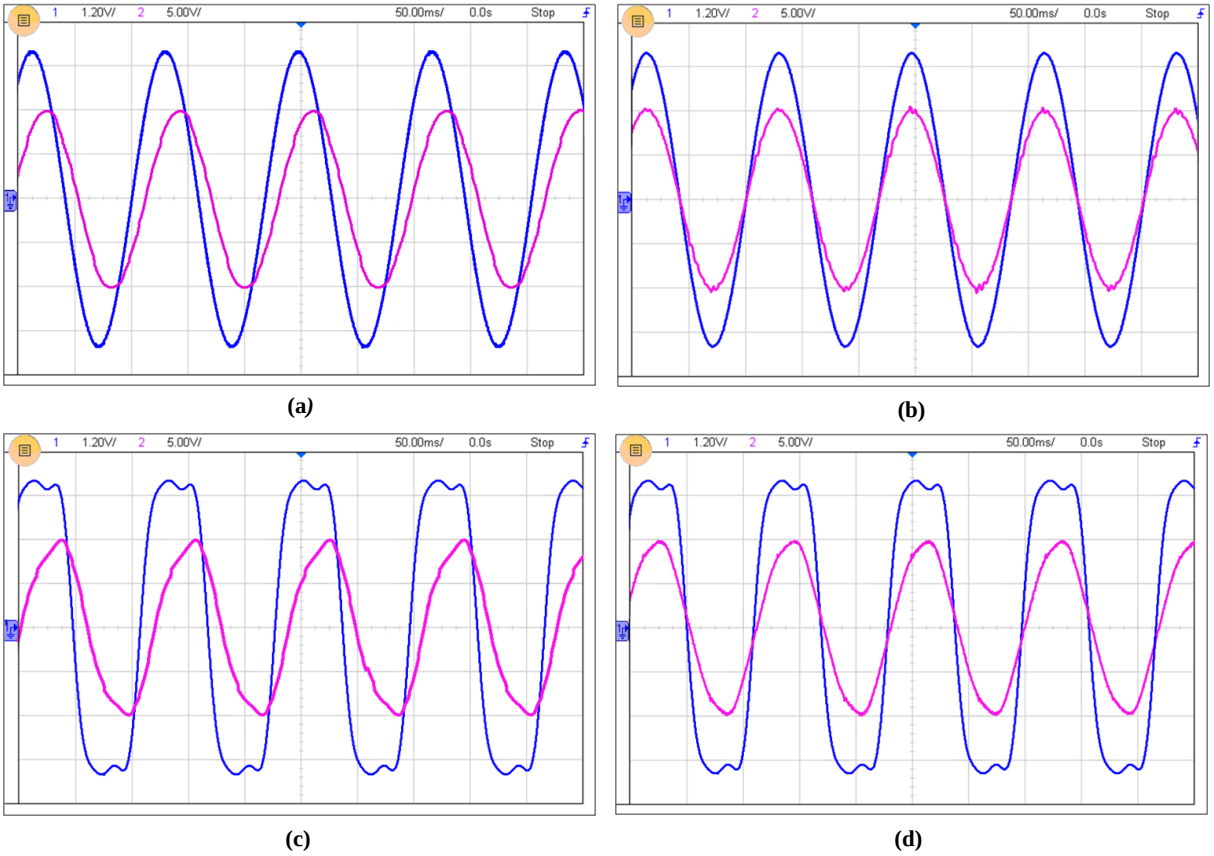

Fig. 4.8 PCC1 Waveforms captured at OPAL-RT analog output module terminal. (a) Phase a voltage and current response using PFs under ideal voltage. (b) Phase a voltage and current response using HAPF under ideal voltage. (c) Phase a voltage and current response using PFs under non-ideal voltage. (d) Phase a voltage and current response using HAPF under non-ideal voltage

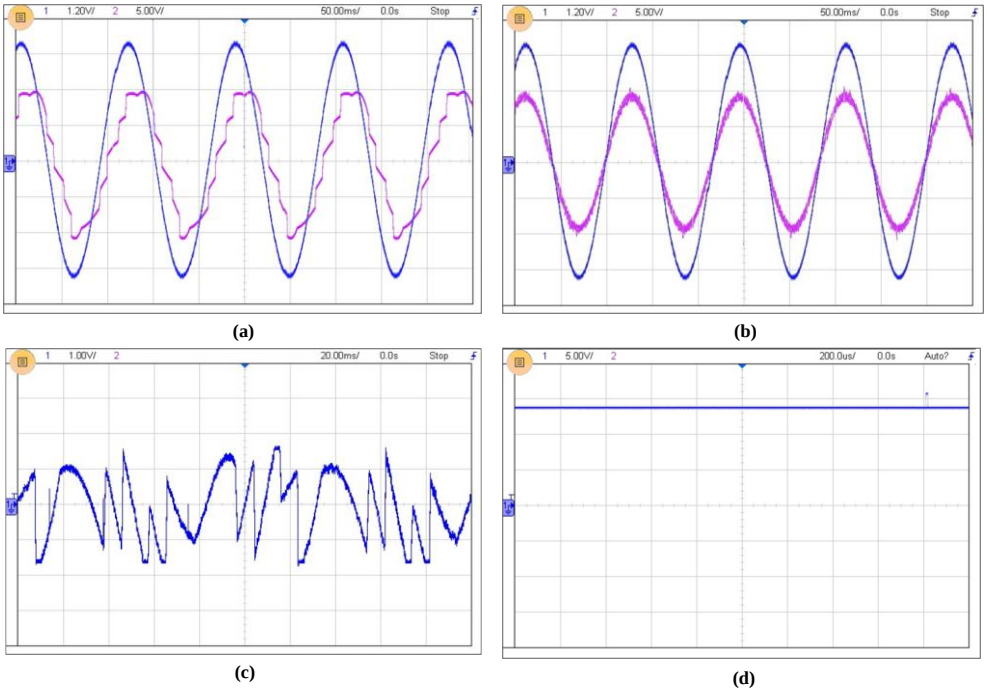

Fig. 4.9 PCC2 Waveforms under ideal voltage captured at OPAL-RT analog output module terminal (a) Phase a voltage and current response using PFs. (b) Phase a voltage and current response using HAPF. (c) Phase a reference current generated by CPT. (d) DC-link voltage

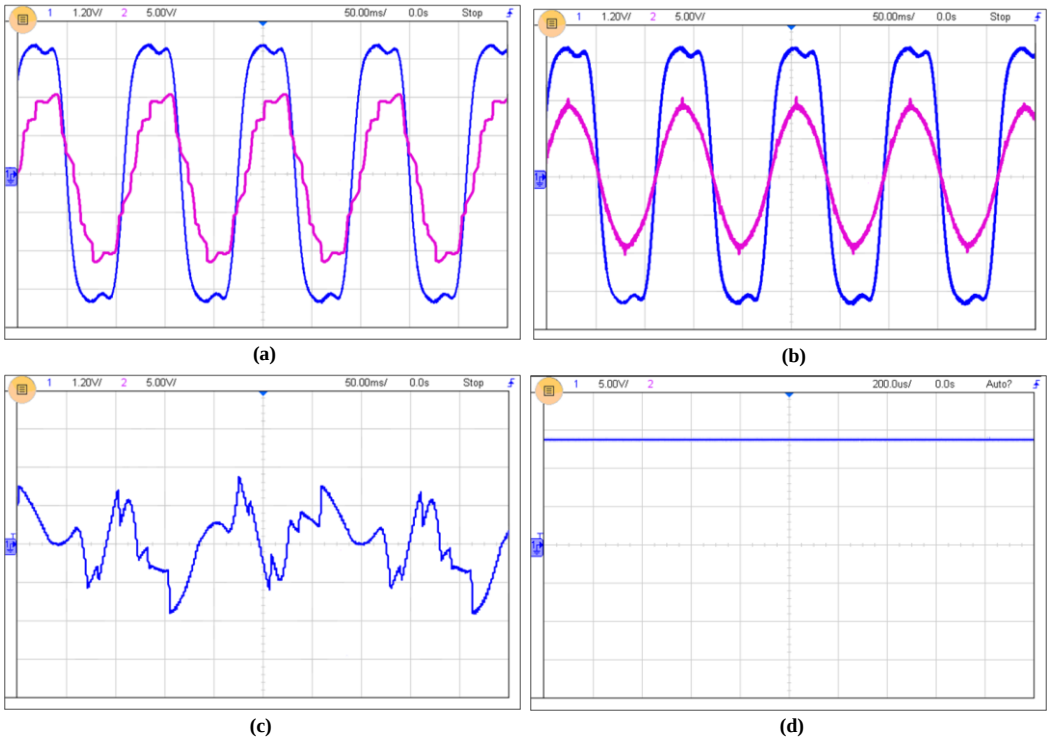

Fig. 4.10 PCC2 Waveforms under non-ideal voltage condition captured at OPAL-RT analog output module terminal (a) Phase a voltage and current response using PFs. (b) Phase a voltage and current response using HAPF. (c) Phase a reference current generated by CPT. (d) DC-link voltage

4.7 Results and Discussion

The summary of the real-time results such as displacement power factor (DPF), load current %THD and unbalance at PCC1 and PCC2 of the industrial power system under ideal and non-ideal voltage conditions with PFs and CPT based HAPF are tabulated in Table 4.4. Based on the above results it is evident that the HAPF with Type-II current controller using CPT enhances the system performance under ideal and non-ideal voltage conditions. The real-time results demonstrate the effectiveness of the HAPF performance in the industrial power system.

Table 4.3 Harmonic FFT analysis at PCC1 and PCC2 with PFs and CPT based HAPF

	PFs				**HAPF**			
	Ideal voltage		**Non-ideal voltage**		**Ideal voltage**		**Non-ideal voltage**	
Harmonic order	%Ipcc1	%Ipcc2	%Ipcc1	%Ipcc2	%Ipcc1	%Ipcc2	%Ipcc1	%Ipcc2
1	100	100	100	100	100	100	100	100
3	0.05	0.19	3.28	3.56	0.02	0.05	2.70	2.11
5	0.73	2.98	3.75	6.23	0.11	0.34	2.10	1.77
7	1.10	4.79	1.98	6.84	0.17	0.48	0.13	0.44
9	0.02	0.10	0.04	0.12	0.03	0.08	0.03	0.12
11	0.53	2.06	0.63	2.17	0.21	0.53	0.14	0.48
13	0.33	1.30	0.13	0.47	0.22	0.52	0.11	0.37
17	0.65	2.58	0.82	2.81	0.30	0.61	0.18	0.62
19	0.39	1.54	0.54	1.86	0.34	0.45	0.11	0.38
%THD	2.17	8.88	5.68	11.68	1.39	2.49	3.82	3.73

Table 4.4 Summary of the real time results

PCC	**Parameters**	**Ideal voltage**		**Non-ideal voltage**	
		PFs	**HAPF**	**PFs**	**HAPF**
1	Load current % THD	2.17	1.39	5.68	3.82
	DPF	0.78	1.00	0.76	0.91
2	Load current % THD	8.88	2.49	11.68	3.73
	DPF	0.86	1.00	0.88	1.00
	Load current % unbalance	8.10	1.20	5.69	1.8

4.8 Conclusions

An active power filter (APF) hybridized with PFs has been designed by using the principles of the CPT and Type-II current controller has been used to close the loop. The contributions achieved with this work are how to design the CPT based APF for supporting the existing PFs as HAPF, how to properly design the Type-II current controller for the CPT based HAPF and demonstration of successful compensation results of unbalanced, distorted load current and reactive power compensation. The CPT based HAPF was designed initially with a simulation study and validated in the real-time using OPAL-RT. The results obtained with the hybrid filtering are extremely efficient and demonstrate the best performance for retrofitting an industrial power system. This solution totally removes the harmonics, compensating the distorted current component and also minimises the unbalance and reactive power. The Type-II current controller improves the dynamic behaviour of the HAPF. The HAPF compensates all the remaining harmonics of the PFs. The real-time results justify the performance of the system effectively. Hence, the Type-II current controlled HAPF using CPT improves the behaviour of the system.

Publication

This work is published and referenced below:

O.V.S.R.Varaprasad, A.S.Bubshait, D.V.S.S.Siva Sarma, and M.G.Simões. "**Real-Time Control of Hybrid Active Power Filter using Conservative Power Theory in Industrial Power System**," *IET Power Electronics* 10, no.2, 2017, pp. 196-207.

Chapter 5

Think-Ahead Decision Algorithm for Effective Operation of Conservative Power Theory based Three-phase Multi-functional Grid Connected PV Inverter with Auxiliary Battery Storage System

5.1 Introduction

A conservative power theory (CPT) based two-stage three-phase multifunctional grid-connected Photovoltaic (PV) inverter (MGCPI) with auxiliary battery storage system (BSS) is developed in this chapter. The MGCPI improves the PQ and also injects power at the Point of Common Coupling (PCC). The CPT is used for computing the MGCPI current reference signals during the Active Power Filter (APF) operation mode. An intelligent Think-Ahead Decision (TAD) algorithm is developed to decide the best mode of operation of the MGCPI taking into account the State-of-Charge (SOC) of the BSS and the available power at the solar-PV source. The whole system configuration is modelled using MATLAB/Simulink in order to observe the PQ improvement and active power injection capabilities of the MGCPI with TAD algorithm for unbalanced linear and nonlinear loads.

Further the same configuration is implemented and validated its features using OPAL-RT based OP4500 grid emulator. The percentage THD of individual phase currents, true power factor and unbalanced current are measured for various modes of operation. The results demonstrate the effectiveness of the developed approach for unbalanced nonlinear loads in smart electric grid provisioning harmonic-free electrical power.

5.2 Conservative Power Theory based Two-stage Three-phase MGCPI with Auxiliary BSS Configuration

The detailed configuration of the system covered in this chapter is illustrated in Fig 5.1(a) and the linear and nonlinear loads combinations are depicted in Fig 5.1(b). A three-phase four-wire Low-Voltage Distribution Grid (LVDG) connected with different single phase and three-phase linear and nonlinear loads is considered to evaluate the performance

of CPT based two-stage three-phase MGCPI with Auxiliary BSS coordinated by TAD algorithm. The MGCPI is a three-phase four-leg current controlled two-level voltage source inverter. The MGCPI is built with IGBT switches and connected at PCC.

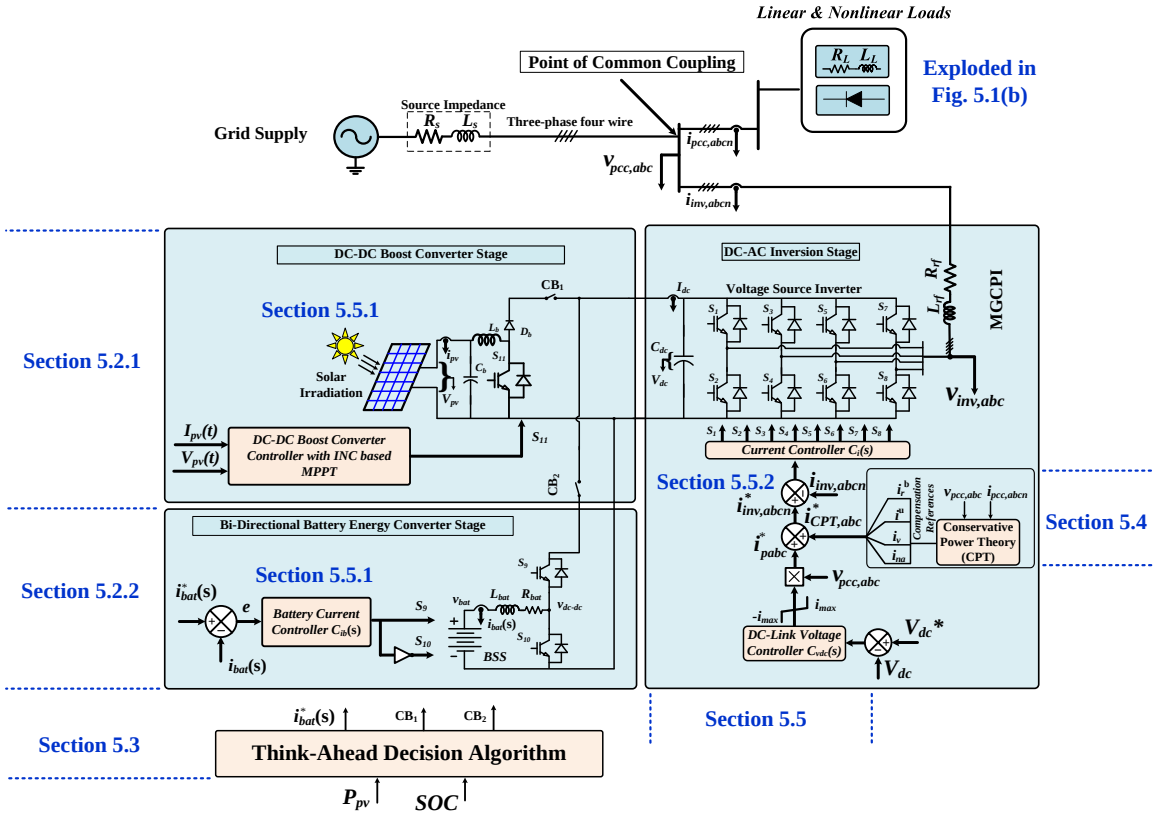

(a)

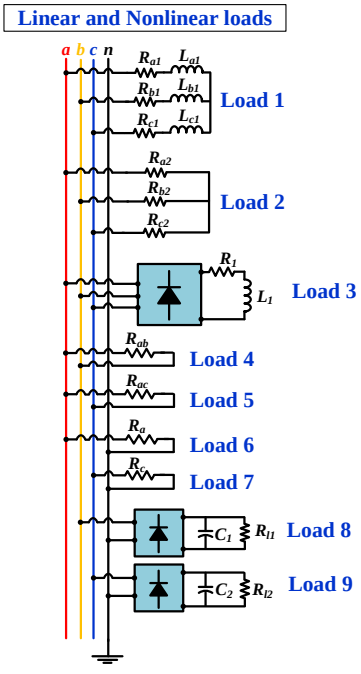

(b)

Fig. 5.1 System Configuration (a) Conservative Power Theory (CPT) and BSS based Three-phase MGCPI with Think-Ahead Decision Algorithm. (b) Linear and Nonlinear loads

The DC-link of the inverter is coupled with PV fed DC-DC boost converter operated by Incremental Conductance (INC) based Maximum Power Point Tracking (MPPT). The PV is designed to deliver a maximum power of 6 kWp. The PV system modeling is described in section 5.2.1. The BSS has a bi-directional DC-DC buck-boost converter to control the bi-directional power flow in order to charge and discharge the BSS. The BSS is rated for 3 kWh. The BSS is discussed in section 5.2.2. The linear and nonlinear loads combinations connected at the PCC are sized as 8 kW as depicted in Fig. 5.1 (b). The system parameters are presented in Table 5.1. The TAD algorithm is explained in section 5.3 in detail.

Table 5.1 Source and load parameters

Parameters	**Values**
Grid supply peak voltage (V_{pabc})	180 V
Grid supply frequency (f)	60 Hz
Source line resistance (R_s)	0.1Ω
Source line inductance (L_s)	0.1mH
Load 1 – resistors (R_{a1}=R_{b1}=R_{c1})	1 Ω
Load 1 – inductors (L_{a1}=L_{b1}=L_{c1})	100 mH
Load 2 – resistors (R_{a2}=R_{b2}=R_{c2})	50 Ω
Load 3 – Three-phase BR side load resistor (R_1)	15 Ω
Load 3 – Three-phase BR side load inductor (L_1)	30 mH
Load 4 – resistor, R_{ab}	130 Ω
Load 5 resistor, R_{ac}	120 Ω
Load 6 resistor, R_a	50 Ω
Load – 10 resistor, R_c	80 Ω
Load 8 – Bridge Rectifier (BR) and load resistor (R_{l1})	200 Ω
Load 8 – BR side load capacitor (C_{l1})	220 µF
Load 9 – BR side load resistor (R_{l2})	300 Ω
Load 9 – BR side load capacitor (C_{l2})	220 µF

The MGCPI parameters are descried in Table 5.2.

Table 5.2 MGCPI parameters

Parameter	**Values**
Ripple filter inductor, (L_{rf})	3mH
Ripple filter resistor (R_{rf})	0.15 Ω
MGCPI DC-link capacitor (C_{dc})	2200μF
MGCPI DC-link voltage (V_{dc})	600 V
Boost converter capacitor (C_b)	100μF
Boost converter inductance (L_b)	3mH
Battery bank rating (Wh)	3 kWh
BSS interfacing Resistance (R_{bat})	0.15 Ω
BSS interfacing inductance (L_{bat})	3mH
MGCPI Switching frequency (f_{sw})	20 kHz
BSS Switching frequency (f_{b_sw})	20 kHz

5.2.1 PV System Modelling

A single diode model is considered as a PV cell for building the PV array in simulation studies [137] as depicted in Fig. 5.2(a). According to the single diode model, the PV output current and power are expressed as follows:

$$I_{pv} = I_{ph} - I_d - I_p \tag{5.1}$$

$$I_{pv} = I_{ph} - I_{sat}\left[exp\left(\frac{q \times \left(V_{pv} + I_{pv}R_{se}\right)}{AkT}\right) - 1\right] - \frac{\left(V_{pv} + I_{pv}R_{se}\right)}{R_p} \tag{5.2}$$

$$P_{pv} = V_{pv}\, I_{pv}. \tag{5.3}$$

The shade-free rooftop space required for the PV installation is considered as 732 sq.ft as per the design procedures discussed in [101]. While building the PV array using a MATLAB/Simulink environment, five series and four parallel SUN POWER SPR-305 WHT PV [138,139] modules were considered to build the PV array, which is capable of generating the 6.1 kWp (kilo-Watt-peak) power using MPPT-controlled DC-DC boost converter. The module specifications are tabulated in Appendix Table A.1. The PV array is designed to deliver a maximum power of 6 kWp with 1000 W/m^2 solar irradiation at 25°C temperature conditions.

Due to the intermittent nature of the solar energy and variation in solar irradiation DC-DC boost converter with MPPT is considered for harvesting the maximum power from PV. The INC-based MPPT technique for the DC-DC boost stage, converters are exploited in this chapter and the INC-based MPPT flow chart is depicted in Fig 5.2(b). Here the control is based on array conductance variation by monitoring the PV voltage and current. The I_{rtpv}-V_{rtpv} and P_{rtpv}-V_{rtpv} characteristics of the PV array concerning the variation of solar irradiation are depicted in Fig 5.2(c).

The mathematical expressions for the INC method are expressed as follows:

$$\frac{dP}{dV} = \frac{d(IV)}{dV} = I + V\frac{dI}{dV} = I + V\frac{\Delta I}{\Delta V} = 0 \tag{5.4}$$

$\frac{\Delta I}{\Delta V} = -\frac{I}{V}$ denotes the condition at MPP (5.5)

$\frac{\Delta I}{\Delta V} > -\frac{I}{V}$ denotes the condition at the left of MPP (5.6)

$\frac{\Delta I}{\Delta V} < -\frac{I}{V}$ denotes the condition at the right of MPP (5.7)

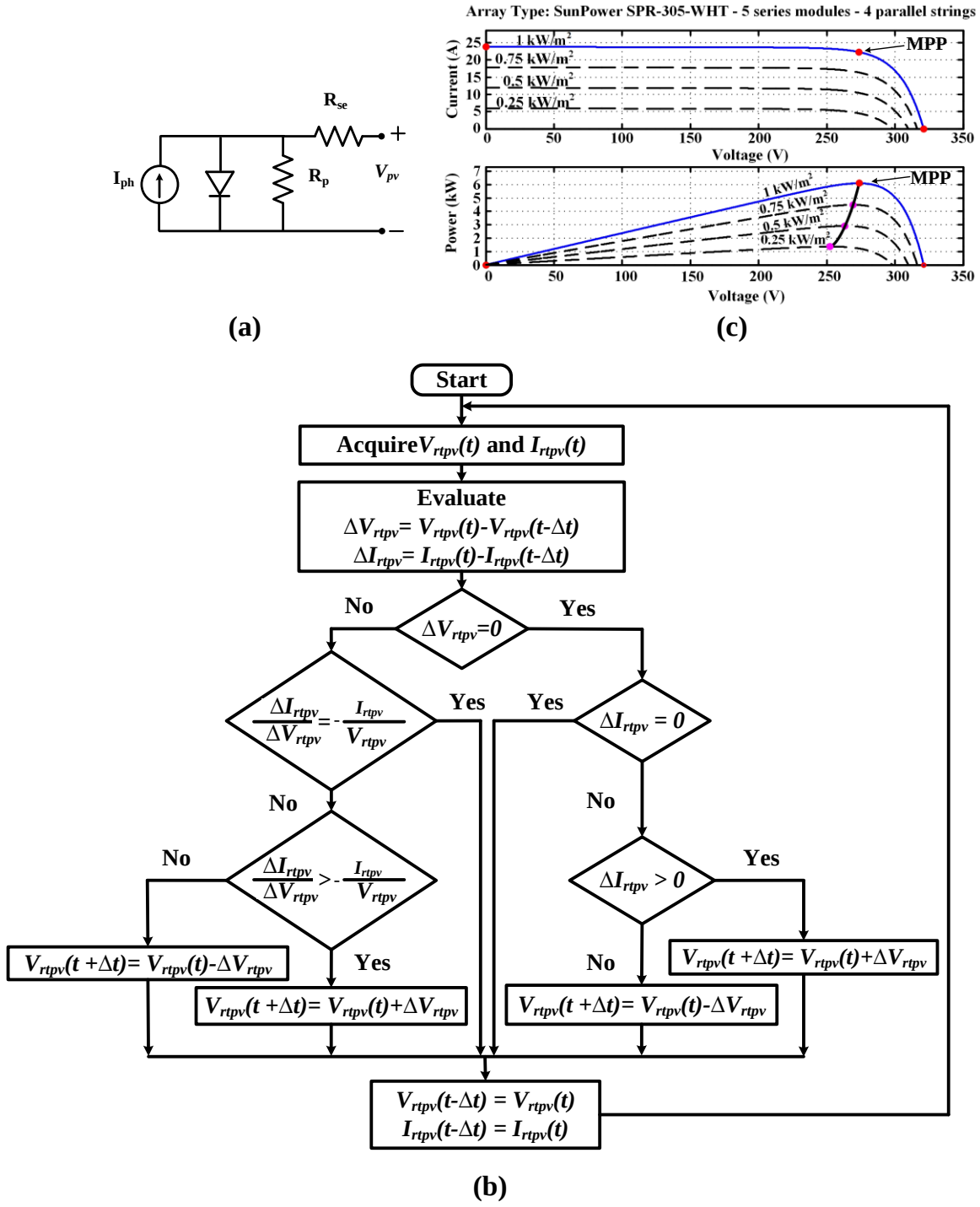

Fig. 5.2 PV system MPPT and characteristics (a) Single diode model of the PV (b) Flow chart of INC-based MPPT algorithm (c) I_{rtpv}-V_{rtpv} and P_{rtpv}-V_{rtpv} characteristics of array at different irradiance with fixed temperature 25^0C

The DC–DC boost converter inductance and the capacitance values are obtained by the following equations.

$$L_b = \frac{V_{mpp} \times D}{\Delta I_{pv} \times f_{sw\_b}} \tag{5.8}$$

$$C_{pv} = \frac{I_{dc} \times D}{\Delta V_{dc} \times f_{sw\_b}} \tag{5.9}$$

The DC-link capacitor (C_{dc}) is designed by the following equation:

$$C_{dc} = \frac{P_{pv}}{2\pi f \times V_{dc} \times V_{ripple}} \tag{5.10}$$

The PV current ripple and the DC-link voltage ripples are considered to be 1% and 10%, respectively as per the design procedure described in [132].

5.2.2 BSS Modelling

The battery model presented in [140] is considered here to build the BSS and is depicted in Fig. 5.3.

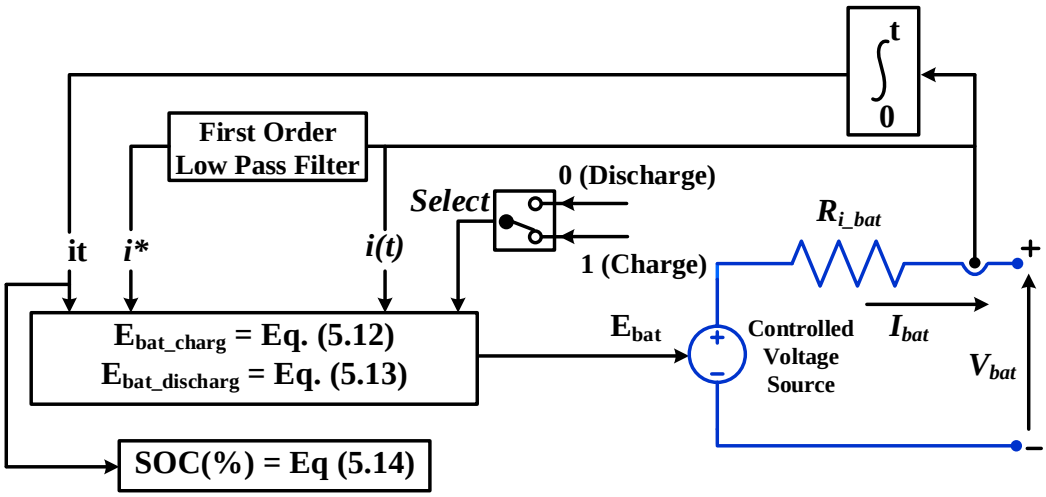

Fig. 5.3 Battery Model used to build the BSS

The mathematical representation of the battery voltage is given by

$$V_{bat} = E_{bat} - R_{i\_bat} I_{bat} \tag{5.11}$$

Where,

V_{bat} = Battery voltage in V.

E_{bat} = No load voltage in V.

I_{bat} = Battery current in A.

R_{i_bat} = Internal resistance of the battery in Ohms.

The no-load battery voltage under charging and discharging is based on the battery extracted capacity, battery current and hysteresis phenomenon of the battery charge and discharge cycles. The charge and discharge voltage is expressed as follows

$$E_{bat\_char} = E_0 - K\frac{Q}{|it| + 0.1 \times Q}i^* - K\frac{Q}{Q - it}it + A.\exp(-B.it) \quad (5.12)$$

$$E_{bat\_dischar} = E_0 - K\frac{Q}{Q - it}i^* - K\frac{Q}{Q - it}it + A.\exp(-B.it) \quad (5.13)$$

Where

E_0 = Constant voltage in V.

K = Polarization constant, in V/Ah. or Polarization resistance, in Ohms.

i = Battery current in A.

i^* = Low-frequency current dynamics, in A.

it = Extracted capacity in Ah.

Q = Maximum battery capacity in Ah.

A = Exponential voltage, in V.

B = Exponential capacity, in Ah

The battery SOC (%) is expressed as follows

$$SOC(\%) = 100\left(1 - \frac{\int idt}{Q}\right) \quad (5.14)$$

5.3 Think-Ahead Decision (TAD) Algorithm

A TAD algorithm coordinates the multifunctional operation of the MGCPI and is intended to perform the grid interactive operation in order to reduce the grid consumption to minimize the electricity tariff as well as to improve the power quality. The PV power and the SOC (%) of the BSS are computed for appropriate operation of CB1 and CB2. The PV power is acquired from the PV using INC based MPPT. The BSS SOC (%) is calculated by using the equation (5.14) described in section 5.2.2. The developed TAD algorithm is simple and easy to implement in the real-time system to coordinate the multifunctional operations smoothly and effectively and is illustrated in Fig. 5.4.

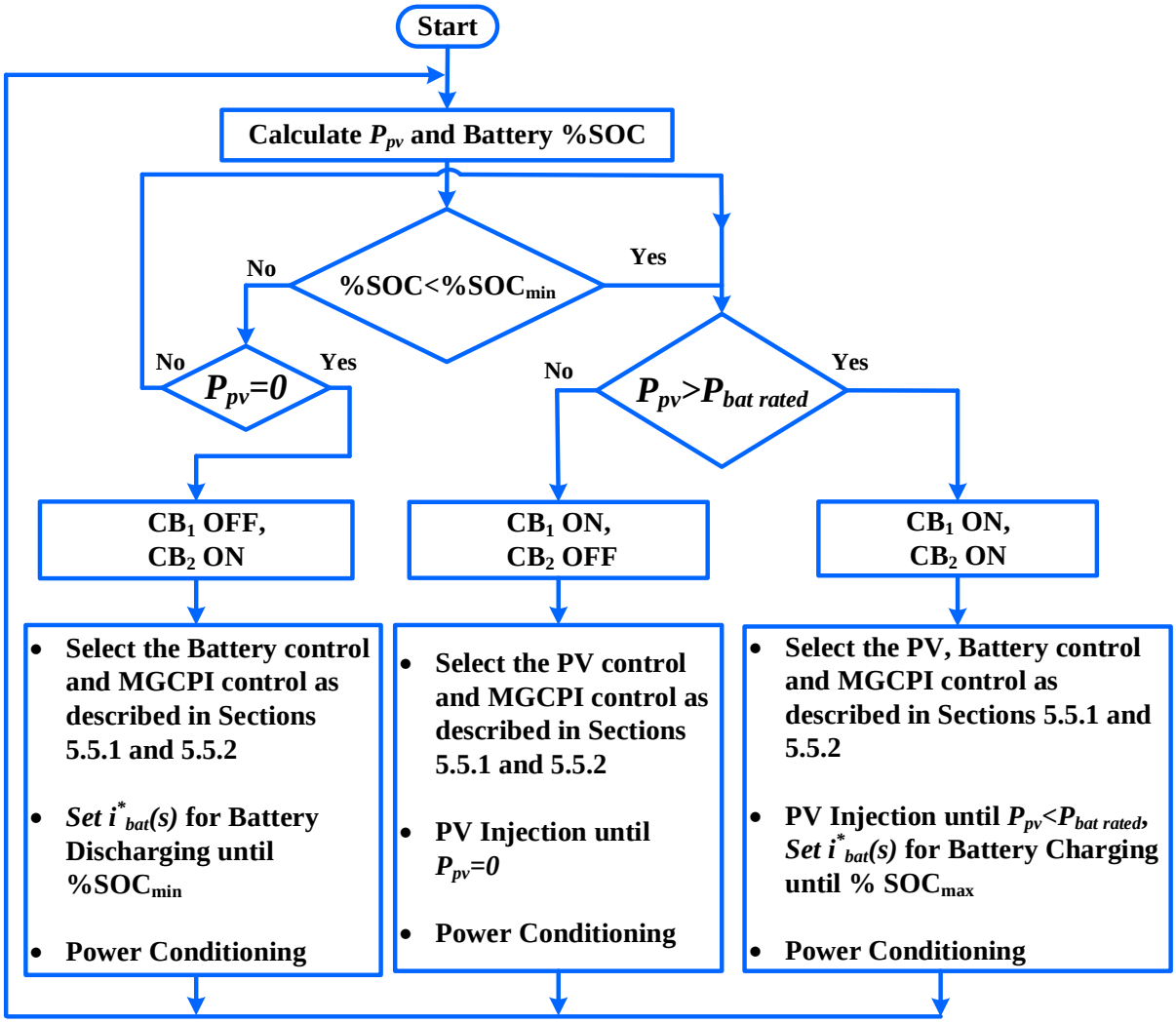

Fig. 5.4 Think-ahead decision algorithm to choose the MGCPI current reference and to coordinate the power injection and power conditioning

The detailed step by step procedure of the TAD algorithm is described below to maintain the power balance and constant DC voltage at the DC-link of the MGCPI.

TAD algorithm:

Step 1:
- Estimate PV power and BSS SOC (%).
- Set maximum and minimum values of the BSS SOC (%) to decide charging or discharging of BSS.

Step 2:
- Check if estimated BSS SOC (%) value is less than BSS SOC (%) minimum value.
- If BSS SOC (%) value is less than the minimum value, proceed to step 3, otherwise, go to step 4.

Step 3:
- Check if PV power is greater than battery rated power.
- If PV power is greater than the battery rated power, then CB_1 and CB_2 are turned ON. In this case, MGCPI activates and injects power, charges battery and acts as a power conditioner simultaneously.
- PCC voltage and current are measured and fed to the CPT block to computes the current compensation reference for MGCPI for effective power conditioning.
- Sets the reference battery current value of BSS controller to charge.
- Go to step 1.

Step 4:
- If PV power is less than the battery rated power, CB_1 is turned on and CB_2 is turned off , the inverter injects active Power and acts as a Power conditioner.

Step 5:
- If BSS SOC (%) value is greater than the BSS SOC (%) minimum value, and checks availability of the PV power. If PV power is available, go to step 3.

Step 6:
- If PV power is absent, CB_1 is turned OFF and CB_2 is turned ON, then the inverter injects active power from the BSS and acts as a Power conditioner.
- Go to step 1.

The performance of the TAD algorithm on the MGCPI configuration as described in section 5.2 is demonstrated by using MATLAB/Simulink based simulation in section 5.6 and validated through OPAL-RT based grid emulator based real-time studies. The mode of operations performed by the MGCPI complies with IEEE 929-2000, IEEE 1547a-2018, IEC 61727 standards.

5.4 Conservative Power Theory frame work

CPT is used in MGCPI exactly in the same manner as it is used for HAPF as described in section 4.3.

The current components are decomposed into the active current, reactive current and void current [19-21]. The active current representation from the CPT definition is as:

$$i_{am} = \frac{\langle v_m, i_m \rangle}{\|v_m\|^2} v_m \tag{5.15}$$

where v_m and i_m are the m phase voltage and current. The reactive current is expressed as:

$$i_{rm} = \frac{\langle \hat{v}_m, i_m \rangle}{\|\hat{v}_m\|^2} \hat{v}_m \tag{5.16}$$

where $\hat{v}_m$ represents the unbiased time integral of the m-phase voltage. The void current is obtained as

$$\underline{i}_{vm} = \underline{i}_m - \underline{i}_{am} - \underline{i}_{rm} \tag{5.17}$$

The balanced and unbalanced current components are derived by using the active and reactive phase currents as given below, where the balanced active current is written as

$$\underline{i}^b_{am} = \frac{\langle \underline{v}, \underline{i} \rangle}{\|\underline{v}\|^2} \underline{v}_m \tag{5.18}$$

The balanced reactive current is given as

$$\underline{i}^b_{rm} = \frac{\langle \underline{\hat{v}}, \underline{i} \rangle}{\|\underline{\hat{v}}\|^2} \underline{\hat{v}}_m \tag{5.19}$$

The unbalanced active current is represented as

$$i^u_{am} = i_{am} - i^b_{am} \rightarrow i^u_{an} \tag{5.20}$$

The unbalanced reactive current is expressed as

$$i^u_{rm} = i_{rm} - i^b_{rm} \rightarrow i^u_{rn} \tag{5.21}$$

The complete reference current using CPT concept is obtained by adding the active and reactive balanced currents, active and reactive unbalanced currents and void current as given below

$$i^*_{CPT} = \underline{i}^b_a + \underline{i}^b_r + \underline{i}^u_a + \underline{i}^u_r + i_v \tag{5.22}$$

The CPT reference currents are used by the current controller to make the MGCPI improves the PQ at the PCC.

5.5 Control Methodologies

The control methodologies of the DC-DC boost converter control with INC based MPPT and BSS, MGCPI are described in the following subsections.

5.5.1 DC-DC Boost Converter and BSS Control methodology

The PV is connected to a DC-DC boost converter to supply the required regulated DC-link voltage to the MGCPI. The boost stage DC-DC converter will amplify the PV array voltage to rated DC-link voltage; simultaneously, it will inject the PV power. The duty cycle (*D*) of the MPPT algorithm for boost operation is computed by using the following expressions:

$$V_{dc} = \frac{V_{rtpv}}{(1-D)} \tag{5.23}$$

$$D = 1 - \left(\frac{V_{rtpv}}{V_{dc}}\right) \tag{5.24}$$

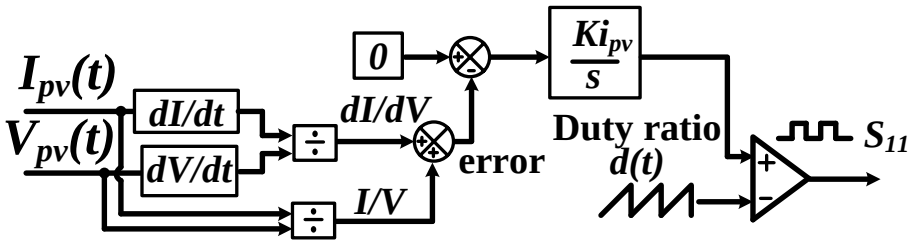

Fig. 5.5 Block diagram of DC-DC converter control loop

The duty cycle to trigger the boost converter is computed according to the INC MPPT algorithm. The DC-DC boost converter control is based on array conductance variation by monitoring the PV voltage and current as depicted in Fig 5.5 using INC based MPPT. An integral-control is used to minimize the conductance error between actual and incremental conductance values and to condense the steady-state ripple oscillations. The output of the integral controller is compared with a saw-tooth wave to produce the switching pulses to the DC-DC boost converter.

The detailed block diagram of the proposed current controller for regulating the BSS current at its reference signals is illustrated in Fig. 5.6.

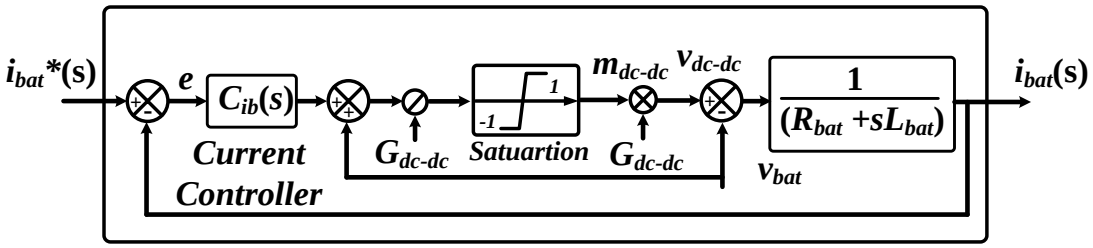

Fig. 5.6 Block diagram of the BSS current control loop

The BSS current dynamics are illustrated by (5.25).

$$L_{bat}\frac{di_{bat}(t)}{dt} + R_{bat}i_{bat}(t) = v_{dc-dc}(t) - v_{bat}(t) \tag{5.25}$$

In (5.25), $i_{bat}(t)$ denotes the state variable, $v_{dc-dc}(t)$ represents the control input, and $v_{bat}(t)$ represents the disturbance input. From (5.26), the BSS control input $v_{dc-dc}(t)$ is proportional to the modulating signal $m_{dc-dc}(t)$.

$$v_{dc-dc}(t) = G_{dc-dc}\, m_{dc-dc}(t) = (V_{dc})m_{dc-dc}(t) \tag{5.26}$$

The last term in (5.25), $v_{bat}(t)$ is mitigated by the feed-forward action. In order to compensate for the dynamic coupling between the BSS and the battery voltage feed-forward compensation is adopted. The transfer function of the battery output filter $G_{bat\_i}(s)$, is expressed as follows:

$$G_{bat\_i}(s) = \frac{i_{bat}(s)}{v_{bat}(s)} = \frac{1}{R_{bat} + sL_{bat}} \tag{5.27}$$

The BSS OLTF is represented in (5.28), where $C_{ib}(s)$ is a PI compensator as given in (5.29)

$$G_{oi\_bat}(s) = G_{bat\_i}(s)C_{ib}(s) \tag{5.28}$$

$$C_{ib}(s) = k_{pb}\left(\frac{sT_b + 1}{sT_b}\right) \tag{5.29}$$

The current controller design parameters are based on the classical frequency response analysis method and are tabulated in Table 5.3.

Table 5.3 BSS current control system parameters

Symbol	Quantity	Values
φ_{PMib}	Desired Phase Margin	90^o
f_{cib}	Desired cut-off frequency	2kHz

The BSS controller parameters are derived as follows:

$$G_{cib} = -|G_{bat-i}(f_{cib})|\ dB = 31.52\ dB = 37.7 \tag{5.30}$$

$$\varphi_{cib} = \varphi_{PMib} - \angle G_{bat_i}(f_{cib}) - 180° = -0.22° \tag{5.31}$$

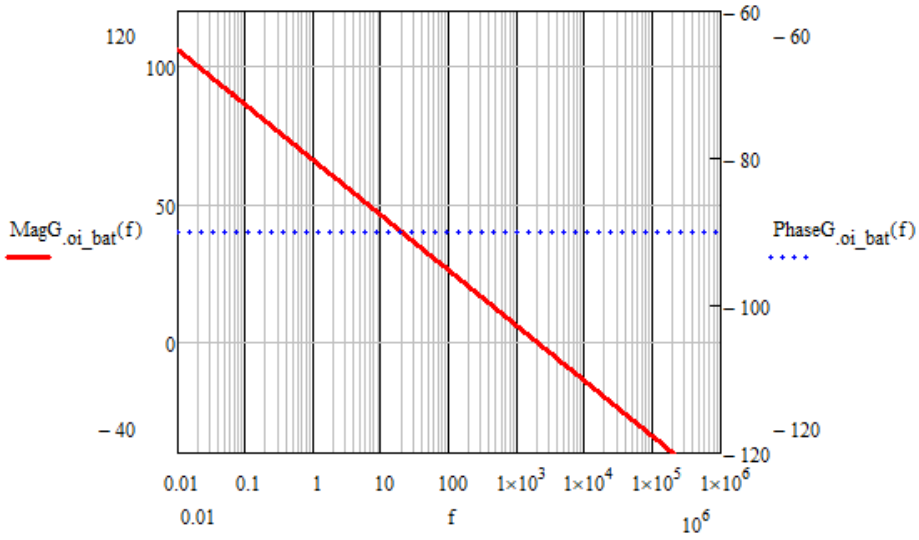

Fig. 5.7 Bode plot of the battery current OLTF

As a result, battery current controller parameters are determined by (5.32) and (5.33).

$$T_b = \frac{\tan(\varphi_{cib} + 90°)}{2\pi f_{cib}} = 20\ ms \tag{5.32}$$

$$k_{pb} = \sqrt{\frac{{G_{cib}}^2}{\frac{T^{-2} + (2\pi f_{cib})^2}{(2\pi f_{cib})^2}}} = 37.7 \tag{5.33}$$

Fig. 5.7 depicts the Bode plot of the BSS current controller OLTF. The OLG of 0 dB and the PM of 90^o are achieved at the cross-over frequency $f_{cib} = 2\ kHz$.

5.5.2 MGCPI Control Methodology

The MGCPI controller consists of two feedback control loops, as depicted in Fig 5.1(a). The first loop is an inner loop related to current control, and the outer loop is a voltage control loop. The inner loop is faster than the outer loop. The detailed block diagram of the proposed current controller for regulating the MGCPI current at its reference signals is illustrated in Fig. 5.8.

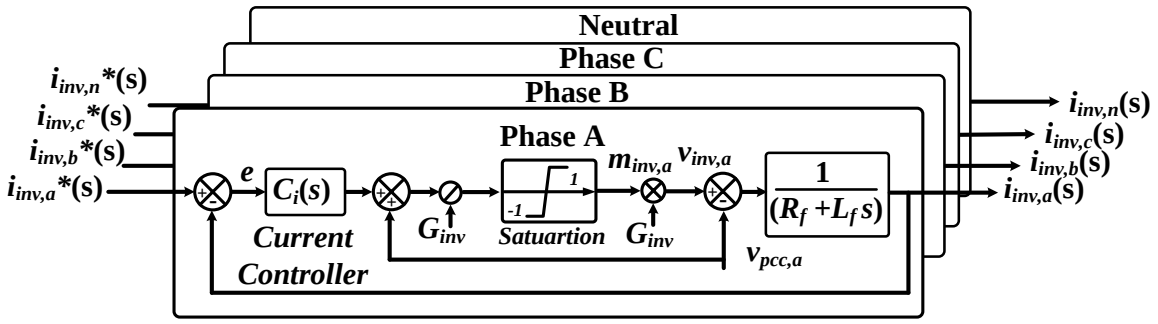

Fig. 5.8 Simplified diagram of the MGCPI current control loop

The current controller is designed in a stationary frame with classical frequency domain analysis method accompanied by the fast dynamic response in reference current tracking generated by CPT. The differential equation which describes the MGCPI current dynamics is illustrated in (5.34).

$$L_f \frac{di_{inv,abcn}(t)}{dt} + R_f i_{inv,abcn}(t) = v_{inv,abcn}(t) - v_{pcc,abcn}(t) \tag{5.34}$$

Where $i_{inv,abcn}(t)$ denotes the state variables, $v_{inv,abcn}(t)$ represents the control inputs, and $v_{pcc,abcn}(t)$ represents the disturbance inputs. From (5.35), the MGCPI control inputs $v_{inv,abcn}(t)$ are controlled by the modulating signal $m_{inv,abcn}(t)$.

$$v_{inv,abcn}(t) = G_{inv}\, m_{inv,abcn}(t) = \left(\frac{V_{dc}}{2}\right) m_{inv,abcn}(t) \tag{5.35}$$

The last term in (5.34) i.e. $v_{pcc,abcn}(t)$ can be eliminated by a feed-forward action. The voltage feed-forward compensation method is used to diminish the dynamic coupling among the MGCPI and the AC LVDG, which will enhance the disturbance elimination capability of the MGCPI. By employing the perturbation & linearization method and applying the Laplace transformation, the transfer function of the MGCPI output filter $G_{inv\_i}(s)$, is expressed in (5.36).

$$G_{inv\_i}(s) = \frac{i_{inv,abcn}(s)}{v_{inv,abcn}(s)} = \frac{1}{R_f + sL_f} \tag{5.36}$$

The open-loop transfer function (OLTF) $G_{oi\_inv}(s)$ of the inverter is presented in (5.37), where $C_i(s)$ is the current controller representing a proportional-integral (PI) compensator as given in (5.38):

$$G_{oi\_inv}(s) = G_{inv\_i}(s) C_i(s) \tag{5.37}$$

$$C_i(s) = k_{pc}\left(\frac{sT_c + 1}{sT_c}\right) \tag{5.38}$$

In (5.38) k_{pc} represents the proportional gain, T_c describes the time constant of the current controller. In order to limit the current control loop reaction to the switching noises, the bandwidth of the current controller is considered as one-tenth of the MGCPI switching frequency to accomplish fast dynamic behavior. The current controller design parameters obtained using classical frequency analysis is depicted in Table 5.4.

Table 5.4 MGCPI current control system parameters

Symbol	Quantity	Values
φ_{PMi}	Desired Phase Margin	60º
f_{ci}	Desired cut-off frequency	2 kHz

The current controller parameters such as the gain and the phase values for PI compensator are obtained according to (5.39) and (5.40), respectively.

$$G_{ci} = -|G_{inv-i}(f_{ci})|\ dB = 31.52\ dB = 37.7 \tag{5.39}$$

$$\varphi_{ci} = \varphi_{PMi} - \angle G_{inv-i}(f_{ci}) - 180° = -30.22° \tag{5.40}$$

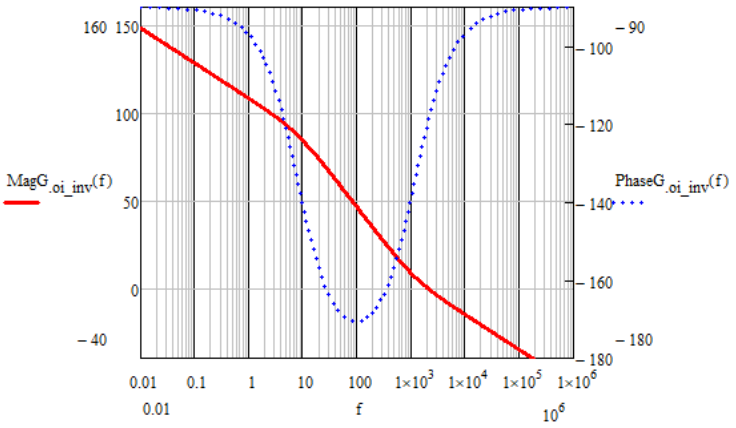

Fig. 5.9 Bode plot of the MGCPI current controller OLTF

As a result, current controller parameters are determined by (5.41) and (5.42), respectively.

$$T_{ci} = \frac{\tan(\varphi_{ci} + 90°)}{2\pi f_{ci}} = 0.13\ ms \tag{5.41}$$

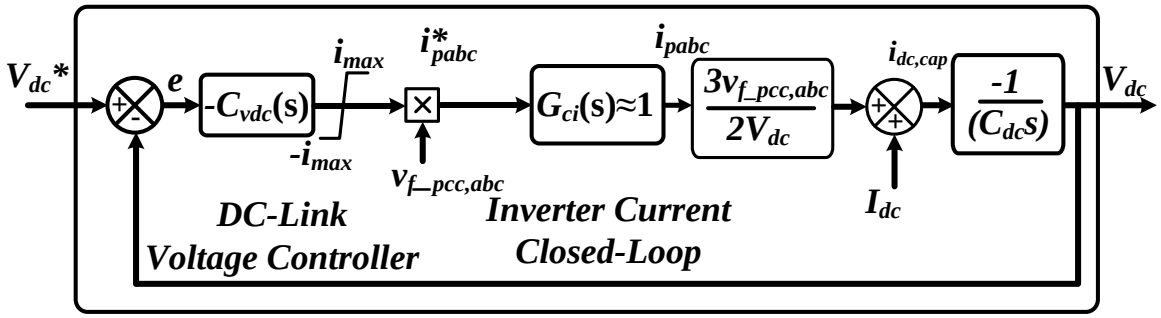

Fig. 5.10 Schematic of the DC-link voltage control loop

$$k_{pc\_i} = \sqrt{\frac{{G_{ci}}^2}{\frac{T^{-2} + (2\pi f_{ci})^2}{(2\pi f_{ci})^2}}} = 32.57 \tag{5.42}$$

Fig. 5.9 depicts the bode plot of the current controller OLTF. The open-loop gain (OLG) and the phase margin (PM) achieved at the cross-over frequency $f_{ci} = 2\ kHz$ are 0dB and 60^o respectively.

The MGCPI output current behavior is illustrated by (5.43). From which it is clear that the output current of the MGCPI is dependent on the reference current. Consequently, with the feed-forward compensation method, the MGCPI is analogous to a self-regulating current source observed by the distribution system.

$$i_{inv,abcn}(s) = \frac{C_i(s)}{L_f s + R_f + C_i(s)} i^*_{inv,abcn}(s). \tag{5.43}$$

The reference active current (i_{pabc}), obtained from the MGCPI current controller is utilized to active power injection, which is harvested from the PV or BSS through the MGCPI. The reference active current signal is derived from the sensed fundamental PCC voltage component ($v_{f\_pcc,abc}$), constituting sinusoidal current. Hence, the active current component is a pure sinusoidal current, which is in phase with the PCC voltage fundamental component. The MGCPI DC-link voltage controller is designed by deriving the transfer function in between the DC-link voltage and the reference active current. The expression for MGCPI power balance is given below

$$P_{ac} + P_{PV+bat} + P_{cap} = 0. \tag{5.44}$$

$$\frac{3}{2} v_{f\_pcc,abc} i_{pabc} + V_{dc} I_{dc} + V_{dc} i_{dc,cap} = 0 \tag{5.45}$$

The V_{dc} is the regulated DC-link voltage for the MGCPI, $i_{dc,cap}$ is the capacitor current of the DC-link and factor 3/2 derived from the average ac power using its peak values. The DC-link capacitor current is expressed as given below:

$$i_{dc,cap} = C_{dc}\frac{dV_{dc}}{dt} = -\left(\frac{3v_{f\_pcc,abc}i_{pabc}}{2V_{dc}} + I_{dc}\right) \tag{5.46}$$

After rearranging the (5.46)

$$\frac{dV_{dc}}{dt} = -\frac{1}{C_{dc}}\left(\frac{3v_{f\_pcc,abc}i_{pabc}}{2V_{dc}} + I_{dc}\right) \tag{5.47}$$

In (5.47), the DC-link voltage regulation is taken care by the active current (i_{pabc}). The block diagram of the DC-link voltage control methodology is depicted in Fig. 5.10. In order to deal with the negative sign of the DC-link voltage dynamics, the DC-link voltage controller $C_{vdc}(s)$ is multiplied by -1. The DC-link voltage control scheme transfer function $G_{vdc}(s)$, is illustrated in (5.48). The DC-link voltage control loop OLTF, $G_{ovdc}(s)$, is depicted in (5.49) with the DC-link voltage controller $C_{vdc}(s)$. The bandwidth of the DC-link voltage control loop is selected to be less than two orders of amplitude lesser than that of the current control loop.

Consequently, the MGCPI current controller loop can be supposed ideal for the DC-link voltage controller design purposes. Hence it is replaced by unity. A PI compensator is chosen for $C_{vdc}(s)$ as described in (5.50) for MGCPI DC-link voltage tracking.

$$G_{vdc}(s) = \frac{3\ {v_{f\_pcc,abc}}^2}{2V_{dc}}\frac{1}{C_{dc}s} \tag{5.48}$$

$$G_{ovdc}(s) = G_{vdc}(s)C_{vdc}(s) \tag{5.49}$$

$$C_{vdc}(s) = k_{pvdc}\left(\frac{sT_{vdc}+1}{sT_{vdc}}\right) \tag{5.50}$$

The DC link voltage controller design parameters are tabulated in Table 5.5.

Table 5.5 MGCPI voltage control system parameters

Symbol	Quantity	Values
φ_{PMvdc}	Desired Phase Margin	60^o
f_{cvdc}	Desired cut-off frequency	6Hz

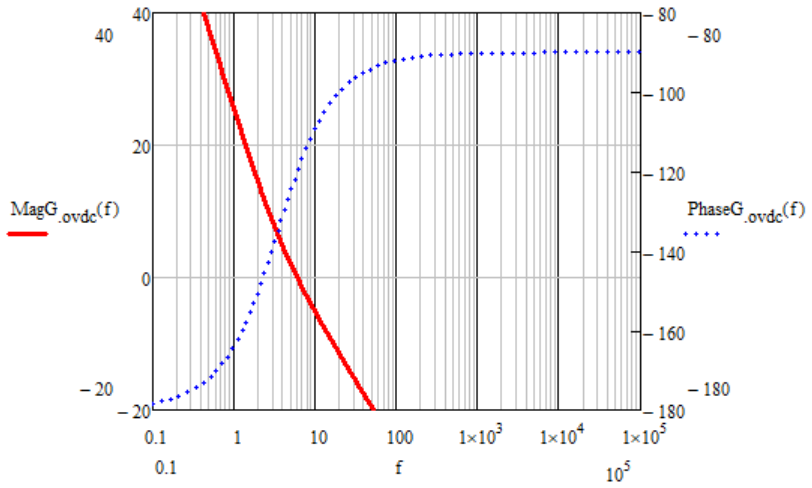

Fig. 5.11 Bode plot of the DC-link voltage controller OLTF

Fig. 5.11 shows the DC-link voltage controller open-loop frequency response where the OLG of 0 dB and the PM of 60^0 are attained at the crossover frequency.

While designing the DC-link voltage controller parameters the gain and the phase values for PI compensator are attained according to (5.51) and (5.52), respectively.

$$G_{cvdc} = -|G_{vdc-i}(f_{cvdc})|\ dB = -115.35\ dB = 1.7\ \times\ 10^{-6} \tag{5.51}$$

$$\varphi_{cvdc} = \varphi_{PMvdc} - \angle G_{vdc}(f_{cvdc}) - 180° = -30° \tag{5.52}$$

As a result, current controller parameters are derived by (5.53) and (5.54), respectively.

$$T_{vdc} = \frac{\tan(\varphi_{cvdc} + 90°)}{2\pi f_{cvdc}} = 45.9\ ms \tag{5.53}$$

$$k_{pvdc} = \sqrt{\frac{{G_{cvdc}}^2}{\frac{T^{-2} + (2\pi f_{cvdc})^2}{(2\pi f_{cvdc})^2}}} = 1.47\ \times\ 10^{-6} \tag{5.54}$$

5.6 Simulation Results

System configuration as described in section 5.2 with system parameters **and** illustrated in table 5.1 is modelled in MATLAB/Simulink 2013. The operation of the three-phase MGCPI is demonstrated for the following five modes:

- Mode 1: MGCPI is OFF, then there is no power injection and power conditioning. This mode exhibits the behaviour of the linear and nonlinear loads connected to the LVDG.
- Mode 2: MGCPI is ON, then the inverter injects active power and acts as a power conditioner. This mode illustrates the power injection and power conditioning functionality of the MGCPI under low irradiation.

- Mode 3: MGCPI is ON, with power injection, power conditioning and battery charging. This mode demonstrates the power injection, power conditioning and battery charging functionality of the MGCPI under full irradiation.
- Mode 4: MGCPI is ON, with power injection using BSS and selective compensation. This mode demonstrates the power injection through battery and the selective compensation features of CPT by selecting the active, reactive and void current references under full irradiation.
- Mode 5: MGCPI is ON, with power injection and power conditioning under dynamic Load change. This mode illustrates the dynamic behaviour of power injection and power conditioning under load variation.

5.6.1 Mode 1: MGCPI OFF, with No Power Injection or Power Conditioning

The system behaviour is observed under No compensation at PCC with MGCPI OFF position. Due to the effect of nonlinear and unbalanced loads the grid is polluted by current harmonics, phase current unbalances, reactive power and neutral current are illustrated in Fig. 5.12, where Fig. 5.12(a) shows the three-phase voltages at PCC, Fig. 5.12 (b) shows the three-phase currents at the PCC indicates evidence of harmonics, Fig. 5.12(c) depicts neutral current at PCC. Fig. 5.12 (d) illustrates the power consumption at PCC. It is necessary to compensate these issues for the safe, reliable working of the distribution system and the neighbouring loads.

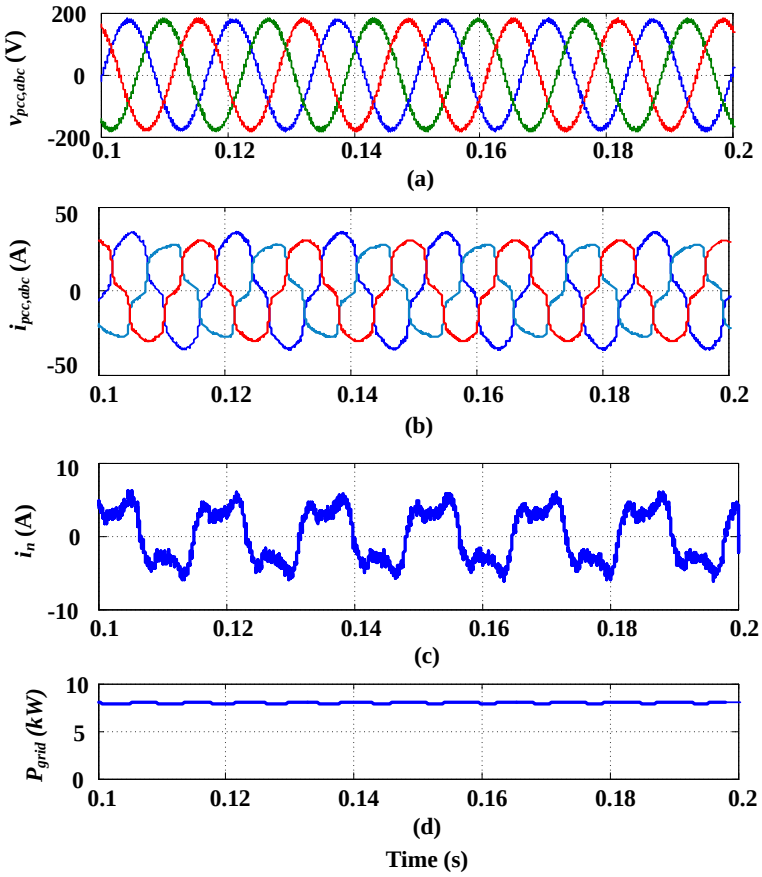

Fig. 5.12 No compensation case (a) Three-phase voltages at PCC (b) Three-phase currents at PCC (c) Neutral current at PCC (d) grid power

5.6.2 MGCPI is ON with Power Conditioning and Power Injection Mode

The MGCPI is turned ON to compensate the PQ issues and also to inject the active power to reduce the grid consumption. The power injection is dependent on solar irradiation. When the irradiation is low and the generated PV power is less than the BSS rated power per hour then the system harvested active power feeds the loads and the MGCPI performs the power conditioning as discussed in the TAD algorithm in Fig 5.4.

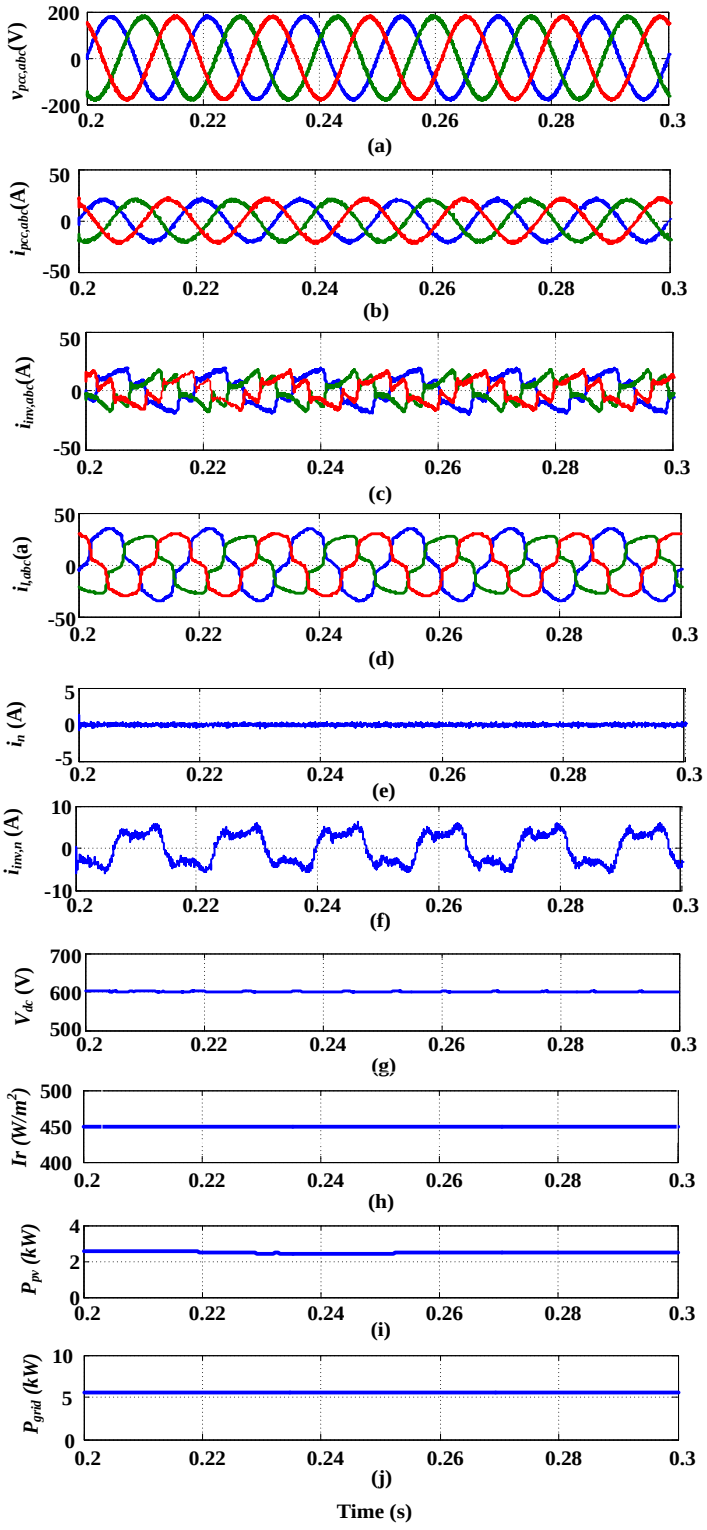

Fig. 5.13 PV injection and Power Conditioning when *Ppv* < 3kW Mode (a) Three phase voltages at PCC (b) Three phase source currents at PCC (c) Three phase inverter current (d) Three phase load currents (e) Neutral current at PCC (f) Neutral compensating current (g) DC-link voltage (h) Irradiation (i) PV power (j) grid power

For example, the irradiation is considered as 450 W/m^2 and the PV power generated for this irradiation value as per the MPPT is around 2 kW. The BSS rated power is 3kW/hr, here the generated PV power is less than the BSS power. As a result, the generated PV power is injected to the grid. The active power drawing from the grid is reduced from 8 kW to 6 kW, when the irradiation is 1000W/m^2. Here the MGCPI is performing the full compensation using the CPT control concept. The three-phase voltages, currents at PCC, the inverter compensating currents and load currents are shown in Fig 5.13(a) to Fig 5.13(d). Here the DC-link voltage is stable to perform the multifunctional operation as presented in Fig 5.13(e). The neutral current is compensated effectively by the MGCPI. The neutral current response, before and after compensation is depicted in Fig 5.13(e) and (f). In this mode the PQ issues are compensated effectively and the PV power is pumped to the local loads thereby the grid consumption is reduced as depicted in Fig 5.13(j).

5.6.3 MGCPI is ON with Power Conditioning and Power Injection and BSS Charging Mode

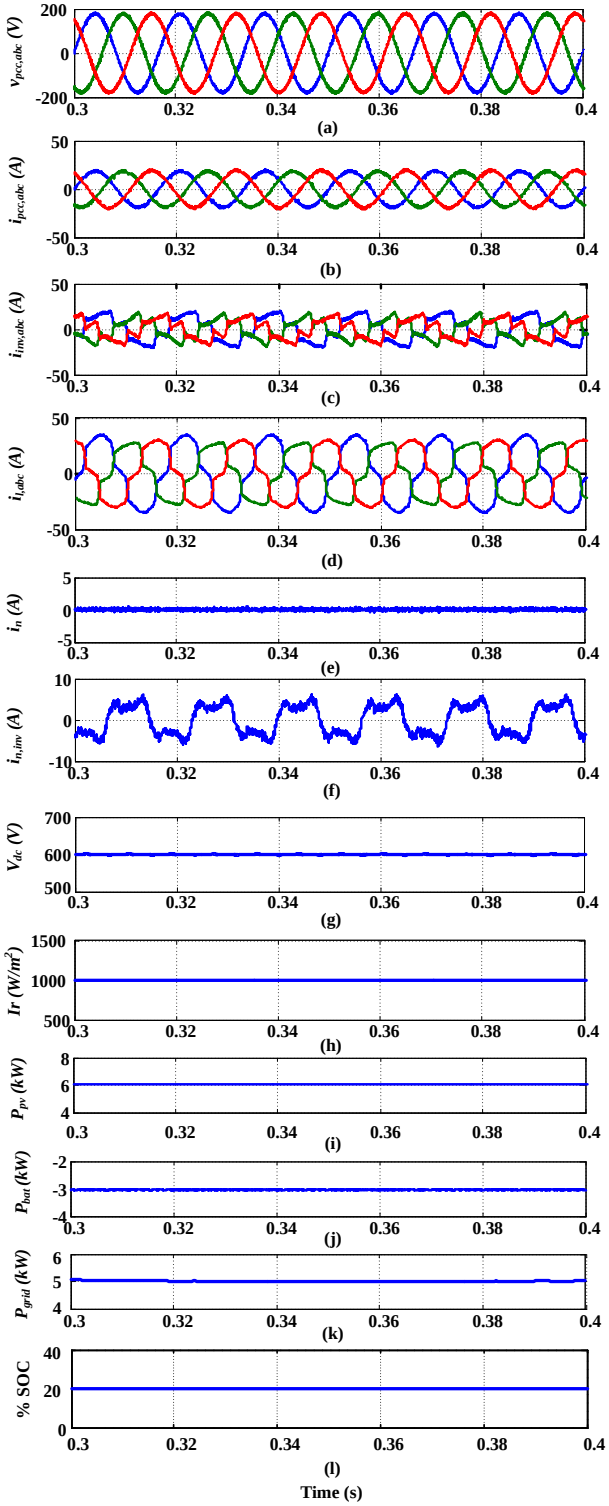

Fig. 5.14 PV injection, Power Conditioning and Battery Charging when Ppv > 3kW Mode (a) Three-phase voltages at PCC (b) Three-phase source currents at PCC (c) Three-phase inverter current (d) Three-phase load currents (e) Neutral current (f) Neutral compensation current (g) DC-link voltage (h) Irradiation (i) PV power (j) BSS power (k) Grid power (l) % SOC of the BSS

This mode demonstrates the power injection, power conditioning and BSS charging capabilities of the MGCPI when the battery SOC (%) is less than the minimum value and PV power is greater than the BSS rated power per hour. The PV power under full irradiation is 6kWp using the MPPT algorithm. Therefore, half of the PV power is used for battery charging (*i.e.,* 3kW) and remaining power is fed to the local loads which will reduce the grid consumption. The MGCPI will also perform the full compensation such as harmonics, reactive power, unbalance and neutral current compensation as depicted in Fig 5.14. The grid consumption is reduced from 8 kW to 5 kW.

5.6.4 MGCPI is ON, Selective Compensation and Battery Discharging Mode under PV power absence

The selective compensation features of the MGCPI using CPT control concept are explored. The battery takes the power injection due to the absence of PV power as the battery SOC (%) is greater than the minimum value. The selective operations such as harmonic compensation, reactive power compensation, and unbalance compensation are illustrated in Fig. 5.15. Here the inverter is tested to perform the selected operations individually by selecting the respective CPT reference currents. The detailed representation of harmonic compensation is shown in Figs 5.15(a) to (c) and only reactive power compensation is depicted in Figs. 5.15(d) to (f) and unbalance compensation is illustrated in Figs 5.15(g) to (i). From the Figs 5.15(a) to (c) only harmonics are compensated by selecting the harmonic current reference from the CPT. Here the neutral current is compensated partially. Whereas in reactive power compensation, the reactive current reference is selected from the CPT. Here the effect of harmonic and neutral current is not mitigated as illustrated in Figs 5.15(d) to (f). The unbalance compensation is demonstrated by showing the two-phase balanced source currents in Figs 5.15(g) to (i). The BSS percentage SOC is depicted in Fig. 5.15(j).

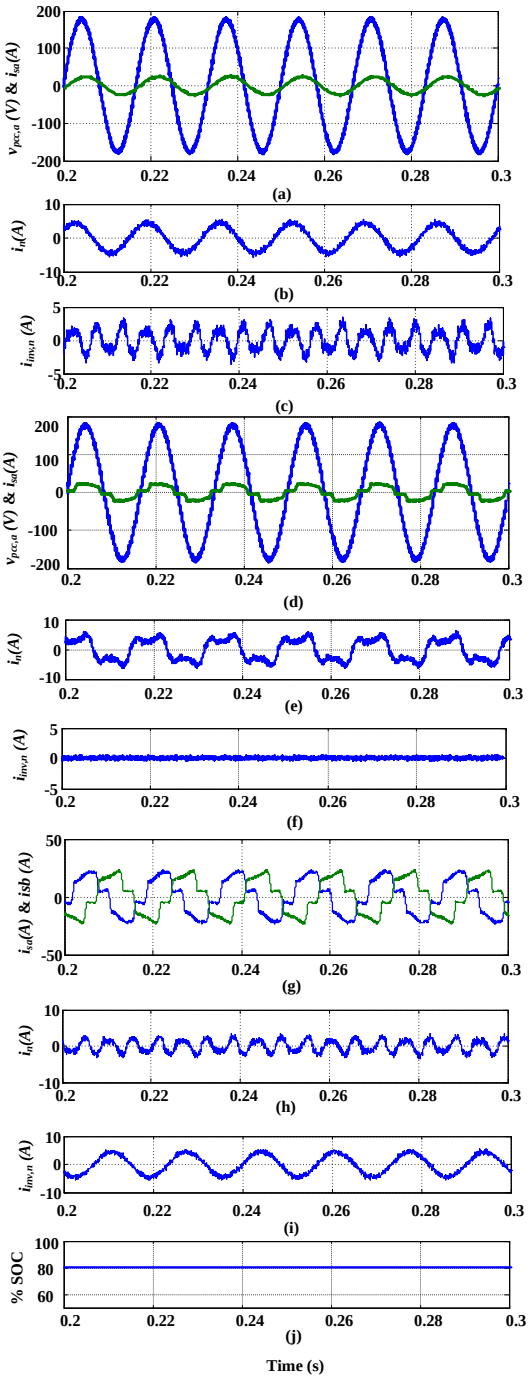

Fig. 5.15 Selective compensation and Battery discharging Mode during PV power absence (a) Phase 'a' voltage and current at PCC with only harmonic current compensation (b) Neutral Current during harmonic current compensation (c) Neutral compensating current during harmonic current compensation (d) Phase 'a' voltage and current at PCC with only reactive current compensation (e) Neutral Current during reactive current compensation (f) Neutral compensating current during reactive current compensation (g) Phase 'a' and Phase 'b' currents at PCC with only unbalance compensation (h) Neutral Current during unbalance compensation (i) Neutral compensating current during unbalance compensation (j) % SOC of the BSS

Nevertheless, the neutral current is compensated partially. In this mode of operation battery is injecting the active power which is around 3 kW; Thereby the grid consumption is reduced from its rated 8 kW to 5 kW. In all the above-stated modes the active power is injected to the grid continuously using the MGCPI supported by BSS. This mode is explored to exhibit the selective functionality of the proposed TAD algorithm based co-ordinated control.

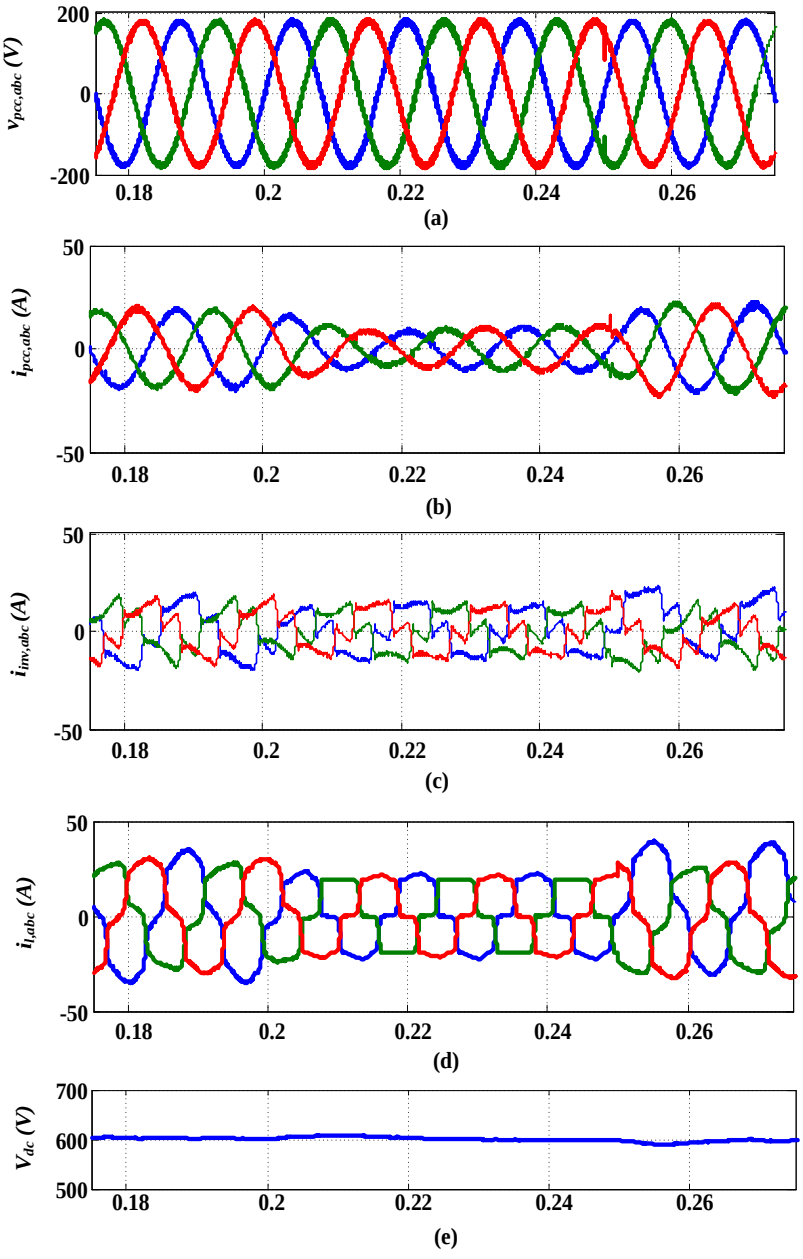

Fig. 5.16 Dynamic load Change Mode (a) Three-phase voltages at PCC (b) Three-phase source currents at PCC (c) Three-phase inverter current (d) Three-phase load currents (e) DC-link voltage

5.6.5 MGCPI is ON Power Conditioning and Power Injection under dynamic load change Mode

In this mode, the MGCPI is designated to verify the dynamic behaviour functionalities. From the Fig 5.16. It is evident that under dynamic load change, also the MGCPI is performing the power conditioning and power injection simultaneously and effectively without any disturbance. The three-phase PCC currents illustrate the smooth transition of the load change without any transients and ripples. The load behaviour and the compensating currents are depicted in Fig 5.16.

From the simulation studies the multifunctional capabilities of the two-stage MGCPI coupled with BSS are verified. The results exhibit the effective performance of the MGCPI as power conditioner and power injector simultaneously, as the average % THD of the all phases obtained from the simulation studies are 2.72 %, which is well within the limits of IEEE 1547a-2018 standard (i.e. %THD < 5%) for Interconnection and Interoperability of Distributed Energy Resources with associated Electric Power Systems Interfaces. It is also observed that the MGCPI is also capable to perform the selective compensation. The dynamic behaviour of the MGCPI is also verified and it has smooth performance under load change.

5.7 Real-Time Experimental Validation

In order to validate the proposed CPT and BSS based two-stage MGCPI functionality in real-time, the system depicted in Fig 5.1(a) was modeled and validated by the OPAL-RT based OP 4500 RT grid simulator. The laboratory test-bed for RT simulation is illustrated in Fig 5.17.

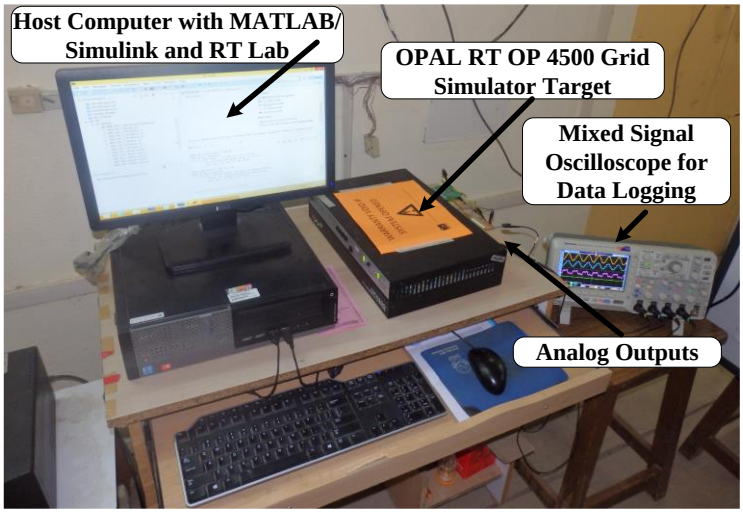

Fig. 5.17 OPAL-RT based RT simulator laboratory test-bed

OP 4500 using RT-Lab performs the rapid control prototyping, hardware-in-loop testing, and software-in-loop testing accurately. This will allow precise modelling of system controllers, with selective sampling for specific control loop [134-136,141-144].

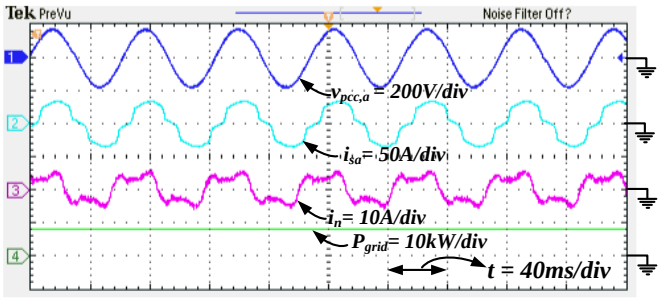

Fig. 5.18 No Power Conditioning and No Power Injection Mode

5.7.1 Mode 1: MGCPI OFF, No Power Conditioning, and No Power Injection

Fig. 5.18 demonstrates that OPAL-RT results for phase "*a*" are comparable with the MATLAB simulation results of phase A as illustrated in Fig 5.12. Percentage THD, True Power Factor and unbalance current compensation for this mode are tabulated in Table 5.6.

5.7.2 Mode 2: MGCPI is in ON Power Conditioning and Power Injection

Fig. 5.19 demonstrates that OPAL-RT results for phase "*a*" are comparable with the MATLAB simulation results of phase "*a*" as illustrated in Fig 5.13. Percentage THD, True Power Factor and unbalance current compensation for this mode are tabulated in Table 5.5.

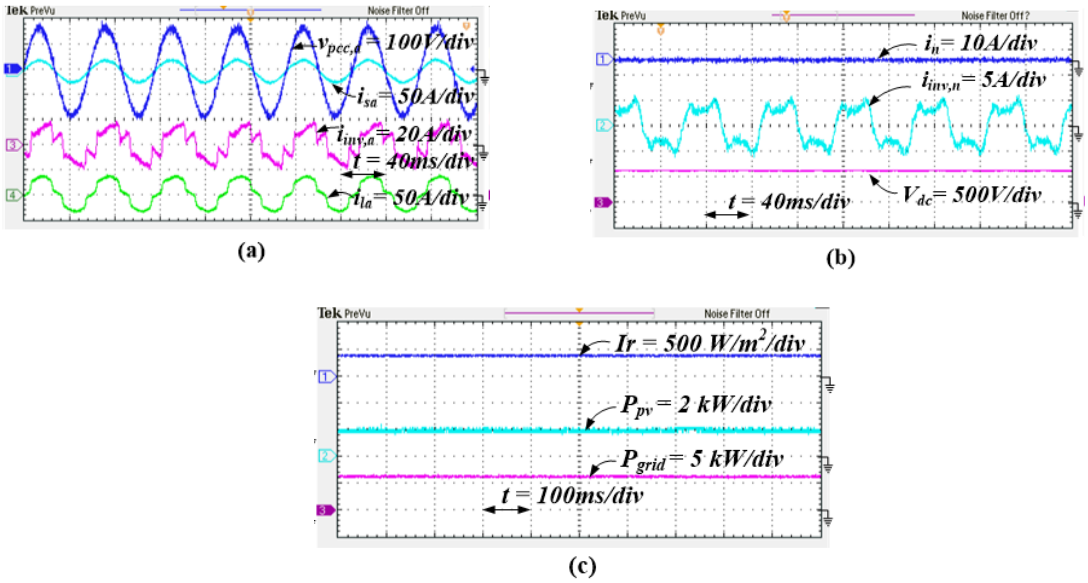

Fig. 5.19 PV injection and Power Conditioning Mode (when $P_{pv} < P_{bat\_rated}$)

The output response of the phase '*a'* PCC voltage, source, inverter ($i_{inv,a}$) and load (i_{la}) currents are illustrated in Fig. 5.19(a). Here the current harmonics and reactive power are compensated effectively. The neutral current compensation with the help of inverter neutral current ($i_{inv,n}$) is illustrated in Fig. 5.19(b). Here the DC-link voltage (V_{dc}) is regulated to its rated value of 600 V as shown in Fig. 5.19(b). The PV injection to the grid as interactive grid behavior is presented in Fig. 5.19(c). The RT results are identical to the simulation results.

5.7.3 Mode 3: MGCPI is in ON Power Conditioning, Power Injection, and Battery Charging

Fig. 5.20 demonstrates that OPAL RT results for the phase *"a"* are comparable with the MATLAB simulation results of phase A as illustrated in Fig 5.14. Percentage THD, True Power Factor and unbalance current compensation for this mode are tabulated in Table 5.6.

This mode demonstrates the power injection, power conditioning and battery charging capabilities of the MGCPI when the battery SOC (%) is less than the minimum value and PV power is greater than the battery rated power per hour. The PV power under full irradiation is 6kWp using the MPPT algorithm. Therefore, half of the PV power is used for battery charging (i.e., 3kW) and remaining power is fed to the local loads which will reduce the grid consumption. The MGCPI will also perform full compensation such as harmonics, reactive power, unbalance and neutral current compensation as depicted in Fig 5.20. Here also the PV system is pumping the active power continuously to the grid, in addition to that it will also perform the power conditioning and battery charging as per the TAD algorithm. Fig 5.20(a) demonstrates the power conditioning capabilities of the MGCPI by maintaining the sinusoidal source currently under nonlinear loading. Fig. 5.20(b) illustrates the neutral compensation, battery charging by showing the battery current (i_{bat}) absorption under rated DC-link voltage. The PV power sharing between the grid and battery for the Ir = 1000 W/m^2 is depicted in Fig. 5.20(c).

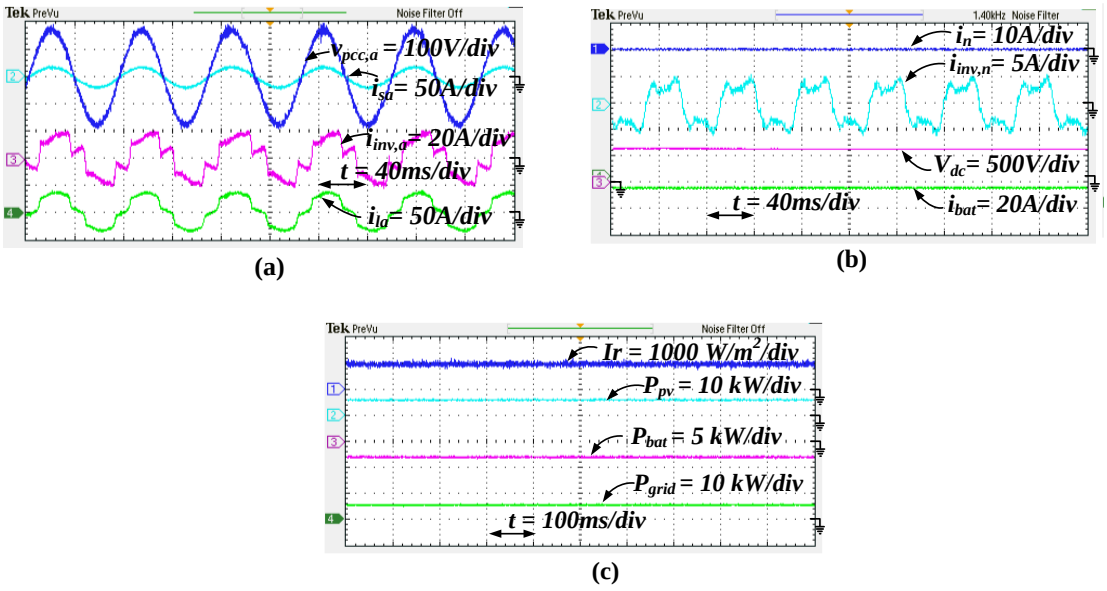

Fig. 5.20 PV injection, Power Conditioning, and Battery charging Mode (when $P_{pv} > P_{bat}$ rated)

5.7.4 Mode 4: MGCPI in ON Selective Compensation and BSS Discharging during PV Power Absence

Fig. 5.21 and Fig 5.22 demonstrates that OPAL RT results for phase "a" are comparable with the MATLAB simulation results of phase "*a*" as illustrated in Fig 5.15.

In this mode, the selective compensation features of the MGCPI using CPT control concept are explored. The battery takes the power injection due to the absence of PV power as the battery SOC (%) is greater than the minimum value. The selective operations such as harmonic compensation, reactive power compensation, and unbalance compensation are illustrated in Fig. 5.21. Here the MGCPI is tested to perform the selected operations individually by selecting the respective CPT reference currents. The detailed representation of harmonic compensation is shown in Fig. 5.21(a) and only reactive power compensation is depicted in Fig. 5.21(b) and unbalance compensation is illustrated in Fig. 5.21(c). From the Fig. 5.21(a) only harmonics are compensated by selecting the harmonic current reference from the CPT. Here the neutral current is compensated partially. Whereas in reactive power compensation the reactive current reference is selected from the CPT. Here the effect of harmonic and neutral current is not mitigated as illustrated in Fig. 5.21(b). The unbalance compensation is demonstrated by showing the two-phase balanced source currents in Fig. 5.21(c).

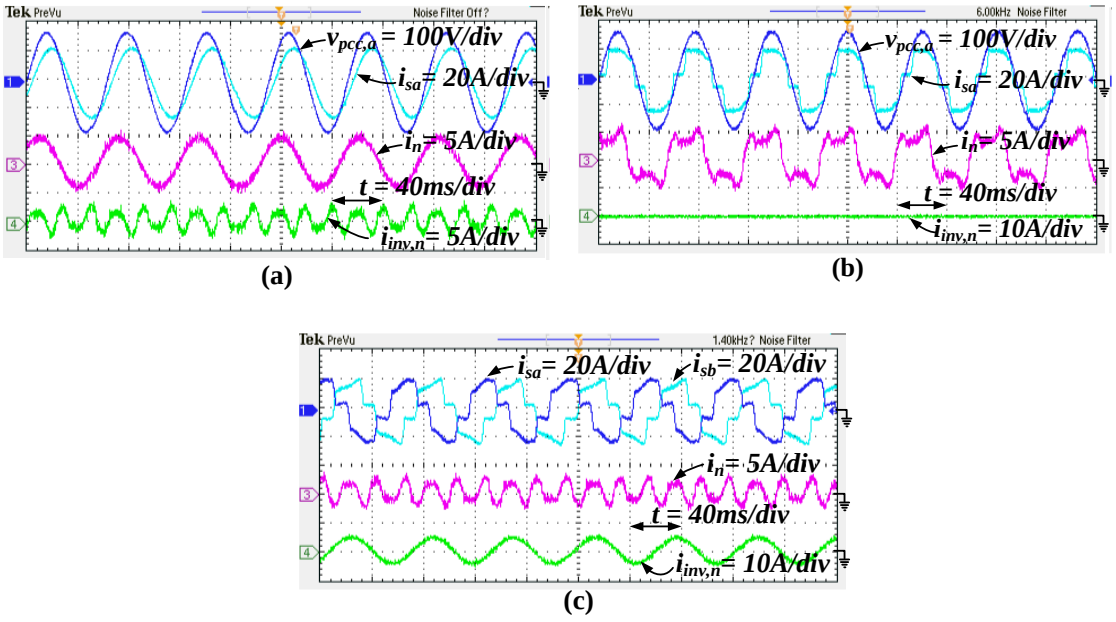

Fig. 5.21 Selective compensation and Battery discharging Mode during PV power absence

Nevertheless, the neutral current is compensated partially. In this mode of operation BSS is injecting the active power which is around 3kW; Thereby the grid consumption is reduced from its rated 8kW to 5kW as shown in Fig. 5.22. In all the above-stated modes the active power is injected to the grid continuously using the MGCPI supported by BSS. This mode is explored to exhibit the selective functionality of the proposed TAD algorithm based co-ordinated control.

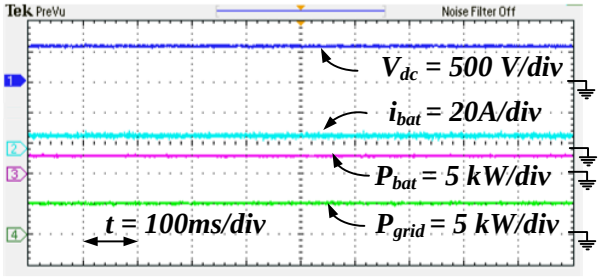

Fig. 5.22 Power injection during selective compensation Mode

5.7.5 Mode 5: MGCPI in ON Power Conditioning and Power Injection under Dynamic Load Change

Fig. 5.23 demonstrates that OPAL RT results for phase "***a***" are comparable with the MATLAB simulation results of phase "***a***" as illustrated in Fig 5.16. In this mode, the MGCPI is designated to verify the dynamic behavior functionalities. The dynamic load change response is depicted in Fig. 5.23. Here it is evident that under dynamic load change also the MGCPI is performing the power conditioning and power injection simultaneously and effectively without any disturbance. From the above studies, the multifunctional capabilities

of the MGCPI coupled with BSS are validated in RT. The results exhibit the robustness and effective performance of the MGCPI as a seamless power conditioner and power injector simultaneously.

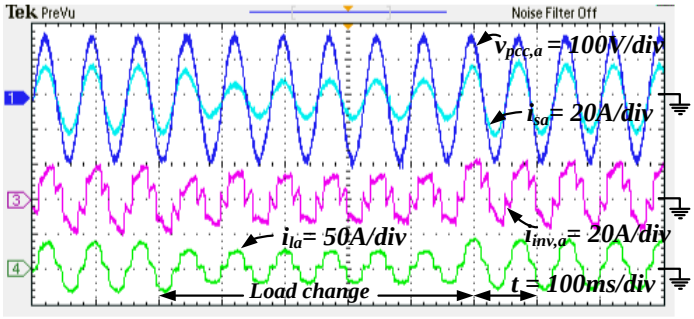

Fig. 5.23 Dynamic load change mode

The dynamic behavior of the MGCPI is also verified, and it has smooth performance under load change as an active power injector and power conditioner. The performance indices of the MGCPI are tabulated in Table 5.6.

5.8 Results and Discussion

Concerning the below results summary depicted in Table 5.6, it is witnessed that the MGCPI will perform the active power injection and power conditioning effectively and continuously. These results demonstrate the effectiveness of the think-ahead decision algorithm to coordinate the MGCPI coupled BSS operation on the three-phase four-wire distribution system. Moreover, the proposed MGCPI meet the requirements of IEEE 929-2000 recommended practice for utility interface of Photo-Voltaic (PV) Systems, IEEE 1547a-2018 standard for Interconnection and Interoperability of Distributed Energy Resources with associated Electric Power Systems Interfaces, IEC 61727 standard for Photovoltaic (PV) systems – Characteristics of the utility interfaces.

Table 5.6 MGCPI results summary

Parameters	Mode 1	Mode 2	Mode 3
% THD of the '***a***' ph current	14.2	2.90↓	2.66↓
% THD of the '***b***' ph current	18.24	2.72↓	2.83↓
% THD of the '***c***' ph current	16.1	2.55↓	2.71↓
True Power Factor	0.89	0.99↑	0.99↑
% Current unbalance at PCC	14.61	1.35↓	1.38↓
Grid active power (P)	8 kW	6 kW↓	5 kW↓
Grid reactive power (Q)	2.5 kVAR	10 VAR↓	9.5 VAR↓

5.9 Conclusions

This chapter demonstrated a Think-Ahead Decision Algorithm for the effective operation of CPT based Three-phase MGCPI with auxiliary BSS. The multifunctional capabilities of the MGCPI have been demonstrated satisfactorily. An effective TAD algorithm to determine the best mode of operation for the MGCPI taking into account the SOC (%) of the BSS and the available power at the PV source has been illustrated. The CPT is used for computing the MGCPI current reference signals during the APF operation mode. The detailed control methodologies are explained in detail. The experimental results showed that the proposed MGCPI performed multi-functionalities in the right manner. The evaluated scenarios do not show any unpredictable oscillatory behavior. Therefore, the proposed configuration is a holistic solution to integrate the PV system into the distribution grid and contributes to the sustainability of the smart-grids without any negative impact on power quality.

Chapter 6

Multi Band-Hysteresis Current Control based Single-Phase Multifunctional Grid-Connected PV Inverter for Low-Voltage Distribution Grid

6.1 Introduction

A scaling factor based multi-band hysteresis current control (MB-HCC) for the two-stage single-phase multi-functional grid-connected PV inverter (MGCPI) is presented in this chapter, which enhances MGCPI efficiency for active power injection and the PQ of the Low-Voltage Distribution Grid (LVDG). The MB-HCC uses simple switching logic and outperforms in its multi-functional tasks such as active power injection and power conditioning. The bandwidths of the MB-HCC are adjusted as per the current reference value using scaling factors under ideal and distorted grid conditions. In the two-stage MGCPI configuration, the DC-DC boost converter stage is controlled with the Incremental Conductance (INC) based maximum power point tracking (MPPT) to extract the maximum power from Roof-top solar photovoltaic (RTSPV), and the MGCPI stage is operated with the MB-HCC, with scaling factors to execute the multifunctional operations to reduce the grid consumption and improve the PQ of the LVDG.

The detailed comparison of the HCC based single-phase grid-tied inverter literature [115-123] is exhibited in Table 6.1., in view of the performance under weak grid (PWG), active power injection (API), PQ improvement (PQI), steady-state and transient characteristics (SS & TC), inverter peak efficiency (IPE), inverter efficiency under low irradiation (IELI), average switching frequency (ASF), and implementation complexity (IC). Table 6.1 summarizes the merits and limitations of HCC method application in single-phase grid-connected inverter operation. The performance under weak grid (PWG) needs to be explored with reference to the literature [115-123]. HCC method has been widely used in single-phase grid-connected system for Active Power Injection (API) and Power Quality Improvement (PQI) as described in [109,116-120]. However, the performance characteristics are dependent on the selection of the

appropriate optimum hysteresis band and the inverter switching frequency based on the tracking current between the hysteresis bands [121,123].

Table 6.1 Comparison of previous hysteresis current control (HCC)-based single-phase grid-tied inverter literature

HCC Type	PWG	API	PQI	SS& TC	IPE	IELI	ASF	IC
GI-based HCC by H.Saxena *et al.* (2018) [109]	NR [1]	Yes	Yes	Good	M [5]	Low	High	M [5]
SB-HCC by N.A.Rahim *et al.* (2007) [115]	NR [1]	Yes	NR [1]	Good	Low	Low	High	High
Grid-interactive system using HCC by R.D.Patidar *et al.* (2010) [116]	NR [1]	Yes	Yes	Good	M [5]	Low	High	M [5]
Single-phase instantaneous power theory based HCC by A.Helal *et al.* (2012) [117]	NR [1]	Yes	Yes	Good	High	Low	High	High
SB-HCC by A.Martins *et al.* (2014) [118]	NR [1]	Yes	Yes	VG [3]	Low	Low	High	M [5]
Modified instantaneous power theory-based HCC by P.K.Sahoo *et al.* (2017) [119]	NR [1]	Yes	Yes	Good	M [5]	Low	High	M [5]
SOGI-based HCC by Y.Singh *et al.* (2018) [120]	NR [1]	Yes	Yes	VG[3]	High	Low	High	M [5]
DB-HCC by P.A.Dahono *et al.* (2009) [121] and its improvised version by H.Komurcugil *et al.* (2015) [123]	NR [1]	NR[1]	Yes	VG[3]	NR[1]	NR [1]	M [5]	Low
VDB-HCC by E.R.Priandana *et al.* (2014) [122]	NR [1]	Yes	NR[1]	VG[3]	High	NR [1]	M [5]	Low
MB-HCC in this thesis	Ex[2]	Yes	Yes	Ex [2]	VH [4]	M [5]	Low	Low

[1] NR = Not Reported, [2] Ex = Excellent, [3] VG = Very Good, [4] VH = Very High, [5] M = Medium.

The HCC has better Steady State & Transient Characteristics (SS&TC). However, the Inverter Peak Efficiency (IPE) and Inverter Efficiency under Low Irradiation (IELI) is dependent on the reference generation technique of the HCC and the switching frequency. The unit vector template-based reference generation technique reported in [123] is simple and efficient method over other methods summarized in Table 6.1. Moreover, the Implementation Complexity (IC) of the unit vector template-based reference generation technique and the HCC method is low compared to other methods listed in Table 6.1. However, the highly variable switching frequency of the HCC leads to poor efficiency under distorted source and load conditions. Because the switching losses of the inverter switches are directly proportional to

switching frequency, Hence, the higher the switching frequency, the switching losses are high, thereby the efficiency of the inverter decreases. To improve the inverter efficiency by reducing the switching losses of the inverter the DB-HCC [121,123] exhibits unipolar switching characteristics, but during the zero modulation index case, it has a limitation of the high switching frequency. Moreover, the inverter switches are triggered with imbalance switching pulses. In addition to that, the inverter multi-functional capabilities need to be explored using DB-HCC. Usually, the inverter operating switching frequency is in the ranges of 10-20 kHz [109,115-123]. However, based on the nature of the harmonic distortion, the switching frequency is variable, which will increase the *di/dt* stress on the inverter switches leading to switching losses. Hence it is necessary to maintain a nearly constant average switching frequency to reduce the switching losses for the better efficiency of the inverter. To maintain a nearly constant average switching frequency the optimum selection of the hysteresis band is crucial and needs to be explored.

The selection of the appropriate MPPT for boost converter is also important, to extract the maximum power from RTSPV under variable environmental conditions in order to support the multi-functional capabilities of MGCPI. Further, it is also necessary to consider the effect of the distorted grid condition while designing the control method for MGCPI as per IEEE 519-2014 [10].

Based on the literature survey of different HCC methods such as single-band (SB) HCC, double-band (DB) HCC and Variable DB HCC (VDB-HCC), the selection of the optimum hysteresis bandwidth to attain highest conversion efficiency and nearly constant switching frequency is still under investigation. The MB-HCC using scaling factor approach is an idle candidate to improve the efficiency and also to attain the nearly constant switching frequency. The switching logic and the performance improvement over VDB-HCC has been detailed in this chapter with both simulation and real-time studies. The MB-HCC based two-stage MGCPI system configuration is modelled and simulated in a MATLAB/Simulink environment using SIM power system toolbox. The simulated results are validated in real-time (RT) using OPAL-RT based grid simulator.

6.2 Roof-top Solar PV (RTSPV) Interfaced Single-phase MGCPI Configuration

The detailed schematic of the RTSPV interfaced two-stage MGCPI configuration for LVDG applications is depicted in Fig 6.1, where stage-1 is RTSPV coupled DC-DC converter and stage-2 is single-phase MGCPI.

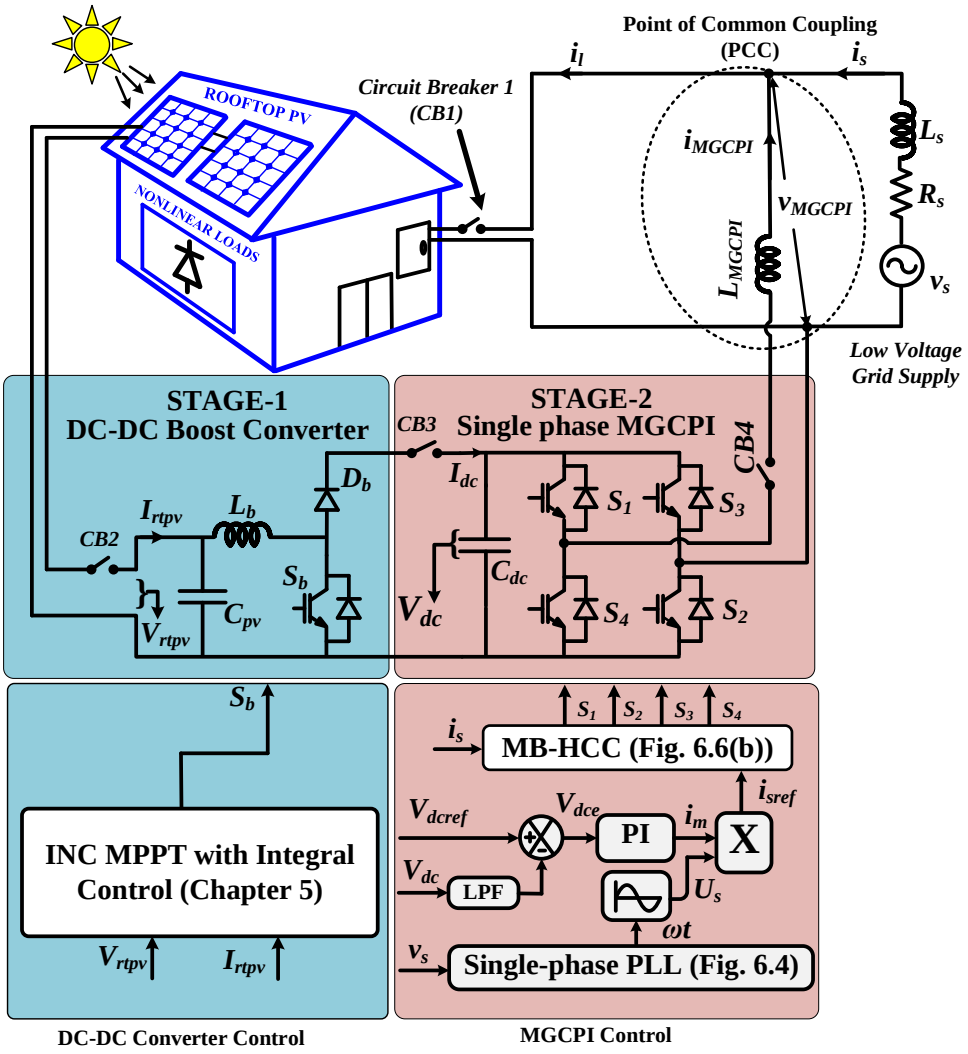

Fig. 6.1 MB-HCC-based two-stage single-phase MGCPI for LVDG

The single-phase distribution system is modelled as an ideal AC voltage source in series with the source impedance, and it is connected to the nonlinear loads in a single-phase residential building. The stage-1 DC-DC converter is controlled by an INC-based MPPT to extract maximum power from the RTSPV. The stage-2 MGCPI is controlled by MB-HCC. The RTSPV interfaced single-phase MGCPI is connected at the point of common coupling to execute the multifunctional operations.

Table 6.2 System parameters

Parameter	**Value**
Ideal v_s	230 V (RMS), 50 Hz
Distorted v_s	230 V (RMS), 50 Hz + Voltage harmonics (30 V at 150 Hz; 25 V at 350 Hz)
Source Impedance	Source Resistance (R_s) = 0.1 Ω, Source Inductance (L_s) = 0.01 mH
1-ϕ Non-linear load 1	Frontend Bridge rectifier with RL (R = 35 Ω, L = 400 mH) and parallel RC (R = 1Ω, C = 250 μF)
1- ϕ Non-linear load 2	Frontend Bridge rectifier with RL (R = 35 Ω, L = 400 mH)
1- ϕ Non-linear load 3	Frontend Bridge rectifier with RL (R = 12 Ω, L = 20 mH)
1- ϕ Non-linear load 4	Frontend Bridge rectifier with RL (R = 30 Ω, L = 6 mH) and parallel RC (R = 1Ω, C = 200 μF)
C_{pv}	100 μF
L_b	5 mH
Integral control gain	5
C_{dc}	3700 μF
V_{dc}	500 V
L_{MGCPI}	3 mH
P_{pv}	6.1 kWp @ Ir = 1000 W/m^2 and T = 25 °C
V_{dc}	500 V
Sampling Frequency	50 kHz

6.2.1 RTSPV coupled DC-DC converter stage outline

The RTSPV coupled DC-DC converter described in chapter 5 is used here to energize the DC-link of the single-phase MGCPI stage as shown in Fig 6.1. The DC-DC converter is controlled by INC based MPPT method in order to extract the maximum power from the RTSPV. The RTSPV is designed to deliver a maximum power of 6 kWp.

6.2.2 Single-phase MGCPI stage outline

A single-phase four-switch H-bridge Voltage source inverter (VSI) is considered as MGCPI to execute the active power injection and power conditioning operations. The inverter is connected to the PCC by a ripple filter (L_{MGCPI}) as shown in Fig 6.1. Here the source current (i_s) is sensed and compared with the reference current (i_{sref}) generated by the sine-based unit vector template approach, then processed through the proposed MB-HCC method to perform the multifunctional operation with reduced switching frequency. The system parameters used

in this study are tabulated in Table 6.2. The detailed control configuration is presented in the next section.

6.3 RTSPV Interfaced MGCPI Control Configuration

The RTSPV interfaced two-stage MGCPI has two control sections, where the stage-1 DC-DC converter is controlled by INC based MPPT method and the stage-2 single-phase MGCPI is controlled by MB-HCC method. The objective of the controller was to pump the harvested maximum power from RTSPV to the PCC of the LVDG through the MGCPI and enhancement of PQ at PCC. The active power generated from the MGCPI is expressed as follows:

$$\boldsymbol{P_{MGCPI} = P_{pv} + P_{losses}} \tag{6.1}$$

While converting the DC power from RTSPV to AC power using MGCPI, various losses, P_{losses} occur and P_{losses} constitutes the majority of switching losses of the MGCPI. If the losses are reduced by minimizing the inverter switching losses, which improves efficiency of MGCPI. Hence, the MB-HCC switching logic was designed to reduce the switching losses by reducing the variable switching frequency. The MGCPI controller configuration designed to improve the MGCPI efficiency and PQ of the LVDG is detailed in the below, where in the controller has two control loops, the first loop is for inverter DC-link voltage control, and the second loop is for current control.

6.3.1 Incremental Conductance (INC) MPPT based DC-DC conveter control

Due to intermittent nature of solar irradiation, the boost converter with MPPT is essential to extract the maximum power from the RTSPV. The switching pulse (S_b) to the DC-DC converter for boost operation is calculated according to the INC based MPPT algorithm to maintain the set value of MGCPI DC-link voltage and also to harvest the maximum power from the RTSPV for grid injection. The INC based MPPT control is detailed in chapter 5.

6.3.2 MB-HCC based MGCPI control

The detailed block diagram of the MB-HCC based MGCPI control is illustrated in Fig 6.1. The MGCPI has two control loops, where one is DC-link voltage control loop driven by PI controller and another one is current control loop governed by the MB-HCC switching logic.

In the DC-link voltage control loop, the DC-link voltage supplied from the DC-DC converter stage was processed by a low-pass filter (LPF) to reduce the DC-link voltage ripples compared with its reference DC-link voltage value. To regulate the DC-link voltage, the error voltage was processed through the proportional–integral (PI) voltage controller. The DC-link voltage error (V_{dce}) sample value at nth point is expressed as follows

$$\boldsymbol{V_{dce}(n) = V_{dcref}(n) - V_{dc}(n)} \tag{6.2}$$

This output of the PI voltage controller is the peak value of the source current. The output expression of the discrete PI voltage controller is represented as

$$i_m(n) = i_m(n-1) + k_p\big(V_{dce}(n) - V_{dce}(n-1)\big) + k_i\, V_{dce}(n) \tag{6.3}$$

Where the k_p and k_i gain values are obtained by using the Ziegler-Nichols second method [145,146]. Initially, the k_p gain value was set by the Ziegler–Nichols second method table value as 0.6, then the tuning procedure was continued by the proportional-integral-derivative (PID) controller autotuning in the MATLAB/Simulink environment to obtain the k_i value for improved performance. After successful tuning using the PID auto-tuning procedure in the MATLAB/Simulink environment, the k_i gain value was obtained as 10. The main objective of this tuning is for attaining the lowest percentage total harmonic distortion (THD) of the grid current which is within the limits of IEEE 519-2014 and IEEE 1547 standards, respectively [10,105]. The PI controller gains of the DC-link voltage loop were tuned for a low crossover of the frequency range, i.e., in between 10 Hz to 20 Hz, to attenuate the high-magnitude ripple content in MGCPI DC-link voltage. The Bode plot of the tuned PI controller with the obtained gain values of the MGCPI DC-link voltage control loop which regulated the DC-link voltage and reduced the steady-state error is depicted in Fig 6.2.

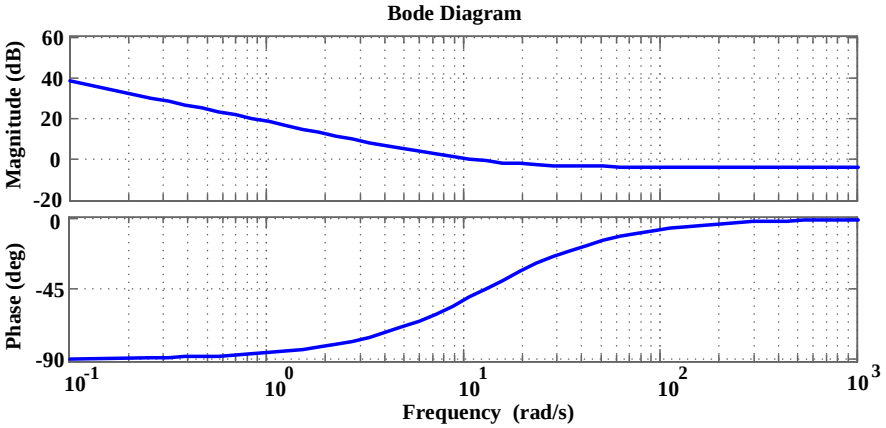

Fig. 6.2 Bode plot of the MGCPI DC-link voltage proportional–integral (PI) controller

The unit vector (U_s) is generated by using the grid synchronizing angle (ωt), which is obtained from a phase-locked loop (PLL) [147–149]. The PLL used in the MGCPI control under both ideal and distorted grid conditions is illustrated in Fig 6.3.

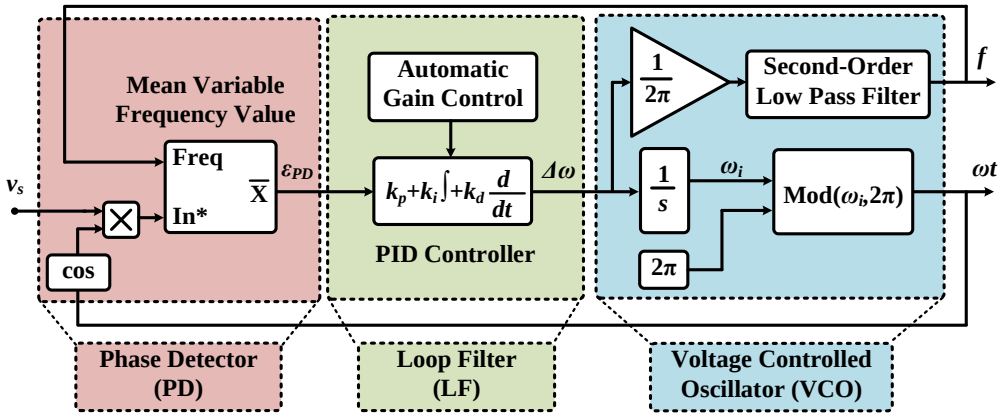

Fig. 6.3 Single-phase phase-locked loop (PLL) used for both ideal and distorted grid

The PLL parameters selected in the MATLAB/Simulink 2013 environment for both simulation and RT implementation are tabulated in Table 6.3.

Table 6.3 PLL parameters

Parameter	**Value**
Minimum Frequency	45 Hz
Initial Phase and Frequency	0 and 50 Hz
PID Controller gains (k_p, k_i, k_d)	k_p = 180, k_i = 3200, k_d = 1
The time constant for derivative action	10^{-4} s
The maximum rate of change of frequency	12 Hz/s
Filter cut-off frequency for frequency measurement	25 Hz
Sample time	20 µs
Automatic gain control	enable

The main objective of this PLL was to obtain the synchronization angle accurately under ideal and distorted grid conditions, in order to generate the sine unit vector template (U_s). The peak value of the source current (i_m) was multiplied by the U_s to generate the source current reference (i_{sref}) in phase with source voltage at unity power factor. To purge the harmonics and reactive power under ideal and distorted grid conditions, it was necessary to force the source current to maintain a sinusoidal nature, and it should be in phase with the source voltage.

The sine unit vector template and reference source current expressions under ideal and distorted grid conditions are given as follows:

$$U_s = \sin(\omega t) \tag{6.4}$$

$$i_{sref} = U_s \times i_m \tag{6.5}$$

In the current control loop the reference current (i_{sref}) and the actual current (i_s) are processed through the MB-HCC switching block as illustrated in Fig.6.1. In the MB-HCC switching block, two hysteresis bands are derived based on the scaling factors approach. The detailed flowchart of the MB-HCC algorithm is illustrated in Fig 6.4.

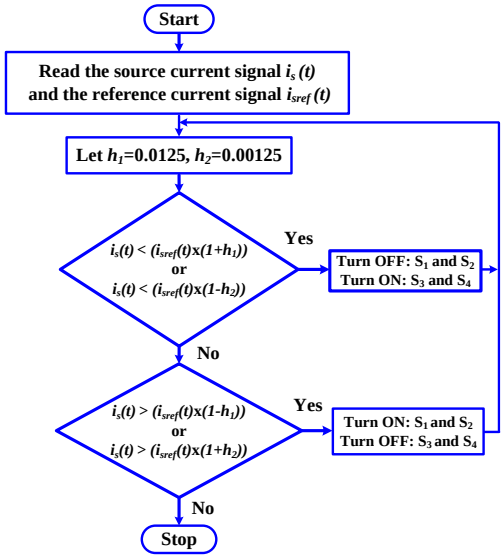

Fig. 6.4 Detailed representation of the stage-2 MB-HCC method

The MB-HCC method controls the MGCPI switches in such a way that it can force the actual source current (i_s) to rise and fall and closely tracks reference current (i_{sref}) between the main and sub hysteresis bands (HB1 and HB2) as depicted in Fig 6.5.

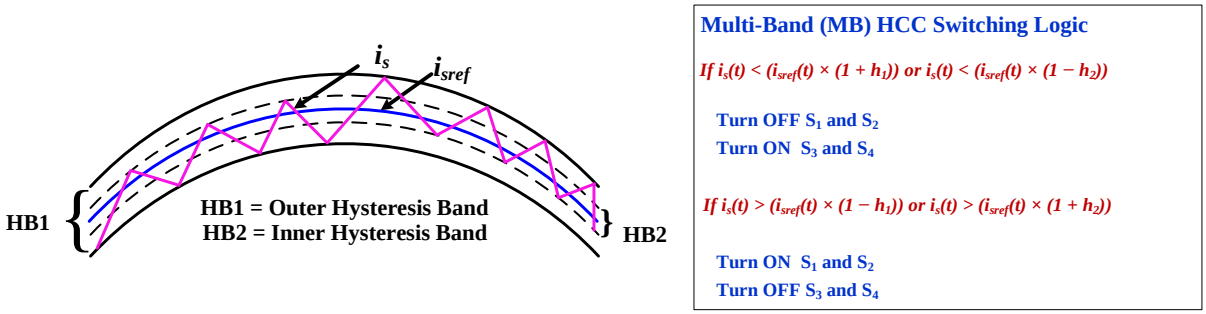

Fig. 6.5 Multi-Band (MB) – HCC method

The switching pulses are generated through tracking current response between dual hysteresis bands (HB1 and HB2). In contrast to the VDB-HCC method [122], the MB-HCC method balances the switching frequency based on the current tracking uniformly, as shown in Fig 6.6(b).

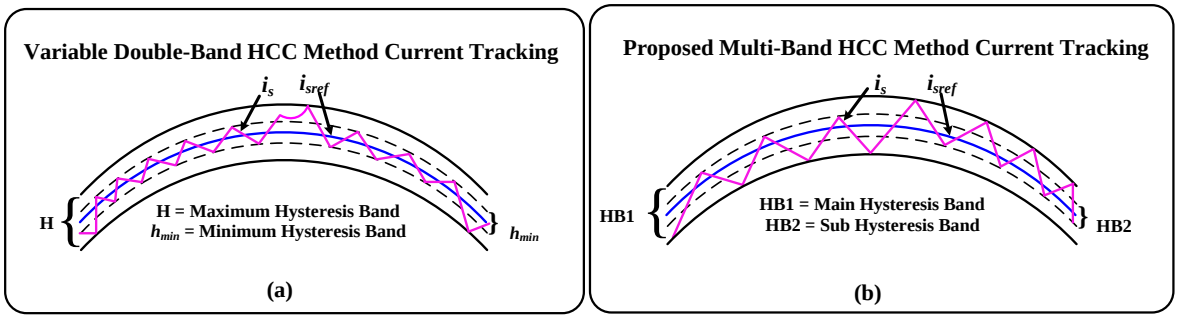

Fig. 6.6 Comparison of the MB-HCC method and VDB-HCC method current tracking; (a) VDB-HCC current tracking; (b) MB-HCC current tracking

The h_1 and h_2 are the scaling factors of the dual hysteresis bands (HB1 and HB2) of the MB-HCC. The optimum values of the scaling factors were set and verified by the RT simulation studies to obtain the reduced THD as well as the MGCPI switching frequency simultaneously.

In the MB-HCC method, the ranges of the two hysteresis bands are adjusted based on the reference current (i_{sref}) and their scaling factors (h_1 and h_2), whereas in the VDB-HCC method, the hysteresis band is determined by using Equation (6.6).

The scaling factors are obtained by the following step by step procedure:

Step-by-step procedure for MB-HCC scaling factor selection	
Step 1:	Initially, the hysteresis band scaling factor (h_1) range is obtained as 0.01 to 0.1 by using the generalized instantaneous switching frequency formula reported in Reference [150] to get the lowest % THD at the reduced switching frequency (f_{sw}).
Step 2:	The scaling factor (h_2) is considered as 10% of the h_1 to prevent the offset issues.
Step 3:	MATLAB and RT simulations are performed for the range of scaling factors 0.01 to 0.1 in order to obtain the optimum scaling factors for accurate tracking of the actual source current (i_s).
Step 4:	Based on the series of simulation studies with nonlinear loads, the current tracking is accurate with the scaling factor values of h_1 = 0.0125 and h_2 = 0.00125 (i.e., 10% of h_1). Moreover, the % THD low and the average instantaneous switching frequency is nearly constant by considering these scaling factors in MB-HCC method for different nonlinear loads under ideal and distorted grid conditions.

The simple switching logic of the MB-HCC method is as follows:

MB-HCC Switching Logic for MGCPI

- If $i_s(t) < (i_{sref}(t) \times (1 + h_1))$ or $i_s(t) < (i_{sref}(t) \times (1 - h_2))$
  - Turn OFF S_1 and S_2
  - Turn ON S_3 and S_4
- If $i_s(t) > (i_{sref}(t) \times (1 - h_1))$ or $i_s(t) > (i_{sref}(t) \times (1 + h_2))$
  - Turn ON S_1 and S_2
  - Turn OFF S_3 and S_4

Unlike the VDB-HCC, in the MB-HCC method, the hysteresis bandwidths are determined by using the reference current and scaling factors as illustrated in Fig 6.5, in order to determine the optimum bandwidths for improved efficiency and PQ. The MGCPI switches are triggered by the switching pulses as per the sequence illustrated in Fig 6.5. These switching pulses generate a pulse width modulated (PWM) AC voltage at the MGCPI output side (v_{MGCPI}). This voltage causes a current (i_{MGCPI}) to flow through the ripple inductor (L_{MGCPI}), which is

injected at PCC to reduce the grid consumption and mitigate the current harmonics and induced reactive power.

6.3.3 Comparison of MB-HCC with Variable Double-Band (VDB)-HCC

In the VDB-HCC, the switching logic was derived by considering the two hysteresis bands (HBs), where the HBs bandwidths were comprised of a minimum band value and a maximum band value. Here, the maximum band was multiplied by one fundamental periodic cycle [122]. The switching logic of the VDB-HCC method used is illustrated as given below:

VDB-HCC Switching Logic for MGCPI

- *If* $i_s(t) > (i_{sref}(t) + h_{min})$
  - Turn ON S_1 and S_2
  - Turn OFF S_3 and S_4
- *If* $i_s(t) > (i_{sref}(t) + HB_{VDB})$
  - Turn OFF S_1, S_3 and Turn ON S_2, S_4; alternatively, Turn ON S_1, S_3 and Turn OFF S_2, S_4
- *If* $i_s(t) < (i_{sref}(t) - h_{min})$
  - Turn OFF S_1 and S_2
  - Turn ON S_3 and S_4
- *If* $i_s(t) < (i_{sref}(t) - HB_{VDB})$
  - Turn ON S_1, S_3 and Turn OFF S_2, S_4; alternatively, Turn OFF S_1, S_3 and Turn ON S_2, S_4

where the HB is expressed as follows

$$HB_{VDB} = h_{min} + H|\sin\theta| \tag{6.6}$$

$$HB_{VDB_{avg}} = h_{min} + \frac{2H}{\pi} \tag{6.7}$$

By considering the average hysteresis band expression, various combinations are derived as listed in Reference [122]. Among the various combinations of maximum and minimum hysteresis bandwidth values, h_{min} = 0.005 and H = 0.149226 are selected in view of the better performance indices. The main limitation of the VDB-HCC is the high variable switching frequency during the variations in solar irradiation and nonlinear load compensation requirements. The inverter switches Turned ON and OFF for a long time during the source current touched the maximum hysteresis band as shown in Fig 6.6(a). Moreover, efficiency was low for the modulation index value of less than 0.7.

The mathematical expression for switching frequency (f_{sw}) of the single-phase inverter using VDB-HCC described in Reference [122] is expressed as

$$f_{sw} = \frac{V_{dc}}{2L_{MGCPI}HB_{VDB}}(1 - k_m \sin\theta)k_m \sin\theta \quad (6.8)$$

In the MGCPI configuration the DC-link voltage (V_{dc}) and ripple reduction interfacing inductor (L_{MGCPI}) values are fixed values. Hence, the switching frequency can be controlled by varying the hysteresis bandwidths as represented in Equation (6.8). The reported bandwidth values are not optimum for the multifunctional operation of the inverter. Moreover, the optimum bandwidths of the hysteresis bands to attain high efficiency are not yet reported. These limitations are overcame by the MB-HCC method.

6.4 Simulation Results

System configuration as described in section 5.2 with system parameters illustrated in table 6.2 is modelled in MATLAB/Simulink 2013. A set of simulations on the proposed MB-HCC-based MGCPI configuration was carried out using the MATLAB/Simulink software environment to validate the multi-functionalities under ideal and distorted grid voltage conditions. The voltage was considered as the third- and seventh-order harmonic distorted voltage, in accordance with the limits of IEEE 519-2014 standard [10], i.e., the voltage percentage THD is 8%. The nonlinear loads connected to the LVDG were modelled using a frontend diode bridge rectifier fed with RL and RC elements. The performance of the RTSPV interfaced MGCPI was demonstrated in four modes, under both ideal and distorted grids, which were classified as follows:

- Mode 1: MGCPI is OFF, and there is no power injection and power conditioning. This mode exhibits the behaviour of the nonlinear loads on LVDG without using MGCPI.
- Mode 2: MGCPI is ON, with grid sharing or power conditioning. This mode demonstrates the grid sharing and power conditioning functionality of the MGCPI under full-load condition.
- Mode 3: MGCPI is ON, with grid feeding and power conditioning. This mode illustrates the grid feeding and power conditioning functionality under reduced load condition.
- Mode 4: MGCPI is ON, with grid sharing and power conditioning during irradiation change. The dynamic behaviour of the MGCPI during irradiation change has been demonstrated in this mode, where the MGCPI is exhibiting the functionality of grid sharing and power conditioning. All the modes of operations are detailed in the below sub sections.

6.4.1 Mode 1: MGCPI OFF, with No Power Injection or Power Conditioning

Initially, the load behaviour at PCC under MGCPI OFF condition was assessed by simulation studies, and the simulation results illustrate the source current harmonic distortion and reactive power effect under ideal and distorted grid conditions as depicted in Fig 6.7.

6.4.1.1 Ideal Grid Voltage Case

Under ideal grid conditions, the source current had a THD percentage of 34.08%. The active and reactive power profiles at PCC under ideal grid conditions are depicted in Fig 6.7(a). The loads draw an active power of 9.068 kW from the grid under the ideal grid condition as shown in Fig 6.7(a). The reactive power under the ideal grid case was 1.005 kVAR.

6.4.1.2 Distorted Grid Voltage Case

The percentage THD of the source current under a distorted grid condition was 42.69%. The active and reactive power profiles at PCC under the distorted grid condition is depicted in Fig 6.7(b). The active power consumed from the grid under a distorted grid condition was 9.331 kW as described in Fig 6.7(b). The reactive power under a distorted grid case was 0.655 kVAR.

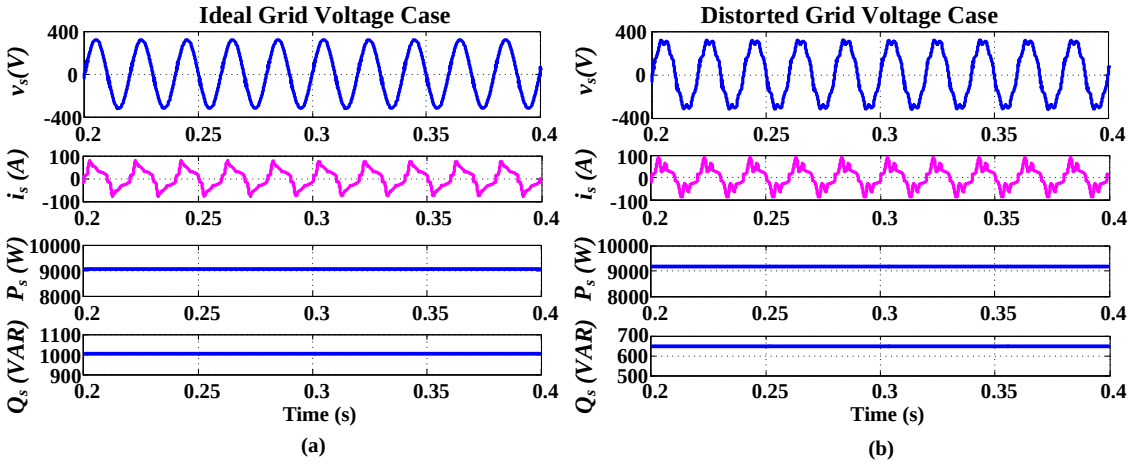

Fig. 6.7 Simulated waveforms under MGCPI OFF mode; (a) ideal grid source voltage, current, active, and reactive power; (b) distorted grid source voltage, current, active, and reactive power

In both cases, the harmonics and reactive power were deteriorating the LVDG power quality. Therefore, it is necessary to compensate for the harmonics and reactive power to improve the operating efficiency and reliability of the LVDG under both ideal and distorted grid conditions.

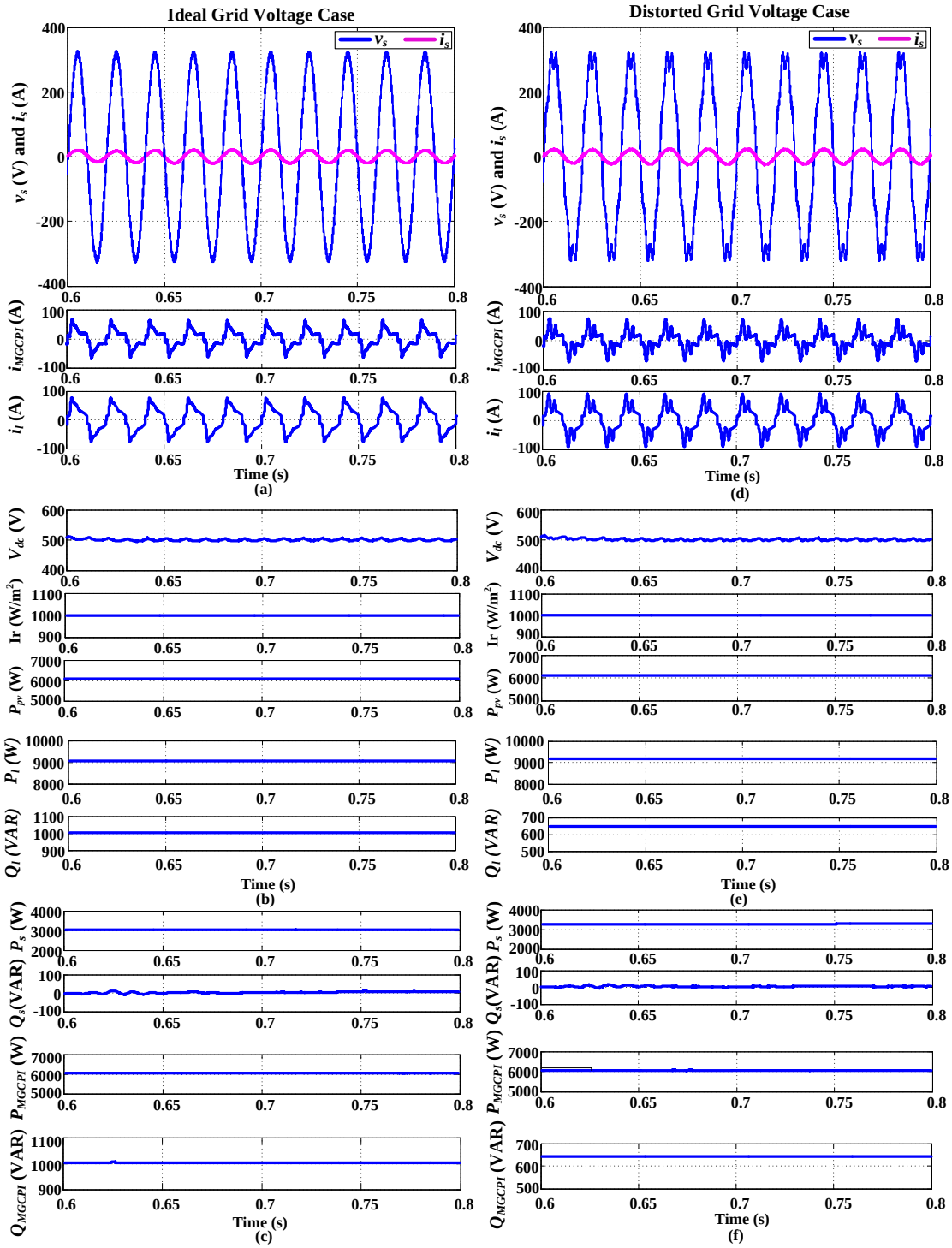

Fig. 6.8 Simulated output waveforms under MGCPI ON, grid sharing, and power conditioning mode (a) Ideal grid input voltage, current, MGCPI current, and load current; (b) MGCPI DC-link voltage, solar irradiation, PV power, and load active and reactive power under ideal grid; (c) source active power, reactive power, and MGCPI active and reactive power under ideal grid; (d) distorted grid input voltage, current, MGCPI current, and load current; (e) MGCPI DC-link voltage, solar irradiation, PV power load, and active and reactive power under distorted grid; (f) source active power, reactive power, and MGCPI active and reactive power under distorted grid

6.4.2 Mode 2: MGCPI is ON, with Grid Sharing and Power Conditioning

The MGCPI functionality as active power injector—to reduce the grid consumption by sharing the RTSPV power and power conditioner to compensate the harmonics and reactive power at PCC are exhibited in this mode under both ideal and distorted grid cases.

6.4.2.1 Ideal Grid Voltage Case

The source voltage and current responses after compensation of harmonics and reactive power under the ideal grid condition are depicted in Fig 6.8(a) along with MGCPI and load currents. From the above results, it is observed that the source current harmonics were compensated, and it was in-phase with the source voltage. Thus, the power conditioning task is achieved effectively. Moreover, grid consumption was also minimized simultaneously. The detailed response of RTSPV power generation at irradiation of 1000 W/m^2 and the DC-link voltage responses are presented in Fig 6.8(b). These results confirm that the DC-link voltage is maintained stably at a rated value of 500 V. The load active and reactive power profiles are also illustrated in Fig 6.8(b). The grid sharing response is depicted in Fig 6.8(c); from this, the source power consumption was reduced, which was owing to the active power feeding from the MGCPI. It is also supplied the necessary reactive power to reduce the source side reactive power close to zero, as shown in Fig 6.8(c).

6.4.2.2 Distorted Grid Voltage Case

In Fig 6.8(d) the source voltage and current responses after compensation of harmonics and reactive power, under the distorted grid voltage condition, are represented along with MGCPI and load currents. Here, the source current was transformed to sinusoidal and in-phase with the source voltage, irrespective of the load current nature, with the help of the MGCPI current. The inverter DC-link and RTSPV generation at an irradiation level of 1000 W/m^2 is depicted in Fig 6.8(e), where the DC-link was stable at 500 V, and the RTSPV power was 6 kW. In addition to that, the load active and reactive power profiles under distorted grid conditions are also illustrated in Fig 6.8(e). The source reactive power was also reduced close to zero by injecting the required reactive power, as shown in Fig 6.8(f). Based on the listed active and reactive power summary of the source, load, and MGCPI under both ideal and distorted grid voltage conditions in Table 6.4, the MGCPI performed the grid sharing and power conditioning tasks effectively.

Table 6.4 Active and reactive power summary of the source, MGCPI, and load under grid sharing mode

MGCPI ON	**Full Load – Grid Sharing**	
Parameters	**Ideal Grid**	**Distorted Grid**
P_s (kW)	3.046	3.318
Q_s (kVAR)	0.007	0.015
P_{MGCPI} (kW)	6.022	6.003
Q_{MGCPI} (kVAR)	1.005	0.64
P_l (kW)	9.068	9.321
Q_l (kVAR)	1.012	0.655

6.4.3 Mode 3: MGCPI is ON, with Grid Feeding and Power Conditioning

In this mode, the grid feeding and power conditioning operations of the MGCPI during the reduced load condition under both ideal and distorted grid situations are demonstrated.

6.4.3.1 Ideal Grid Voltage Case

The source voltage and current responses under grid feeding and power conditioning mode are illustrated in Fig 6.9(a). Here the source current is out of phase with the source voltage, which means that the surplus current, after injecting to the local loads at PCC, is feeding to the grid; the reduced load current nature due to the reduction of the loads is illustrated in Fig 6.9(a). Here, the MGCPI was serving the local load simultaneously, pumping the excess power to the grid. The inverter DC-link voltage response and the active and reactive power profiles of the loads are presented in Fig 6.9(b). The active and reactive power supplied by the MGCPI is depicted in Fig 6.9(c).

6.4.3.2 Distorted Grid Voltage Case

The simulation studies verify the MGCPI performance under distorted grid voltage condition. Here, Fig 6.9(d) illustrates the source voltage and source current responses after compensation of harmonics and reactive power along with MGCPI current and load current. In this condition, the source current was out of phase with the source voltage, similar to the ideal

grid case, which enumerates the grid feeding of surplus MGCPI current in sinusoidal form, irrespective of source voltage disturbance.

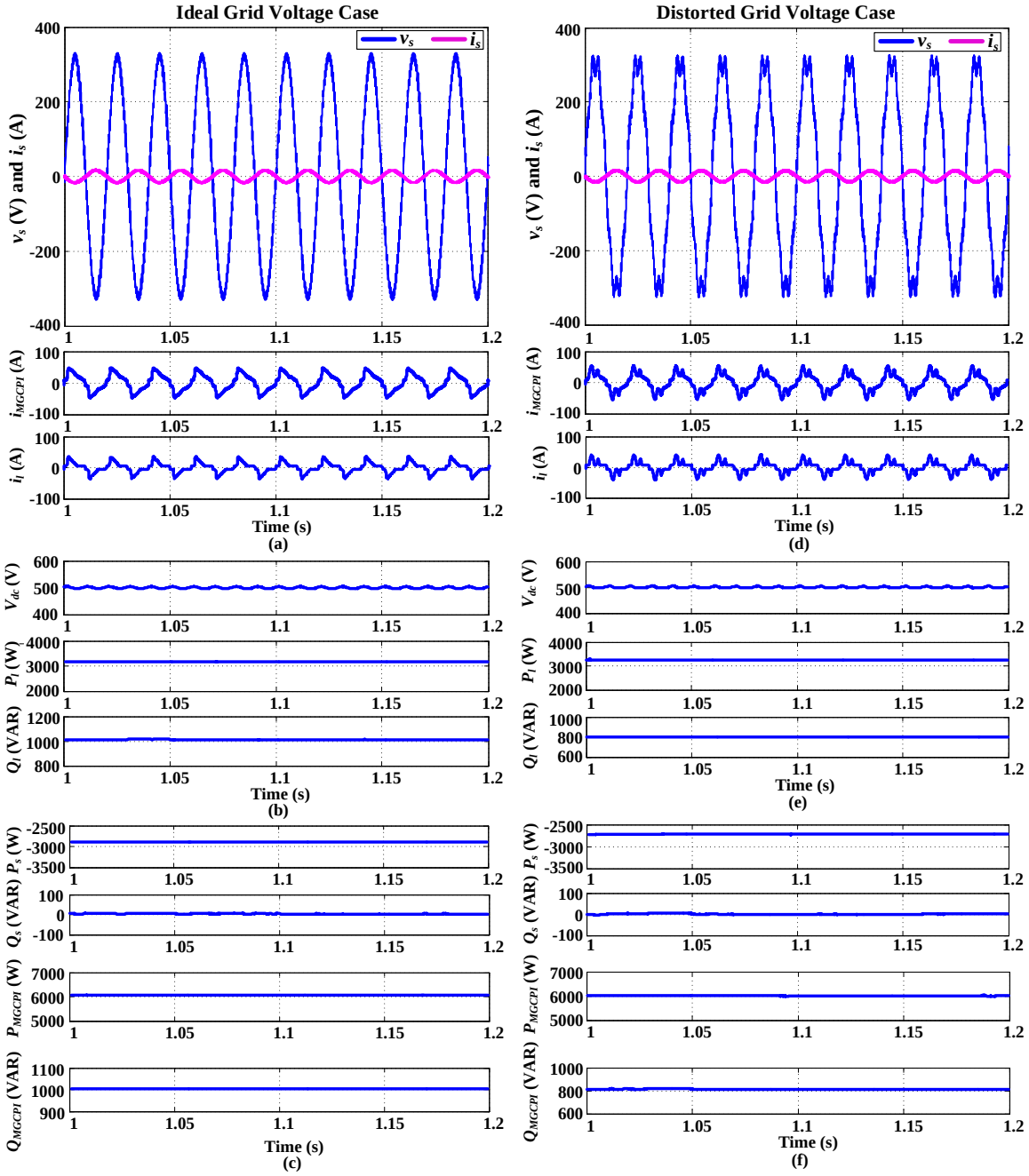

Fig. 6.9 Simulated output waveforms under MGCPI ON with grid feeding and power conditioning mode; (a) ideal grid input voltage, current, MGCPI current, and load current; (b) MGCPI DC-link voltage, and load active and reactive power under ideal grid; (c) source active power, reactive power, and MGCPI active and reactive power under ideal grid; (d) distorted grid input voltage, current, MGCPI current, and load current; (e) MGCPI DC-link voltage, and load active and reactive power under distorted grid; (f) source active power, reactive power, and MGCPI active and reactive power under distorted grid

The inverter DC-link voltage response and the partial load active and reactive power profiles under the distorted grid condition are presented in Fig 6.9(e). The active and reactive power profiles of the source and MGCPI are illustrated in Fig 6.9(f). Given the listed active and reactive power summaries of the source, MGCPI, and load under both ideal and distorted grid conditions in Table 6.5, the MGCPI executed the grid feeding and power conditioning tasks successfully.

Table 6.5 Active and reactive power summary of the source, MGCPI, and load under grid feeding mode

MGCPI ON	**Full Load—Grid Sharing**	
Parameters	**Ideal Grid**	**Distorted Grid**
P_s (kW)	−2.895	−2.789
Q_s (kVAR)	0.003	0.008
P_{MGCPI} (kW)	6.022	6.013
Q_{MGCPI} (kVAR)	1.009	0.788
P_l (kW)	3.127	3.224
Q_l (kVAR)	1.012	0.796

6.4.4 Mode 4: MGCPI is ON, with Grid Sharing and Power Conditioning during Irradiation Change

6.4.4.1 Ideal Grid Voltage Case

In this mode of operation, the MGCPI performance during irradiation change under ideal and distorted grid conditions is illustrated in Fig 6.10(a),(b). In the current response depicted in Fig 6.10(a), there was a rise in amplitude during the irradiation change from 1000 W/m^2 to 500 W/m^2 at time t = 1.6 s because of the reduction in RTSPV power. This means the grid consumption was raised. However, the source current harmonics were compensated for successfully. The inverter current injected at the PCC, and the load current responses are illustrated in Fig 6.10(a). The DC-link voltage and PV power concerning the variation in solar irradiation are described in Fig 6.10(b) at t = 1.6 s. Even though the solar irradiation was decreased, the MGCPI could supply the active power corresponding to that irradiation as per

the INC-based MPPT characteristics. Thereby, the MGCPI was performing the grid sharing partially and power conditioning without interruption.

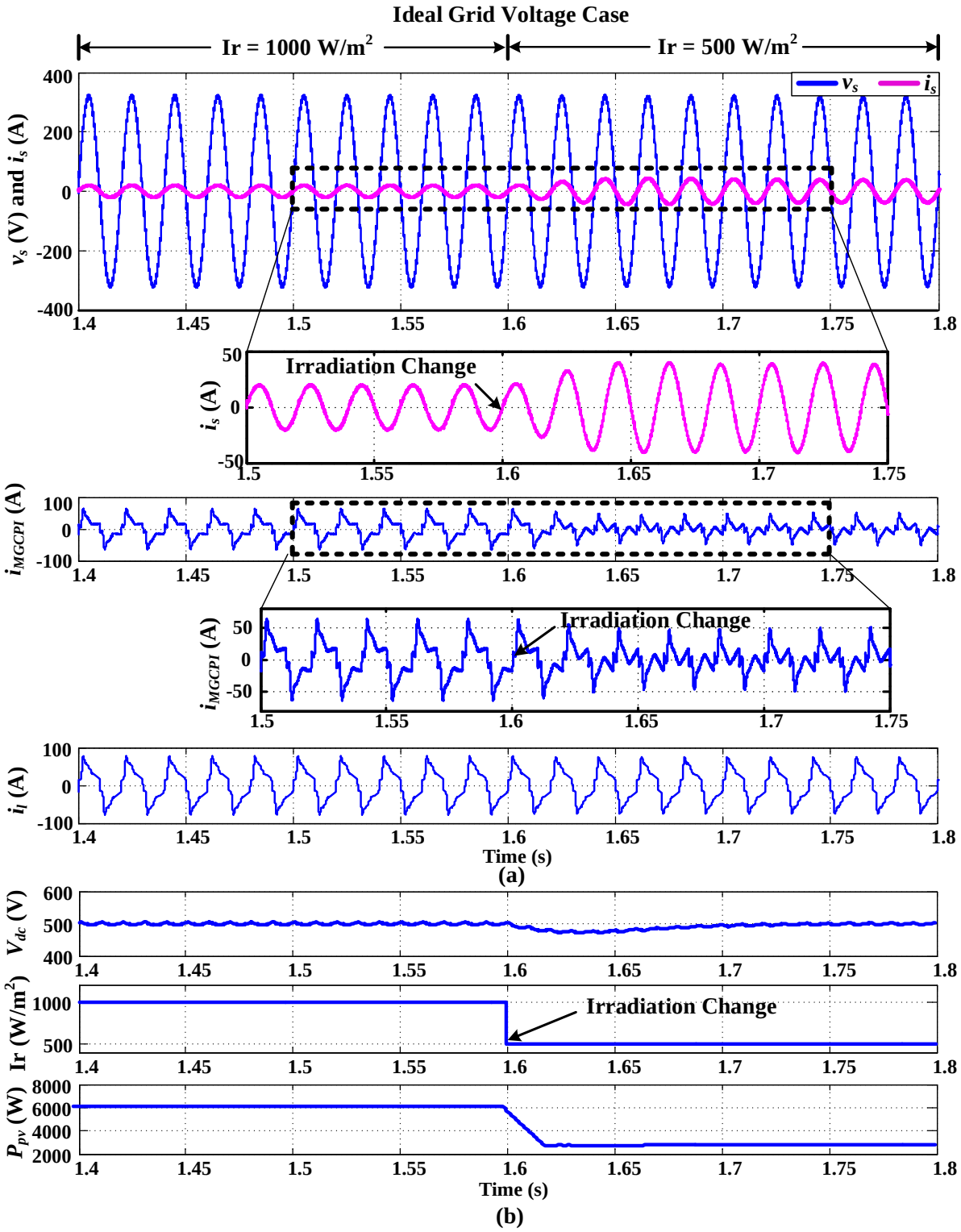

Fig. 6.10 Dynamic response at PCC during grid sharing and power conditioning; (a) ideal grid input voltage, current, MGCPI current, and load current; (b) MGCPI DC-link voltage, solar irradiation, and PV power under the ideal grid

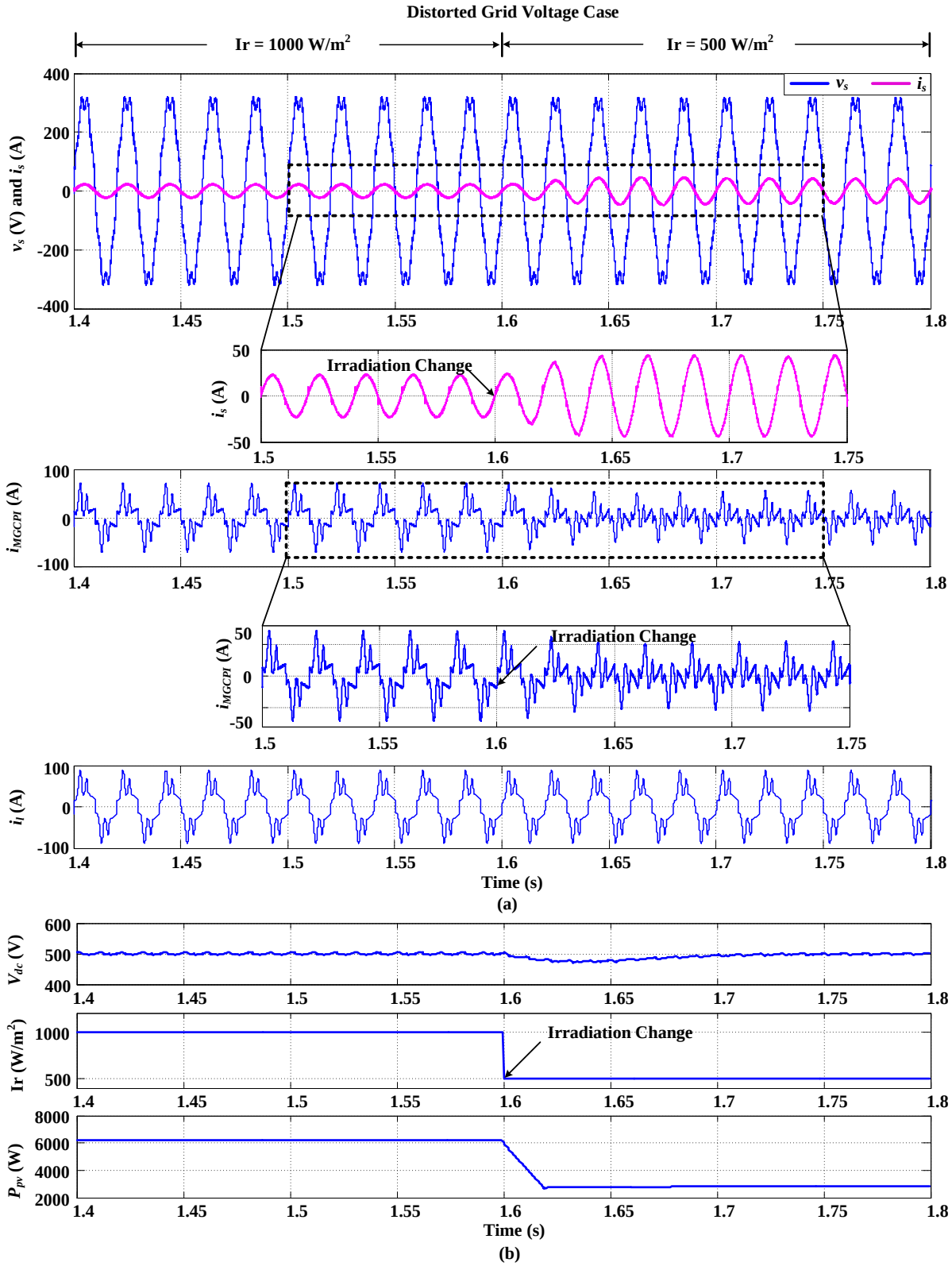

Fig. 6.11 Dynamic response at PCC during grid sharing and power conditioning; (a) distorted grid input voltage, current, MGCPI current, and load current; (b) MGCPI DC-link voltage, solar irradiation, and PV power under the distorted grid

6.4.4.2 Distorted Grid Voltage Case

The dynamic response of the system during the solar irradiation change under the distorted grid condition is presented in Fig 6.11(a),(b). In this case, the current consumption from the grid was increased due to the reduction in PV power because of the irradiation change as shown in Fig 6.11(a). However, the MGCPI executed the power conditioning effectively. The MGCPI was capable of extracting the maximum power with respect to the reduced irradiation as per the INC-based MPPT effectively. Thus, the MGCPI is successful in executing the multi-functional tasks simultaneously without interruption.

6.5 Real-Time Experimental Validation

The RT software in loop (SIL) testing of the MB-HCC based MGCPI integrated to the LVDG is presented in this section. The proposed RTSPV integration system with the LVDG loads was modelled in the RT-LAB environment and tested in RT using the OP4500 RT grid simulator [134-136,141-144]. The main purpose of validating in RT is to understand the proposed MGCPI system behaviour for real-world implementation. The OP4500 is one of the commercially available RT power grid simulators. The detailed architecture and specifications are illustrated in Reference [144]. The laboratory test setup for RT validation is shown in Fig 6.12.

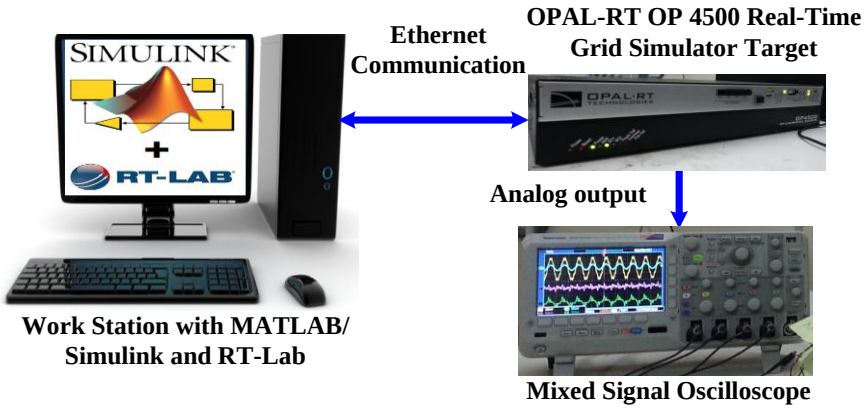

Fig. 6.12 Laboratory test setup of real-time (RT) software in loop (SIL) validation

6.5.1 SIL RT Test Results of Mode 1: MGCPI OFF

The SIL RT test results of the LVDG during the MGCPI OFF condition are depicted in Fig 6.13. These responses are identical to the simulation results depicted in Fig 6.7, and showcase the harmonic and reactive power effects at the PCC of the LVDG under both ideal and distorted grid conditions. Hence, it is essential to improve the LVDG power quality for efficient and reliable operation.

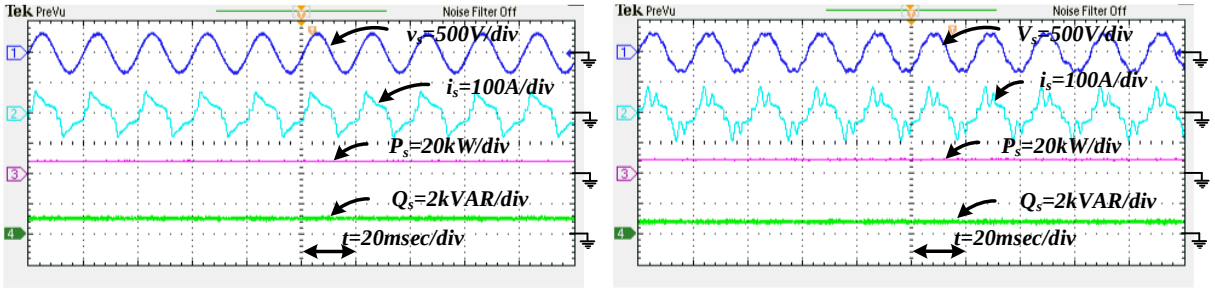

(a) **(b)**

Fig. 6.13 RT SIL test waveforms under MGCPI OFF mode under (a) the ideal grid and (b) the distorted grid

6.5.2 SIL RT Test Results of Mode 2: MGCPI is ON, with Grid Sharing and Power Conditioning

6.5.2.1 Ideal Grid Voltage Case

The SIL RT results of the MGCPI in grid sharing and power conditioning mode are presented in Fig 6.14(a)–(c). The RT results authenticate the simulated results of MGCPI grid sharing and power conditioning operations presented in Fig 6.8. Here, the source current harmonics were compensated, and the source voltage and source current were an in-phase nature. The compensated current injected at the PCC by the MGCPI to make the source current sinusoidal is presented in Fig 6.14(a). However, the load draws the nonlinear current as shown in Fig 6.14(a). The regulated DC-link voltage of 500 V and the RTSPV maximum power of 6 kW extracted at the solar irradiation of 1000 W/m^2 are illustrated in Fig 6.14(b). In Fig 6.14(c), the active and reactive power profiles of the source and MGCPI are depicted. This enumerates the reduction of grid consumption from 9 kW to 3 kW. Furthermore, the source reactive power is reduced to zero by the MGCPI, as described in simulated results.

The simulated DC-link voltage controller had high bandwidth and responded instantaneously, including to the high-frequency current harmonics flowing through the capacitor, observed by rapid variations in the DC-link voltage, as depicted in Fig 6.8. However, in the RT-implemented system, the DC-link voltage was discretized; the whole bandwidth decreased, and there was also moving-average filtering of the analog-to-digital converter (ADC) feedback signals. Therefore, the closed-loop response for such a DC-link voltage control loop was not so rapid, the capacitor voltage had fewer fluctuations, and had less ripple when compared to the simulated case-study, as observed in Fig 6.14. Such a smoother capacitor voltage in RT control is, indeed, a very desirable feature.

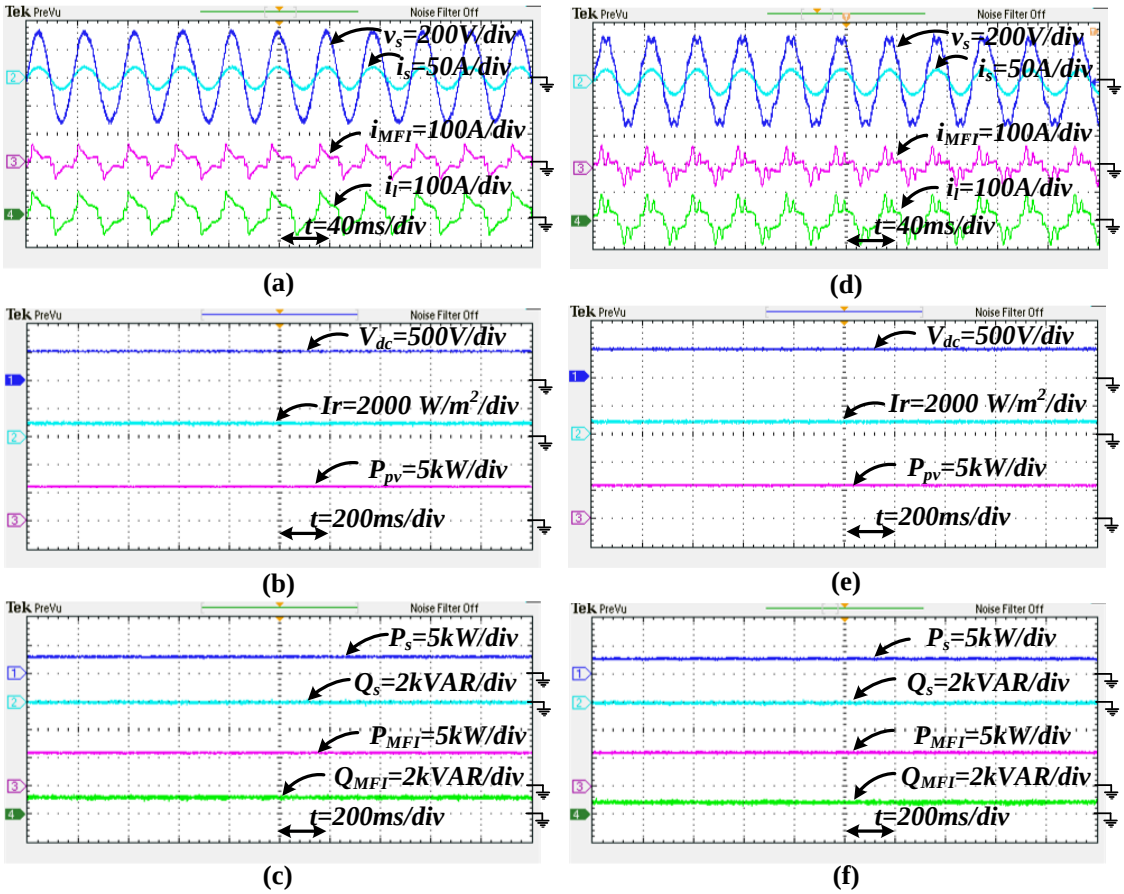

Fig. 6.14 RT SIL test output waveforms under the MGCPI ON, with grid sharing and power conditioning mode; (a) ideal grid input voltage, current, MGCPI current, and load current; (b) MGCPI DC-link voltage, solar irradiation, and PV power under the ideal grid; (c) source active power, reactive power, and MGCPI active and reactive power under the ideal grid; (d) distorted grid input voltage, current, MGCPI current, and load current; (e) MGCPI DC-link voltage, solar irradiation, and PV power under the distorted grid; (f) source active power, reactive power, MGCPI active and reactive power under the distorted grid

6.5.2.2 Distorted Grid Voltage Case

The RT results of the MGCPI grid sharing and power conditioning operation under the distorted grid condition are presented in Fig 6.14(d)–(f). These RT results were identical to the simulated results of the MGCPI grid sharing and power conditioning mode, as illustrated in Fig 6.8(d)–(f). In this case, the source current was sinusoidal, and it was in-phase with the source voltage. However, the load behavior was nonlinear as illustrated in Fig 6.14(d). The MGCPI current injected at the PCC to compensate for the harmonic distortion is described in Fig 6.14(d). The DC-link voltage regulated at 500 V and the RTSPV maximum power of 6 kW extracted at the solar irradiation of 1000 W/m^2 under the distorted grid are illustrated in Fig

6.14(e), which are similar to the simulated results. In Fig 6.14(f), the active and reactive power profiles of the source and MGCPI obtained by the RT simulation are illustrated. These profiles enumerate the reduction of grid consumption from 9 kW to 3 kW, as discussed in the simulated results. Furthermore, the reactive power effect was compensated for successfully.

6.5.3 SIL RT Test Results of Mode 3: MGCPI is ON, with Grid Feeding and Power Conditioning

6.5.3.1 Ideal Grid Voltage Case

The MGCPI grid feeding and power conditioning responses under the ideal grid case when the load consumption as reduced are described in Fig 6.15(a)–(c).

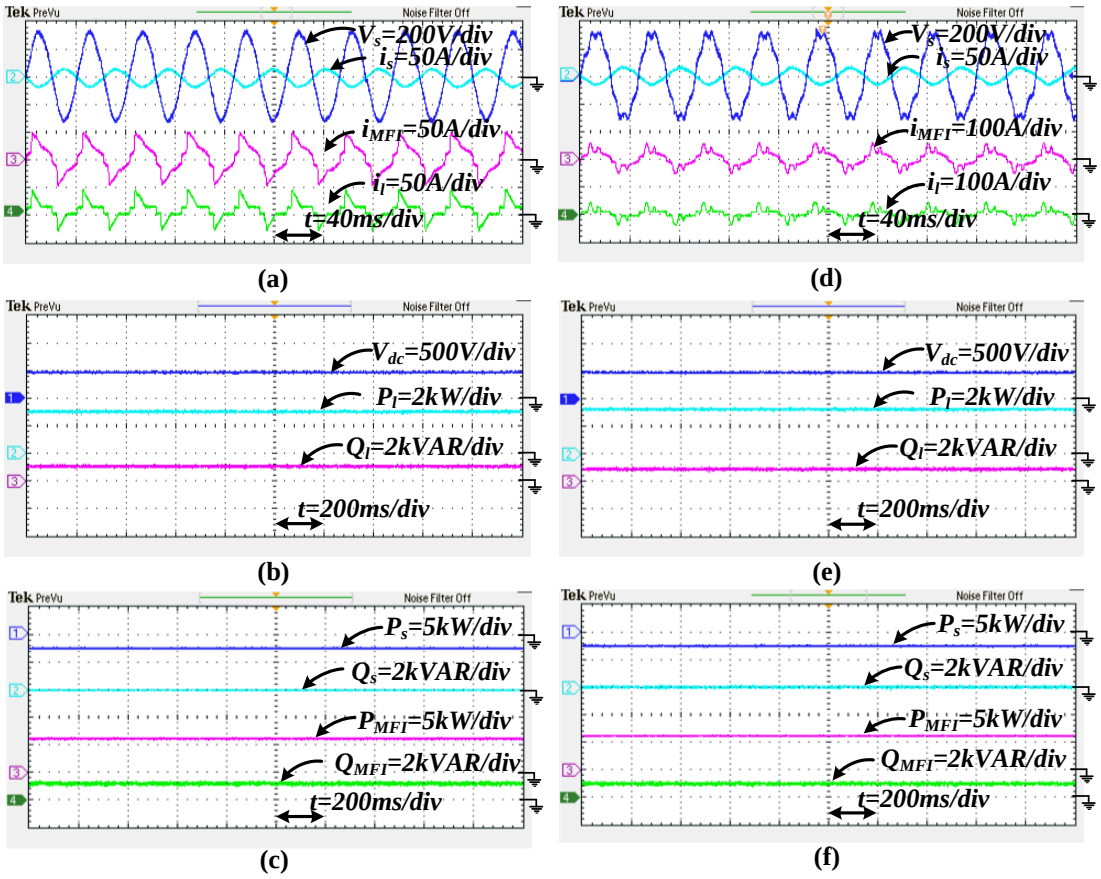

Fig. 6.15 RT SIL test output waveforms under MGCPI ON, with grid feeding and power conditioning mode; (a) ideal grid input voltage, current, MGCPI current, and load current; (b) MGCPI DC-link voltage, solar irradiation, and PV power under the ideal grid; (c) source active power, reactive power, and MGCPI active and reactive power under the ideal grid; (d) distorted grid input voltage, current, MGCPI current, and load current; (e) MGCPI DC-link voltage, solar irradiation, and PV power under the distorted grid; (f) source active power, reactive power, and MGCPI active and reactive power under the distorted grid

In this case, the MGCPI was feeding the load as well as the grid, simultaneously. Moreover, it is also taking care of the harmonic and reactive power compensation. The DC-link voltage regulated at 500 V and the reduced load power and reactive power responses are presented in Fig 6.15(b). The active and reactive power profiles under grid feeding mode are depicted in Fig 6.15(c). Here, the negative response of the active power represents the grid feeding operation; simultaneously, the reactive power at the source side was reduced to zero. The RT results are identical to the simulated results.

6.5.3.2 Distorted Grid Voltage Case

The MGCPI grid feeding and power conditioning responses under the distorted grid case when the load consumption was reduced are described in Fig 6.15(d)–(f). In this case, the MGCPI was feeding the load as well as the grid, simultaneously. Moreover, it as also taking care of the harmonic and reactive power compensation. The DC-link voltage regulated at 500 V and the reduced load power and reactive power responses are presented in Fig 6.15(e) The active and reactive power profiles under the grid feeding mode are depicted in Fig 6.15(f). Here, the negative response of active power represents the grid feeding operation. Moreover, the reactive power at the source side was reduced to zero, simultaneously. The RT results are identical to the simulated results.

6.5.4 SIL RT Test Results of Mode 4: MGCPI is ON, with Grid Sharing and Power Conditioning during Irradiation Change

The pictorial representations of the dynamic source current variation during irradiation change under both the ideal and distorted grid conditions are represented in Fig 6.16(a)–(d). Here, the source current magnitude was increased because of the drop in active power delivery from the MGCPI due to irradiation change from 1000 W/m^2 to 500 W/m^2. Fig 16 responses are identical to the simulation responses of Figs 6.10 and 6.11. Hence, in RT it was also confirmed that the proposed RTSPV interfaced MGCPI performs the power conditioning and power injection for ideal and distorted supply conditions effectively during the irradiation change.

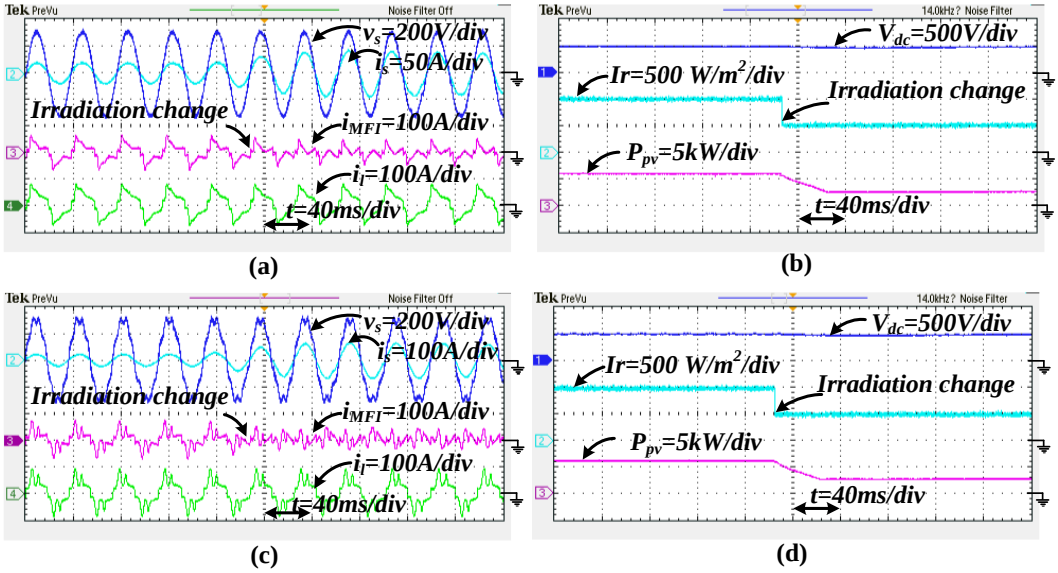

Fig. 6.16 RT SIL test dynamic response at PCC under grid sharing and power conditioning mode during Solar irradiation change (a) Ideal Grid Input Voltage, Current, MGCPI current and load current; (b) MGCPI DC-link voltage, solar Irradiation and PV power under ideal grid; (c) Distorted Grid Input Voltage, Current, MGCPI current and load current; (d) MGCPI DC-link voltage, solar Irradiation and PV power under distorted grid

6.5.5 Active and Reactive Power Exchange

The summary of the active and reactive power profiles of the source, MGCPI, and loads obtained from the RT SIL test are tabulated in Table 6.6.

Table 6.6 Active and reactive power summary under ideal and distorted grid conditions, where Ir = 1000 W/m^2 at 25^{o}C

MGCPI ON		**Full Load – Grid Sharing**		**Reduced Load – Grid Feeding**	
Parameters		**Ideal Grid**	**Distorted Grid**	**Ideal Grid**	**Distorted Grid**
P_s	*(kW)*	3.036	3.329	− 2.877	− 2.755
Q_s	*(kVAR)*	0.004	0.005	0.005	0.003
P_{MGCPI}	*(kW)*	6.039	6.008	6.032	6.020
Q_{MGCPI}	*(kVAR)*	1.002	0.655	1.015	0.800
P_l	*(kW)*	9.075	9.337	3.155	3.265
Q_l	*(kVAR)*	1.006	0.660	1.020	0.803

6.6 Results and Discussion

In this section, the detailed summary of the SIL RT results of the proposed RTSPV integration system and its comparison with the VDB-HCC method presented in Reference [122] are discussed.

6.6.1 MGCPI Switching Frequency

The instantaneous switching frequency values of VDB-HCC and MB-HCC are calculated concerning the switching frequency formula given in Reference [150]. The instantaneous average switching frequency of MGCPI using MB-HCC was maintained at 10 kHz, whereas that of VDB-HCC was at 16 kHz under nonlinear load conditions. The precise tracking of the current in between the two bands (HB1 and HB2) and the corresponding switching logic of inverter resulted in a reduction of switching frequency and hence the switching losses were reduced during the multifunctional operation.

6.6.2 MGCPI Efficiency

The MGCPI efficiency concerning the solar irradiation under both full load and reduced load conditions using VDB-HCC are presented in Fig 6.17.

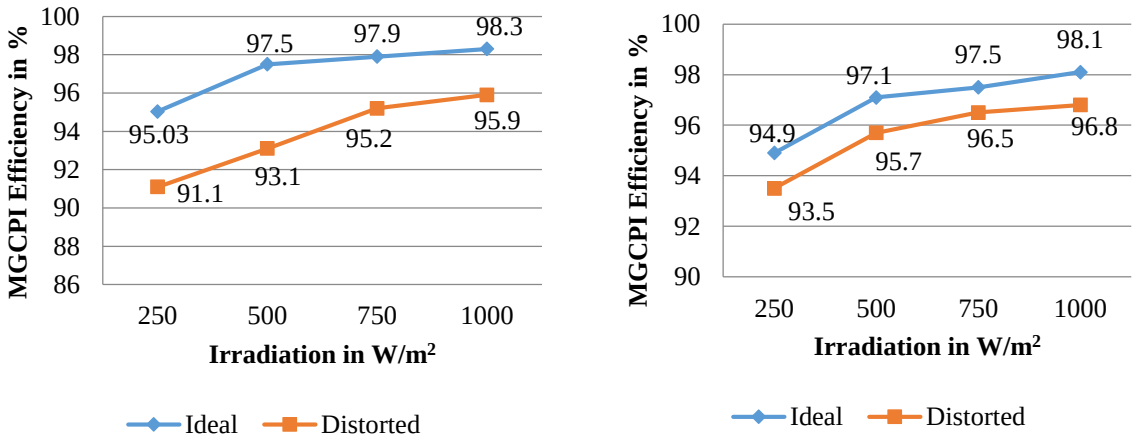

Fig. 6.17 MGCPI efficiency using VDB-HCC: (a) full load; (b) reduced load

The MGCPI had a peak efficiency of 98.3% and an average efficiency of 97.18% under the ideal grid condition at full load. In a distorted grid case, the MGCPI had a peak efficiency of 95.9% and an average efficiency of 93.82% at full load condition. In the reduced load case, the MGCPI had a peak efficiency of 98.1% and an average efficiency of 96.9% under the ideal grid voltage case, whereas in the distorted grid condition, the peak efficiency was 96.9% and

average efficiency was 95.62%. The MGCPI efficiency variation concerning the solar irradiation under both the full load and reduced load conditions using MB-HCC are presented in Fig 6.18. The peak efficiency of the MGCPI was 99.01%, and the average MGCPI efficiency under the ideal grid voltage was 98.77% at the fully loaded condition, whereas in the distorted grid voltage case, the peak efficiency was 98.5% and average efficiency was 97.56%.

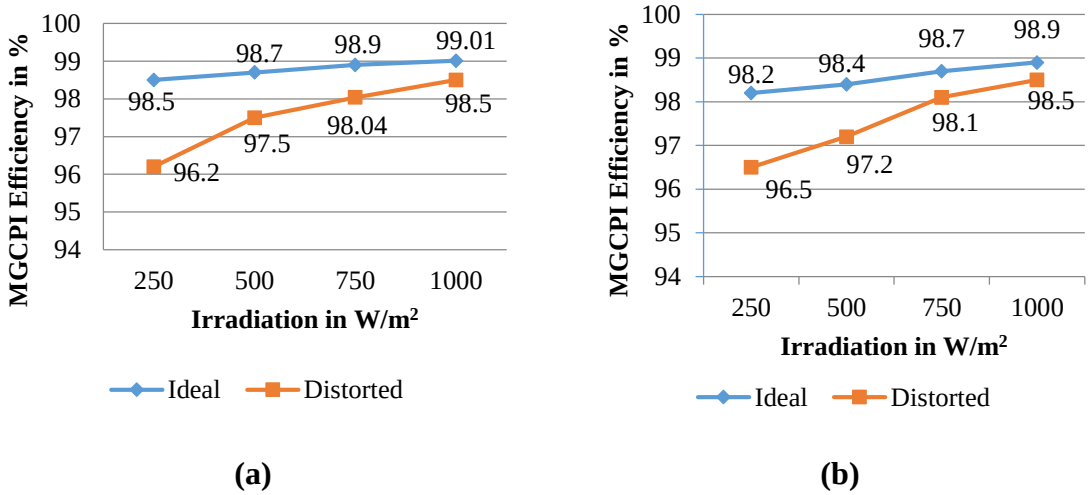

Fig. 6.18 MGCPI efficiency using MB-HCC (a) Full Load; (b) Reduced Load

During the reduced load case, the peak efficiency of the MGCPI was 98.9%, and the average MGCPI efficiency under the ideal grid voltage was 98.55%. In a distorted grid voltage condition, the peak efficiency was 98.5%, and the average efficiency was 97.57%. This means that the MGCPI exhibited better efficiency using MB-HCC under both ideal and distorted grid voltage conditions when compared to the VDB-HCC method. The MGCPI inverter efficiency was reasonable under the lower irradiation case when compared to the VDB-HCC method. However, in the proposed MB-HCC method, the MGCPI efficiency under the lower irradiation condition (i.e., <500 W/m^2) in a distorted grid case was slightly lower when compared to the peak efficiency of the MGCPI at irradiation >500 W/m^2, but the power conditioning task performed effectively as per the requirements of IEEE 519-2014 and IEEE 1547. This was because, under the lower irradiation case, the MB-HCC based MGCPI was more efficient in compensating for the highest percentage THD when compared to the ideal voltage case nonlinear load percentage THD.

6.6.3 Percentage THD at Point Common Coupling

The %THD at PCC during without compensation and with MGCPI compensation cases under ideal and distorted grid voltage conditions using the VDB-HCC method is illustrated in Fig 6.19. The %THD was brought down from 34.08% to 3.56% under the ideal voltage

condition at full load. For the reduced load case, it as reduced from 53.79% to 3.19%. In a distorted grid voltage condition, the %THD was reduced from 42.69% to 2.64% at full load case. In the reduced load case, the %THD was minimized from 64.5% to 3.4%.

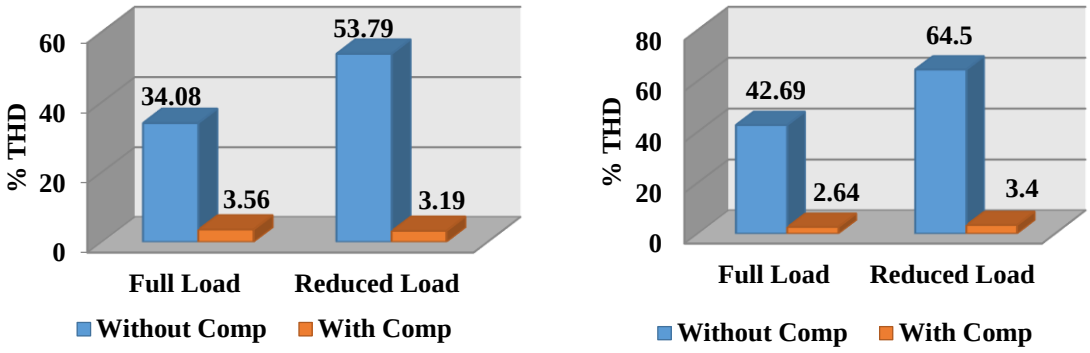

(a) (b)

Fig. 6.19 Percentage THD at PCC using VDB-HCC: (a) ideal grid condition; (b) distorted grid condition

The %THD comparison at PCC during no compensation and with MGCPI compensation using MB-HCC method under ideal and distorted grid conditions are depicted in Fig 6.20. The %THD at full load was brought down from 34.08% to 2.34% under the ideal grid condition, whereas in the half load case it was reduced from 53.79% to 2.98%. In a distorted grid condition, the %THD was reduced from 42.69% to 2.04% under the full load case. In the reduced load case, the %THD was minimized from 64.5% to 2.77%. The %THD results using VDB-HCC and the proposed MB-HCC methods comply with the IEEE 519-2014 and 1547 standards.

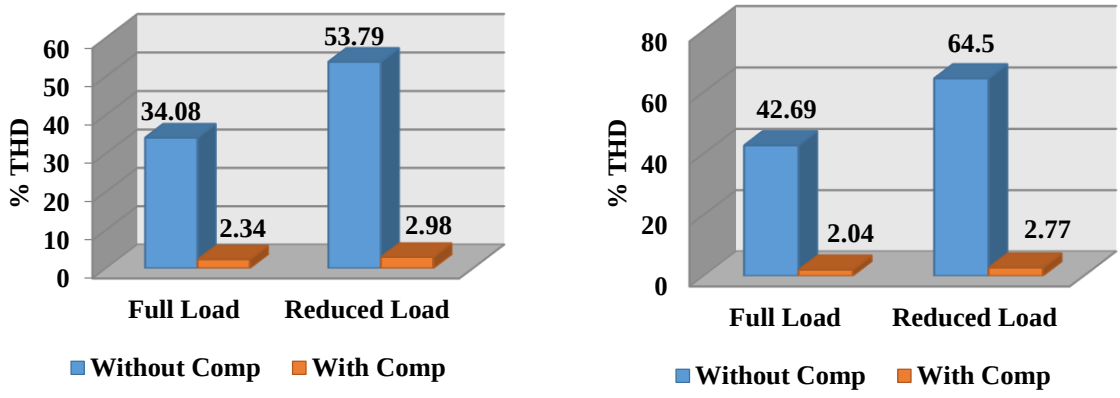

(a) (b)

Fig. 6.20 Percentage THD at PCC using MB-HCC: (a) ideal grid condition; (b) distorted grid condition

6.6.4 True Power Factor at Point of Common Coupling

The true power factor (TPF) at PCC before and after compensation of reactive power, under ideal and distorted grid voltage conditions, using the VDB-HCC method is described in Fig 6.21. Under the ideal grid voltage condition, the TPF was improved from 0.9407 to 0.9993 at full load, whereas in the half load case it was improved from 0.8379 to 0.9990. In a distorted grid condition, the TPF was enhanced from 0.9174 to 0.9996 at full load. In the reduced load case, the TPF was enhanced from 0.816 to 0.9989. The power factor (PF) at PCC before and after compensation of reactive power, under ideal and distorted grid voltage conditions, using the MB-HCC method, are described in Fig 6.22.

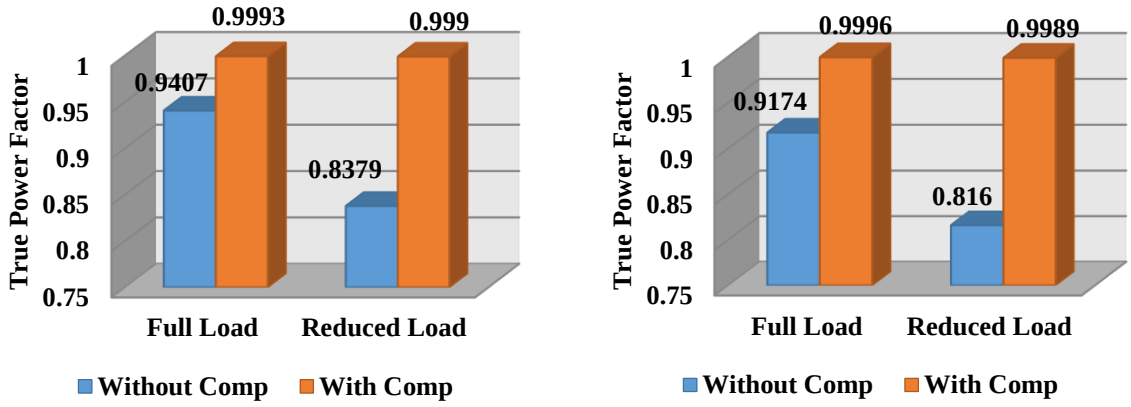

(a) (b)

Fig. 6.21 True power factor at PCC using VDB-HCC: (a) ideal grid condition; (b) distorted grid condition

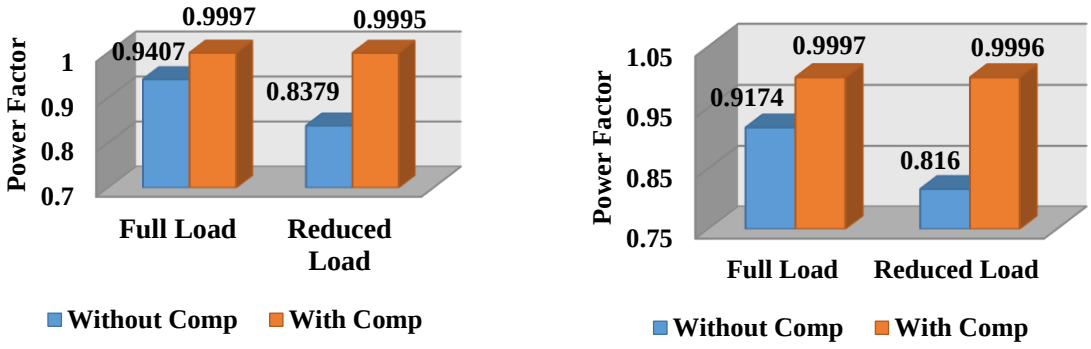

(a) (b)

Fig. 6.22 True power factor at PCC using MB-HCC: (a) ideal grid condition; (b) distorted grid condition

The TPF was improved from 0.9407 to 0.9997 at full load under the ideal grid voltage, whereas in the half load case it was improved from 0.8379 to 0.9995. The TPF under the distorted grid condition was enhanced from 0.9174 to 0.9997 at the full load case. In the reduced load case, the TPF was enhanced from 0.816 to 0.9996. Given the TPF results of the VDB-HCC and MB-HCC methods, both will maintain the TPF close to the unity value. From the summary of the results presented in Table 6.7, it is justified that the MGCPI efficiently performs the power feeding at PCC as per the solar irradiation and compensates the source harmonics and reactive power with reduced switching frequency as per the IEEE 519-2014 and IEEE-1547 standards. These results exhibit the scalability and feasibility of the proposed system in LVDG under ideal and distorted grid conditions.

Table 6.7 RT results summary

	VDB-HCC [122]				**Proposed MB-HCC**			
	Full load		**Reduced Load**		**Full load**		**Reduced Load**	
	Ideal Grid	**Distorted Grid**	**Ideal Grid**	**Distorted Grid**	**Ideal Grid**	**Distorted Grid**	**Ideal Grid**	**Distorted Grid**
Average Efficiency	97.18	93.82	96.9	95.62	↑98.77	↑97.56	↑98.55	↑97.57
% THD	3.56	2.64	3.19	3.4	↓2.34	↓2.04	↓2.98	↓2.77
TPF	0.9993	0.9996	0.999	0.9989	↑0.9997	↑0.9997	↑0.9995	↑0.9996

6.7 Conclusions

The main contributions of this chapter are as follows:

- Scaling factor-based MB-HCC was proposed to MGCPI for power injection and power conditioning operations.
- Verified the proposed MB-HCC MGCPI operation under both ideal and distorted grid conditions using simulation and RT experimental studies.
- Compared the proposed MB-HCC method effectiveness with the VDB-HCC method reported in Reference [30].

This chapter has demonstrated a two-stage RTSPV integration system using a DC-DC boost converter with INC-based MPPT and single-phase MGCPI with the proposed scaling factor-based MB-HCC method. The importance of the RTSPV interfaced MGCPI for grid sharing and feeding capabilities were investigated by a MATLAB/Simulink simulation and

validated with OPAL-RT results. The proposed MB-HCC triggers insulated-gate bipolar transistor (IGBT) switches of the MGCPI through tracking current response between inner and outer hysteresis bands, leading to reduced switching frequency which, in turn, reduces switching losses. The RT results enumerated the potential of the proposed system regarding efficiency and improved PQ capabilities as per IEEE 519-2014 and IEEE 1547 standards. During the variation of solar irradiation, the proposed MGCPI had a peak efficiency of 99.01% and an average output efficiency of 98.77% under the ideal grid, and in the distorted grid case the peak efficiency was 98.5%, and the average efficiency was 97.31%. Moreover, the percentage of total harmonic distortion under ideal and distorted grid conditions was brought down to below 5%, and reactive power compensation was effective, resulting in unity power factor operation. The MGCPI efficiency under the full load condition was elevated by the proposed MB-HCC over the VDB-HCC by 1% under the ideal grid condition and 4% in the distorted grid condition. In the reduced load condition, the MGCPI efficiency was raised by the proposed MB-HCC over the VDB-HCC by 2%, under both ideal and distorted grid conditions. MB-HCC is scalable for variations in the solar irradiation and efficient over the VDB-HCC. The average percentage of THD was reduced up to 2.75%, and the source side power factor was close to unity. The simulation and RT results substantiate the hypothesis of higher efficiency and scalability of the MB-hysteresis current controlled MGCPI for a single-phase LVDG. The proposed two-stage MGCPI with MB-HCC is a unified solution to reduce grid consumption and maintain the PQ of the single-phase LVDG, and hence it is ideal for adoption in support of global green energy initiative.

Publication

This work is published and referenced below:

- **O.V.S.R.Varaprasad**, D.V.S.S.Siva Sarma and M.G.Simões. "**Scalable Single-Phase Multi-Functional Inverter for Integration of Rooftop Solar-PV to Low-Voltage Ideal and Weak Utility Grid,"** *Electronics,* 8, no. 3 (2019): 302.

Chapter 7

Conclusions & Future Scope

7.1 Conclusions

The total harmonic distortion (THD) of current due to various real-world nonlinear loads are growing day by day as nonlinear loads are in the rise which is well above the recommended Institute of Electrical and Electronics Engineers (IEEE) standard of 519-2014 [10]. Chapter 1 comprehensively reviewed the state of art of research in estimation and control of these harmonics for the past two decades.

Chapter 1 exploited PLIS based DSLIFFT with 4-Term MSCW for estimation of current harmonics in smart electric grid. The PLIS-based DSLIFFT with 4MSCW has better accuracy and precision under non-synchronous sampling, low amplitude, and fractional harmonic frequency when compared to previous DSLIFFT solutions. Simulation and experimental results corroborate the effectiveness, using the techniques described in this thesis for current harmonic estimation under variable frequency conditions. Improved performance indices were examined with experimental results by considering real-world load harmonic signals. The simulation and experimental results satisfy requirements of international standards such as IEC 61000-4-7, 4-30, and IEEE 1159-2009. Therefore, the developed PLIS-based DSLIFFT with 4MSCW can estimate current harmonics at variable grid frequencies in real-time, ready to retrofit any power system or smart-grid installation.

Chapter 2 described an Adaptive PLIS based DSLIFFT with First-order Polynomial Time Window (PTW) and 4-Term MCSW for estimation of time-varying harmonics and inter-harmonics under noise effect in a smart electric grid. The adaptive PLIS-based DSLIFFT with 4MSCW can estimate current harmonics and inter-harmonics, under time-varying distorted conditions and variable grid frequencies in real-time.

Both PLIS based DSLIFFT and adaptive PLIS-based DSLIFFT with 4-Term MSCW are highly accurate and is useful for utilities to introduce policies to penalize residential, commercial and industrial consumers that indirectly pollute grid with higher-order harmonics into the distribution system which cause damages to the distribution transformer and other protection equipment of distribution grid. Chapter 2 and Chapter 3 have clearly demonstrated the estimation capabilities of the developed algorithms.

Once the harmonics attract penalty, consumers would turn their attention towards compensation of harmonics locally therefore compensation of harmonics using Conservative Power Theory (CPT) based Hybrid Active Power Filter (HAPF) on industrial power systems is described in chapter 4. The CPT based Type-II current controlled HAPF solution removes the harmonics, compensating the distorted current component and also minimizes the unbalance and reactive power effectively without replacing the existing PFs. It compensates all the leftover harmonics of the PFs. The real-time results justify the performance of the system adequately. Hence, the Type-II current controlled HAPF using CPT improves the behavior of the system.

CPT and Battery Storage System (BSS) based Two-stage Three-phase MGCPI with Think-Ahead Decision (TAD) algorithm for power conditioning and power injection was demonstrated in chapter 5. A CPT based three-phase Multifunctional grid-connected PV inverter (MGCPI) coupled with a Battery Storage System (BSS) exhibited the multifunctional capacity consisted of improving the power quality in the point of common coupling (PCC) and active power injection simultaneously. The CPT is used for computing the MGCPI current reference signals during the APF operation mode. An effective TAD algorithm is developed to determine the best mode of operation for the MGCPI, taking into account the State-of-Charge of the BSS and the available power at the PV source. The controllers for the MGCPI and the BSS as well as an Incremental-Conductance (INC) based MPPT algorithm are described in detail. The experimental results showed that the MGCPI performed multi-functionalities in the right manner. The evaluated scenarios do not show any unpredictable oscillatory behavior. Therefore, the configuration is a holistic solution to integrate the PV system into the distribution grid and contributes to the sustainability of the smart electric grids without any negative impact on quality of power.

Chapter 6 illustrated the MB-HCC based single-phase MGCPI for power injection and power conditioning on single-phase distribution system with improved efficiency. Local compensation of harmonics through MGCPI is advisable as it is fool proof and requires no additional reactive compensation on consumer front.

The real-time results enumerated the potential of the MB-HCC based MGCPI system regarding efficiency and improved power quality capabilities as per IEEE 519-2014 and IEEE 1547 standards. During the variation of solar irradiation, the MGCPI had a peak efficiency of 99.01% and an average output efficiency of 98.77% under the ideal grid, and in the distorted grid case the peak efficiency was 98.5%, and the average efficiency was 97.31%. Moreover, the percentage of total harmonic distortion under ideal and distorted grid conditions was brought down to below 5%, and reactive power compensation was adequate, resulting in a unity power factor operation. The MGCPI efficiency under the full load condition was elevated by the MB-HCC over the VDB-HCC by 1% under the ideal grid condition and 4% in the distorted

grid condition. In the reduced load condition, the MGCPI efficiency was raised by the MB-HCC over the VDB-HCC by 2%, under both ideal and distorted grid conditions. MB-HCC is scalable for variations in the solar irradiation and efficient over the VDB-HCC. The average percentage of THD was reduced up to 2.75%, and the source side power factor was close to unity. The simulation and RT results substantiate the hypothesis of higher efficiency and scalability of the MB-HCC based MGCPI for a single-phase LVDS. The two-stage MGCPI with MB-HCC is a unified solution to reduce grid consumption and maintain the PQ of the single-phase LVDS, and hence, it is ideal for adoption in support of global green energy initiative.

This work is very relevant to the utility, commercial and residential consumers through highly accurate and simple estimation of current harmonics of all types and controlling these harmonics by designing suitable control methodologies for improving the effectiveness of compensation devices in the modern electric grid. This work takes care of every possible type of non-linear loads now and in the future. The thesis clearly demonstrates the harmonic estimation and compensation methods necessary for transforming the smart electric grid.

7.2 Future Scope

The PLIS based DSLIFFT with new windows can be further explored for estimation of harmonic and synchro phasor simultaneously. Moreover PLIS based DSLIFFT with 4-term MSCW can be adopted for wide-area monitoring systems and also to exploit its application for smart energy meters is one of the topic of interest in order to quantify the level of harmonic distortion from the consumer front and to insist penalties by the utility in their electricity tariffs for polluting the distribution grid to encourage harmonic compensation at the same.

The Conservative power theory (CPT) application on reduced switch count multi-level inverters for multifunctional operation on high power applications is one of the topics of interest. Further PLIS based DSLIFFT and CPT based MGCPI with machine learning algorithms for automating the smart electric grid featuring the self-healing capability from the harmonic pollution.

Bibliography

[1] H.Gharavi, R.Ghafurian, eds., "Smart grid: The electric energy system of the future," *Proc. IEEE*, vol. 99, no. 6, pp. 917-921, Jun, 2011.

[2] V.Agarwal, LH.Tsoukalas, "Smart grids: importance of power quality," in *Intern. Conf on Energy-Efficient Computing and Networking*., Athens, Greece, 2010, pp. 136-143.

[3] J.Sousa, M.T.C.de Barros, M.Covas, A.Simoes, "Harmonics and flicker analysis in arc furnace power systems," in *Proc. Intern. Conf. Power Systems Transients.,* Budapest, Hungary, 1999, pp. 626-630.

[4] J.Arrillaga, N.R.Watson, "Power system harmonics," iind ed. West sussex, England, John Wiley & Sons, 2004.

[5] O.A.M.Astorga, J.L.Silveira, J.C.Damato, "The influence of harmonics from non-linear loads in the measuring transformers of electrical substations," *Renew. Energy & Power Qulaity Journal*, vol.1, no.4, pp. 275–280, Apr 2006.

[6] A.Iagar, G.N.Popa, C.M.Dinis, "The influence of home nonlinear electric equipment operating modes on power quality," *WSEAS Trans. Sys.,* vol.13, pp. 357-367, Jan 2014.

[7] http://www.powergrid.in/sites/default/files/footer/climate_change/Swachh_Power.pdf

[8] P.M.Nicolae, R.F.Marinescu, D.C.Marinescu, M.S.Nicolae, I.D.Nicolae, "Harmonics induced by inverters from a photovoltaic plant in the power grid," in *Proc. 2008 IEEE Intern. Symp. Electromag. Compatibility and 2018 IEEE Asia-Pacific Symposium on Electromagnetic Compatibility (EMC/APEMC)*, Singapore, 2018, pp. 821-826.

[9] C.Francisco, "Harmonics, power systems, and smart grids," iind ed. CRC Press, Boca Raton, Florida, USA, 2015, pp. 1-278.

[10] IEEE Standard 519-2014 (Revision of IEEE Std 519-1992), IEEE Recommended Practice and Requirements for Harmonic Control in Electric Power Systems, NY, USA, 2014.

[11] X.Yu, C.Carlo, T.E.Dillon, M.G.Simões, "The New Frontier of Smart Grids," *IEEE Indus. Elec. Magazine*, vol. 5, no. 3, pp. 49-63, Oct 2011.

[12] A.R.Jerin, N.Prabaharan, N.M.Kumar, K.Palanisamy, S.Umashankar, P.Siano, "Smart grid and power quality issues," in *Hybrid-Renewable Energy Systems in Microgrids*, 2018, Woodhead Publishing Series in Energy, Jan 1, pp. 195-202.

[13] M.H.Bollen, I.Y.Gu, "Signal processing of power quality disturbances," IEEE Press and John Wiley & Sons, 2006.

[14] P.F.Ribeiro, editor. "Time-varying waveform distortions in power systems". IEEE Press and John Wiley & Sons, 2009.

[15] P.F.Ribeiro, C.A.Duque, P.M.Ribeiro, A.S.Cerqueira, "Power systems signal processing for smart grids," John Wiley & Sons, 2013.

[16] L.R.M.Silva, C.A.Duque, P.F.Ribeiro, "Smart signal processing for an evolving electric grid," *EURASIP Journal on Advances in Signal Processing*, vol. 44, no. 1, pp. 1-13, Dec 2015.

[17] IEC Standard 61000-4-7: General Guide on Harmonics and Interharmonics Measurements and Measuring Instruments for Power Supply Networks and Attached Devices Used for the Measurements, Geneva, Switzerland, 2009.

[18] IEC Standard 61000-4-30: Power Quality Measurement Methods, Geneva, Switzerland, 2015.

[19] IEEE Standard 1159-2009: IEEE Recommended Practice for Monitoring Electric Power Quality, NY, USA, 2009.

[20] S.K.Jain, S.N.Singh, "Harmonics estimation in emerging power system: Key issues and challenges," *Electr. Power Syst. Res*., vol. 81, no. 9, pp. 1754–1766, Sep 2011.

[21] C.I.Chen, Y.C.Chen, "Comparative study of harmonic and interharmonic estimation methods for stationary and time-varying signals," *IEEE Trans. Ind. Elec*., vol.61, no. 1, pp. 397–404, Jan 2013.

[22] C.Tao, D.Shanxu, R.Ting, L.Fangrui, "A robust parametric method for power harmonic estimation based on M-estimators," *Measurement*, vol. 43, no. 1, pp. 67-77, Jan 2010.

[23] L.Zhou, X.Li, H.Xu, P.Zhu, "Multi-innovation stochastic gradient method for harmonic modelling of power signals," *IET Signal Processing*, vol. 10, no. 7, pp. 737-42, Sep 2016.

[24] P.Nayak, S.Jena, "Estimation of Harmonics in Microgrid using Unscented Kalman Filter," *Int. J. Pure Appl. Math*., vol. 114, no. 9, pp. 73-81, 2017.

[25] G.S.Hu, F.F.Zhu, "An improved Chirplet transform and its application for harmonics detection," *Circuits and Systems*, vol. 2, no. 03, pp. 107-11, Jul 2011.

[26] F.Zhang, Z.Geng, W.Yuan, "The algorithm of interpolating windowed FFT for harmonic analysis of electric power system," *IEEE Trans. Power Deliv.*, vol. 16, no. 2, pp. 160–164, Apr 2001.

[27] F.J.Harris, "On the use of windows for harmonic analysis with the discrete Fourier transform," *Proc. IEEE*, vol. 66, no. 1, pp. 51-83, Jan 1978.

[28] K.M.M.Prabhu, "Window Functions and Their Applications in Signal Processing," ist ed., CRC Press: Boca Raton, FL, USA, 2013.

[29] P.Singla, T.Singh, "Desired order continuous polynomial time window functions for harmonic analysis," *IEEE Trans. Instr. Meas*., vol. 59, no. 9, pp. 2475-2481, Sep 2010.

[30] G.W.Chang, C.I.Chen, Y.J.Liu, M.C.Wu, "Measuring power system harmonics and interharmonics by an improved fast Fourier transform-based algorithm," *IET Gen. Tran. Dist.*, vol. 2, no. 2, pp. 193–201, Mar 2008.

[31] K.F.Chen, Y.F.Li, "Combining the Hanning windowed interpolated FFT in both directions," *Comput. Phys. Commun*., vol. 178, no. 12, pp. 924–928, Jun 2008.

[32] H.Wen, Z.Teng, S.Guo, J.Wang, B.Yang, Y.Wang, T.Chen, "Hanning self-convolution window and its application to harmonic analysis," *Sci. China Ser. E Technol. Sci.*, vol. 52, no. 2, pp. 467–476, Feb 2009.

[33] B.Zeng, Z.Teng, "Parameter estimation of power system signals based on cosine self-convolution window with desirable side-lobe behaviors," *IEEE Trans. Power Deliv*., vol. 26, no. 1, pp. 250–257, Jan 2011.

[34] H.Wen, Z.Teng, Y.Wang, B.Zeng, X.Hu, "Simple interpolated FFT algorithm based on minimize sidelobe windows for power-harmonic analysis," *IEEE Trans. Power Electron.*, vol. 26, no. 9, pp. 2570–2579, Feb 2011.

[35] B.Zeng, Y.Zhou, Z.Teng, G.Li, "A novel approach for harmonic parameters estimation under nonstationary situations," *Int. J. Elec. Power Energy Syst.*, vol. 44, no. 1, pp. 930–937, Jan 2013.

[36] O.V.S.R.Varaprasad, D.V.S.S.S.Sarma, R.K.Panda, "Advanced windowed interpolated FFT algorithms for harmonic analysis of electrical power system" in *Proc. of the National Power System Conference (NPSC)*, IIT, Guwahati, India, 2014; pp. 1–6.

[37] H.Wen, H.Dai, Z.Teng, Y.Yang, F.Li, "Performance comparison of windowed interpolation FFT and quasisynchronous sampling algorithm for frequency estimation," *Math. Probl. Eng*., pp. 1–7, 2014.

[38] S.R.Chintakindi, O.V.S.R.Varaprasad, D.V.S.S.S.Sarma, "Improved Hanning window based interpolated FFT for power harmonic analysis," *in Proc. TENCON 2015–2015 IEEE Region 10 Conference*, Macao, China, 2015, pp. 1–5.

[39] P.Rai, O.V.S.R.Varaprasad, D.V.S.S.S.Sarma, "An overview of power harmonic analysis based on Triangular Self Convolution window," in Proc. *National Power System Conference (NPSC)*, IEEE, Bhubaneswar, India, pp. 1–5, Dec 2016.

[40] T.A.Tianyuan, C.H.Wenjuan, L.Kaipei, N.Xiong, J.Zhang, W.A.Junhua, "Harmonic analysis based on time domain mutual-multiplication window," *J. Mod. Power Syst. Clean Energy*, vol. 4, no. 1, pp. 47–53, Jan 2016.

[41] T.Jin, Y.Chen, R.C.Flesch, "A novel power harmonic analysis method based on Nuttall-Kaiser combination window double spectrum interpolated FFT algorithm," *J. Electr. Eng.*, 2017, vol. 68, no. 6, pp.435–443, Nov 2017.

[42] Y.Zhu, Y.Wang, T.Lin, C.Feng, J.Chen, Y.Gao, "Harmonic Analysis of Power System Based on Nuttall self-convolution Window Triple-spectral-line Interpolation FFT," *in Proc. 2nd International Conference on Control, Automation and Artificial Intelligence (CAAI 2017), Advances in Intelligent Systems Research*, Sanya, China, Atlantis Press, vol. 134, pp. 438–441, Jun 2017.

[43] C.Gherasim, J.Driesen, R.Belmans, "Real-time implementation and comparison of time-varying harmonic measurement methods," *in 2006 IEEE PES Power Systems Conference and Exposition*, Atlanta, GA, USA, 2017, pp. 239–245.

[44] J.R.Carvalho, C.A.Duque, M.V.Ribeiro, A.S.Cerqueira, P.F.Ribeiro, "Time-varying harmonic distortion estimation using PLL based filter bank and multirate processing," in Proc. VII Brazilian Conference on Electric Power Quality (Conferência Brasileira sobre Qualidade de Energia Elétrica), Santos-SP, Brasil, 2007, pp. 1-6.

[45] Y.B.Lim, S.W.Sohn, J.J.Yun, H.D.Bae, H.Choi, "Time varying harmonics estimation of power signal based on filter banks and adaptive filtering," *in Proc. 2010 IEEE Instrumentation & Measurement Technology Conference*, 2010, pp. 829-834.

[46] C.A.Duque, P.M.Silveira, T.L.Baldwin, P.F.Ribeiro, "Tracking simultaneous time-varying power harmonic distortions using filter banks," in *Proc. 2010 IEEE Industrial and Commercial Power Systems Technical Conference*., Tallahassee, FL, USA, 2010, pp. 1-9.

[47] S.K.Jain, D.Saxena, S.N.Singh, "Adaptive wavelet neural network based harmonic estimation of single-phase systems," in *Proc. 2011 International Conference & Utility Exhibition on Power and Energy Systems: Issues and Prospects for Asia (ICUE)*, Pattaya City, Thailand, 2011, pp. 1-7.

[48] M.Biswal, P.K.Dash, "Estimation of time-varying power quality indices with an adaptive window-based fast generalised S-transform," *IET Sci., Meas. & Tech.*, vol. 6, no. 4, pp. 189-197, Jul 2012.

[49] S.K.Jain, S.N.Singh, "ESPRIT assisted artificial neural network for harmonics detection of time-varying signals," in *Proc. 2012 IEEE Power and Energy Society General Meeting*, 2012, San Diego, CA, USA pp. 1-7.

[50] C.A.Marques, M.V.Ribeiro, C.A.Duque, E.A.da Silva, "Parameters Estimation of Time-Varying Harmonics," in *Power Quality Issues*, 2013 Apr 17. IntechOpen. Available from: https://www.intechopen.com/books/power-quality-issues/parameters-estimation-of-time-varying-harmonics

[51] S.K.Jain, S.N.Singh, "Fast harmonic estimation of stationary and time-varying signals using EA-AWNN," *IEEE Trans. Instr.Meas.*,vol. 62, no. 2, pp. 335-343, Feb 2013.

[52] C.I.Chen, Y.C.Chen, "Comments on Time-Varying Harmonic and Interharmonic Estimation Methods," in *Proc. 2014 International Symposium on Computer, Consumer and Control*, Taichung, Taiwan, 2014, pp. 585-588.

[53] P.Nayak, B.N.Sahu, "A robust extended Kalman filter for the estimation of time varying power system harmonics in noise," in *Proc. 2015 IEEE Power, Communication and Information Technology Conference (PCITC)*, Bhubaneswar, India, 2015, pp. 635-640.

[54] S.K.Jain, "Algorithm for dealing with time-varying signal within sliding-window for harmonics estimation," *IET Sci., Meas. & Tech.*, , vol. 9, no. 8, pp. 1023-1031, Nov 2015.

[55] W.Yao, Z.Teng, Q.Tang, Y.Gao, "Measurement of power system harmonic based on adaptive Kaiser self-convolution window," *IET Gen. Tran. Distr.*, vol. 10, no. 2, pp. 390–398, Feb 2016.

[56] J.C.Das, "Passive filters-potentialities and limitations," *IEEE Trans. Indus Applic*., vol. 40, no. 1, pp. 232–241 , Jan-Feb 2004.

[57] M.Maciążek, D.Grabowski, M.Pasko, M.Lewandowski, "Compensation based on active power filters–The cost minimization" *Applied Mathematics and Computation*, vol. 267, pp. 648-654, Sep 2015.

[58] B.Singh, K.Al-Haddad, A.Chandra, "A review of active filters for power quality improvement," *IEEE Trans. Ind. Electron.*,vol. 46, no. 5, pp 960–971, Oct 1999.

[59] H.Akagi, "Active harmonic filters," *Proc. IEEE*, vol. 93, no. 12, pp. 2128-2141, Dec 2005.

[60] H.Fujita, T.Yamasaki, H.Akagi, "A hybrid active filter for damping of harmonic resonance in industrial power systems," *IEEE Trans. Power Elec*., vol. 15, no. 2, pp. 215-222, Mar 2000.

[61] S.P.Litrán, P.Salmeron, "Analysis and design of different control strategies of hybrid active power filter based on the state model," *IET Power Elec*., vol. 5, no. 8, pp. 1341–1350, Sep 2012.

[62] C.S.Lam, X.X.Cui, W.H.Choi, M.C.Wong, Y.D.Han, "Minimum inverter capacity design for LC-hybrid active power filters in three-phase four-wire distribution systems," *IET Power Elec*., vol. 5, no. 7, pp. 956-968, Aug 2012.

[63] C.S.Lam, M.C.Wong, Y.D.Han, "Hysteresis current control of hybrid active power filters," *IET Power Elec*., vol. 5, no. 7, pp 1175-1187, Aug 2012.

[64] P.Dey, C.M.Reza, T.M.Masum M.M.Rahman, A.U.Ahmed, F.Bin Aziz, "Performance evaluation of reference current extraction methods for hybrid active power filter" *in Proc. 2013 International Conference on Informatics, Electronics and Vision (ICIEV)*, Dhaka, Bangladesh, 2013, pp. 1-6.

[65] T.Demirdelen, M.Inci, K.Ç.Bayindir, M.Tümay, "Review of hybrid active power filter topologies and controllers," *Proc. In 4th International Conference on Power Engineering, Energy and Electrical Drives*, Istanbul, Turkey, 2013, pp. 587-592.

[66] S.Rahmani, A.Hamadi, K.Al-Haddad, L.A.Dessaint, "A combination of shunt hybrid power filter and thyristor-controlled reactor for power quality," *IEEE Trans. Ind. Elctron*., vol. 61, no. 5, pp. 2152-2164, May 2014.

[67] T.N.Nguyen, A.Luo, Z.Shuai, M.TChau, M.Li, L.Zhou, "Generalised design method for improving control quality of hybrid active power filter with injection circuit," *IET Power Elec*. vol. 7, no. 5, pp. 1204-1215, May 2014.

[68] L.Herman, I.Papic, B.Blazic, "A proportional-resonant current controller for selective harmonic compensation in a hybrid active power filter," *IEEE Trans. Power Del*., vol. 29, no. 5, pp. 2055-2065, Aug 2014.

[69] A.K.Unnikrishnan, S.J.TG, A.S.Manju, A.Joseph,"Shunt hybrid active power filter for harmonic mitigation: A practical design approach," *Sadhana*, vol. 40, no. 4, pp. 1257–1272, Jun 2015.

[70] T.L.Lee, Y.C.Wang, J.C.Li, J.M.Guerrero, "Hybrid active filter with variable conductance for harmonic resonance suppression in industrial power systems," *IEEE Trans. Indus. Elec.* vol. 62, no. 2, pp. 746-756, Aug 2015.

[71] P.Dey, S.Mekhilef, "Current harmonics compensation with three-phase four-wire shunt hybrid active power filter based on modified D–Q theory" *IET Power Elec*., vol. 8, no. 11, pp. 2265-80, Nov 2015.

[72] H.Akagi, E.H.Watanabe, M.Aredes, "Instantaneous Power Theory and Applications for Power Conditioning," Wiley-IEEE Press, 2007, pp. 41-102.

[73] L.Asiminoaei, F.Blaabjerg, S.Hansen, "Detection is key-Harmonic detection methods for active power filter applications," *IEEE Indus. Appl. Magazine*, vol. 13, no. 4, pp. 22-33, Jul 2007.

[74] M.Maciążek, "Power theories applications to control active compensators" In 'Power Theories for Improved Power Quality' Springer London, 2012, pp. 49-116.

[75] M.E.Balci, M.H.Hocaoglu, "Quantitative comparison of power decompositions" *Elec. Power Systems Res.*, vol. 78, no. 3, pp. 318-329, Mar 2008.

[76] M.E.Balci, M.H.Hocaoglu, "A power resolution for nonsinusoidal and unbalanced systems—Part II: Theoretical background," *Proc.7th IEEE Intern. Conf. Elec. Electron. Eng. (ELECO)*, Bursa, Turkey, 2011, pp. I-173-I-178.

[77] M.E.Balci, M.H.Hocaoglu, "Addendum to a power resolution for nonsinusoidal and unbalanced systems: Evaluation examples" *Proc.7th IEEE International Conference on Electrical and Electronics Engineering (ELECO)*, Bursa, Turkey, 2011, pp.I-179-I-182.

[78] P.Tenti, H.K.M.Paredes, P.Mattavelli, "Conservative power theory, a framework to approach control and accountability issues in smart microgrids," *IEEE Trans. Power Elec*., vol. 26, no. 3, pp. 664-673, Mar 2011.

[79] Gaëtan Masson, Mary Brunisholz, PVPS., "Snapshot of global photovoltaic markets 2016 (Report IEA-PVPS T1-31, 2017)", pp. 1-16.

[80] SolarPower Europe., "Global market outlook for solar power 2017-2021 (Solar power europe report, Brussels, Belgium)," pp. 1-60.
https://resources.solarbusinesshub.com/images/reports/172.pdf

[81] S.Chatterjee, P.Kumar, S.Chatterjee, "A techno-commercial review on grid connected photovoltaic system," *Renew. Sust. Energy Rev*., vol. 81, no. 2, pp. 2371–2397, Jan 2018.

[82] A.Anzalchi, A.Sarwat, "Overview of technical specifications for grid-connected photovoltaic systems," *Energy Conv. and Manag*., 152, pp. 312-327, Nov 2017.

[83] B.Kroposki, C.Pink, R.DeBlasio, H.Thomas, M.G.Simões, P.K.Sen, "Benefits of power Electronic Interfaces for Distributed Energy Systems," *IEEE Trans. Energy Conversion*, vol. 25, no. 3, pp. 901-908, Sep 2010.

[84] B.K.Bose, "Power Electronics, Smart Grid, and Renewable Energy Systems," *Proc. IEEE*, vol. 105, no. 11, pp. 2011-2018, Sep 2017.

[85] Y.K.Wu, J.H.Lin, H.J.Lin, "Standards and guidelines for grid-connected photovoltaic generation systems: A review and comparison," *IEEE Trans. Ind. Appl*., vol. 53, no. 4, pp. 3205-3216, Mar 2017.

[86] Z.Zeng, H.Yang, R.Zhao, C.Cheng "Topologies and control strategies of multi-functional grid-connected inverters for power quality enhancement: A comprehensive review," *Renew. Sust. Energy Rev*., vol. 24, pp. 223-270, Aug 2013.

[87] L.Hassaine, E.OLias, J.Quintero, "Overview of power inverter topologies and control structures for grid connected photovoltaic systems," *Renew. Sust. Energy Rev*., vol. 30, pp. 796-807, Feb 2014.

[88] O.V.S.R.Varaprasad, D.Bharath Kumar, D.V.S.S.S.Sarma, "Three Level Hysteresis Current Controlled VSI for power injection and conditioning in grid connected solar PV systems," *Proc. Int. Conf. Power Electronics, Drives and Energy Systems (PEDES)*, Mumbai, India, 2014, pp. 1-5.

[89] M.V.M.Kumar, M.K.Mishra, C.Kumar,"A grid-connected dual voltage source inverter with power quality improvement features," *IEEE Trans. Sust. Energy*, vol. 6, no. 2, pp. 482-490, Feb 2015.

[90] Z.Zeng, H.Li, S.Tang, H.Yang, R.Zhao "Multi-objective control of multi-functional grid-connected inverter for renewable energy integration and power quality service," *IET Power Elec.*, vol. 9, no. 4, pp. 761-770, Mar 2016.

[91] F.Harirchi, M.G.Simões, M.Babakmehr, A.Al-Durra, "Multi-functional double mode inverter for power quality enhancement in smart-grid applications," *Proc. Int. Conf. Industry Applications Society Annual Meeting*, Portland, OR, USA, 2016, pp. 1-8.

[92] M.Parvez, M.F.Elias, N.A.Rahim, N.Osman, "Current control techniques for three-phase grid interconnection of renewable power generation systems: A review," *Solar Energy*, 2016, vol. 135, pp. 29-42.

[93] D.Campos-Gaona, R.Pena Alzola, J.L.Monroy-Morales, M.Ordonez, O.Anaya-Lara, W.E.Leithead, "Fast selective harmonic mitigation in multifunctional inverters using internal model controllers and synchronous reference frames," *IEEE Trans. Indus. Elec*., vol. 64, no. 8, pp. 6338-6349, Mar 2017.

[94] A.Safa, E.M.Berkouk, Y.Messlem, A.Gouichiche, "An improved sliding mode controller for a multifunctional photovoltaic grid tied inverter," *Journal of Renew. Sust. Energy*, vol. 9, no. 6, 065506, Nov 2017.

[95] M.A.G.De Brito, L.Galotto, L.P.Sampaio, "Evaluation of the main MPPT techniques for photovoltaic applications," *IEEE Trans. Indus. Elec*., 2013, vol. 60, no. 3, pp. 1156-1167, Mar 2013.

[96] A.Gupta, Y.K.Chauhan, R.K.Pachauri, "A comparative investigation of maximum power point tracking methods for solar PV system," *Solar Energy*, vol. 136, pp.236-253, Oct 2016.

[97] A.Nicholls, R.Sharma, T.K.Saha, "Financial and environmental analysis of rooftop photovoltaic installations with battery storage in Australia," *Applied Energy*, vol. 159, pp. 252-264, Dec 2015.

[98] W.Cole, H.Lewis, B.Sigrin, R.Margolis, "Interactions of rooftop PV deployment with the capacity expansion of the bulk power system," *Applied Energy*, vol. 168, pp. 473-481, Apr 2016.

[99] S.Sundaray, L.Mann, U.Bhattacharjee, S.Garud, A.K.Tripathi, "Reaching the sun with rooftop solar, New Delhi, India, The Energy and Resources Institute (TERI). 2014 62pp, http://mnre.gov.in/file-manager/UserFiles/Rooftop-SPV-White-Paper-low.pdf.

[100] P.Bhati, R.Kalsotra, "Solar Rooftop: Replacing diesel generators in residential societies," Centre for Science and Environment, New Delhi. 2017 http://cseindia.org/userfiles/Policy-Brief-Solar-Rooftop-Replacing-Diesel-Generators-in-Residential-Societies.pdf.

[101] S.Deambi, "Photovoltaic System Design: Procedures, Tools and Applications," ist ed. CRC Press, Boca Raton, Florida, USA, 2016, pp.1-280.

[102] K.Fekete, Z.Klaic, L.Majdandzic, "Expansion of the residential photovoltaic systems and its harmonic impact on the distribution grid," *Renewable Energy*, vol. 43, pp. 140-148, Jul 2012.

[103] Y.Yang, K.Zhou, F.Blaabjerg, "Current harmonics from single-phase grid-connected inverters—Examination and suppression" *IEEE Journ. Emerg. Selected Topics Power Elec*., vol. 4, no. 1,pp. 221-233, Mar 2016.

[104] A.R.Boynuegri, M.Uzunoglu, O.Erdinç, E.Gokalp, "A new perspective in grid connection of electric vehicles: Different operating modes for elimination of energy quality problems," *Applied Energy*, vol. 132, pp. 435-451, Nov 2014.

[105] S.S.Rangarajan, E.R.Collins, J.C.Fox, D.P.Kothari, "A survey on global PV interconnection standards," *Proc. Power and Energy Conference at Illinois (PECI)*, Champaign, IL, USA, 2017, pp. 1-8.

[106] S.B.Kjaer, J.K.Pedersen, F.Blaabjerg, "A review of single-phase grid-connected inverters for photovoltaic modules," *IEEE Trans. Ind. App.*, vol. 41, no. 5, pp. 1292-1306, Sep 2005.

[107] Y.Yang, F.Blaabjerg, "Overview of Single-phase Grid-connected Photovoltaic Systems," *Electric Power Comp. Sys.*, vol. 43, no. 12, pp. 1352-1363, Jul 2015.

[108] A.Panda, M.K.Pathak, S.P.Srivastava, "Enhanced power quality based single phase photovoltaic distributed generation system," *Intern. Journal of Elec.*, vol. 103, no. 8, pp. 1262-1278, Aug 2016.

[109] H.Saxena, A.Singh, J.N.Rai, "Design and performance analysis of generalised integrator-based controller for grid connected PV system," *Intern. Journal of Elec.*, vol. 105, no. 7, pp. 1079-1096, Jul 2018.

[110] S.Deo, C.Jain, B.Singh, "A PLL-less scheme for single-phase grid interfaced load compensating solar PV generation system," *IEEE Tran. Ind.Inf.*, vol. 11, no. 3, pp. 692-699, Apr 2015.

[111] A.F.Cupertino, H.A.Pereira, W.U.da Costa, S.R.Silva, "Multifunctional Inverters Applied in Grid-Connected Photovoltaic Systems," in *Proc. Fifth Brazilian Symposium on Electrical Systems – SBSE*, Foz do Iguaçu – Paraná, Brazil, 2014, pp. 1-7.

[112] L.S.Xavier, A.F.Cupertino, H.A.Pereira, "Ancillary services provided by photovoltaic inverters: Single and three phase control strategies," *Computers & Electrical Engineering*, vol. 70, pp. 102-121, Aug 2018.

[113] A.Chatterjee, K.Mohanty, V.S.Kommukuri, K.Thakre, "Design and experimental investigation of digital model predictive current controller for single phase grid integrated photovoltaic systems," *Renewable Energy*, vol. 108, pp. 438-448, Aug 2017.

[114] I.S.Kim, "Sliding mode controller for the single-phase grid-connected photovoltaic system," *Applied Energy*, vol. 83, no. 10, pp. 1101-1115, Oct 2006.

[115] N.A.Rahim, J.Selvaraj, "Implementation of hysteresis current control for single-phase grid connected inverter," in *Proc. 7th International Conference on Power Electronics and Drive Systems (PEDS)*, Bangkok, Thailand, 2007, pp. 1097-1101.

[116] R.D.Patidar, S.P.Singh, D.K.Khatod, "Single-phase single-stage grid-interactive photovoltaic system with active filter functions," in *Proc. Power and Energy Society General Meeting*, Providence, RI, USA, 2010, pp. 1-7.

[117] A.Helal, A.Nour, I.El-Mohr, "Multifunctional Single-Phase Single-Stage Grid-Connected PV System," in *Proc. Intern. Conf. Renewable Energies and Power Quality (ICREPQ'12)*, Santiago de Compostela, Spain, 2012, pp. 1-6.

[118] A.Martins, S.Vale, V.Sobrado, A.Carvalho, "Comparison of current control methods for grid-connected low-power single-phase converters," in *Proc. 40th Annual Conference of the IEEE Industrial Electronics Society (IECON)*, Dallas, TX, USA, 2014, pp. 4211-4217.

[119] P.K.Sahoo, P.K.Ray, P.Das, "Power quality improvement of single phase grid connected photovoltaic system," *Inter. Journal of Emerg. Elec. Power Sys*., vol. 18, no. 1, Feb 2017.

[120] Y.Singh, I.Hussain, B.Singh, S.Mishra, "Implementation of grid interfaced photovoltaic system with active power filter capabilities," *Inter. Trans. Elec. Energy Sys*., vol. 28, no. 11, e2616, pp. 1-13, Nov 2018.

[121] P.A.Dahono, "New hysteresis current controller for single-phase full-bridge inverters," *IET Power Elec*., vol. 2, no. 5, pp. 585-594, Sep 2009.

[122] E.R.Priandana, M.Saputra, Y.Prabowo, P.A.Dahono, "Analysis and design of variable double-band hysteresis current controller for single-phase full-bridge bidirectional converters," in *Proc. Intern. Symposium on the Technology Management and Emerging Technologies (ISTMET)*, Bandung, Indonesia, 2014, pp. 143-148.

[123] H.Komurcugil, "Double-band hysteresis current-controlled single-phase shunt active filter for switching frequency mitigation," *Intern. Jour. Elec. Power & Energy Sys*., vol. 69, pp. 131-140, Jul 2015.

[124] NI. Compact-RIO. Available online: http://www.ni.com/pdf/manuals/375714a.pdf

[125] https://www.opal-rt.com/wp-content/themes/enfold-opal/pdf/L00161_0331.pdf

[126] L.U.An, X.U.Qianming, M.A.Fujun, C.H.Yandong, "Overview of power quality analysis and control technology for the smart grid," *Journ. Mod. Power Syst. Clean Energy*, vol. 4, no. 1, pp. 1-9, Jan 2016.

[127] K.Nagaraju, P.S.Varma, B.R.Varma, "A current-slope based fault detector for digital relays," *in Proc. 2011 Annual IEEE India Conf., Hyderabad, India*, 2011, pp. 1-4.

[128] NI. NI-9239 Analog Module: http://www.ni.com/pdf/manuals/374184l.pdf .

[129] Tek. PA4000 Power Analyzer: https://www.tek.com/datasheet/pa4000-power-analyzer-datasheet

[130] A.Mortezaei, C.Lute, M.G.Simões, F.P.Marafão, A.Boglia, "PQ, DQ and CPT control methods for shunt active compensators—A comparative study," *in Proc. IEEE Energy*

Conversion Congress and Exposition (ECCE), Pittsburgh, PA, USA, 2014, pp. 2994-3001.

[131] A.Yazdani, R.Iravani, "Voltage-sourced converters in power systems: modeling, control, and applications," John Wiley & Sons, 2010, pp. 160-203.

[132] D.W.Hart, "Power electronics" Tata McGraw-Hill Education, 2011.

[133] A.Ghosh., S.Banerjee, "Design and implementation of type-II compensator in DC-DC switch-mode step-up power supply," *Proc. IEEE 3rd Int. Conf. on Computer, Communication, Control and Information Technology (C3IT-2015*), Academy of Technology, Hooghly, India, 2015, pp. 1–5.

[134] M.Haddad, S.Ktata, S.Rahmani, K.Al-Haddad, "Real time simulation and experimental validation of active power filter operation and control," *Mathematics and Comp. in Simulation*, vol. 130, pp. 212-222, Dec 2016.

[135] R.Patel, A.K.Panda, "Real time implementation of PI and fuzzy logic controller based 3-phase 4-wire interleaved buck active power filter for mitigation of harmonics with id–iq control strategy," *Intern. Journ. Electr. Power Energy Syst*., vol. 59, pp. 66–78, Jul 2014.

[136] J.Bélanger, P.Venne, J.N.Paquin, "The what, where and why of real-time simulation" *Proc. Planet RT*, 2010, pp. 37-49. https://www.opal-rt.com/wp-content/themes/enfold-opal/pdf/L00161_0436.pdf.

[137] E.Koutroulis, F.Blaabjerg, "Overview of maximum power point tracking techniques for photovoltaic energy production systems," Elec. Power Comp. Sys., vol. 43, pp. 1329-1351, Jul 2015.

[138] A.Gupta, Y.K.Chauhan and R.K.Pachauri,"A comparative investigation of maximum power point tracking methods for solar PV system," *Solar Energy*, vol. 136, pp. 236-253, Oct 2016.

[139] SolardesignTool:<http://www.solardesigntool.com/components/modulepanelsolar/Sunpower/514/SPR-305-WHT U/specification-data-sheet.html>

[140] J.P.Torreglosa, F.Jurado, P.García, L.M.Fernández, "Hybrid fuel cell and battery tramway control based on an equivalent consumption minimization strategy," *Control Engineering Practice*, vol. 19, no. 10, pp.1182-1194, Oct 2011.

[141] S.K.Khadem, M.Basu, M.F.Conlon, "Intelligent islanding and seamless reconnection technique for microgrid with UPQC," *IEEE Journal of Emerging and selected topics in Power Electronics*, vol. 3, no. 2, pp. 483-492, Jun 2014.

[142] L.Ibarra, A.Rosales, P.Ponce, A.Molina, R.Ayyanar, "Overview of real-time simulation as a supporting effort to smart-grid attainment," *Energies*, vol. 10, no. 6, 817, Jun 2017.

[143] Z.Jiang, G.Konstantinou, Z.Zhong, "Real-time digital simulation based laboratory test-bench development for research and education on solar pv systems," *in Proc. Univ. Power Engg. Conf. (AUPEC)*, Melbourne, Australia, 2017, pp. 1-6.

[144] OPAL-RT OP4500/4510: https://www.opal-rt.com/wp-content/themes/enfold-opal/pdf/L00161_0124.pdf.

[145] T.L.Mohamed, R.H.Mohamed, Z.Mohamed, "Development of auto tuning PID controller using graphical user interface (GUI)," *in Proc. of the Second Intern. Conf. Computer Engineering and Applications (ICCEA-2010)*, Bali Island, Indonesia, 2010, pp. 491-495.

[146] J.Garrido, M.Ruz, F.Morilla, F.Vázquez, "Interactive Tool for Frequency Domain Tuning of PID Controllers," *Processes*, vol. 6, no. 10, pp. 197, Oct 2018.

[147] Y.Yang, L.Hadjidemetriou, F.Blaabjerg, E.Kyriakides, "Benchmarking of phase locked loop based synchronization techniques for grid-connected inverter systems," *in Proc. 9th Intern. Conf. Power Electronics and ECCE Asia (ICPE ECCE Asia)*, Seoul, South Korea, 2015, pp. 2517-2524.

[148] Z.Zhang, Y.Yang, R.Ma, F.Blaabjerg, "Zero-voltage ride-through capability of single-phase grid-connected photovoltaic systems," *Applied Sciences*, vol. 7, no. 4, pp. 315, Mar 2017.

[149] https://in.mathworks.com/help/physmod/sps/powersys/ref/pll.html

[150] S.Gautam, R.Gupta, "Unified time-domain formulation of switching frequency for hysteresis current controlled AC/DC and DC/AC grid connected converters," *IET Power Elec.*. vol. 6, no. 4, pp. 683-692, Apr 2013.

Appendix

Appendix A

Table A.1 Rooftop PV module specifications

Parameter	Value
Peak Power (+/-5%) *(P_{max})*	305 W
Number of cell per module –monocrystalline silicon	96
Rated voltage *(V_{mp})*	54.7 V
Rated current *(I_{mp})*	5.58 A
Open circuit voltage *(V_{oc})*	64.2 V
Short circuit current *(I_{sc})*	5.96 A
Series resistance *(R_s)*	0.037998
Parallel resistance *(R_p)*	993.51 Ω
Saturation current *(I_{sat})*	1.1753×10^{-8} A
Photovoltaic current *(I_{ph})*	5.9602 A

Publications from this Research Work

Journals: Published (SCI/Scopus Indexed)

- **O.V.S.R.Varaprasad**, A.S.Bubshait, D.V.S.S.Siva Sarma, and M.G.Simões. "**Real-Time Control of Hybrid Active Power Filter using Conservative Power Theory in Industrial Power System**," ***IET Power Electronics*** 10, no.2, **(2017)**: *pp. 196-207.*
- **O.V.S.R.Varaprasad**, D.V.S.S.Siva Sarma, H.K.M.Paredes, and M.G.Simões. "**Enhanced Dual-Spectrum Line Interpolated FFT with Four-Term Minimal Sidelobe Cosine Window for Real-Time Harmonic Estimation in Synchrophasor Smart-Grid Technology.**" ***Electronics,*** 8, no. 2 **(2019)**: 191.
- **O.V.S.R.Varaprasad**, D.V.S.S.Siva Sarma and M.G.Simões. "**Scalable Single-Phase Multi-Functional Inverter for Integration of Rooftop Solar-PV to Low-Voltage Ideal and Weak Utility Grid," *Electronics,*** 8, no. 3 **(2019)**: 302.

Journals: In draft

- **O.V.S.R.Varaprasad**, D.V.S.S.Siva Sarma, A.Mortezaei, T.D.C.Busarello, M.G.Simões. "**Conservative Power Theory Battery Storage based Multifunctional Grid-Connected PV Inverter for a Think-Ahead Decision High-Quality Power Algorithm"**
- **O.V.S.R.Varaprasad**, D.V.S.S.Siva Sarma "**Adaptive Windowed Interpolated FFT algorithm for Time-Varying Multi Harmonic Estimation"**

Conferences: Published

- **O.V.S.R.Varaprasad**, D.Bharath Kumar and D.V.S.S.Siva Sarma **"Three Level Hysteresis Current Controlled VSI for Power Injection and Conditioning in Grid Connected Solar PV Systems"** IEEE International Conference On Power Electronics, Drives And Energy Systems (PEDES 2014), IIT Bombay, Mumbai, India, during December 16^{th}- 19^{th}, 2014.
- **O.V.S.R.Varaprasad**, D.V.S.S.Siva Sarma and Rakesh Kumar Panda **"Advanced Windowed Interpolated FFT Algorithms for Harmonic Analysis of Electrical Power System"** 18^{th} National power System Conference (NPSC 2014), IIT Guwahati, Guwahati, India, during December 18^{th}- 20^{th}, 2014.

CURRICULUM-VITAE

Name:	O.V.S.R.Varaprasad
Post-Secondary Education and Degrees:	• Pondicherry University, Pondicherry, 2002-2006, Bachelor of Technology in Electrical and Electronics Engineering. • Jawaharlal Nehru Technological University Hyderabad, 2008-2010, Master of Technology in Power Electronics and Electric Drives.
Professional Skills	Research, Teaching, Consulting.
Software packages:	MATLAB/Simulink 2010, 2011, 2013, PSIM, LabVIEW 2014, RT-Lab 11, Microsoft Word, Power point, Excel, Microsoft Visio 2007, 2010, Code composer studio 3.3,5.
Hardware Exposure:	dSpace 1104, National Instruments cRIO - 9082, TMS 320F28335 Experimental kit, OPAL-RT OP 4500
Programming Languages:	C, HTML
Operating System:	Windows XP, 7,10
Honours, awards and funding during Doctor of Philosophy at National Institute of Technology Warangal, Telangana State, INDIA. (2012-2019)	• Ministry of Human Resources and Development (MHRD), INDIA Fellowship for Doctoral Study at National Institute of Technology Warangal, June 2012 – June 2016. • Bhaskara Advanced Solar Energy (BASE) Internship funded by Department of Science and Technology, Govt. of India through its Solar Energy Research Initiative, and the Indo-U.S. Science and Technology Forum (IUSSTF) to do collaborative research with Prof. Marcelo Godoy Simões for one semester at Advanced Control of Energy Power Systems Laboratory, Colorado School of Mines, 1610 Illinois Street Golden, CO 80401, USA, June 2015 – November 2015. • Power System Operation Corporation Limited (POSOCO) India - Power System Award – 2017 for the current Ph.D. work under Doctoral Category, February 2017.